TECHNISCHE UNIVERSITÄT MÜNCHEN

Lehrstuhl für Flugsystemdynamik

Structurally Constrained Lateral Control of a Diamond-Shaped Unmanned Aircraft

Dipl.-Ing. Univ. Stanislav Braun

Vollständiger Abdruck der von der Fakultät für Maschinenwesen der Technischen Universität München zur Erlangung des akademischen Grades eines

Doktor-Ingenieurs

genehmigten Dissertation.

Vorsitzender:	Prof. Dr.-Ing. Manfred Hayek
Prüfer der Dissertation:	1. Prof. Dr.-Ing. Matthias Heller
	2. Prof. Dr.-Ing. Mirko Hornung

Die Dissertation wurde am 06.12.2018 bei der Technischen Universität München eingereicht und durch die Fakultät für Maschinenwesen am 02.07.2019 angenommen.

Vorwort

"A righteous man falls down seven times and gets up."
— King Solomon, Proverbs, 24:16

Die vorliegende Arbeit entstand während meiner Tätigkeit als wissenschaftlicher Mitarbeiter am Lehrstuhl für Flugsystemdynamik in den Jahren 2009 bis 2017.

Mein Dank gilt Herrn Univ.-Prof. Dr.-Ing. Matthias Heller für die fachliche Betreuung dieser Arbeit und für die Zeit, die er sich für unzählige spannende Diskussionen genommen hat. Ich danke dem Lehrstuhlinhaber Herrn Univ.-Prof. Dr.-Ing. Florian Holzapfel für die Möglichkeit an sehr vielen interessanten Projekten mitgewirkt haben zu dürfen und das mir entgegengebrachte Vertrauen. Ferner bedanke ich mich bei Herrn Univ.-Prof. Dr.-Ing. Mirko Hornung für die Übernahme des Koreferats und bei Herrn Univ.-Prof. Dr.-Ing. Manfred Hayek für die Führung des Prüfungsvorsitzes.

Ich danke meinen Kolleginnen und Kollegen am Lehrstuhl für Flugsystemdynamik für die Unterstützung bei der Bewältigung der Projektarbeit. Besonders hervorheben möchte ich die Kollegen Markus Geiser, Philip Wolze, Benjamin Braun, Martin Kügler und David Seiferth.

Ganz besonderer Dank gilt meiner Ehefrau Sweta, die mich stets bedingungslos unterstützte. Dabei war sie bereit, meine Träume zu ihren zu machen und in der langen Zeit auf Vieles zu verzichten.

München, Dezember 2018 Stanislav Braun

Contents

Acronyms

AC/AH	Attitude-Command/Attitude-Hold
A/C	Aircraft
ACE	Actuator Control Electronics
ADM	Aerodynamic Data Module
ADS	Air Data System
AFS	Auto Flight System
AGL	Above Ground Level
AHRS	Attitude and Heading Reference System
ALT	Altitude
AMS	Attainable Moment Subset
AoA	Angle-of-Attack
AoF	Flank Angle
AoS	Angle-of-Sideslip
ATOL	Automatic Takeoff and Landing
BFCC	Basic Flight Control Computer
BFCS	Basic Flight Control System
BIT	Built-In-Test
BLOS	Beyond Line Of Sight
CAP	Control Anticipation Parameter
CEA	Constrained Eigenstructure Assignment
CFD	Computational Fluid Dynamics
CG	Center of Gravity
CFRP	Carbon Fiber Reinforced Plastic
COTS	Commercial-Off-The-Shelf
CPS	Cumulative Power Spectrum
CSAS	Control and Stability Augmentation System
DC	direct current
DGPS	Differential Global Positioning System
DLR	Deutsches Zentrums für Luft- und Raumfahrt

DoF	Degrees of Freedom
EA	Eigenstructure Assignment
ECU	Engine Control Unit
EMC	Electromagnetic Compatibility
EP	External Pilot
EPCS	External Pilot Control Station
EPDL	External Pilot Data Link
FCC	Flight Control Computer
FCS	Flight Control System
FDL	Flight Data Link
FF	First Flight
FFT	Fast Fourier Transformation
FMCS	Flight Management Control Station
FMS	Flight Management System
FO	Flight Operator
FPV	First Person View
FSD	Institute of Flight System Dynamics, Technical University of Munich
FTI	Flight Test Instrumentation
GCE	Gear Control Electronics
GCS	Ground Control Station
GNSS	Global Navigation Satellite System
GPS	Global Positioning System
HDG	Heading
HIL	Hardware-In-The-Loop
HLC	High-Level Commands
HOS	High Order System
H/W	Hardware
IAS	Indicated Air Speed
IMU	Inertial Measurement Unit
LAHOS	Landing Approach Higher Order System
LATHOS	Lateral Higher Order System
LF	Level Flight
LLC	Low-Level Commands
LOES	Low Order Equivalent System

LOI	Level Of Interoperability
LOS	Line Of Sight
LPV	Linear Parameter Varying
LQG	Linear-Quadratic-Gaussian
LQR	Linear-Quadratic regulator
LTI	Linear Time Invariant
MDL	Mission Data Link
MDTOW	Maximum Design Take Off Weight
MEMS	Microelectromechanical systems
MIL	Model-In-The-Loop
MIMO	Multiple Input Multiple Output
MLC	Medium-Level Commands
MLW	Maximum Landing Weight
MMS	Mission Management System
MO	Mission Operator
MPCS	Mission and Payload Control Station
MTOW	Maximum Take Off Weight
NAV	Navigation System
NED	North-East-down coordinate system
OAT	Outside Air Temperature
OLOP	Open Loop Onset Point
OWE	Operating Weight Empty
PDU	Power Distribution Unit
PFD	Primary Flight Display
PIO	Pilot-In-The-Loop Oscillation
PU	Pull-Up
PO	Push-Over
PSD	Power Spectral Density
QLT	Quick Look Terminal
RC	Remote Control
RC/AH	Rate-Command/Attitude-Hold
RMIA	Radio Modem Interface Air
RMIG	Radio Modem Interface Ground
RMS	Root Mean Square

RPA	Remotely Piloted Aircraft
RPAS	Remotely Piloted Aircraft System
RPV	Remotely Piloted Vehicle
RTB	Return to Base
SE	System's Engineer
SISO	Single Input Single Output
SPM	simplified precision model
SPD	Speed
S/W	Software
TOW	Take Off Weight
UAS	Unmanned Aircraft System
UAV	Unmanned Aerial Vehicle
UCAV	Unmanned Combat Aerial Vehicle
UCE	Usable Cue Environment
UHF	Ultra High Frequency
VHF	Very High Frequency
VLO	Very Low Observability
VT	Vertical Tail
V&V	Validation & Verification
WGS84	World Geodetic System 84
WoW	Weight-on-Wheel

Symbols

$\boldsymbol{A}_{cl}$	closed-loop system matrix
b	wing span
C_{ij}	aerodynamic derivatives
$\bar{c}$	mean aerodynamic chord
e_x	the error in variable x w.r.t. the commanded x
F	force
f	frequency
$G_{\delta n}$	noise sensitivity transfer function from noise input to actuator output
h	altitude
l_δ	control surface reference length
l_{VT}	effective lever arm from aerodynamic reference point to the vertical tail
M_{H,δ_i}	hinge moment at i-th flap
N	dynamic scaling factor
n	white noise
n_y	acceleration in body's y-axis, normalized by g
n_z	load factor
p	roll rate
p_s	static pressure
p_t	total pressure
q	pitch rate
$\bar{q}$	dynamic pressure
R	transmission ratio
r	yaw rate
$(r_{inh})_{DR}$	inherent ratio of Dutch-roll eigenvector entries Φ and β
S	reference area
S_δ	control surface reference area
s	reference length for lateral motion or Laplace variable
T_R	roll subsidence time constant
T_S	spiral mode time constant

T_2	time to double amplitude
t_s	settling time
V	speed or voltage
V_A	aerodynamic speed
v_x	entry in eigenvector v that is related to the state x
α	angle of attack
β	sideslip angle
β_A	aerodynamic angle of sideslip
β_W	sideslip angle resulting from wind
β_f	flank angle
β_{crab}	crab angle
γ	flight path angle
δ	control surface deflection
δ_{equiv}	equivalent control surface deflection
ζ_0	outboard flap preloading
μ_A	aerodnymic flight path bank angle
μ_K	flight path bank angle
σ	standard deviation
σ_n	standard deviation of the noise
τ_d	time delay
τ_e	effective time delay
τ_p	phase delay
Φ	bank angle
χ	course angle
Ω	spatial frequency
ω	angular frequency
ω_0	natural frequency
ω_{BW}	bandwidth frequency
$\omega_{BW,phase}$	bandwidth determined from phase
$\omega_{BW,gain}$	bandwidth determined from gain
ω_c	unity gain crossover frequency
ω_{onset}	onset frequency
I_{xx}, I_{yy}, I_{zz}	moments of inertia (entries reciding on the diagonal of the moment of intertia tensor)
L, M, N	roll, pitch and yaw moments

X, Y, Z	component of force in x,y,z-axis
f_x, f_y, f_z	component of specific force
u, v, w	component of speed in x,y,z-axis
u_W, v_W, w_W	wind components in body-fixed coordinate system
ξ, η, ζ	equivalent control surface deflections (aileron, elevator and rudder)
$\varphi, \dot{\varphi}, \ddot{\varphi}$	deflection, deflection rate and acceleration of the actuator

Subscripts

0	reference operating point or outboard flaps preloading
A	aerodynamic
ach	achievable
act	actuator
av	average
B	body-axes coordinate system
cl	closed-loop
$crab$	crab angle
d	delay
des	desired
DR	Dutch-roll
dyn	dynamic
$equiv$	equivalent
f	filter
fb	feedback
ff	feed-forward
H	hinge
inh	inherent
K	kinematic
l	roll moment
$land$	touchdown on ground
LE	leading edge
lo	lower limit
m	pitch moment
$meas$	measured
n	yaw moment or white noise
nom	nominal
osc	oscillation
R	roll subsidence or roll mode
req	requirement or required
S	stability-axes coordinate system
S	spiral mode
s	specified
$sens$	sensor
$stat$	static
TE	trailing edge
tol	tolerance
$turb$	turbulence
u	unspecified
up	upper limit
VT	vertical tail
W	wind

1. Introduction

Today, the availability of powerful computers along with effective virtualization of engineering processes, has made it possible to implement, test and demonstrate complex systems entirely in a simulated environment. Unfortunately, a large portion of engineering research in the field of flight control remains in this virtual environment forever with the resultant journal papers and conference proceedings often finishing in a dead end.

Bringing research into life and demonstrating the results in real world applications is especially important when considering complex technologies with a high degree of modeling uncertainties and many unknowns. It provides the ultimate and irrevocable confirmation of research results. Furthermore, the demonstration of research in real world makes it accessible to the non-specialized audience and hence tangible, increasing its radiance and paving the way for application of new technologies in our daily life.

Today, the popularity of unmanned aircraft is on the rise. The hope is that such systems will perform dull, dirty and dangerous jobs for the mankind. The present work aims at contributing to the evolution of unmanned flight by providing a real world application showcase of a flight control system for a novel innovative diamond-shaped aircraft configuration.

1.1. Initial Situation and Motivation

In recent years multiple governments and companies around the world have undertaken substantial efforts to promote the development of a new generation of unmanned combat aircraft with advanced stealth characteristics. The use cases for unmanned stealth aircraft are manifold. They range from surveillance and strategic intelligence gathering to air-to-ground attacks. Unmanned stealth technology enables penetration deep into hostile territories without endangering the pilot. In the near future, novel applications in the context of manned-unmanned teaming may arise where unmanned aircraft could support manned missions being, for example, wingmen of fighter aircraft. By removing the pilot from the cockpit, limitations resulting from a human pilot being on board are eliminated. The relocation of the pilot to the ground broadens the design space. The systems become smaller and the space gained can be used for (e.g.) an increase in payload. New configurations with enhanced capabilities can be developed and thereby, new aircraft classes may be established.

In this context, many research programs were launched in the last few decades from which multiple demonstrator aircraft evolved. In the early 2000s, US companies Boeing and Northrop Grumman built, part of the J-UCAS program, their unmanned combat air vehicle demonstrators X-45 and X-47. In a follow-up program of the United States Navy UCAS-D, the X-47 demonstrator (see figure 1.1) was further developed and subsequently its carrier landing capabilities were demonstrated in 2012.

European companies, as well, recognized the importance of unmanned systems for future armed forces. In the late 1990s, the company Dassault Aviation launched the

Figure 1.1.: Northrop Grumman X-47B (photo: US Navy)

LOGIDUC Program, with the aim to develop its UCAV design capabilities [59]. The program incorporated three phases. In the first phase the small scale demonstrator, AVE-D Petit Duc was built and tested. The focus was on feasibility of the stealth concept. In the second phase, in 2004, a significantly more complex AVE-C Moyen Duc was developed by Dassault. As one of the results of the program, the European experimental stealth UCAV nEUROn (see figure 1.2) evolved and had its maiden flight in 2012. In parallel to Dassault and its European partners, BAE Systems developed a comparable configuration named Taranis, which had its maiden flight in 2013. Further notable configurations are the Russian MIG Skat or the Indian DRDO AURA.

All these systems can be categorized as Blended Wing Body aircraft with a "λ-wing". In their final design configuration, the aircraft are tailless. That means that they do not incorporate vertical stabilizers. Most of these aircraft are driven by single engines, which are embedded in the fuselage of the aircraft. Engine in- and out-take are often located on the upper side of the aircraft, in order to reduce the radar signature.

In addition to the financial heavyweight industrial projects mentioned above, a large variety of low-budget, small-scale and highly innovative projects have been developed by young researchers around the world. Their strength is in their flexibility, agility and independence. The resulting solutions often have a high degree of novelty and their contribution to the overall process of innovation is very important.

This innovative strength was recognized by some managers of the AIRBUS R&D team. In the late 2000s, an attempt was made to involve German research institutions in a national free research project in order to bring industry and science together, and to merge the best of both worlds into a single project. Consequently, AIRBUS Defence and Space (formerly EADS Defence & Security) launched the so-called Open Innovation initiative to allow academia and industry to join forces in the field of research on Unmanned Aerial Vehicle (UAV) technologies. The aim of this initiative is to increase the readiness level of key technologies, in order to pave the way towards development of a future European UAV.

Figure 1.2.: nEUROn (photo: Alenia Aermacchi)

SAGITTA is the first project within the framework of the Open Innovation initiative. It consists of two complementary development areas which are advanced in parallel, namely: research in the field of key technologies for future UAVs, and the development of a tailless jet-powered, diamond-shaped research aircraft (hereinafter referred to as the SAGITTA Demonstrator) as a platform for testing these technologies. Multiple national research organizations have joined the consortium and contribute their know-how and expertise to the project.

Several use cases were defined by AIRBUS in earlier studies. One of the use cases for application of the SAGITTA Demonstrator is provided in [29]. It describes a so-called target identification task, that is, reconnaissance incorporating a high degree of automation w.r.t. flight guidance, navigation and control and automatic target identification and categorization. This, and further use cases pose challenging requirements especially on the stealth characteristic of the aircraft and eventually culminate in basic configuration parameters of the system: the SAGITTA Demonstrator will represent an aircraft of 12 m wingspan constructed to a scale of 1:4 [58]. The scaled demonstrator shall have a maximum takeoff weight of 150 kg. The basic form of the aircraft is given by a rhombus with a leading edge wing sweep of $\varphi_{LE} = 55°$ and a trailing edge sweep of $\varphi_{TE} = 25°$. The airfoil is symmetrically shaped in order to enable permanent "inverted" flight, hence an orientation with a bank angle of $\Phi = 180°$. In its final configuration, the aircraft is tailless, and therefore, has no vertical tail. The aircraft shall incorporate two jet engines and a retractable tricycle landing gear. As a result, the engine intakes and outtakes as well as the landing gear openings shall all be located on the same side of the aircraft.

Most of these prerequisites to the design of the system are driven by the requirements of the stealth characteristics of the aircraft. They represent fundamental features for the development of the SAGITTA Demonstrator and its systems.

The project is divided into multiple phases. The target of the first phase is to design and build the Remotely Piloted Aircraft System (RPAS). This incorporates all basic systems that are required for automatic performance of the intended flight mission. The first phase ends with the first flight campaign and by putting the aircraft into experimental operation. Hence, this phase is a major foundation for any future development. Relying on the results of the project's first phase, further phases focus on novel technologies and their validation in the SAGITTA Demonstrator.

In order to master the first flight campaign safely, and as means of risk reduction, several modifications are applied to the system. In the initial project phase the aircraft was expected to be neutrally stable or unstable in the lateral motion and difficult to stabilize using lateral control effectors. Hence, two detachable vertical tails were added to the aircraft in order to increase its inherent lateral stability margins. Furthermore, the decision has been made to keep the landing gear deployed during the first flight campaign. Therefore, in the first project phase it will not be necessary to consider either the retraction mechanism itself or adjustments of the control system w.r.t. (for example) the Center of Gravity (CG) shift due to landing gear retraction. Further simplification is achieved by avoiding complex maneuvering in the first flight campaign, such as rolling the aircraft into inverted flight orientation and back.

1.2. Major Objectives, Scope of Work and Challenges

The present work focuses on flight dynamics and control of the SAGITTA Demonstrator. It provides a deep insight into the challenges, the work processes and the outcomes in the field of flight control on the way towards the first flight of the SAGITTA Demonstrator. The goal of the work is the design of a robust Flight Management System (FMS), which addresses the challenges that arise from the novel aircraft shape and takes into account configuration- and project-specific constraints. Thereby, the focus is on the algorithm, gain design and validation of the Control and Stability Augmentation System (CSAS) for lateral motion, which is a major component of the FMS. For the sake of completeness, further topics, like system architecture design, are briefly discussed enabling a holistic view on the system.

As with most novel aircraft, the design of the SAGITTA Demonstrator is accompanied by a high degree of technical risk and multiple technical challenges. Many of them are posed by the flight dynamics of the configuration. Some of these challenges are briefly discussed in the following.

The aircraft provides low lateral stability margins. Even with vertical tails attached, the aircraft requires artificial stability augmentation in order to satisfy the requirements on Flying Qualities. Hence, it is only capable of being flown safely, when such artificial stabilization is active. Furthermore, due to the high wing sweep, the aircraft is subject to high roll-yaw couplings, leading to undesired oscillations in flight and creating difficulties in controlling the aircraft. The novel control surface layout that is described in [84] poses another challenge to the design of the control system. Due to the small aspect ratio of the wing, the forward sweep of the trailing edge of the aircraft and the location of the control surfaces relative to the vertical tails, large undesired control-induced couplings are expected. These couplings occur through interference of the control surfaces between each other and with the vertical tail. This will be discussed in chapter 3 in more detail. Furthermore, due to complex aerodynamic characteristics of the flap system, the inherent aircraft dynamics and the effectiveness of control surfaces especially, are subject to a high degree of uncertainty. Further problems arise from the down-scaling of the aircraft, whereby one of the problems is the lack of available requirements w.r.t. Flying Qualities of scaled aircraft. This is addressed in chapter 4.

As can be seen from the discussion above, the development of the FMS must address a multitude of technical issues. The system to be designed shall improve the stability characteristics of closed-loop lateral dynamics, reduce the motion couplings to an acceptable degree, and be able to cope with the high aerodynamic uncertainties arising from the complex aerodynamics of the aircraft shape in combination with the novel flaps layout. Furthermore, new requirements w.r.t. flight dynamics of scaled aircraft need to be determined and applied to the system in order to achieve excellent Flying Qualities.

In addition to the presented challenges in the field of aircraft flight dynamics, further issues arise from the aircraft configuration. These are, inter alia, the reduction in available space and restrictions on weight. Moreover, the limited amount of funds for procurement and development of components are further constraints that must be managed. While the components need to be lighter and affordable, and thus must rely on new miniaturization technologies such as MEMS, the requirements w.r.t. navigation accuracy of the overall system are not significantly altered compared to those of manned systems. These challenges need to be addressed, which, as will be shown in this work, will significantly influence the design of the FMS.

Since great importance is attached to formal verification and clearance of the Flight Management System by the industrial partner, a further major challenge is the mastery of processes of large scale industry by a small research and development team.

1.3. Approach and Outline

This work provides an insight into the development, validation and verification of the CSAS for lateral dynamics. Longitudinal control, the development of outer control loops and other system functionalities are not within the scope of this work, and thus, are only briefly described, where needed, to aid the understanding.

As described above, the major objective of the present work lies in the design, analysis and clearance of the inner control loops (CSAS) for a novel unmanned aircraft. Prior to the design of the CSAS, a comprehensive requirements analysis is compiled. The often neglected topics related to Flying Qualities of scaled unmanned aircraft are discussed and analyzed, taking into account the particularities of the Attitude-Command/Attitude-Hold (AC/AH) system resulting from the chosen controller structure. The consequent incorporation of requirements in the controller structure and in the gain design of the inner control loops, as well as the verification of the controller against the requirements are further central aspects of this work.

A comprehensive step-by-step evolution of the controller structure and the gain design is presented. Thus, intermediate stages of the development are discussed in great detail and thought processes, as well as causation of decisions are made transparent to the reader. Design decisions resulting from analysis are explained and countermeasures to identified problems are proposed.

Great importance is attached to the physical interpretation and simplicity of the controller structure. Therefore, unusual and abstract arrangements in the controller structure are avoided. In general, the performance of the system is given up in favor of robustness.

The verification of the CSAS is mainly based on linear analysis and classical well-established methods. It provides a complete set of analyses enabling the approval of the controller for the first flight. Beyond the well-established flight control clearance analyses, methods that are based on Power Spectral Density (PSD) are tailored to the problem at hand and applied to analyze the impact of sensor characteristics and atmospheric disturbances on closed-loop dynamics, which is one of the unique features of this work.

Last but not least, model-based design, validation and verification techniques play an important role. The consequent modeling of realistic system behavior and system's environment together with the consideration of uncertainties and failure scenarios, provides the only available means to predict the system's possible range of behavior in flight. This approach led to a significant success, namely a successful first flight.

1.4. Contribution of the Thesis, Novelties

The main contributions of this thesis to future UAV development are as follows.

Comprehensive assessment of Flying Qualities requirements for lateral control of unmanned aircraft

This work provides a comprehensive analysis of the applicability of existing lateral Flying Qualities requirements for manned aircraft to unmanned systems. In contrast to, for example [18], the focus is not on automatic flight, but on manual control by an external pilot. The work discusses the specifics of an AC/AH response type for fixed wing aircraft and provides an analysis of applicable Flying Qualities specifications and Pilot-In-The-Loop Oscillation (PIO) analysis methods. In order to obtain a complete picture, the analysis is not only based on de facto standards for fixed wing aircraft, but also considers standards for rotorcraft, research reports and proposals for extension of Flying Qualities-related standards.

Furthermore, the approach of tailoring the requirements to the aircraft size by means of dynamic scaling, which is exemplary applied in [22], is consequently implemented for lateral Flying Qualities requirements of the SAGITTA Demonstrator.

Proposal of systematic flight control structure design based on extended eigenvector sensitivity analysis

This work documents a step-by-step evolution of a flight control algorithm architecture. The approach is based on the so-called eigenvector sensitivity analysis. For the work at hand, the eigenvector sensitivity analysis has been further developed in order to enable a systematic feedback gain suppression which finally results in a significant simplification of the flight controller structure. Furthermore, the developed approach leads to a novel, non-standard eigenstructure specifications which is used for gain design of the controller.

Application of Constrained Eigenstructure Assignment to a novel innovative aircraft design

The main challenge of this work is to deal with the extraordinary aircraft dynamics. One contribution therefore, is the application of the Constrained Eigenstructure Assignment-based output feedback method to a novel type of aircraft. Due to the physical constraints of the configuration, a new specification for the Dutch-roll eigenvector is derived, providing reduction of roll-yaw couplings rather than complete decoupling.

Further contributions

Further important contributions of this work are:

- presentation of a methodology to incorporate turn compensation into the Eigenstructure Assignment process
- feed-forward filter design based on the Open Loop Onset Point (OLOP) analysis methodology
- novel signal filter design for controller feedback, providing a methodology for selection of the filter's natural frequency based on actuator activity requirements

1.5. Clarification of Wording

UAV, UAS, RPA, RPAS

In recent years, a multitude of definitions and abbreviations has been created to refer to aircraft without a human pilot on board. One of the most common names is Unmanned Aerial Vehicle. In this term, the focus is on the aircraft itself. As the unmanned technology has evolved, systems, that are associated with the aircraft, namely the ground control station and ground support equipment have become more and more important. To reflect this, the term Unmanned Aircraft System (UAS) was introduced. The UAS describes the sum of all components that are required to operate an unmanned aircraft. It may include several aircraft, Ground Control Stations (GCSs), Mission and Payload Control Stations (MPCSs), aircraft launch devices, and further on-ground and in-air infrastructure such as Differential Global Positioning System (DGPS) base stations, relays aircraft etc.

Lately the terms Remotely Piloted Aircraft (RPA) and RPAS have become popular. They nicely illustrate the operational concept of most unmanned aircraft and the fact, that today's unmanned aircraft and their systems typically are controlled by human pilots and do not take decisions autonomously. It is important to make this point known, in order to improve the acceptance of unmanned systems by the general public. The terms RPA and RPAS have become de facto standard and are currently used by most governmental and rule-making authorities.

In this work, the terms UAV and RPA are used synonymously to describe the aircraft and all the components that are integrated into the aircraft shell. By comparison, when using the terms UAS and RPAS the focus is on the overall system including on-ground and in-air elements.

FMS and CSAS

Due to project constraints, the definition of the FMS may differ from those used in standard literature. The FMS includes all airborne sensors for flight control, flight control computers and communication systems in the SAGITTA Demonstrator. For a detailed overview of the FMS the reader is referred to chapter 2. The flight control algorithms implemented in the FMS typically incorporate several cascaded controllers and can be separated into multiple systems. One of the systems, often referred to as the "Inner Loop" due to its location, is the so-called CSAS. As the name suggests, the main function of the CSAS is the basic aircraft stabilization throughout the flight envelope by feeding back the aircraft state measurements and outputs to the control surfaces, and the provision of a consistent and predictable aircraft behavior to pilot inputs and outer controller cascades (e.g. the autopilot and trajectory controller).

2. The Platform: SAGITTA Demonstrator

Within the framework of the Open Innovation initiative a novel Remotely Piloted Aircraft System has been developed. The main elements of the RPAS are the so-called SAGITTA Demonstrator which is an unmanned aircraft of a diamond shape incorporating the FMS and the Ground Control Station including a DGPS base station. In this chapter, the aircraft, as well as the main components relevant for flight control, are presented. Furthermore, the control concept and the reference mission are featured.

2.1. The Aircraft

The SAGITTA Demonstrator is a diamond-shaped unmanned aircraft with a wingspan of 3 m and a Maximum Design Take Off Weight (MDTOW) of 144 kg. It is almost entirely built of Carbon Fiber Reinforced Plastic, and is equipped with two BF-300F jet engines manufactured by BF Turbines. Each of the engines provides 300N of uninstalled thrust. The aircraft has a retractable landing gear in a tricycle configuration featuring nose wheel steering and an electro-hydraulic braking system. A three-side view of the aircraft is provided in figure 2.1.

In order to achieve Very Low Observability (VLO), openings in the fuselage are concentrated on one side of the aircraft. Air intakes and outtakes, as well as landing gear and maintenance doors, are located on the so-called "dirty side" or "dirty shell" of the aircraft. The other side is called the "clean side" or "clean shell" since it has almost no scattering sources and thus is hardly detectable by the radar. The aircraft takes off with the dirty side facing to the ground. After takeoff, the aircraft is intended to change into inverted flight causing the clean shell to be turned towards the ground. For landing, the aircraft returns to its initial orientation. The hull of the SAGITTA Demonstrator is therefore almost symmetrical to ensure it performs equally well in both normal (dirty shell pointing down) and inverted (dirty shell pointing up) flight.

The SAGITTA Demonstrator is equipped with eight control surfaces. The inboard and midboard flaps are simple, conventional control devices with their hinge line located parallel to the trailing edge of the aircraft. The left and right outboard flaps are in fact split flaps, with each having two independently movable surfaces. One of the surfaces is located on the clean side of the aircraft and the other on the dirty side. The outboard flaps have their hinge lines at the leading edge of the aircraft. The control surface layout is shown in figure 2.2 and more information is provided in [84], where the layout is referred to as "Conventional Flap Layout". All control surfaces are driven by electro-mechanical actuators. Due to the kinematics employed, the movement of the outboard flaps is limited to positive deflections (downwards) for dirty-side flaps and to negative deflections (upwards) for clean-side flaps.

A convention for the naming of the control surfaces using abbreviations has been established. The names of the flaps are abbreviated using either two or three letters. In this convention, the first letter indicates the flap location, "o" for outboard, "m" for midboard or "i" for inboard. The second letter indicates whether the flap is on the

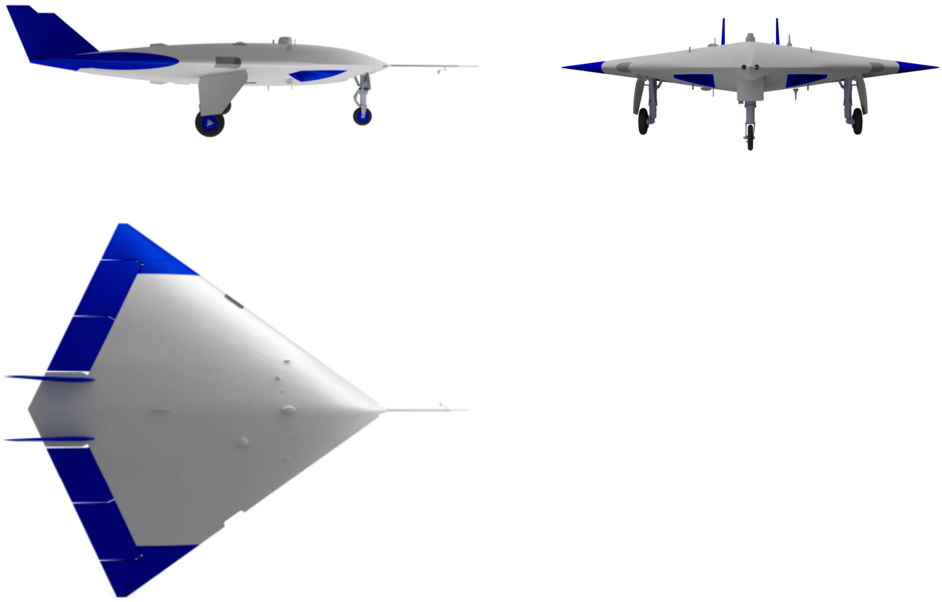

Figure 2.1.: Three-view rendering of the SAGITTA Demonstrator with detachable vertical tail and deployed landing gear

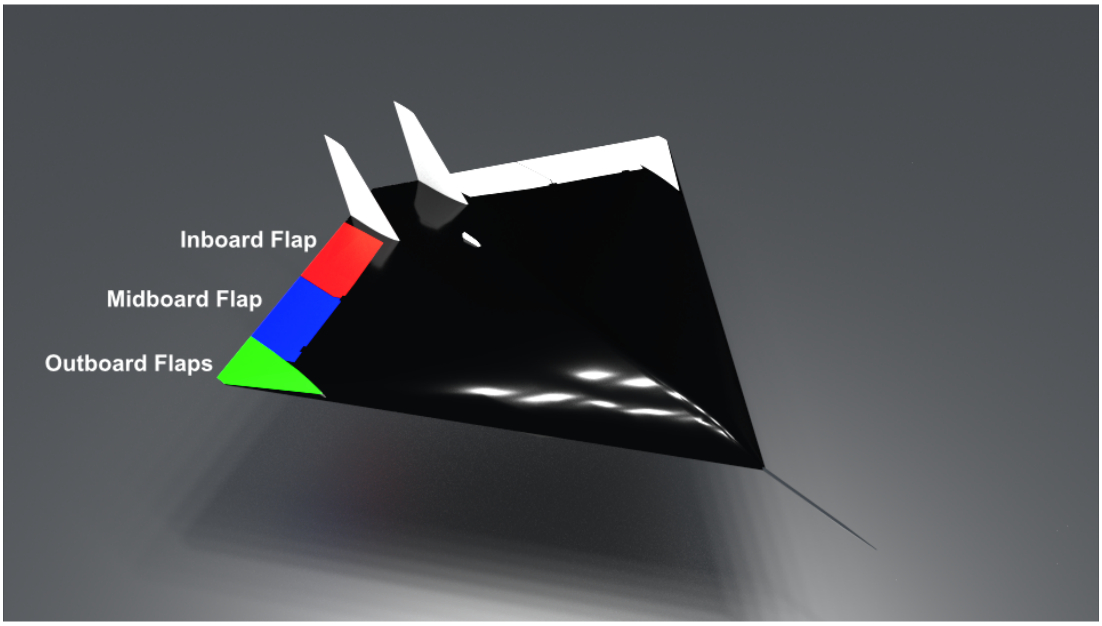

Figure 2.2.: Control Surface Layout

First character	Outboard, Midboard, Inboard	$\boldsymbol{o}xx, \boldsymbol{m}x, \boldsymbol{i}x$
Second character	left (port), right (starboard)	$x\boldsymbol{l}(x), x\boldsymbol{r}(x)$
Third character (Split Flaps only)	dirty side, clean side	$ox\boldsymbol{d}, ox\boldsymbol{c}$

Table 2.1.: Control surface abbreviation scheme

left (l) or right (r) side of the aircraft. A third letter is used to distinguish between the clean (c) and dirty (d) sides of the outboard split flap. In table 2.1 an overview of the convention for the naming of control surfaces is provided, in which x is used as placeholder for all flaps of a particular kind. Some examples are provided as follows. The abbreviation ***xl*** signifies midboard and inboard flaps on the left-hand side, while ***oxd*** refers to all outboard flaps on the dirty side of the aircraft, hence ***old*** and ***ord***. The flap named ***orc*** is the clean-side outboard flap located on the right (starboard) side of the aircraft.

The evolution of the RPA is planned in three main steps or phases. The first step is directed towards the first flight of the aircraft. For this test phase, as a means of risk reduction, the aircraft is equipped with two removable vertical tails without control surfaces, to augment the aircraft's inherent lateral-directional stability. The second and third phases of the project will focus on implementation of the already completed research work. For the second step, the aircraft with vertical tails will be equipped with several cameras mounted on a gimbal, that will be installed on the dirty side of the aircraft. The vertical tails will be removed in the third phase of testing. The scope of this phase is the envelope expansion including inverted flight and evaluation of novel flight control approaches.

From the three development steps, three different aircraft versions will evolve. They are called "setups" rather than "configurations", which is used to signify whether the landing gear is deployed or not. The three setups differ in regard to aerodynamics, weight and weight distribution, and therefore must be analyzed separately. Since the present work only considers the development towards the first flight mission, only the first flight setup (wing + vertical tail or wing_vt) will be discussed further.

2.2. The Aircraft Systems

The components of the aircraft are organized in a system breakdown structure, which is for the most part inspired by the common numbering system for aircraft documentation, the so-called ATA 100. The highest level of this breakdown structure is divided into green aircraft systems, blue aircraft systems, the termination system, flight test instrumentation and ground equipment. In further course, only the green and the blue systems are considered.

The green system incorporates all components that are essential for the performance of flight. These are the aircraft structure, the propulsion system, the electric power generation, the fuel system, the FMS, the landing gear, the Environmental Control System and the wiring. The blue system consists of mission relevant systems like the Mission Management System (MMS) and its payload (e.g. electro-optical sensors). In order to enable easier interpretation of the complex system architecture, figure 2.3 provides a greatly simplified diagram showing systems relevant to the FMS design. In this, the original grouping have been dropped and new system groups are defined, in order to create a clearer system boundaries and to make understanding easier.

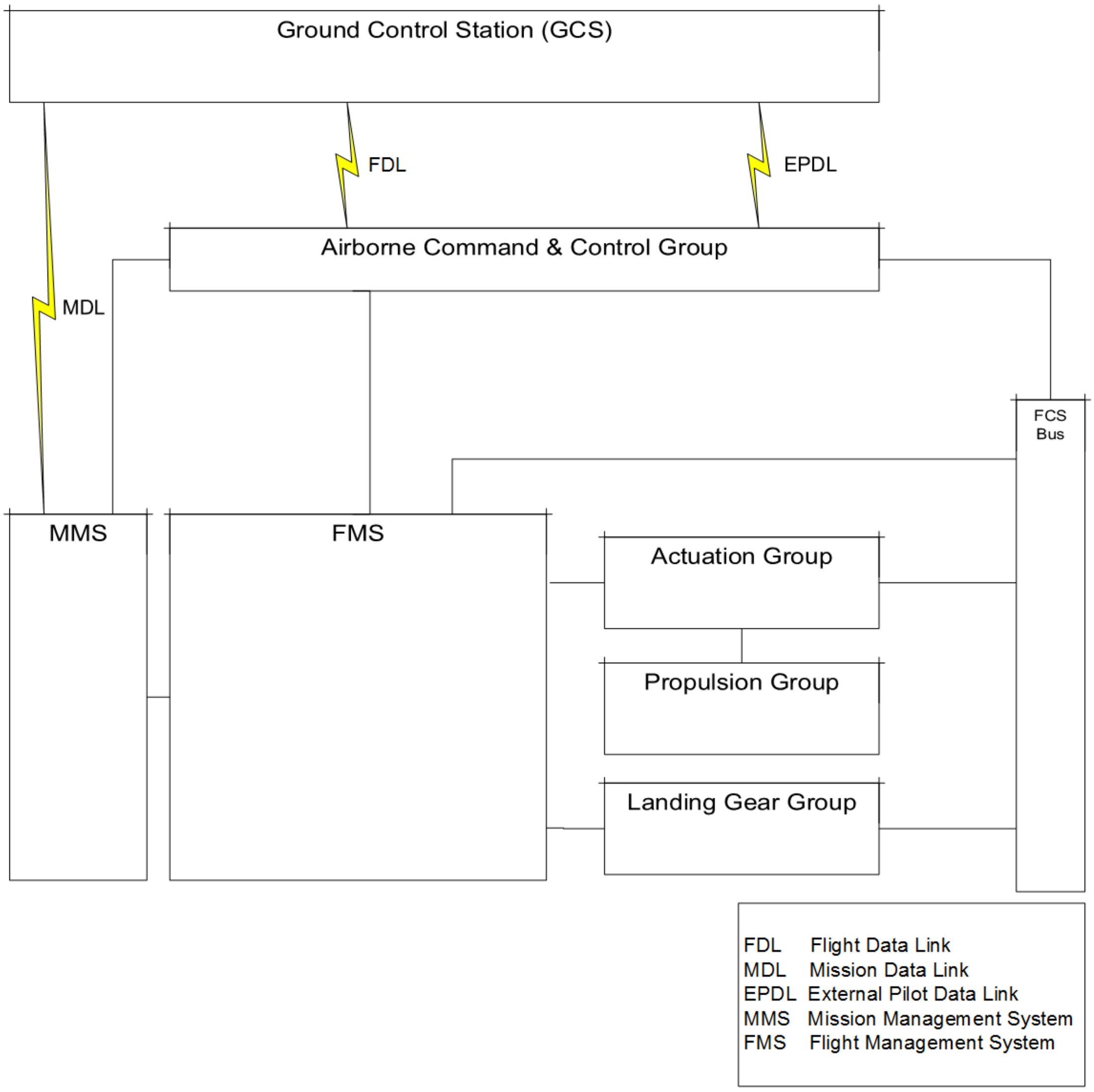

Figure 2.3.: Simplified System Overview

The FMS is located in the center of the architecture. The FMS consists of the Flight Control System (FCS) and the Basic Flight Control System (BFCS), which will be described in section 2.3. It communicates via the Airborne Command & Control Group with the GCS. In additional, it is connected to the MMS and the three actuation elements, namely the Actuation Group, the Propulsion Group and the Landing Gear Group.

The Actuation Group consists of eight control surface actuators: four on each side of the aircraft. The port actuators are assigned to the so-called left-hand Actuator Control Electronics (ACE) and the starboard actuators are assigned to the right-hand ACE. Each ACE is responsible for provision of commands to its respective actuators. The ACE monitors the states of the actuators and provides the information to (e.g) the flight control computer. Additional functionalities that are incorporated in the ACE are the calibration of actuators and provision of the Built-In-Test (BIT) interface. More details on the Actuator Control Electronics are provided in [6].

The Propulsion Group consists of two jet engines. Each of the engines is controlled via an Engine Control Unit (ECU) connected to an ACE, which commands the spool speed to the ECU and consolidates feedback from the engine for further processing by the

FMS. The ECU incorporates a fuel pump which delivers the fuel from the central tank to the engines (see [6]).

The Landing Gear Group consists of three Gear Control Electronics (GCE). Each GCE controls the actuators of the corresponding landing gear leg deployment mechanism and provides the consolidated status information from Weight-on-Wheel (WoW) sensors to the Flight Management System. In addition to landing gear deployment, the GCE-Nose or GCEN, which is related to the nose gear of the aircraft, is responsible for steering, while the GCE-Left or GCEL, which is related to the left main gear, is connected to the wheel brakes actuator and thus is responsible for transmission of brake commands from the Flight Control Computer (FCC) to the braking system. The landing gear design is described in [6, 64].

In addition to the FMS, the aircraft incorporates an MMS. The MMS is a beyond-state-of-the art cognitive system for task-based mission performance. Among other tasks, it is responsible for situation dependent in-flight mission planning and generation of inputs (e.g. waypoints) to the aircraft guidance. For this purpose it is equipped with sensors for advanced perception of the mission environment and the so-called decision engine. In the final phase of the project, the system is intended to perform long- and mid-term flight planning and to provide waypoints to the FMS which in turn will undertake the task of short-term flight guidance (based on three upcoming waypoints). More details on the design of the MMS can be found in [29, 87]. In the first flight test phase, the MMS will be passive and hence, will not intervene in the flight guidance of the aircraft.

The communication between the ground control station and the aircraft is implemented via three types of data link. One of the data links is the so-called Flight Data Link (FDL). The uplink of the FDL is operating in the Ultra High Frequency (UHF) waveband, while the downlink is using the Very High Frequency (VHF) band. Both, up- and downlinks are controlled by Radio Modem Interfaces: RMIG in the GCS and RMIA in the Airborne Command & Control Group. Furthermore, the Airborne Command & Control Group incorporates four COTS 2.4 GHz RC receivers, which establish the External Pilot Data Link (EPDL). Signals from the RC receivers are consolidated by the Radio Modem Interface Air (RMIA) to a single External Pilot (EP) command. The third data link, the so-called Mission Data Link (MDL), establishes the connection between the MMS and the GCS. Since the MMS is also connected to the FMS, it can provide the MDL data to the FMS and vice versa. Hence, the MDL can be used as a redundant path of communication between the FMS and the GCS. A more detailed description of the communication between the ground control station and the aircraft is provided by the designers of the system in [91].

The electric power of the aircraft is generated by lithium polymer accumulators, which are managed by the Power Distribution Unit (PDU). As the name suggests, the PDU distributes the power to all systems in the aircraft by means of multiple, partially redundant, independent power channels (see [6]).

Further important systems of the aircraft are the Flight Test Instrumentation (FTI) system, which logs relevant data to a storage medium for e.g. post flight analysis, and the Termination System. In the event of system malfunction the Termination System orders the deployment of a parachute and switches off the aircraft's fuel pumps. The termination command can be sent manually from the ground or may be issued automatically in the event of a link loss (there is a dedicated data link for the Termination System). The goal of the Termination System is the immediate and deterministic end of flight. By activation of the termination mechanism, the splash pattern of the aircraft is reduced. In contrast to a Rescue System, the Termination System does not provide any means to protect the aircraft from damage.

2.3. The Flight Management System

The definition of the FMS in the SAGITTA program goes far beyond the conventional definition of Flight Management Systems in manned aircraft. Besides the management of flight plans, trajectory calculation, and generation of commands for vertical and lateral guidance, the FMS incorporates further functionalities such as automatic takeoff and landing. The autopilot and the CSAS are integrated into the FMS. Furthermore, the FMS monitors the health state of aircraft components.

The elements of the FMS are depicted in figure 2.4. They are grouped into two systems: the FCS and the BFCS. The FCS forms the primary flight control system of the aircraft and consists of a central processing unit, the FCC - a multi-processor embedded computer. The FCS incorporates a sensor suite consisting of the Navigation System (NAV), the magnetometer and the Air Data System (ADS), which serve as primary sources of data for guidance and control. The aircraft is equipped with a radar, which is installed on the dirty side of the aircraft. Furthermore, the FCS has access to an Attitude and Heading Reference System (AHRS), which is part of the BFCS. The Flight Control System exchanges information with the Flight Management Control Station (FMCS) via two of the previously mentioned data links, namely the FDL and the MDL, and provides commands to the left and right ACEs, which in turn control the engines and the flaps actuators.

In parallel to the FCS, the FMS architecture includes the so-called Basic Flight Control System. The BFCS comprises a single processor Basic Flight Control Computer (BFCC) supplied by the Institute of Flight System Dynamics, Technical University of Munich (FSD). It is equipped with an AHRS and is connected with the ground station via the FDL. In addition, it has access to the ADS of the Flight Control System (FCS). Just like the FCS, it provides commands to the ACE which are then relayed to the engine and the control surface actuators.

In nominal conditions, the aircraft is controlled via the FCS and all functionalities of the system are available. In the event of a malfunction of critical elements of the FCS, the FMS can be reconfigured. In such situations the control of the aircraft is handed over by the ACEs to the BFCS, which provides the minimum amount of functionality required for safe flight. In addition to a simplified CSAS, the BFCS engages a rudimentary autopilot. Functionalities requiring complex calculations, the handling of large amounts of data or state machines are not implemented in the BFCS. Hence, one fundamental premise of the BFCS is the simplicity of its architecture and the minimization of the dependence on sensor measurement. This increases the system's availability and consequently, the survivability of the aircraft. In the BFCS an "inertial-only" control algorithm is employed, which utilizes measurements available from the AHRS, but which does not rely on air data. Details from a feasibility study of an "inertial-only" controller for the SAGITTA Demonstrator, which was completed in a preliminary project stage, are provided in [7]. In order to achieve a high degree of reliability, the BFCS Hardware (H/W) is chosen to be significantly simpler than that of the FCS and consequently to deliver a higher Mean Time Between Failure (MTBF). The redundancy concept is completed by a redundant power supply.

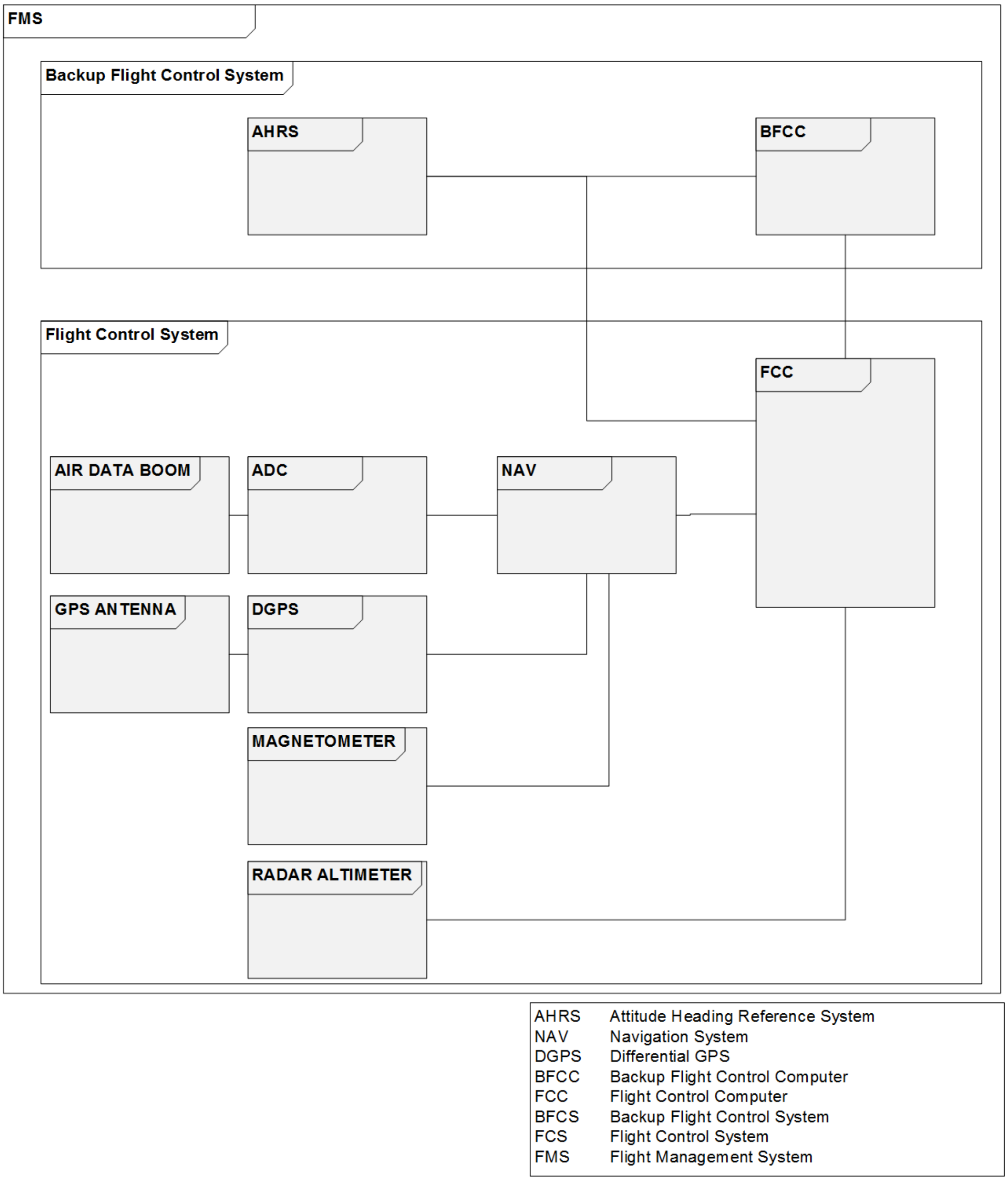

Figure 2.4.: Flight Management System (simplified)

By setting up the parallel structure presented here, a segregation between the minimum functionality required for safe flight in the BFCS and the higher level functionalities of the more complex FCS is achieved. Due to the simplicity of the Software (S/W) that is implemented in the BFCS, the risk of an undetected S/W design error is significantly reduced, since for such a system full test coverage can be achieved even with limited resources. This is not the case for the complex S/W in the FCS.

The drawback of such system design, compared to conventional redundant system architectures (e.g. triplex H/W redundancy), is the difficulty of failure detection. Since the present architecture is partially duplex redundant, a failure in the system can be detected by comparison of both systems, but it cannot be immediately assigned to one of the two systems. Therefore, more complex voting algorithms are required which, among other courses of action, may involve functional monitoring by taking e.g. knowledge of flight dynamics as an additional source of information into account. Functional monitoring represents a separate field of research. A detailed discourse on this topic is not in the scope of this work.

The benefit of the minimal (duplex) dissimilar system architecture is primary the reduction in the number of components and therefore, of the required space and weight compared to triplex or quadruplex architectures. Due to the reduced system complexity of the BFCS, a gapless verification is more likely to be achieved by smaller teams with few resources available for such activities. The proposed architecture might be especially interesting for experimental aircraft. By fusing a reliable, fully tested, flight control "backbone" in the BFCS, and by shifting complex and experimental functionalities to a system which can be isolated in case of failure, it is easily possible to incorporate innovations in flight control within the FCS without the need to modify the flight cleared safety critical BFCS. In this way, cycle times for development of experimental algorithms from initial concept to test flight can be reduced significantly.

As such, the proposed architecture represents a compromise between keeping the system's complexity as low as possible without sacrificing all redundancy, taking into account the needs for short development cycle times, and at the same time considering the space and weight constraints of the SAGITTA Demonstrator.

Due to project constraints, the AHRS is the only component of the BFCS which is operational in the first phase. Hence, the first flight configuration of the FMS is in some parts of the architecture a single-string system having no redundancy.

2.4. The Ground Control Station

The core element of the Ground Control Station is the FMCS. The Flight Operator (FO), typically a trained pilot, controls and monitors the aircraft during flight via the FMCS, which provides the possibility to control the aircraft via a waypoint list or by issuing autopilot commands. The GCS of the SAGITTA Demonstrator is equipped with a DGPS Base Station. From its known location, the DGPS Base Station calculates, for each visible satellite, the location error (resulting from, for example ionospheric effects) and provides the data to the aircraft's GPS receiver to increase the accuracy information for automatic takeoff and landing. This is especially relevant for Automatic Takeoff and Landing (ATOL) on narrow and short runways, where a high degree of accuracy is required.

The third important element of the Ground Control Station is the Quick Look Terminal (QLT). Operated by the System's Engineer (SE), the QLT provides a thorough insight into the system under test. The QLT filters the data stream for relevant information and exhibits it as time histories, via analog or digital displays. It is used for pre-flight and in-flight analysis of the FMS and other components of the green system.

A second means to control the aircraft is introduced in the SAGITTA Demonstrator's ground station. The so-called MPCS is a beyond-state-of-the-art Ground Control Station. Instead of directly commanding the autopilot, the Mission Operator (MO) communicates a high level task to be performed by the aircraft to the MPCS. The MPCS, together with the MMS, calculates the sequence of aircraft and payload commands required to execute the specific task, and sends these to the relevant subsystems of the aircraft. These commands are continuously updated based on evolving conditions, such as the sudden emergence of threats. The FMCS hands over control to the MPCS for execution of experiments that are allocated to the Mission Management System. During other experiments the MPCS remains passive. The functionalities that are required to control the aircraft via the MPCS are not available in the first phase of the project. The communication between MPCS and aircraft is implemented via a broadband data link, the so-called MDL. Additionally, the MDL is used as a redundancy means for the FDL by providing a partial duplication of the communication exchanged between aircraft and FMCS. Third means of controlling the aircraft is via the External Pilot Control Station (EPCS). The EPCS consists of two COTS 2.4 GHz (ISM band) model airplane transmitters and is operated by two EPs, typically well-trained model aircraft pilots. The EPCS is located outdoor, near the runway and communicates with the aircraft via the EPDL. Since the chosen EPCS provides no feedback of the current aircraft states to the EP, it is intended for operations within visual line-of-sight only.

2.5. The Control Concept

The control concept of the SAGITTA Demonstrator is based on three underlying levels of commands. The Low-Level Commands (LLC) consists of the aircraft attitude and thrust lever settings. These commands are directly provided to the CSAS which in its turn calculates actuator deflection commands. The second level is the so-called Medium-Level Commands (MLC). This level is primarily defined by the SPD (Speed)/ HDG (Heading) / ALT (Altitude) interface of an autopilot. Hence, controlling the SAGITTA Demonstrator by means of MLC is comparable to operating the autopilot in a manned aircraft. The third level is defined by High-Level Commands (HLC). By utilization of HLC, predefined waypoint lists can be activated and complex trajectories or loiter pattern can be flown. The waypoint lists are defined by multiple WGS-84 coordinates including latitude, longitude and altitude. In addition, each waypoint definition includes a speed command and the waypoint type (fly-over or fly-by). For more information on waypoint lists and trajectory generation in the SAGITTA Demonstrator, the reader is referred to [75].

The FMCS provides access to MLC and HLC of the aircraft. Thus, the FO can operate the aircraft utilizing the autopilot, or he can select one of the predefined waypoint lists and activate trajectory following. Both modes can be superimposed. For instance, while being in HLC in horizontal plane, the vertical plane can be controlled using the autopilot interface (MLC). Furthermore, a Return to Base (RTB) command can be issued via the FMCS. In case RTB is triggered, the aircraft flies towards a predefined waypoint, which is typically located near the runway. This might be necessary, in case of emergency, where immediate landing is desired. Finally, the FMCS provides an interface to automatic takeoff and landing functionalities, which represents the highest level of automation of the FMS. A more detailed description of the FMCS interface and the corresponding functionalities of the aircraft can be found in [40].

The EPCS implements the interface to LLC. For this, the longitudinal and lateral stick deflections of the transmitter are mapped to pitch and bank angle commands respectively. The reasoning for implementation of an AC/AH will be given later in this work. The stick representing the thrust lever command is directly mapped to the normalized engine spool speed of the two engines.

The flight via EP is accompanied by a higher risk compared to automatic flight. This is due to the unusual aircraft configuration which results in poor visibility and difficulty of determination of aircraft orientation and attitude. Furthermore, since no direct feedbacks of essential parameters like Indicated Air Speed (IAS) are directly available to the EP, his situational awareness is limited. Nevertheless, in case of malfunction of FDL

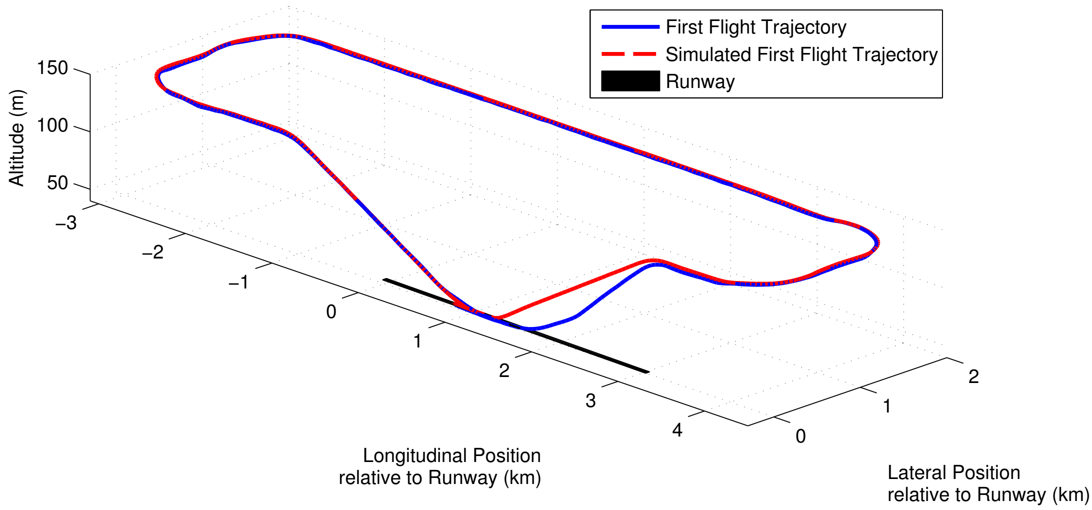

Figure 2.5.: Reference Mission [41]

and MDL or missing Global Positioning System (GPS) reception (which is required for flight using MLC), manual control via the EPCS is the last means for safely landing the aircraft. Thus, at least for the first flight campaign, the flight with EP in control is considered an important backup functionality.

2.6. The Reference Mission

The reference mission of the SAGITTA Demonstrator consists of an automatic takeoff from paved runway according to [42] and a subsequent climb to enroute altitude at app. 150 m Above Ground Level (AGL). At enroute altitude, the aircraft flies for instance a racetrack pattern according to a selected predefined waypoint list using HLC. During the racetrack, the FO can switch to MLC and continue the flight by utilizing the autopilot (SPD/HDG/ALT). Alternatively, the FO can trigger an immediate loiter command anytime in flight to "park" the aircraft for a certain amount of time. The landing is commanded by the FO and is performed automatically. The preconditions for automatic landing are presented in [43]). A go-around is automatically or manually triggered, in case a successful landing is not possible. Moreover, when the aircraft is within the visual range of the EP, he can take over command and perform low level maneuvers, and eventually manually land the aircraft in case of emergency. In figure 2.5 the reference mission is visualized. Furthermore, in anticipation of the flight test results, the first flight track is provided.

3. Modeling Aspects, Inherent Dynamics and Control Analysis

For the analysis of flight performance and flight dynamics, as well as for the design, validation and clearance of control laws of the SAGITTA Demonstrator, a nonlinear 6-DOF simulation model is used. A detailed description of the model can be found in [23].

The following discussion does not focus on the nonlinear simulation model itself, but addresses modeling aspects that are specific to the SAGITTA Demonstrator and that are of relevance for lateral controller design. The aerodynamics, sensor and actuator characteristics are presented, and distinctive features are briefly discussed. The resulting constraints and the design decisions for CSAS are highlighted. Furthermore, this chapter briefly outlines the derivation of the linear state-space models and their formulation for controller design and analysis. Finally, dynamic characteristics derived from linear state-space models representing lateral motion are discussed.

3.1. Preliminary Considerations

The introduction of a novel aircraft configuration entails many unknowns which result in various uncertainties. This fact must be taken into account during the design of the FCS.

Main sources of uncertainty in the SAGITTA project are in the aerodynamic characteristics. In this section, the impact of the quality of the aerodynamic data set on the design of the CSAS is discussed. The design drivers and design decisions, as well as their impact on further development, are presented in detail.

Aerodynamic Data Module Quality and Resulting Constraints

The Aerodynamic Data Module (ADM) is one of the core elements of a flight dynamics simulation. It calculates the forces and moments using aerodynamic data tables according to corresponding application rules. The ADM of the SAGITTA Demonstrator is derived from multiple data sources. The main source is data from wind tunnel tests that have been performed using a scaled SAGITTA Demonstrator model. Computational Fluid Dynamics (CFD) are applied to the clean setup for determination of damping derivatives (see [35]). Contribution of the vertical tail to dynamic derivatives C_{Yr} and C_{nr} is incorporated using measurements of C_Y from wind tunnel tests according to the following rules:

$$\begin{aligned} C_{Yr,VT} &= -C_{Y\beta,VT}\frac{l_{VT}}{V_A} \\ C_{nr,VT} &= C_{Yr,VT}\frac{2l_{VT}}{b}. \end{aligned} \tag{3.1}$$

C_{m0}	$\pm$ 0.005	C_{l0}	$\pm$ 0.005	C_{n0}	$\pm$ 0.005
$C_{m\alpha}$	$\pm$ 20%	$C_{l\beta}$	$\pm$ 20%	$C_{n\beta}$	$\pm$ 20%
C_{mq}	$\pm$ 50%	C_{lp}	$\pm$ 50%	C_{np}	$\pm$ 50%
$C_{m\eta}$	$\pm$ 20%	C_{lr}	$\pm$ 50%	C_{nr}	$\pm$ 50%
		$C_{l\xi}$	$\pm$ 20%	$C_{n\xi}$	$\pm$ 20%
		$C_{l\zeta}$	$\pm$ 20%	$C_{n\zeta}$	$\pm$ 100% $\forall \lvert\delta_{oxx}\rvert < 20°$
					$\pm$ 20% $\forall \lvert\delta_{oxx}\rvert \geq 20°$

Table 3.1.: Absolute and relative Air Data Module tolerances [65]

Neither the influence of the vertical tail on rolling motion nor the interference effects of control surfaces are modeled.

The resultant ADM is of low to medium fidelity [65] with large uncertainties. The uncertainties result from (e.g.) the limited quality of the scaled aircraft model used in wind tunnel tests, the post-processing of data (e.g. symmetrization of data) and the lack of reproducibility of the wind tunnel measurements. Further uncertainties are due to late changes in aircraft configuration after completion of the wind tunnel tests (e.g. modification of landing gear position and changes to the shape of the landing gear doors).

An estimation of the aerodynamic uncertainties is specified by the provider of the ADM. It is shown in table 3.1. The large uncertainty in control efficiency of the outboard flap for small surface deflections ($C_{n\zeta}$) is especially worth mentioning. Even though measurements of the outboard flaps' aerodynamic properties were repeated several times, no clear trend could be determined for their control efficiency with respect to yaw moment at small surface deflections. Due to the inconsistent behavior during wind tunnel measurements, the tolerances in the range $0° \leq |\delta_{oxx}| < 20°$ have been fixed at 100%. Such large uncertainties prohibit use of the outboard flaps in this deflection range, since in the worst case, a total loss of control authority must be assumed. For this reason, this particular deflection range is to be avoided for the first flight campaign until a resilient data base is available and more confidence in the ADM has been gained. The deflection range is avoided by application of so-called preloading ζ_0, i.e. a redefinition of the minimum position of the outboard flaps by adding a symmetric offset to the outboard flap's deflection angle on both the clean and dirty sides of each wing. In other words, the zero-deflection position of the outboard flaps is set to $\delta_{oxc} = -20°$ and $\delta_{oxd} = 20°$. The resulting control allocation including preloading of outboard flaps is defined as follows:

$$\begin{aligned} \delta_{old} &= && (\zeta_{equiv} + |\zeta_{equiv}|)/2 + \zeta_0 \\ \delta_{olc} &= - && (\zeta_{equiv} + |\zeta_{equiv}|)/2 - \zeta_0 \\ \delta_{ord} &= && (\zeta_{equiv} - |\zeta_{equiv}|)/2 + \zeta_0 \\ \delta_{orc} &= - && (\zeta_{equiv} - |\zeta_{equiv}|)/2 - \zeta_0 \end{aligned} \tag{3.2}$$

with ζ_{equiv} being the equivalent rudder deflection. In figure 3.1, the nominal split flap efficiency w.r.t. roll moment (C_l), yaw moment (C_n) and side force (C_Y) coefficient is depicted over the relevant range of Angle-of-Attack (AoA). For this evaluation, the preloading is set to $\zeta_0 = 0°$. Here the impact of preloading on flight control becomes clear. One major benefit, besides the reduction in uncertainty of the model, is the linear yaw control moment build-up over the range of deflection, which reduces the linearization error in the state-space model used for controller design and assessment. A further benefit can be observed in the plot of roll efficiency. By avoiding the deflection range within which the uncertainties are large, the steep slope in the roll coefficient is

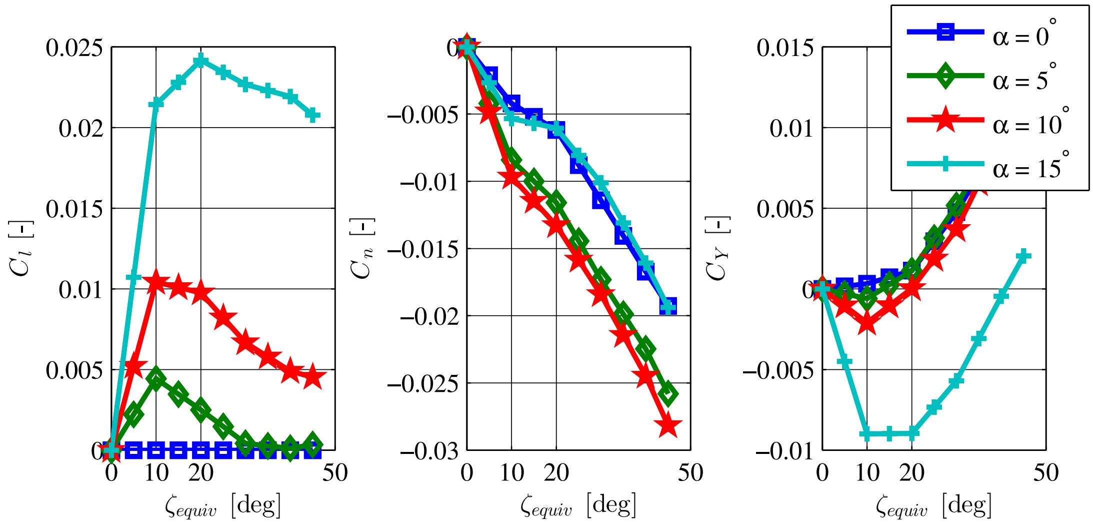

Figure 3.1.: Split Flap Efficiency ($\zeta_0 = 0°$)| α grid

α [deg]	0	3	6	9	12	15	18
$\frac{(Cn)_{max,\zeta 0,20}}{(Cn)_{max,\zeta 0,0}}$	0.68	0.62	0.52	0.52	0.59	0.69	0.84
$\frac{(C_D)_{\zeta 0,20}}{(C_D)_{\zeta 0,0}}$	1.31	1.29	1.27	1.21	1.14	1.07	1.04

Table 3.2.: Control efficiency and drag before and after preloading

bypassed and thus the strong, undesired coupling of roll and yaw moment generated by the outboard flap is significantly reduced. This simplifies independent control of roll and yaw motion.

Offsetting the above-mentioned benefits are a loss of control power in yaw axis and a significant amount of additional drag that is induced by preloading. Table 3.2 shows the ratios of control moment and the corresponding increase of drag coefficient over AoA for the preloading settings $\zeta_0 = 20°(\zeta_{0,20})$ versus $\zeta_0 = 0°(\zeta_{0,0})$. This shows that the high amount of additional drag produced by the outboard flaps dramatically degrades the flight performance. Hence, after the first flight campaign, as one of the first means of flight performance improvement, the possibility of reducing the preloading shall be investigated. This could be achieved by (e.g.) detailed analysis of the outboard flaps' efficiency in further wind tunnel trials and CFD calculations.

Control Surface Linkage

The aircraft is equipped with eight independently controllable control surfaces, as described in chapter 2. In order to simplify the control task, these surfaces are linked to provide logically coupled control units. For this reason the following new equivalent control units are defined: ξ_{equiv} standing for an equivalent aileron deflection, η_{equiv} for an equivalent elevator deflection and ζ_{equiv} representing an equivalent rudder deflection. The linkage is implemented in S/W, which is part of the application that is executed in the FCC.

Two different types of control linkage are considered in this work. The first, "simple" or "aileron" control linkage couples the two inboard flaps to an elevator and the midboard flaps to ailerons according to equation (3.3).

$$\begin{aligned} \delta_{il} &= \delta_{ir} = \eta_{equiv} \\ \delta_{ml} &= -\xi_{equiv} \\ \delta_{mr} &= \xi_{equiv} \end{aligned} \tag{3.3}$$

The second, namely the "elevon" control linkage, which is typically used in delta-wing fighter aircraft, couples inboard and midboard flaps to one large single control surface, the so-called elevon that is used for both, pitch and roll according to equation (3.4),

$$\begin{aligned} \delta_{il} &= \delta_{ml} = \eta_{equiv} - \xi_{equiv} \\ \delta_{ir} &= \delta_{mr} = \eta_{equiv} + \xi_{equiv} \end{aligned} \tag{3.4}$$

where η_{equiv}, ξ_{equiv} and ζ_{equiv} are the equivalent elevator, aileron and rudder deflections. In both control linkage types the outboard flaps are linked as described in equation (3.2).

As the name suggests, the advantage of the first control linkage is its simplicity. Each control surface is assigned to a single functionality. However, several disadvantages are associated with this approach. The "simple" control linkage utilizing just two control surfaces for longitudinal trimming leads to higher trim deflections of the inboard flaps compared to the "elevon" type linkage, where the trim moment is generated by four control surfaces. The higher deflections are accompanied by higher hinge moments and thus lead to higher loads on the actuators, thereby reducing their service life. Furthermore, the "simple" control linkage leads to large gaps between adjoining flaps increasing the interference drag of the flap system. Both these disadvantages degrade the performance of the aircraft. The higher drag of the "aileron" control linkage is illustrated in figure 3.2. The figure on the left shows the required thrust lever settings δ_T for steady-state level flight, while the figure on the right depicts the maximum trimmable (steady-state) flight path angle γ_K, when the aircraft is in Open Climb (thrust lever set to maximum). It can be seen that, especially at low speeds, the "elevon" control linkage requires up to 1 % less thrust compared to the aircraft using the "aileron" or "simple" linkage which corresponds to a higher climb performance. Nevertheless, the effect is lower than expected, one reason which is the previously mentioned unmodeled flaps interaction in the ADM.

Another drawback of the "simple" control linkage in terms of flight dynamics is the generation of adverse yaw. Adverse yaw due to aileron deflection is well-known and affects most aircraft. The effect is provoked by an increase in drag on the wing which is subject to a downward flap deflection at the same time as the drag on the opposite wing is decreased. This leads to a yaw moment in the opposite direction of roll. Adverse yaw is highly undesirable. It can be reduced by means of (e.g.) differential aileron mechanization. The "simple" linkage is predicted to reinforce the adverse yaw that is induced by equivalent aileron deflection. This is due to the combination of the right inboard flap's negative trim deflection and the right midboard flap's positive deflection during initiation of negative roll. The same situation is observed on the left side of the aircraft during initiation of positive roll. The two adjoining flaps, one of which is deflected in a negative direction at the same time as the other is deflected in a positive direction, form a split flap generating drag and therefore a yawing moment that counteracts the intended rolling motion. This is not the case for the "elevon" linkage, where both adjoining flaps move in the same direction.

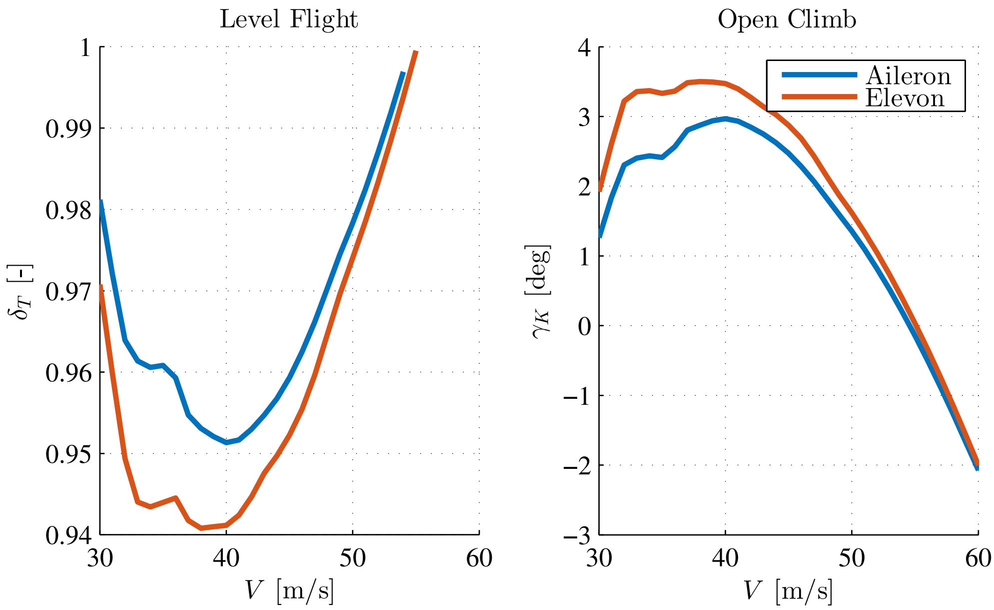

Figure 3.2.: Comparison of "aileron" and "elevon" control allocation w.r.t. flight performance in Trimmed Level Flight (left) and Open Climb (right)

The yaw characteristics can be analyzed by evaluation of the yaw moment derivative in stability axes (denoted by the index S) w.r.t. to the roll control surface deflection. The conditions for proverse and adverse yaw respectively are given in equation (3.5),

$$(N_\xi)_S = \begin{cases} < 0 & \text{proverse yaw} \\ > 0 & \text{adverse yaw} \end{cases} \tag{3.5}$$

where $(N_\xi)_S$ is the yaw control efficiency. By elimination of the moment of deviation $I_{zx} = 0$ the yaw control efficiency is calculated according to equation (3.6).

$$(N_\xi)_S = \frac{\bar{q}Ss}{I_{zz}} \left(C_{n\xi} \cos(\alpha) - \frac{I_{zz}}{I_{xx}} C_{l\xi} \sin(\alpha) \right) \tag{3.6}$$

In order to obtain the yaw characteristics, it is sufficient to evaluate the expression in parentheses. Following the nomenclature used for the Weismann criterion in e.g. [27], the expression is defined as $C_{n\xi,dyn}$:

$$C_{n\xi,dyn} = C_{n\xi} \cos(\alpha) - \frac{I_{zz}}{I_{xx}} C_{l\xi} \sin(\alpha). \tag{3.7}$$

Figure 3.3 shows the evaluation of $C_{n\xi,dyn}$ for the two control linkage options. For simplicity reasons, the trim deflection is set to $\eta_{equiv,trim} = 0°$ for both, aileron and elevon linkage types. It can be seen that both curves change their sign over the AoA envelope. At low AoAs both provide proverse yaw, while at higher AoAs they change to adverse yaw. At AoAs $\alpha > 11°$, the "elevon" linkage type leads to a stronger adverse yaw, compared to the "aileron" linkage. From the results of the evaluation provided in figure 3.3, a further interesting observation can be made. As the SAGITTA Demonstrator has a symmetrical wing shape an aileron deflection is expected to generate a similar drag increase on each wing and therefore a neutral yaw characteristic is predicted. However, it is observed that at $\alpha = 0°$, both linkage types provide proverse yaw. This characteristic is a result of the location of control surfaces relative to the vertical tail. The reason the configuration produces proverse yaw is the significant redirection of

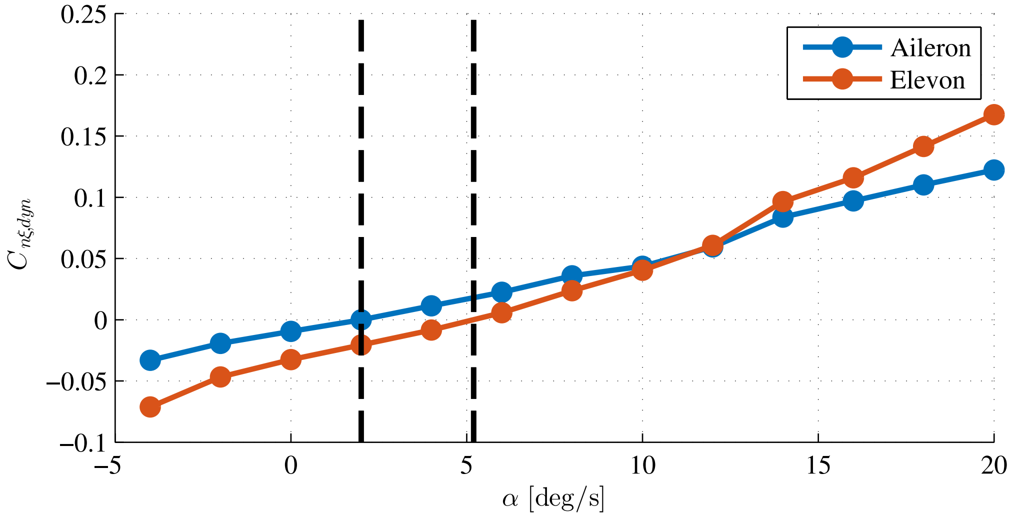

Figure 3.3.: Comparison of yaw characteristics of "aileron" and "elevon" control allocation

the streamlines towards the vertical tail caused by the high pressure area in front of the upward-deflected midboard and / or inboard flaps. The streamlines hitting the vertical tail generate side force and consequently a proverse yaw moment which is more pronounced if both adjoining flaps are deflected (as is the case for the "elevon" linkage type). The effect described here can be seen in surface streamline plots generated from CFD calculations in [36].

On the basis that the assumed nominal AoA range (maneuver envelope) is between 5° and 15°, it can be concluded that the elevon linkage is superior to the aileron linkage in the lower AoA regions (between 5° and 10°) where it generates a smaller amount of adverse yaw. At AoAs around $\approx 10°$, both linkage characteristics are comparable in terms of generated yaw moment. At AoAs $> 10°$ the aileron linkage type is preferred, since in this AoA region the adverse yaw is less pronounced.

It should be noted that the change from adverse to proverse yaw for the elevon linkage is at an AoA, which is within the expected flight envelope. Hence, compensation of the yaw moment induced by ξ_{equiv} using the elevon linkage will require a sign change in the command. This leads to a sign change in the controller gains, which is highly undesirable, as it makes the system prone to sensor errors. This particular issue does not arise with the aileron linkage type, since here, the sign change takes place at smaller AoA, which is assumed to be outside, or at the boundary of the flight envelope. Therefore, it is anticipated that implementation of the aileron linkage type will result in a controller that is less susceptible to sensor errors. Furthermore, by using aileron linkage, no prioritization scheme between longitudinal and lateral motion will be required, which will result in a simpler control architecture and enable independent controller development of longitudinal and lateral CSAS. Thus, as means of reducing both, complexity and risk, and in order to obtain a better physical insight and easier comparison with conventional aircraft, the simple control linkage with surfaces that can be assigned to particular functionalities is implemented and used in the course of this work. As soon as aerodynamic data incorporating the flap interaction phenomena becomes available, the analysis of control coupling shall be revised, since it is expected that the modeling of interference drag of the flaps will significantly alter the overall aerodynamic characteristics, which in turn might lead to a revised conclusion regarding the control linkage.

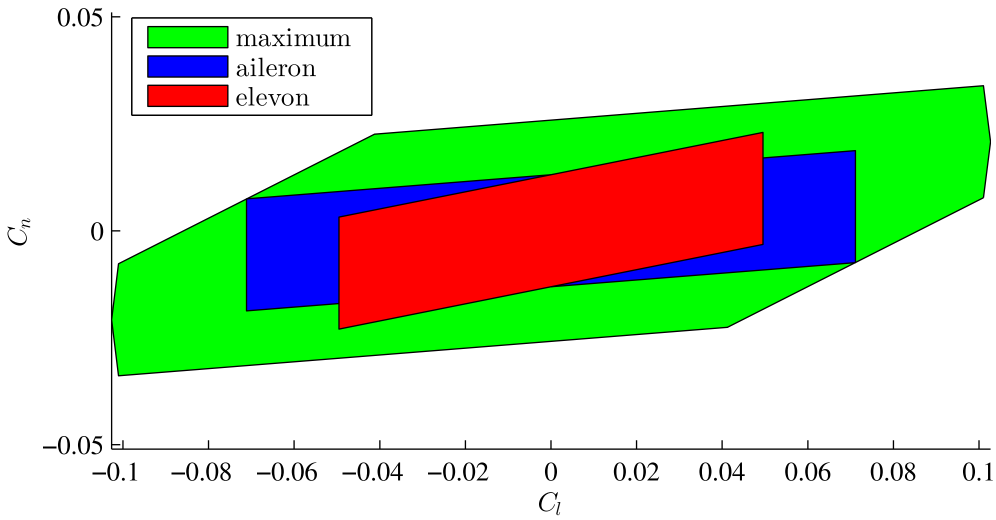

Figure 3.4.: Comparison of attainable moment subset of "aileron" and "elevon" control linkage types

To conclude the topic of control linkages, the two variants are compared w.r.t. roll and yaw moment generation. In figure 3.4, the attainable moment coefficients for both linkage types at $\alpha = 0°$ are compared to the maximum available moment space which is obtained by arbitrary, non-linked combinations of inboard and midboard flaps deflections. From the first look the aileron linkage seems to be beneficial, since it provides almost the same yaw moment potential as the elevon but at the same time it enables a larger maximum roll moment. Both control linkage types discussed significantly reduce the achievable control moment space, and consequently limit the potential maneuvering capability of the aircraft. In future development stages, once experience has been gained of the dynamic characteristics of the aircraft, and the uncertainties w.r.t. the aerodynamic characteristics have been reduced, it is expected that a more advanced control allocation scheme exploiting the full maneuvering potential of the aircraft will be developed. Again, for this purpose, a higher fidelity model of the flaps' aerodynamics is required, which amongst other things takes into account aerodynamic effects resulting from flap interference.

3.2. Aircraft Geometry and Dimensions

The SAGITTA Demonstrator is designed for a MDTOW of 144 kg. With an Operating Weight Empty (OWE) of 114 kg, this results in a maximum fuel mass of $m_{fuel} = 30\,\text{kg}$. In preliminary design phases the Maximum Take Off Weight (MTOW) for the first flight campaign was reduced to 135 kg leading to a maximum fuel mass at take-off of $m_{fuel} = 21\,\text{kg}$. An overview of the different mass specifications is given in table 3.3. Later on in this paper, the fuel mass is referred to as m_{fuel}, and the two extreme load conditions are represented by $m_{fuel} = 0\,\text{kg}$ and 21 kg. Two further conditions analyzed are represented by $m_{fuel} = 11\,\text{kg}$ which corresponds to the aircraft at Maximum Landing Weight (MLW) and $m_{fuel} = 3\,\text{kg}$ where a minimum, unusable amount of fuel is present in the tank.

In table 3.4, the relevant geometric properties of the aircraft with its landing gear deployed are given for the fuel mass quantities $m_{fuel} = 0\,\text{kg}$ and $m_{fuel} = 21\,\text{kg}$.

Weight	[kg]
MDTOW	144
MTOW	135
MLW	125
OWE	114

Table 3.3.: Aircraft weight specification

	Symbol	**Value** $m_{fuel} = 0\,\text{kg}$	$m_{fuel} = 21\,\text{kg}$	**Unit**
Center of Gravity	x_{CG}	1.2602	1.2586	m
	y_{CG}	0		m
	z_{CG}	0.0349	0.0205	m
Aerodynamic reference point	x_A	1.36		m
	y_A	0		m
	z_A	0		m
Fuselage length	$l_{A/C}$	3		m
Wing span	b	3.088		m
Wing ref. area	S	4.748		m^2
Mean aerodynamic chord	$\bar{c}$	2		m
Moments of Inertia	I_{xx}	25.6	26.7	$\text{kg}\,\text{m}^2$
	I_{yy}	39.9	40.8	$\text{kg}\,\text{m}^2$
	I_{zz}	62.5	63.3	$\text{kg}\,\text{m}^2$
Lever arm of vertical tail	l_{VT}	1.3		m

Table 3.4.: Aircraft geometry for deployed landing gear

3.3. Aerodynamics

The Aerodynamic Data Module provides dimensionless coefficients of forces and moments in body-fixed (B) and stability-axes (S) coordinate systems. For definitions of the coordinate systems the reader is referred to appendix A. Each coefficient is calculated from the aerodynamic data tables according to equation (3.8) and consists of a static part (stat), a dynamic part (dyn) and a part representing the influence of control surfaces (δ_i).

$$C_{k,tot} = \sum C_{k,stat} + \sum C_{k,\delta_i} + C_{k,dyn}. \tag{3.8}$$

In equation (3.8), the generic index k is a placeholder for the forces (X, Y, Z) and moments (M, L, N).

The static part includes contributions from the aircraft body (b), the landing gear (lg), gimbal (gbl, not applicable for FF configuration), and ground effect (g):

$$\sum C_{k,stat} = C_{k,b} + C_{k,lg} + C_{k,g}. \tag{3.9}$$

The respective contributions to the coefficients are applied as functions of AoA and AoS as follows:

$$\begin{aligned} C_{k,b} &= C_{k,b}(\alpha, \beta) \\ C_{k,lg} &= C_{k,lg}(\alpha, \beta) \\ C_{k,g} &= \begin{cases} C_{k,g}(\alpha) & \text{for} \quad h_{AGL} \leq 60\,\text{m} \\ 0 & \text{for} \quad h_{AGL} > 60\,\text{m}. \end{cases} \end{aligned} \tag{3.10}$$

The increment of control surfaces is constructed according to equation (3.11),

$$\sum C_{k,\delta_i} = C_{k,old} + C_{k,olc} + C_{k,ml} + C_{k,il} + C_{k,ir} + C_{k,mr} + C_{k,ord} + C_{k,olc} \tag{3.11}$$

with the following dependencies

$$C_{k,\delta_i} = C_{k,\delta_i}\left(\alpha, \beta, \delta_i\right), \tag{3.12}$$

where δ_i is the deflection of the control surface under consideration, hence $old, olc, ml, il, ir, mr, orc$ or ord. The application rule for the dynamic coefficient is given in equation (3.13).

$$\begin{aligned} C_{k_{dyn}} =& C_{k\dot{\alpha}} \cdot \tilde{\dot{\alpha}} + C_{k\dot{\beta}} \cdot \tilde{\dot{\beta}} + \\ & C_{kp} \cdot \tilde{p} + C_{kq} \cdot \tilde{q} + C_{kr} \cdot \tilde{r} \end{aligned} \tag{3.13}$$

with the dimensionless rates

$$\begin{aligned} \tilde{\dot{\alpha}} = \dot{\alpha}\frac{\bar{c}}{V} \quad & \tilde{\dot{\beta}} = \dot{\beta}\frac{b}{2V} \\ \tilde{p} = p\frac{b}{2V} \quad \tilde{q} = q\frac{\bar{c}}{V} \quad & \tilde{r} = r\frac{b}{2V}. \end{aligned} \tag{3.14}$$

The dynamic derivatives are implemented as functions of AoA.

The forces and moments are calculated from the coefficients derived above according to equation (3.15).

$$\begin{aligned} F_X = C_X\bar{q}S \qquad F_Y = C_Y\bar{q}S \qquad F_Z = C_Z\bar{q}S \\ L = C_l\bar{q}sS \qquad N = C_n\bar{q}sS \qquad M = C_m\bar{q}\bar{c}S \end{aligned} \tag{3.15}$$

In addition to the coefficients for forces, moments and control surface efficiency, the ADM provides hinge moment coefficients for each control surface as a function of AoA, AoS and control surface deflection. The hinge moments are calculated according to equation (3.16)

$$M_{H,\delta_i} = \left(C_{H,\delta_i}\right)\bar{q}l_{\delta_i}S_{\delta_i} \tag{3.16}$$

with l_{δ_i} and S_{δ_i} being the control surface reference length and area respectively, and C_{H,δ_i} being the hinge moment coefficient of control surface δ_i. The hinge moments are used as inputs to the actuator models.

In the following, the modeled aerodynamics of the aircraft are analyzed. Whereas the aerodynamic coefficients are directly available as outputs of the ADM, the corresponding derivatives are determined by numerical differentiation in post-processing. In subsequent analyses, the preloading of $\zeta_0 = 20°$ is taken into account. For the purpose of comparison, three aircraft have been selected, namely: the General Dynamics F-16 [63], a Blended Wing Body concept in [12] and the BAE Systems Demon[9]. The latter is of particular interest due to the similarity of the Demon and SAGITTA configurations.

In figure 3.5 the aerodynamic derivatives describing the characteristics of lateral motion of the SAGITTA Demonstrator are plotted versus AoA. From the diagrams it can be seen that at AoAs in the range 0° to 10°, the SAGITTA Demonstrator shows $C_{l\beta}$ characteristics comparable to those of the General Dynamics F-16 aircraft. The roll damping, which is associated with C_{lp}, is very close to the roll damping of the F-16, while the aerodynamic data of the Demon shows significantly higher values for C_{lp}. The yaw moment due to sideslip derivative $C_{n\beta} > 0$ indicates weathercock stability. The $C_{n\beta}$ is in the range between that of the Demon 50% scale model ($C_{n\beta} = 0.12$) and that of the F-16 aircraft ($C_{n\beta} = 0.18$). However, while the two benchmark configurations

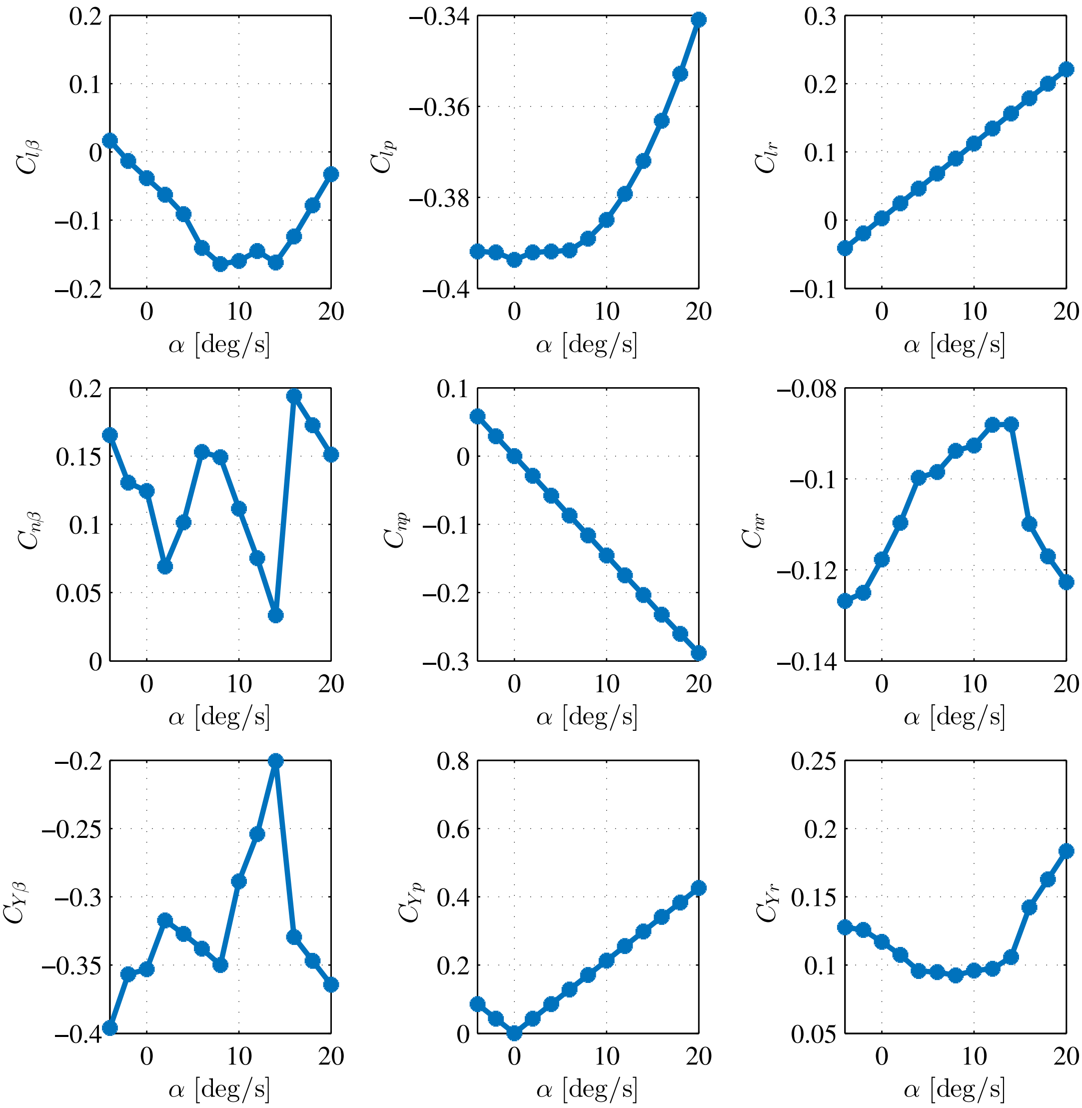

Figure 3.5.: Aerodynamic derivatives of the rigid body

provide only minor variation in $C_{n\beta}$, the SAGITTA Demonstrator dataset shows strong scattering with outliers leading to a significantly smaller $C_{n\beta}$ at (e.g.) $\alpha = 2°$ or $\alpha = 14°$. The main contributor to the $C_{n\beta}$ is the vertical tail. This can be concluded by comparing the SAGITTA Demonstrator setup with vertical tail and the ADM of the "Clean Setup" without the vertical tail. The derivative C_{np} of the SAGITTA Demonstrator is negative for all $\alpha > 0$ and its values are relatively large. One possible explanation for this is the lack of modeling of vertical tail's contribution to C_{np}, which is typically positive, and therefore, counteracts the effect of the tilted lift vector resulting from roll rate, which in turn leads to an adverse yawing moment. The yaw damping derivative C_{nr} is negative for all AoA. Compared to both the F-16 and Demon, the yaw damping of the SAGITTA Demonstrator is significantly lower. Whereas, for the relevant AoAs the values of C_{nr} for the F-16 are in the range -0.373 to -0.55, and those of the Demon are between -0.28 and -0.393, the C_{nr} of the SAGITTA Demonstrator is between -0.125 and -0.09.

In figure 3.6, the derivatives w.r.t. the control surfaces are shown for the "aileron" linkage type. For completeness and comparison, the corresponding derivatives for the "elevon" linkage type are also shown. The relatively small yaw control power of the

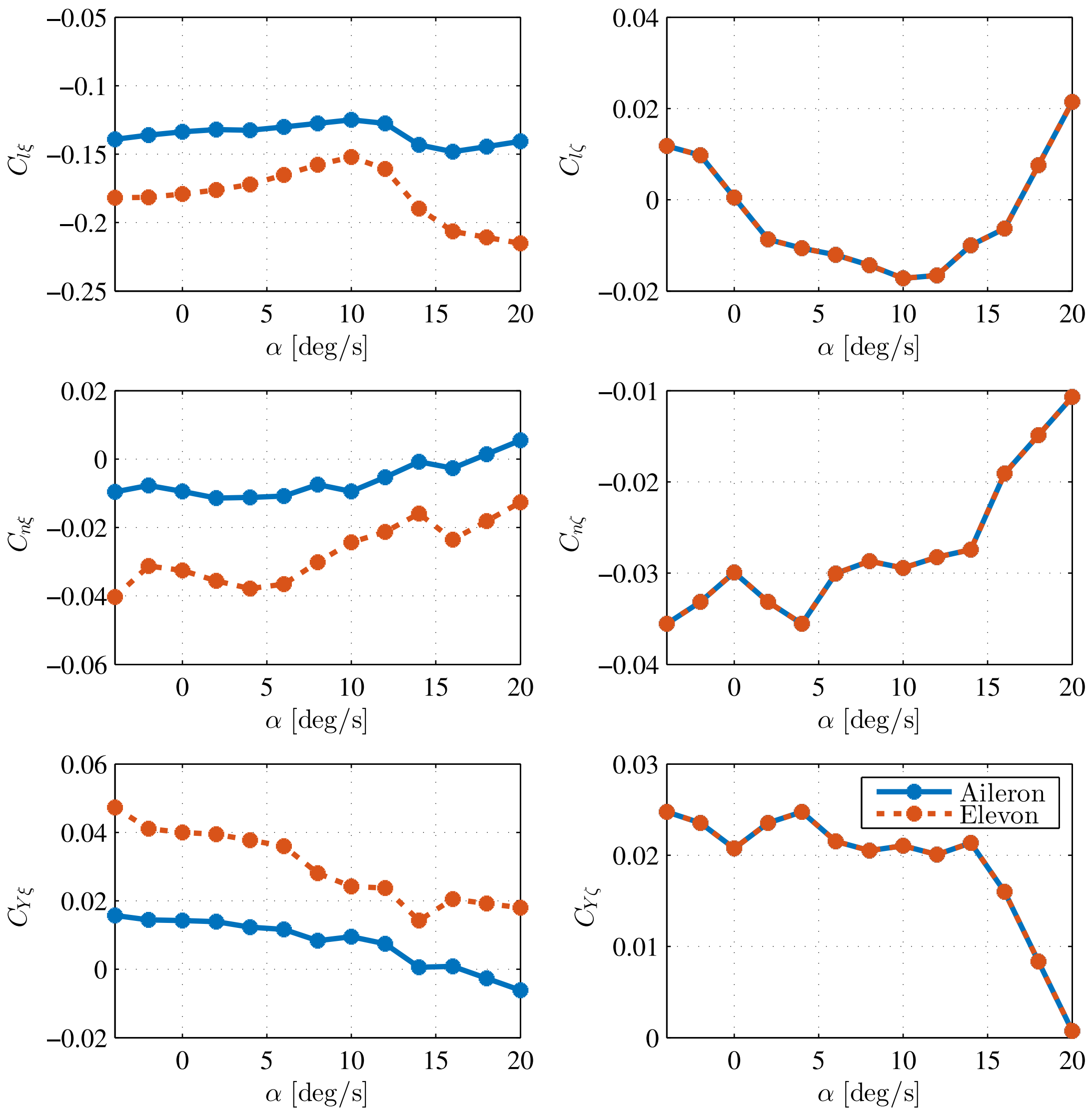

Figure 3.6.: Aerodynamic derivatives w.r.t control surfaces

outboard flaps and the high ratio of $C_{n\xi}/C_{n\zeta}$ indicating high control couplings are noticeable. Furthermore, strongly pronounced nonlinearities are visible in all derivatives that are related to ζ_{equiv}. The values of $C_{Y\zeta}$ and $C_{n\zeta}$ drastically decrease at AoSs$> 14°$, indicating a reduction of yaw control power at high angles-of-attack.

To summarize, it can be stated that the aerodynamic characteristics of lateral motion of the SAGITTA Demonstrator are comparable to those of known delta wing aircraft. The differences to the reference configurations may result from the relatively small vertical tail and the unconventional split flap design of the configuration under study, but may also be attributed to unmodeled or neglected aerodynamic effects. Regarding the ADM, it should be noted that it shows unexpected behavior w.r.t. some derivatives. Particularly conspicuous is $C_{n\beta}$ which is subject to very large scattering. In conclusion, and taking into account the ADM characteristics discussed in section 3.1, a considerable risk remains that the actual aircraft characteristics will lie outside of the specified tolerance band given in table 3.1.

	PT$_2$		MILS Model	
V_{DC}[V]	$f_{0,act}$ [Hz]	$\zeta_{0,act}$	$f_{0,act}$ [Hz]	$\zeta_{0,act}$
22	5.85	0.5	6.98	0.5
24	6.3	0.5	7.65	0.5
26	6.5	0.5	8.3	0.5
28	6.8	0.5	8.98	0.5

Table 3.5.: Actuator dynamics parameters[67]

3.4. Actuation

The core of the control surface actuator models, provided by the DLR, is a Linear Parameter Varying (LPV) PT$_2$ element, in other words, a nonlinear model that is represented by a linear structure and state dependent varying parameters. The dynamics are parametrized in terms of damping ratio (ζ_{act}) and natural frequency ($\omega_{0,act}$). The corresponding values are calculated as follows:

$$\zeta_{act} = \zeta_{0,act} + k_d T_L \qquad \omega_{0,act} = \omega_{00,act} + k_{\omega 0} V_{DC} \tag{3.17}$$

with

$$\zeta_{0,act} = \zeta_{00,act} + k_{d0} V_{DC} \tag{3.18}$$

and V_{DC} being the supply voltage, and T_L being the load moment acting on the actuator and the actuator specific constants k_{d0}, k_d, $\zeta_{00,act}$, $k_{\omega 0}$ and $\omega_{00,act}$. The load moment T_L at the actuator is calculated using equation (3.19) with R being the linkage transmission ratio between the actuator and the control surface and M_H the hinge moment at the control surface.

$$T_L = R^{-1}(\delta)\left(-M_H(\alpha, \delta)\right) \tag{3.19}$$

Table 3.5 shows the actuator dynamic parameters for different supply voltage levels. Thereby, the following relation applies

$$f_{0,act} = \frac{\omega_{0,act}}{2\pi}. \tag{3.20}$$

The values in the table are provided by the project partner DLR and have been obtained in laboratory tests. The data in the column headed "MILS Model" represents the values implemented in the nonlinear model, the data in column "PT$_2$" corresponds to an approximated linear second-order model, which is used later for linear controller design and assessment. The nonlinear model includes dynamic limiters for angular acceleration and rate, as well as static limiters for command and actuator position representing the mechanical limits. The lower and upper boundaries of the dynamic limiters are calculated according to equations (3.21) and (3.22), with $M_{act,max}$ being the maximum moment that can be generated by the actuator without any load, $V_{DC,max}$ the maximum electric voltage; k_1 an actuator specific constant; and $\dot{\varphi}_{0,max}$ the speed limit at $V_{DC,max}$ and no external load. The moment of inertia $I_{act+flap}$ embodies all elements in the chain from the actuator to the flap.

$$\ddot{\varphi}_{lo} = \frac{-M_{act,max} - T_L}{I_{act+flap}} \qquad \ddot{\varphi}_{up} = \frac{M_{act,max} - T_L}{I_{act+flap}} \tag{3.21}$$

$$\dot{\varphi}_{lo} = -\dot{\varphi}_{0,max}\frac{V_{DC}}{V_{DC,max}} - k_1 T_L \qquad \dot{\varphi}_{up} = \dot{\varphi}_{0,max}\frac{V_{DC}}{V_{DC,max}} - k_1 T_L \tag{3.22}$$

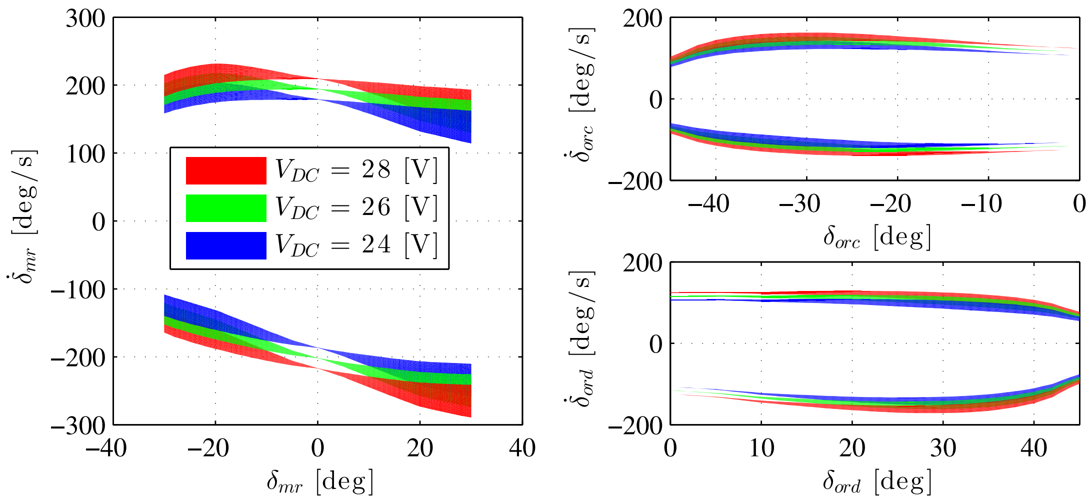

Figure 3.7.: Control Surface Rates

The control surfaces rates attainable for different supply voltage levels are shown in figure 3.7. Thereby, the dimension perpendicular to the paper plane is the Angle-of-Attack. This means that the colored surfaces in the plot are showing the variation envelope of the rate limits over the AoA. Analysis shows that relatively high rates are achievable for the midboard flap in the entire control surface deflection range, so that for a supply voltage of $V = 26\,\text{V}$ a maximum rate of at least $\dot{\delta}_{mx} = 120°$ can be expected. The situation is different for the outboard flaps. Especially in the range $\delta_{oxd} = 40 - 45°$ a dramatic reduction of available maximum control surface rate is observed. The rate is reduced from $\dot{\delta}_{oxd} = 105°/s$ at $\delta_{oxd} = 20°$ to $\dot{\delta}_{oxd} = 79°/s$ at $\delta_{oxd} = 40°$ and achieves a minimum value of $\dot{\delta}_{oxd} = 60°/s$ at $\delta_{oxd} = 45°$. For simplicity reasons, the linear analyses are performed using deflection-independent maximum achievable rate of $\dot{\delta}_{mx} = 120\,°\,\text{s}^{-1}$ and $\dot{\delta}_{oxd} = 60\,°\,\text{s}^{-1}$ respectively. The position limits of the control surfaces are given in table 3.6.

	δ_{oxd}	δ_{oxc}	δ_{mx}	δ_{ix}
max	45°	0°	35°	35°
min	0°	−45°	−40°	−40°

Table 3.6.: Mechanical Control Surface Position Limits

The actuator model implements the following stiffness model:

$$\varphi_a = \varphi_i - k_s T_L, \tag{3.23}$$

with φ_i being the internal actuator position, k_s a system specific stiffness constant and φ_a the actuator position at the system output. The actuator model includes blocks at the input and output representing transport delays of $\tau_d = 10\text{ms}$ each. These delays are introduced into the system through data processing in the ACE, but are modeled as part of the actuator. Figure 3.8 shows the simplified block diagram of the actuator. Thereby, the actuator command is indicated by φ_{cmd} and the measured output of the actuator is φ_m.

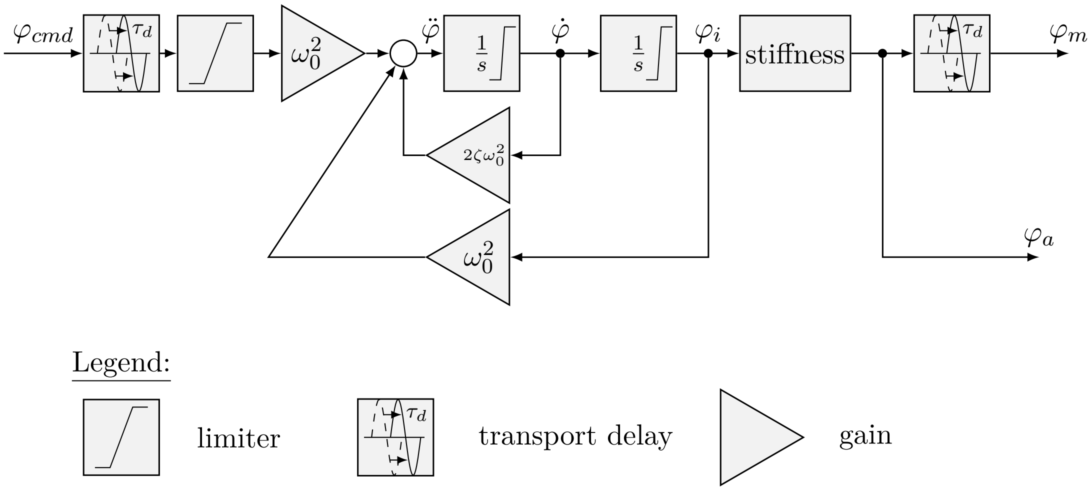

Figure 3.8.: Actuator Block Diagram

3.5. Propulsion

The propulsion system is not directly within the scope of the work on lateral controller and hence, is omitted here. A detailed description of the propulsion system's characteristics can be found in [23].

3.6. Sensors

Air Data System

The Air Data System is one of the major components of a flight control system, since it provides important information on the aircraft's current aerodynamic states, which are directly related to the forces and moments acting on it. Air data measurements are utilized for various functionalities. Common applications of air data in flight control systems are gain scheduling based on impact pressure $(p_t - p_s)$, feedback of AoA and AoS in inner control loops, and the utilization of barometric altitude and vertical speed as control variables in autopilots. Depending on the particular application, the requirements concerning the measurement's accuracy and precision, as well as availability and reliability may vary considerably. Consequently, significant effort is typically invested in the specification and selection of the ADS.

Such an effort could not be invested in the SAGITTA Project due to financial and time constraints. Consequently, the Air Data Boom from the company Space Age (variant 100400) was selected from the limited choice of Commercial-Off-The-Shelf (COTS) Air Data Booms for RPAS. The selection was based on references from partners and from experience in another project at the FSD. At this point, the suitability of the Air Data Boom for the purpose of closed-loop flight control of the SAGITTA Demonstrator was uncertain due to the lack of precise requirements and knowledge of the Air Data Boom's characteristics. In order to evaluate the feasibility of using the ADS measurements for closed-loop control, special attention was paid to its analysis and modeling. A brief outline of this topic is provided below.

The ADS of the SAGITTA Demonstrator consists of an air data computer and an air data boom. The Air Data Boom has openings for total and static pressure measurements

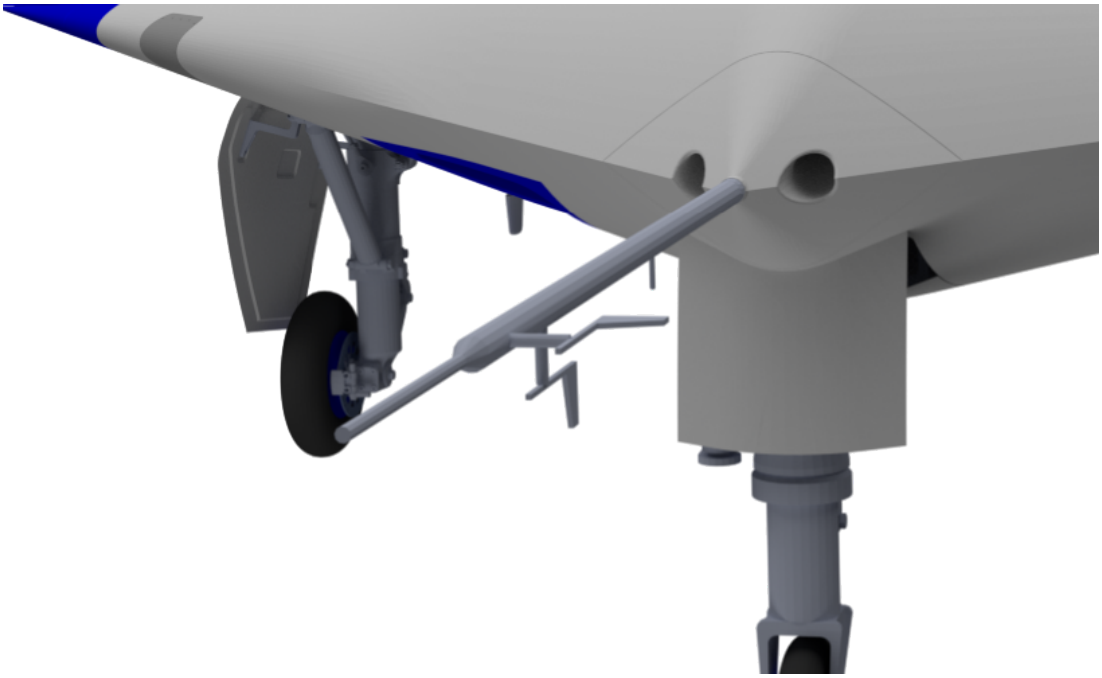

Figure 3.9.: AoA and flank angle vanes location

and is equipped with vanes for determination of aerodynamic flow angles, namely AoA and flank angle. As depicted in figure 3.9, the vanes are located on the left side (port) and below the air data boom and are slightly shifted relative to each other. The AoA vane and the flank angle vane are installed 19.66 cm and 27.28 cm respectively behind the tip of the boom. In addition, the ADS is equipped with a temperature sensor. The Air Data Computer incorporates two pressure sensors and analog-digital converters for digitalization of analogue signals from potentiometers measuring the position of the AoA and flank angle (β_f) vanes. Hence, the ADS of the SAGITTA Demonstrator provides measurements of static and impact pressure, AoA and flank angle, Outside Air Temperature (OAT), and further derived quantities.

The characteristics of the ADS are determined from a wind tunnel test campaign. Using results of the wind tunnel tests, a simulation model is derived at the FSD and provided to the control designers. The model implements the sensor characteristics of the ADS, including sensor bias and noise. Details of the model are presented, and the sensor characteristics are briefly analyzed.

The measurements of AoA, AoS and impact pressure of the Air Data System are modeled as the sum of the physical (true) value, bias and noise according to

$$x_{meas} = x + x_{bias}\left(\alpha, \beta_f\right) + x_{noise}\left(\alpha, \beta_f, \bar{q}\right), \tag{3.24}$$

where, $x = [\alpha, \beta, \bar{q}]$. The static pressure p_s is modeled according the following rule:

$$p_{s,meas} = p_s + p_{s,bias}\left(\alpha, \beta_f\right) + p_{s,noise}\left(\bar{q}\right). \tag{3.25}$$

Figure 3.10 shows the modeled bias and noise at landing speed (low $\bar{q}$) of the SAGITTA Demonstrator as a function of true AoA and AoS. The values of the biases are shown in the left column. In order to obtain a better physical understanding, the biases of static and impact pressure measurements are converted to, and expressed in terms of, altitude and speed. On the right-hand side, the scatter of the sensor noise is given in terms of standard deviation σ.

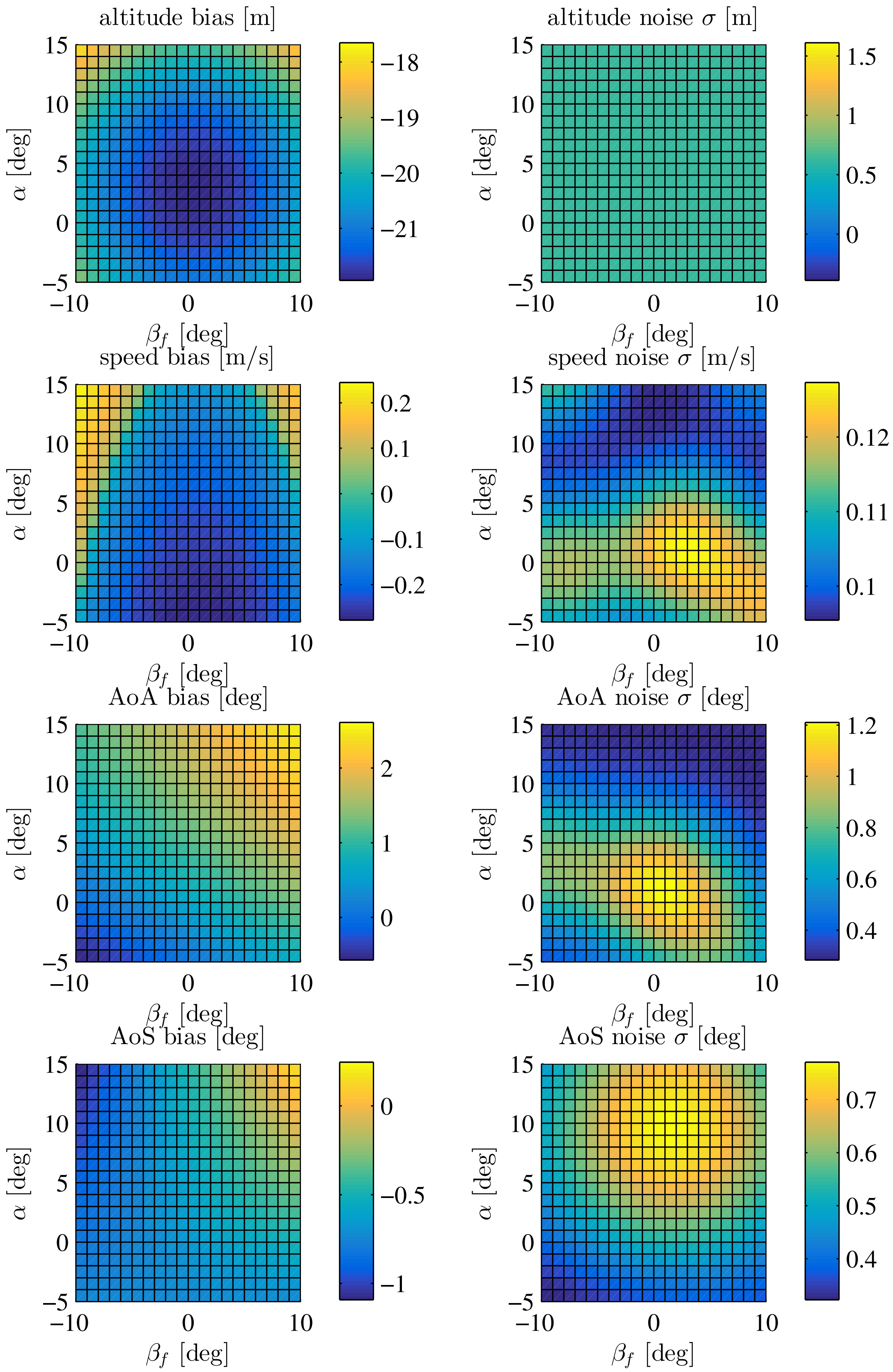

Figure 3.10.: ADS Bias and Noise

The figure shows some unexpected phenomena: An interesting effect is the variation of the bias in the speed measurement with changing AoA and AoS. Initially, it seems counterintuitive, that with increasing aerodynamic flow angle, the impact pressure, and hence the measured airspeed would increase. Before the analysis was completed, the expectation was that the measurement would decrease with both $\cos(\alpha)$ and $\cos(\beta)$. This effect could be partially explained by a decrease in static pressure (see the first plot in the left-hand column of figure 3.10), which in turn could be caused by the air data boom shadowing some openings distributed over its perimeter. However, further influences may contribute also to the observed effect. The bias variation of pitot-static measurements is relatively small. This is especially true if one focuses on the relevant flight envelope and the AoA and AoS range resulting from it. These errors in measurements can be addressed in the FCS by calibration of the respective sensors. In this case, the addition of a static value to the measured one would significantly reduce the error.

In contrast to the pitot-static measurements, the situation regarding the bias of AoA and AoS is more complex. The bias highly depends on the current situation in flight and the values are changing their signs within the operational envelope. Figure 3.10 reveals the extremely large amount of noise in AoA and AoS of up to $\sigma_\alpha = 1.2°$ amplitude for some air data boom orientations: the AoA being considerably more affected than the AoS. Furthermore, the noise levels change significantly with AoA and AoS. This can be attributed to multiple causes. Some of these may be the interference between the air data boom tip and the vanes, interference between the AoA and the AoS vane, or the shadowing of vanes by parts of the air data boom. A further significant contribution to the overall noise level is the structural oscillation of the air data boom which was observed during wind tunnel tests.

The foregoing leads to the conclusion that effective utilization of air flow angles in the flight control system of the SAGITTA Demonstrator poses a challenging task due to: limited sensor quality; strongly varying characteristics over the flight envelope; and significant difficulty of precise calibration.

Two references providing guidance on the dynamic characteristics of air data measurements have been studied during this work. In [38], the dynamics of the vanes for AoA and flank angle are modeled as PT_2 elements with natural frequency being a function of dynamic pressure as given in equation (3.26), and damping being in the range $\zeta = 0.18$ and 0.6.

$$\omega_0 = 1.725\sqrt{\bar{q}} \tag{3.26}$$

An exemplary transfer function for static and dynamic pressure is given in [54] as:

$$G(s) = \frac{1}{0.02s + 1}. \tag{3.27}$$

The dynamic characteristics of the ADS are highly dependent on the construction type of the air data boom and the sensors utilized, and may vary according to how the boom is installed. The values that are provided in the references only give an approximate idea of the dynamic characteristics of the vanes for the AoA and the flank angle. Since no data on dynamic characteristics is available for the Air Data System that is used in the SAGITTA Demonstrator, it has been decided not to model the ADS dynamics.

Navigation System

The Navigation System consists of a MEMS - based Inertial Measurement Unit (IMU), a DGPS receiver and an external magnetometer. Besides accelerations and rotation rates, it provides attitude, position and kinematic velocity information.

For the purpose of CSAS design and analysis, a low fidelity phenomenological model of the Navigation System has been developed. It incorporates the bias and noise characteristics for accelerometers, gyros and attitude measurements. The noise magnitudes are taken from static laboratory tests. Biases for accelerometers and gyros are extracted from the supplier's calibration report. Here, the threshold values that have been specified for acceptance tests (in other words the upper bounds on bias) are chosen as pessimistic estimates. Table 3.7 provides the implemented values for the sensors' bias and noise are given.

Besides bias and noise, the simulation model implements time delays. The value $\tau_d = 27.6\,\mathrm{ms}$ for the time delays assigned to the NAV is derived from rotary table tests of the gyros performed by project partners. It includes both internal data processing and transport delay. Scale factor errors and nonlinearities of accelerometers and gyros

Quantity	**Bias**	**Noise**	**Scale Factor Error**	**Nonlinearity**
$\omega_x, \omega_y, \omega_z$	0.2°/s	$0.66°/s$ RMS	$\leq 0.3\%$	$\leq 0.01\%$
f_x, f_y, f_z	0.01	0.0185 RMS	$\leq 0.3\%$	$\leq 0.08\%$
Φ, Θ		0.1° RMS		

Table 3.7.: Navigation System Characteristics

are provided in table 3.7 for the sake of completeness, but have been omitted during modeling.

3.7. Derivation of the Linear State Space Model

In the discussion above, the relevant subsystems and aircraft characteristics for the development of the SAGITTA Demonstrator's flight control have been described, and their implementation in the simulation model has been briefly discussed. The models of the system components, together with the model of the system environment (gravity, atmosphere and magnetic field), and the 6-DOF equations of motion, are all brought together in a single, nonlinear simulation model. Further details on its implementation can be found in [24, 90].

For the purpose of analysis of the aircraft dynamics and subsequent controller design, a linear state-space model is derived from the nonlinear simulation model by application of numerical linearization. The development of the linear state-space model, which basically follows [20], is described below.

The nonlinear equations of motion of the aircraft have the following form

$$\dot{\boldsymbol{x}} = \boldsymbol{f}\left(\boldsymbol{x}, \dot{\boldsymbol{x}}, \boldsymbol{u}\right) \tag{3.28}$$

with $\boldsymbol{f} = [f_1, f_2, ...f_n]^T$ being nonlinear functions, $\boldsymbol{x} = [x_1, x_2, ...x_n]^T$ representing the system state vector, $\dot{\boldsymbol{x}} = [\dot{x}_1, \dot{x}_2, ...\dot{x}_n]^T$ its derivative and $\boldsymbol{u} = [u_1, u_2, ...u_m]^T$ being the input vector. The corresponding output equations are:

$$\boldsymbol{y} = \boldsymbol{h}\left(\boldsymbol{x}, \dot{\boldsymbol{x}}, \boldsymbol{u}\right). \tag{3.29}$$

In order to obtain linear state-space models, operating points are initially determined by means of trimming the aircraft for given steady-state conditions. The operating points are specified by $\boldsymbol{x}_0, \boldsymbol{u}_0$ and $\dot{\boldsymbol{x}}_0 = 0$. The linearized model is obtained by performing small perturbations from a particular operating point. This can be described in a Taylor Series as follows:

$$\dot{\boldsymbol{x}}_0 + \delta\dot{\boldsymbol{x}} = f\left(\boldsymbol{x}_0, \boldsymbol{u}_0\right) + \left.\frac{\partial \boldsymbol{f}}{\partial \boldsymbol{x}}\right|_{\boldsymbol{x}_0,\boldsymbol{u}_0} \delta\boldsymbol{x} + \left.\frac{\partial \boldsymbol{f}}{\partial \dot{\boldsymbol{x}}}\right|_{\boldsymbol{x}_0,\boldsymbol{u}_0} \delta\dot{\boldsymbol{x}} + \left.\frac{\partial \boldsymbol{f}}{\partial \boldsymbol{u}}\right|_{\boldsymbol{x}_0,\boldsymbol{u}_0} \delta\boldsymbol{u} + H.O.T.. \tag{3.30}$$

By truncating the differential equations 3.30 after the linear term, and by taking into account that, for a steady-state operating point, the following is true:

$$\dot{\boldsymbol{x}}_0 = \boldsymbol{f}\left(\boldsymbol{x}_0, \boldsymbol{u}_0\right) = 0, \tag{3.31}$$

the linearized equations of motion can be written as

$$\delta\dot{\boldsymbol{x}} = \left.\frac{\partial \boldsymbol{f}}{\partial \boldsymbol{x}}\right|_{\boldsymbol{x}_0,\boldsymbol{u}_0} \delta\boldsymbol{x} + \left.\frac{\partial \boldsymbol{f}}{\partial \dot{\boldsymbol{x}}}\right|_{\boldsymbol{x}_0,\boldsymbol{u}_0} \delta\dot{\boldsymbol{x}} + \left.\frac{\partial \boldsymbol{f}}{\partial \boldsymbol{u}}\right|_{\boldsymbol{x}_0,\boldsymbol{u}_0} \delta\boldsymbol{u}. \tag{3.32}$$

The same procedure is applied to the output equation. After the performance of the following substitution:

$$\begin{aligned} \mathbf{A}' &= \left.\frac{\partial \boldsymbol{f}}{\partial \boldsymbol{x}}\right|_{\boldsymbol{x}_0,\boldsymbol{u}_0} & \mathbf{B}' &= \left.\frac{\partial \boldsymbol{f}}{\partial \boldsymbol{u}}\right|_{\boldsymbol{x}_0,\boldsymbol{u}_0} & \mathbf{E}' &= \left.\frac{\partial \boldsymbol{f}}{\partial \dot{\boldsymbol{x}}}\right|_{\boldsymbol{x}_0,\boldsymbol{u}_0} \\ \mathbf{C}' &= \left.\frac{\partial \boldsymbol{h}}{\partial \boldsymbol{x}}\right|_{\boldsymbol{x}_0,\boldsymbol{u}_0} & \mathbf{D}' &= \left.\frac{\partial \boldsymbol{h}}{\partial \boldsymbol{u}}\right|_{\boldsymbol{x}_0,\boldsymbol{u}_0} & \mathbf{F}' &= \left.\frac{\partial \boldsymbol{h}}{\partial \dot{\boldsymbol{x}}}\right|_{\boldsymbol{x}_0,\boldsymbol{u}_0}, \end{aligned} \tag{3.33}$$

and after having dropped the δ for better readability, the implicit linear state-space model can be stated as

$$\begin{aligned} \dot{\boldsymbol{x}} &= \mathbf{A}'\boldsymbol{x} + \mathbf{B}'\boldsymbol{u} + \mathbf{E}'\dot{\boldsymbol{x}} \\ \boldsymbol{y} &= \mathbf{C}'\boldsymbol{x} + \mathbf{D}'\boldsymbol{u} + \mathbf{F}'\dot{\boldsymbol{x}}. \end{aligned} \tag{3.34}$$

The corresponding explicit formulation of the state equation is given in equation (3.35).

$$\dot{\boldsymbol{x}} = \left[\mathbf{I} - \mathbf{E}'\right]^{-1} \mathbf{A}'\boldsymbol{x} + \left[\mathbf{I} - \mathbf{E}'\right]^{-1} \mathbf{B}'\boldsymbol{u} \tag{3.35}$$

The substitution of $\dot{\boldsymbol{x}}$ in the output equation using equation (3.35) leads to its explicit formulation:

$$\boldsymbol{y} = \left[\mathbf{C}' + \mathbf{F}'\mathbf{T}\mathbf{A}'\right]\boldsymbol{x} + \left[\mathbf{D}' + \mathbf{F}'\mathbf{T}\mathbf{B}'\right]\boldsymbol{u}, \tag{3.36}$$

where $\mathbf{T} = [\mathbf{I} - \mathbf{E}']^{-1}$, which finally leads to the well-known explicit linear state-space model:

$$\begin{aligned} \dot{\boldsymbol{x}} &= \mathbf{A}\boldsymbol{x} + \mathbf{B}\boldsymbol{u} \\ \boldsymbol{y} &= \mathbf{C}\boldsymbol{x} + \mathbf{D}\boldsymbol{u} \end{aligned} \tag{3.37}$$

where $\mathbf{A} = \left[\mathbf{I} - \mathbf{E}'\right]^{-1} \mathbf{A}'$ is the system matrix, $\mathbf{B} = \left[\mathbf{I} - \mathbf{E}'\right]^{-1} \mathbf{B}'$ the input matrix; $\mathbf{C} = [\mathbf{C}' + \mathbf{F}'\mathbf{T}\mathbf{A}']$ the output matrix; and $\mathbf{D} = [\mathbf{D}' + \mathbf{F}'\mathbf{T}\mathbf{B}']$ the feed-through matrix. The states of the system are described by $\boldsymbol{x}$, the inputs by $\boldsymbol{u}$ and the outputs by $\boldsymbol{y}$.

In order to provide a better understanding of the numerically linearized state-space models used for controller design, and in order to be able to isolate and understand different physical effects, the analytical representation of the linear state-space model is provided below using the following states, inputs and outputs w.r.t. the body-fixed coordinate system:

$$\boldsymbol{x} = \begin{bmatrix} r \\ \beta \\ p \\ \Phi \end{bmatrix} \qquad \boldsymbol{u} = \begin{bmatrix} \xi \\ \zeta \end{bmatrix} \qquad \boldsymbol{y} = \begin{bmatrix} r \\ \beta \\ p \\ \Phi \\ f_y \end{bmatrix}, \tag{3.38}$$

where $\xi = \xi_{equiv}$ and $\zeta = \zeta_{equiv}$. The linear state-space model describing the lateral motion is defined as follows:

$$\mathbf{A} = \begin{bmatrix} N_r - \frac{N_{\dot\beta}(Y_r - \cos(\alpha_0))}{Y_{\dot\beta}-1} & N_\beta - \frac{N_{\dot\beta}Y_\beta}{Y_{\dot\beta}-1} & N_p - \frac{N_{\dot\beta}(Y_p+\sin(\alpha_0))}{Y_{\dot\beta}-1} & -\frac{N_{\dot\beta}g\cos(\Theta_0)}{V_0\left(Y_{\dot\beta}-1\right)} \\ -\frac{Y_r-\cos(\alpha_0)}{Y_{\dot\beta}-1} & -\frac{Y_\beta}{Y_{\dot\beta}-1} & -\frac{Y_p+\sin(\alpha_0)}{Y_{\dot\beta}-1} & -\frac{g\cos(\Theta_0)}{V_0\left(Y_{\dot\beta}-1\right)} \\ L_r - \frac{L_{\dot\beta}(Y_r-\cos(\alpha_0))}{Y_{\dot\beta}-1} & L_\beta - \frac{L_{\dot\beta}Y_\beta}{Y_{\dot\beta}-1} & L_p - \frac{L_{\dot\beta}(Y_p+\sin(\alpha_0))}{Y_{\dot\beta}-1} & -\frac{L_{\dot\beta}g\cos(\Theta_0)}{V_0\left(Y_{\dot\beta}-1\right)} \\ \tan(\Theta_0) & 0 & 1 & 0 \end{bmatrix}$$

$$\mathbf{B} = \begin{bmatrix} N_\xi - \frac{N_{\dot\beta}Y_\xi}{Y_{\dot\beta}-1} & N_\zeta - \frac{N_{\dot\beta}Y_\zeta}{Y_{\dot\beta}-1} \\ -\frac{Y_\xi}{Y_{\dot\beta}-1} & -\frac{Y_\zeta}{Y_{\dot\beta}-1} \\ L_\xi - \frac{L_{\dot\beta}Y_\xi}{Y_{\dot\beta}-1} & L_\zeta - \frac{L_{\dot\beta}Y_\zeta}{Y_{\dot\beta}-1} \\ 0 & 0 \end{bmatrix} \tag{3.39}$$

$$\mathbf{C} = \begin{bmatrix} 1 & 0 & 0 & 0 \\ 0 & 1 & 0 & 0 \\ 0 & 0 & 1 & 0 \\ 0 & 0 & 0 & 1 \\ a & b & c & d \end{bmatrix}$$

$$\mathbf{D} = \begin{bmatrix} 0 & 0 \\ 0 & 0 \\ 0 & 0 \\ 0 & 0 \\ e & f \end{bmatrix}$$

with

$$\begin{aligned} a &= \frac{\left(N_r - \frac{N_{\dot\beta}(Y_r-\cos(\alpha_0))}{Y_{\dot\beta}-1}\right)V_0\cos(\alpha_0)}{g} - \frac{\left(L_r - \frac{L_{\dot\beta}(Y_r-\cos(\alpha_0))}{Y_{\dot\beta}-1}\right)V_0\sin(\alpha_0)}{g} - \cos(\Theta)\tan(\Theta) \\ b &= \frac{\left(N_\beta - \frac{N_{\dot\beta}Y_\beta}{Y_{\dot\beta}-1}\right)V_0\cos(\alpha_0)}{g} - \frac{\left(L_\beta - \frac{L_{\dot\beta}Y_\beta}{Y_{\dot\beta}-1}\right)V_0\sin(\alpha_0)}{g} \\ c &= \frac{\left(N_p - \frac{N_{\dot\beta}(Y_p+\sin(\alpha_0))}{Y_{\dot\beta}-1}\right)V_0\cos(\alpha_0)}{g} - \frac{\left(L_p - \frac{L_{\dot\beta}(Y_p+\sin(\alpha_0))}{Y_{\dot\beta}-1}\right)V_0\sin(\alpha_0)}{g} - \cos(\Theta) \\ d &= -\frac{N_{\dot\beta}\cos(\Theta)\cos(\alpha_0)}{Y_{\dot\beta}-1} + \frac{L_{\dot\beta}\cos(\Theta)\sin(\alpha_0)}{Y_{\dot\beta}-1} \\ e &= \frac{\left(N_\xi - \frac{N_{\dot\beta}Y_\xi}{Y_{\dot\beta}-1}\right)V_0\cos(\alpha_0)}{g} - \frac{\left(L_\xi - \frac{L_{\dot\beta}Y_\xi}{Y_{\dot\beta}-1}\right)V_0\sin(\alpha_0)}{g} + \frac{V_0Y_\xi}{g} \\ f &= \frac{\left(N_\zeta - \frac{N_{\dot\beta}Y_\zeta}{Y_{\dot\beta}-1}\right)V_0\cos(\alpha_0)}{g} - \frac{\left(L_\zeta - \frac{L_{\dot\beta}Y_\zeta}{Y_{\dot\beta}-1}\right)V_0\sin(\alpha_0)}{g} + \frac{V_0Y_\zeta}{g}. \end{aligned} \tag{3.40}$$

The definitions of the matrix entries, the so-called stability derivatives, can be found in [27]. Typically, the influence of the terms $L_{\dot\beta}$, $N_{\dot\beta}$ and $Y_{\dot\beta}$ is very small. In the case of the SAGITTA Demonstrator, the omission of these entries leads to a relative error of less than 2‰ in the system matrix entries. Hence, in order to obtain a state-space model that provides a good overview of major dynamic effects, small entries are ignored here in order to focus on the main influencing factors. This leads to a much simpler state-space model representation, which is shown in equation (3.41).

$$
\begin{aligned}
&\text{State eq:}\\
&\begin{bmatrix}\dot{r}\\ \dot{\beta}\\ \dot{p}\\ \dot{\Phi}\end{bmatrix} = \begin{bmatrix} N_r & N_\beta & N_p & 0\\ Y_r - \cos(\alpha_0) & Y_\beta & Y_p + \sin(\alpha_0) & \frac{g}{V_0}\cos(\Theta_0)\\ L_r & L_\beta & L_p & 0\\ \tan(\Theta_0) & 0 & 1 & 0 \end{bmatrix} \begin{bmatrix} r\\ \beta\\ p\\ \Phi\end{bmatrix} + \begin{bmatrix} N_\xi & N_\zeta\\ Y_\xi & Y_\zeta\\ L_\xi & L_\zeta\\ 0 & 0\end{bmatrix}\begin{bmatrix}\xi\\ \zeta\end{bmatrix}\\
&\text{Output eq:}\\
&\begin{bmatrix} r\\ \beta\\ p\\ \Phi\\ f_y\end{bmatrix} = \begin{bmatrix} 1 & 0 & 0 & 0\\ 0 & 1 & 0 & 0\\ 0 & 0 & 1 & 0\\ 0 & 0 & 0 & 1\\ a & b & c & 0\end{bmatrix}\begin{bmatrix} r\\ \beta\\ p\\ \Phi\end{bmatrix} + \begin{bmatrix} 0 & 0\\ 0 & 0\\ 0 & 0\\ 0 & 0\\ d & e\end{bmatrix}\begin{bmatrix}\xi\\ \zeta\end{bmatrix}
\end{aligned}
\tag{3.41}
$$

with

$$
\begin{aligned}
a &= \frac{(N_r\cos(\alpha_0) - L_r\sin(\alpha_0))V_0 - g\sin(\Theta_0)}{g}\\
b &= \frac{(N_\beta\cos(\alpha_0) - L_\beta\sin(\alpha_0))V_0}{g}\\
c &= \frac{(N_p\cos(\alpha_0) - L_p\sin(\alpha_0))V_0 - g\cos(\Theta_0)}{g}\\
d &= \frac{(N_\xi\cos(\alpha_0) - L_\xi\sin(\alpha_0) + Y_\xi)V_0}{g}\\
e &= \frac{(N_\zeta\cos(\alpha_0) - L_\zeta\sin(\alpha_0) + Y_\zeta)V_0}{g}
\end{aligned}
\tag{3.42}
$$

It should be noted that, in this work, the linear state-space model for controller design and validation is obtained by means of numerical linearization. Consequently, the small entries which were neglected in the derivation of the analytic state-space model, are inherently part of the numerical results, and thus contribute to gain design, analysis and verification.

3.8. Turbulence and Gust Modeling

In order to analyze the influence of atmospheric disturbances on the aircraft, this work implements the commonly used Dryden turbulence model. Multiple, slightly different definitions of this model exist. The most recent one which is specified in the MIL-HDBK-1797 [57] is used in the following outline.

The turbulence model is defined in terms of PSDs for each component of translational and rotatory wind. The PSDs of the translational turbulence are given in [57] as:

$$
\begin{aligned}
\Phi_{u_W}(\Omega) &= \sigma_{u_W}^2 \frac{2L_u}{\pi(1+(L_u\Omega)^2)}\\
\Phi_{v_W}(\Omega) &= \sigma_{v_W}^2 \frac{L_v(1+12(L_v\Omega)^2)}{\pi(1+4(L_v\Omega)^2)^2}\\
\Phi_{w_W}(\Omega) &= \sigma_{w_W}^2 \frac{L_w(1+12(L_w\Omega)^2)}{\pi(1+4(L_w\Omega)^2)^2}.
\end{aligned}
\tag{3.43}
$$

The corresponding Power Spectra of the rotatory turbulence are provided in the proposed MIL Standard and Handbook-Flying Qualities of Air Vehicles [34] as follows:

$$\begin{aligned}
\Phi_{p_W}(\Omega) &= \sigma_{p_W}^2 \frac{2\bar{L}_p}{\pi(1+(\bar{L}_p\Omega)^2)} \\
\Phi_{q_W}(\Omega) &= \frac{\Omega^2}{1+(\frac{4b\Omega}{\pi})^2}\Phi_{w_W} \\
\Phi_{r_W}(\Omega) &= \frac{\Omega^2}{1+(\frac{3b\Omega}{\pi})^2}\Phi_{v_W},
\end{aligned} \tag{3.44}$$

with Ω being the spatial frequency which is related to the angular frequency (ω) by equation (3.45)

$$\omega = \Omega V. \tag{3.45}$$

In order to preserve the power of the resulting signal, the scaling

$$\Phi(\omega) = \frac{1}{V}\Phi(\Omega) \tag{3.46}$$

between spatial PSD and temporal frequency PSD must be taken into account [47]. The gust intensity σ and scale length L depend on the height of flight operations, whereby three cases are distinguished. For heights below 1000 ft AGL, the values for σ and L are determined according to the Low Altitude Model in military specification MIL-HDBK-1797 as given in equation (3.47),

$$\begin{aligned}
L_w &= h \\
L_u = L_v &= \frac{h}{(0.177+0.000823h)^{1.2}} \\
\sigma_{w_W} &= 0.1u_{20} \\
\sigma_{u_W} = \sigma_{v_W} &= \frac{\sigma_{w_W}}{(0.177+0.000823h)^{0.4}}
\end{aligned} \tag{3.47}$$

with u_{20} being the mean wind speed at 20 ft height above ground (AGL) which is 15 kn at light; 30 kn at moderate; and 45 kn at severe turbulence. The medium and high altitude model, for heights above 2000 ft, specifies the parametrization according to equation (3.48),

$$\begin{aligned}
\sigma_{u_W} = \sigma_{v_W} &= \sigma_{w_W} \\
L_u = 2L_v &= 2L_w
\end{aligned} \tag{3.48}$$

with $L_u = 2L_v = 2L_w = 1750$ ft and σ derived from figure 3.11. If the aircraft is operated between 1000 and 2000 ft, the values for L and σ are obtained by interpolation between the Low Altitude Model and the Medium/High Altitude Model.

Angular turbulence components are calculated using following relationship:

$$\bar{L}_p = \frac{\sqrt{L_w b}}{2.6} \qquad \sigma_{p_W} = \frac{1.9}{\sqrt{L_w b}}\sigma_{w_W}. \tag{3.49}$$

Whether the turbulence around the x- and z-axes of the aircraft is to be applied, is determined by evaluation of the inequalities (3.50). If one of the inequalities provides a true statement, the corresponding angular gust must be taken into account, otherwise it can be neglected.

$$\sqrt{\frac{b}{L_w}}|C_{lp}| > |C_{l\beta}| \quad , \quad \sqrt{\frac{\pi b}{6L_v}}|C_{nr}| > |C_{n\beta}| \tag{3.50}$$

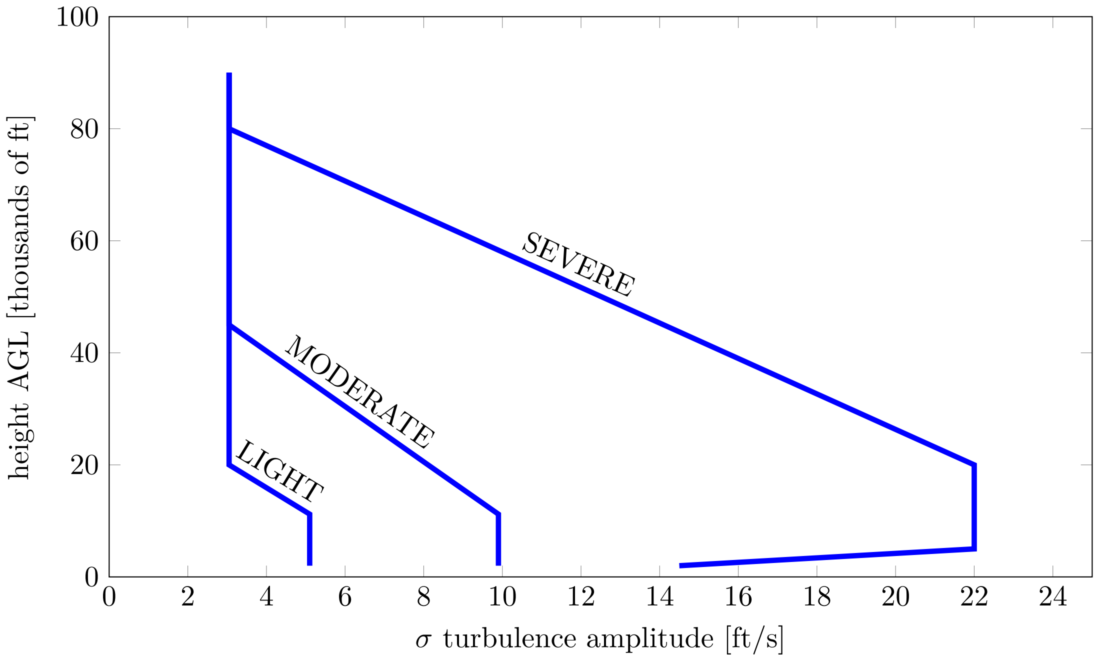

Figure 3.11.: Turbulence Intensity according to Medium/High Altitude Model (reproduced from [60])

The Dryden Turbulence Power Spectrum can be implemented by utilization of respective filters fed by normalized white noise signals with a variance of $\sigma^2 = 1$ using either a continuous or a discrete formulation. The design process of a continuous filter is shown by Cook in [17] for the turbulence specification provided in [60]. Using the same methodology, the continuous filters for the PSD defined in [57] can be defined as follows:

$$G_{v_W}(s) = K_{v_W} \frac{1 + T_n s}{(1 + T_v s)^2} \tag{3.51}$$

with

$$K_{v_W} = \sigma_{v_W} \sqrt{\frac{L_v}{\pi V_0}} \qquad T_n = \sqrt{12}\frac{L_v}{V_0} \qquad T_v = \sqrt{4}\frac{L_v}{V_0}, \tag{3.52}$$

and

$$G_{p_W}(s) = \frac{K_{p_W}}{(1 + T_p s)} \tag{3.53}$$

where

$$K_{p_W} = \sigma_{p_W} \sqrt{\frac{2L_p}{\pi V_0}} \qquad T_p = \frac{L_p}{V_0}, \tag{3.54}$$

and where V_0 describes aircraft's airspeed at the particular operating point, and s is the Laplace variable. To generate the white noise signal n driving the linear filter, a random number generator is used. This must be properly scaled along with the sample time of the simulation (Δt) according to [32]:

$$n = \frac{1}{\sqrt{\Delta t}} \cdot \texttt{randn}, \tag{3.55}$$

where `randn` is the MATLAB function for generation of random numbers. Figure 3.12 shows an example of the filter output. The three translational wind components of turbulence are depicted at an aircraft speed of $40\,\mathrm{m\,s^{-1}}$ and an altitude of $1000\,\mathrm{m}$ AGL.

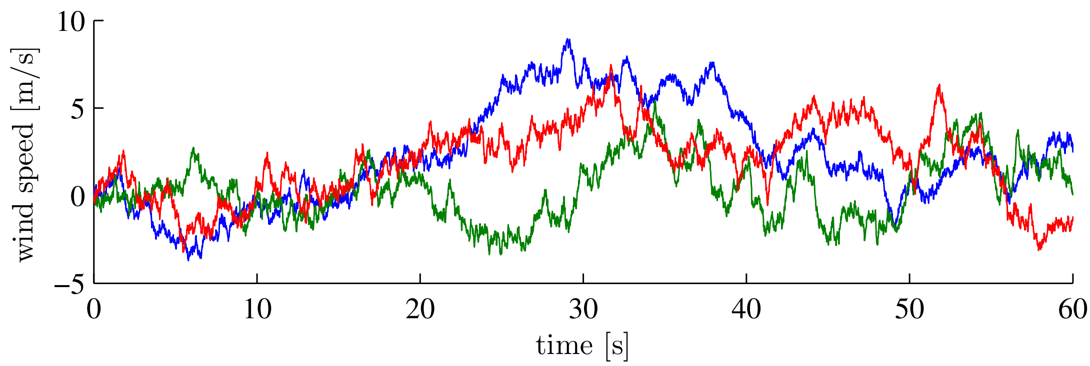

Figure 3.12.: Exemplary time series of turbulence at moderate level

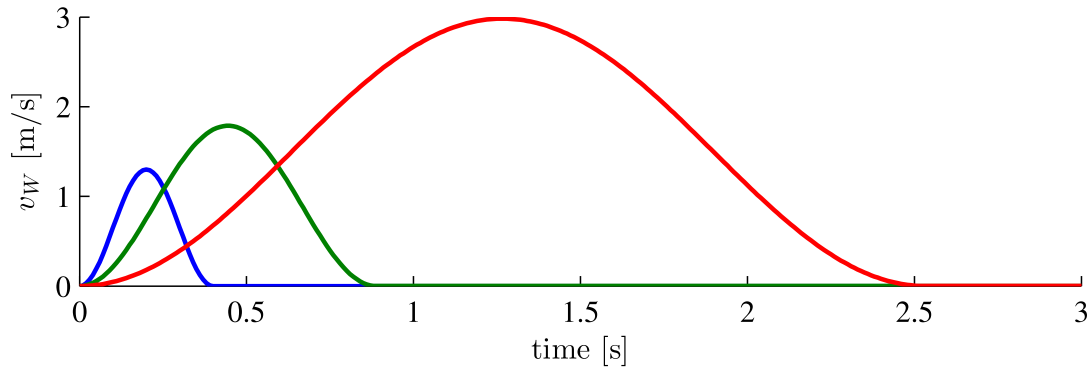

Figure 3.13.: Exemplary time series of lateral gust at moderate level for $d = 9, 20, 57$ [m]

In contrast to the turbulence, the gust model generates a non-stochastic change of wind at a particular instant in time during the simulation. The discrete gust is modeled as a build up of wind of the form presented in equation (3.56), with $V_{W,max}$ being the maximum magnitude of the wind, and d being the gust length according to figure 3.14. In this, x is the current aircraft position relative to the gust.

$$V_W = \frac{V_{W,max}}{2}\left(1 - \cos\frac{\pi x}{d}\right) \tag{3.56}$$

This gust form is used for all three translatory wind components and may be applied as a single gust, or consecutive gusts of different lengths and directions, as described in [57]. Curiously, the gust as well as the turbulence are defined w.r.t. body-fixed coordinate system and hence are moving and rotating with the aircraft. The length d of the gust is typically "tuned" so, that the resulting gust is exciting the natural frequencies of the aircraft. The tuning is performed by setting the argument of the cosine in equation (3.56) equal to the natural frequency of (e.g.) Dutch-roll. Figure 3.13 shows an example of a moderate gust for three different gust lengths. The outputs of the wind model when incorporating both a gust and a turbulence element, are time series of the wind speed vector $\boldsymbol{V}_W$ and the wind rotation rate vector $\boldsymbol{\omega}_W$.

The previously presented dynamic atmosphere model can be incorporated easily into the linear state-space model and is done, based on the so-called wind triangle (shown in figure 3.15 for $w_W = 0$), by establishing the relationship between the kinematic states, the aerodynamic states and the translational wind ($\boldsymbol{V}_W = [u_W, v_W, w_W]^T$) according to equation (3.57),

$$\boldsymbol{V}_A = \boldsymbol{V}_K - \boldsymbol{V}_W \tag{3.57}$$

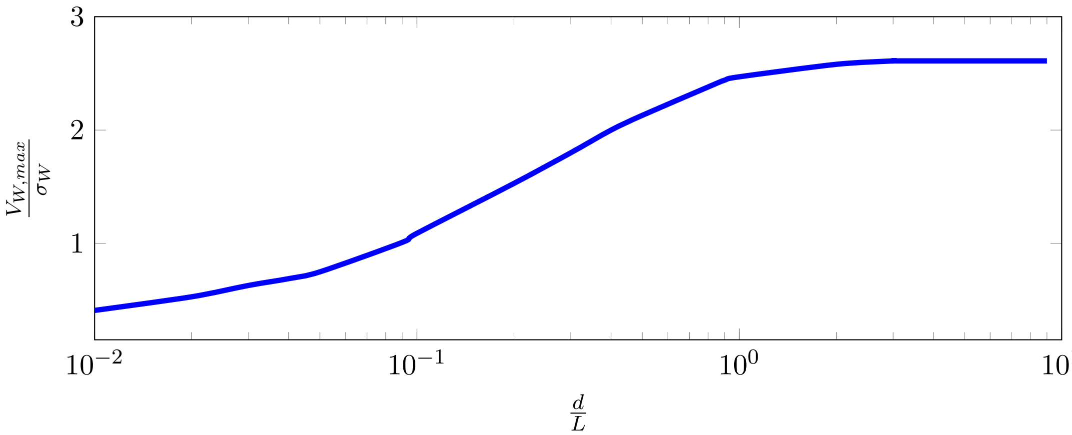

Figure 3.14.: Determination of gust magnitude (reproduced from [60])

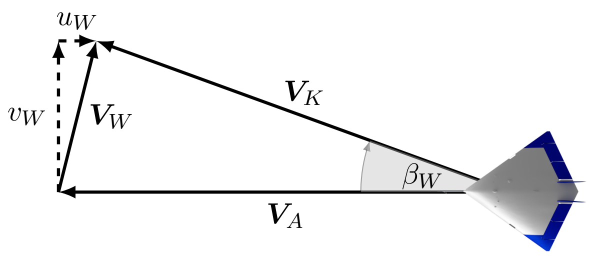

Figure 3.15.: Wind triangle

where index K indicates kinematic quantities and index A indicates aerodynamic quantities. The corresponding relationship for rotatory wind ($\boldsymbol{\omega}_W = [p_W, q_W, r_W]^T$) is given by equation (3.58).

$$\boldsymbol{\omega}_A = \boldsymbol{\omega}_K - \boldsymbol{\omega}_W \tag{3.58}$$

Assuming the presence of only lateral wind components ($u_W << v_W$, $w_W = 0$ and $q_W = 0$), and by using the following approximation from [27]:

$$v_W = \beta_W V_0, \tag{3.59}$$

the translational lateral wind (v_W) can be described in terms of wind-induced AoS (β_W) as follows:

$$\beta_W = \frac{v_W}{V_0}, \tag{3.60}$$

where V_0 is the trim speed at the operating point. The angle β_W introduced here describes the angle between the aerodynamic speed and the kinematic speed vectors as illustrated in figure 3.15. With the assumption stated above concerning lateral wind, and with the introduction of β_W, the disturbance vector to the state-space model are β_W, p_W and r_W.

The disturbance vector can now be included in the linear state-space model. Equation (3.61) shows the state-space representation of the system's dynamics incorporating atmospheric disturbance

$$\dot{\boldsymbol{x}} = \boldsymbol{A}\boldsymbol{x} + \boldsymbol{B}\boldsymbol{u} + \boldsymbol{B}_W \boldsymbol{u}_W \qquad \boldsymbol{y} = \boldsymbol{C}\boldsymbol{u} + \boldsymbol{D}\boldsymbol{u} + \boldsymbol{D}_W \boldsymbol{u}_W \tag{3.61}$$

with $\mathbf{B}_W$ being the disturbance input matrix, $\mathbf{D}_W$ the disturbance feed-through matrix and $\boldsymbol{u}_W$ the wind disturbance vector, and in which $\boldsymbol{x}$ incorporates the kinematic states (inter alia β_K, p_K and r_K). The aerodynamic quantities β_A, p_A and r_A are part of

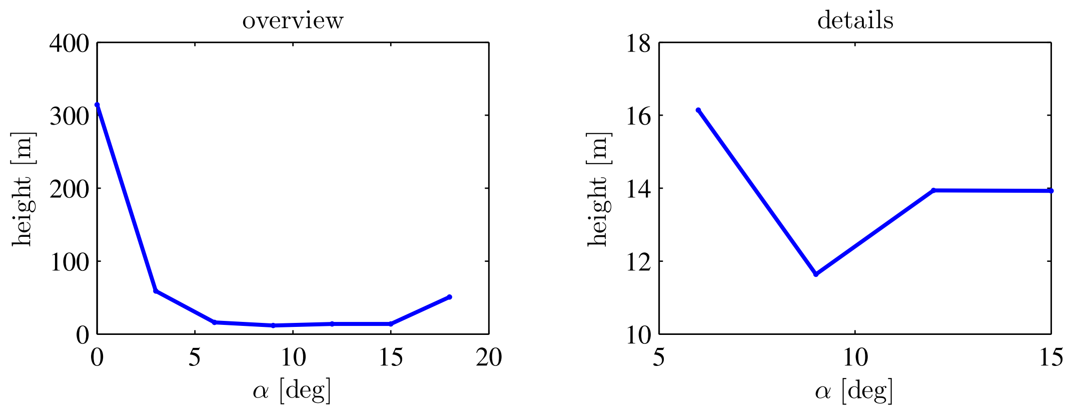

Figure 3.16.: Upper limit for relevance of angular turbulence (p-gust)

the state-space model's output $\boldsymbol{y}$. The matrix $\boldsymbol{B}_W$, describing the influence of the atmospheric disturbance on the aircraft dynamics, can be derived from the respective columns (r_K, β_K and p_K) of the system matrix $\boldsymbol{A}$. According to equations (3.57) and (3.58), these entries are multiplied by -1 and are joined to the disturbance input matrix $\boldsymbol{B}_W$, leading to:

$$\boldsymbol{B}_W \boldsymbol{u}_W = \begin{bmatrix} -N_r & -N_\beta & -N_p \\ -Y_r + \cos(\alpha_0) & -Y_\beta & -Y_p - \sin(\alpha_0) \\ -L_r & -L_\beta & -L_p \\ 0 & 0 & 0 \end{bmatrix} \begin{bmatrix} r_W \\ \beta_W \\ p_W \end{bmatrix}, \tag{3.62}$$

with $\boldsymbol{u}_W = [r_W, \beta_W, p_W]^T$ being the atmospheric disturbance vector consisting of gust and turbulence. The corresponding feed-through matrix $\boldsymbol{D}_W$ is constructed analogously to $\boldsymbol{B}_W$ by applying the relationships in equations (3.57) and (3.58), hence by taking the respective columns of the output matrix $\boldsymbol{C}$ and multiplying the matrix entries by -1.

The evaluation of inequalities (3.50) for rotatory turbulence around the z-axis of the aircraft (r-gust) shows that it can be ignored throughout the envelope. Therefore, the r_W row can be omitted from the input matrix $\boldsymbol{B}_W$, as well as in the corresponding feed-through matrix $\boldsymbol{D}_W$ and the disturbance vector $\boldsymbol{u}_W$. Figure 3.16 shows the height below which the gust around the x-axis (p-gust) becomes relevant for the SAGITTA Demonstrator. From this, it can be concluded, that p-gust around the x-axis needs to be taken into account in terminal flight phases (Flight Phase C) for analysis of the system's gust rejection properties.

Integration of the turbulence model into the aircraft's state-space model is now considered. For this, the wind input β_W in equation (3.62) is expressed as the sum of turbulence-induced wind β_T and gust-induced wind β_G. The time series of the gust-induced wind can be calculated using equation (3.56) and transformed from v_W to β_T by application of equation (3.60). In order to integrate turbulence into the state-space model, the turbulence filter for translational disturbance, presented in equation (3.51), and its counterpart for rotatory turbulence, are first of all transformed into their state-space representation given in equations (3.63) and (3.64), with n_{v_W} and n_{p_W} being the turbulence model inputs for unitary white noise signals.

$$\begin{bmatrix} \dot{x}_T \\ \dot{\beta}_T \end{bmatrix} = \begin{bmatrix} -\frac{2}{T_v} & -\frac{1}{T_v^2} \\ 1 & 0 \end{bmatrix} \begin{bmatrix} x_T \\ \beta_T \end{bmatrix} + \begin{bmatrix} \frac{K_{v_W}}{T_v^2} - \frac{2K_{v_W}T_n}{T_v^3} \\ \frac{K_{v_W}T_n}{T_v^2} \end{bmatrix} n_{v_W} \tag{3.63}$$

$$\dot{p}_T = -\frac{1}{T_p} p_T + \frac{K_{pW}}{T_p} n_{pW} \tag{3.64}$$

The turbulence models, the gust models and the model of the rigid body aircraft can now be combined. The resulting state-space model is shown in equation (3.65),

$$\begin{bmatrix} \dot{r} \\ \dot{\beta} \\ \dot{p} \\ \dot{\Phi} \\ \dot{x}_T \\ \dot{\beta}_T \\ \dot{p}_T \end{bmatrix} = \begin{bmatrix} N_r & N_\beta & N_p & 0 & 0 & -N_\beta & -N_p \\ Y_r - \cos(\alpha_0) & Y_\beta & Y_p + \sin(\alpha_0) & \frac{g}{V_0}\cos(\Theta_0) & 0 & -Y_\beta & -Y_p + \sin(\alpha_0) \\ L_r & L_\beta & L_p & 0 & 0 & -L_\beta & -L_p \\ \tan(\Theta_0) & 0 & 1 & 0 & 0 & 0 & 0 \\ 0 & 0 & 0 & 0 & -\frac{2}{T_v} & -\frac{1}{T_v^2} & 0 \\ 0 & 0 & 0 & 0 & 1 & 0 & 0 \\ 0 & 0 & 0 & 0 & 0 & 0 & -\frac{1}{T_p} \end{bmatrix} \begin{bmatrix} r \\ \beta \\ p \\ \Phi \\ x_T \\ \beta_T \\ p_T \end{bmatrix}$$
$$+ \begin{bmatrix} N_\xi & N_\zeta \\ Y_\xi & Y_\zeta \\ L_\xi & L_\zeta \\ 0 & 0 \end{bmatrix} \begin{bmatrix} \xi \\ \zeta \end{bmatrix}$$
$$+ \begin{bmatrix} -N_\beta & -N_p & 0 & 0 \\ -Y_\beta & -Y_p - \sin(\alpha_0) & 0 & 0 \\ -L_\beta & -L_p & 0 & 0 \\ 0 & 0 & 0 & 0 \\ 0 & 0 & \frac{K_{vW}}{T_v^2} - \frac{2K_{vW}T_n}{T_v^3} & 0 \\ 0 & 0 & \frac{K_{vW}T_n}{T_v^2} & 0 \\ 0 & 0 & 0 & \frac{K_{pW}}{T_p} \end{bmatrix} \begin{bmatrix} \beta_G \\ p_G \\ n_{vW} \\ n_{pW} \end{bmatrix} \tag{3.65}$$

where β_G and p_G represent "1-cosine" gust series inputs, and n_{vW} and n_{pW} white noise time series with unity signal power.

After establishing the nominal linear-state space model with an integrated dynamic atmosphere, the model is enhanced in the following section with models of uncertainties. Further elements are added to the model to simplify the controller design and analysis.

3.9. Incorporation of uncertainties into the state-space model and preparation for controller design

As mentioned in section 3.1, an estimation of aerodynamic uncertainties is provided for the SAGITTA Demonstrator's ADM. In order to take these uncertainties into account for flight dynamics analysis and verification, they are incorporated into the linear state-space model. The aerodynamic uncertainties cannot be applied directly to the state-space model, as they are expressed in terms of aerodynamic derivatives and not in terms of stability derivatives. Consequently, further processing of the ADM is required to derive the corresponding uncertainties for the entries of the state-space model.

The outputs of the ADM are coefficients of aerodynamic forces and moments. In order to obtain the corresponding derivatives, the ADM is numerically linearized. The absolute minimum and maximum values are determined for each nominal aerodynamic derivative, for which a specified uncertainty is provided,

$$C_{ij,max} = C_{ij,nom} + \Delta C_{ij} \quad C_{ij,min} = C_{ij,nom} - \Delta C_{ij}, \tag{3.66}$$

where ΔC_{ij} represents the absolute uncertainty range of the derivative C_{ij} calculated from table 3.1 and the nominal value of C_{ij}. Using $C_{ij,min}$, $C_{ij,nom}$ and $C_{ij,max}$, the minimum, nominal, and maximum absolute values of stability derivatives are calculated according to the respective definitions in [27]. The percentage spread of the resultant uncertain stability derivatives relative to their nominal values is also calculated. It is important to note here, that the nominal value of the stability derivative obtained by the above described procedure may differ significantly from the original state-space model entry obtained by numerical linearization of the 6-DoF nonlinear simulation model. The reason for this is that only aerodynamic effects are taken into account by the application of the procedure described above, whereas the linearization of the 6-DoF nonlinear simulation model also encompasses further effects (such as forces and moments generated by the propulsion system).

In the next step, the calculated uncertainty range of stability derivatives can be applied to the state-space model entries. The tools provided by the Robust Control Toolbox of MATLAB/Simulink are used for this. The uncertain state-space entries are implemented as MATLAB uncertain real parameters and assembled together with further certain entries in the so-called MATLAB uncertain state-space model (`uss`).

Unfortunately, the given uncertainty specification of the ADM omits some aerodynamic effects, such as the uncertainties in the force resulting from flap deflections. While the corresponding moment derivatives are taken into account in the model provided, the forces due to flap deflections are ignored. During the design phase of the simulation environment, the controller design team decided to extend the uncertainty specification by the forces being a function of the respective moments according the following application rule:

$$C_{F_{\delta uncertain}} = C_{F_{\delta nominal}} \frac{C_{M_{\delta uncertain}}}{C_{M_{\delta nominal}}} \tag{3.67}$$

with F standing for the force and M for the moment. The approach presented here assumes that the uncertainty in the moments due to flap deflection is mainly caused by the uncertainty in the respective forces multiplied with the lever arm, which is assumed to be constant taking small flap deflections.

After introduction of aerodynamic uncertainties in the linear state-space model, the next step is to add the actuator dynamics. Thereby, the nonlinear actuator model presented in section 3.4 is replaced by an uncertain linear second order model of the form given in equation (3.68).

$$\begin{bmatrix} \ddot{x} \\ \dot{x} \end{bmatrix} = \begin{bmatrix} -2\zeta_{act}\omega_{0,act} & -\omega_{0,act}^2 \\ 1 & 0 \end{bmatrix} \begin{bmatrix} \dot{x} \\ x \end{bmatrix} + \begin{bmatrix} \omega_{0,act}^2 \\ 0 \end{bmatrix} u \tag{3.68}$$

The model is parametrized by the actuator's natural frequency ($\omega_{0,act}$) and damping ratio (ζ_{act}). The values for these parameters are provided in the "PT$_2$" column of table 3.5 with the actuator dynamics that correspond to the supply voltage of $V = 26\,\mathrm{V}$ being defined as nominal.

The input delay of $\tau_d = 20$ ms, which is present in the actuator system, is not considered for controller design, but added later during V&V activities as part of the overall feedback delay.

The linear state-space model of the aircraft is expanded not only by addition of the atmospheric disturbance and uncertainties, but also by inclusion of sensor noise (see equation (3.69)), where $\boldsymbol{u}_n = [r_n, \beta_n, p_n, \Phi_n, f_{y,n}]^T$ is the sensor noise input and $\boldsymbol{D}_n$ the sensor noise feed-through matrix (identity matrix).

$$\dot{\boldsymbol{x}} = \boldsymbol{A}\boldsymbol{x} + \boldsymbol{B}\boldsymbol{u} + \boldsymbol{B}_W\boldsymbol{u}_W \quad \boldsymbol{y} = \boldsymbol{C}\boldsymbol{u} + \boldsymbol{D}\boldsymbol{u} + \boldsymbol{D}_W\boldsymbol{u}_W + \boldsymbol{D}_n\boldsymbol{u}_n \tag{3.69}$$

The introduction of these disturbance inputs enables the derivation of transfer functions for evaluation of sensitivity of the system to sensor noise in frequency domain, as well as providing the possibility of time domain simulation taking into account sensor characteristics.

In preparation for controller design and verification, the uncertain state-space model is incorporated into a generalized state-space model object that is provided by the Control System Toolbox in MATLAB. The generalized state-space model is typically used to introduce into the system tunable blocks that are utilized for controller design with loop shaping routines such as "systune" or "looptune". One of the controller design blocks that is provided with the control system toolbox is the so-called "loop switch" (or "Analysis Point" in newer versions of MATLAB). Loop switches are very useful when designing and analyzing complex closed-loop systems. They represent points of interest within the system and enable the user to comfortably generate open- or closed-loop transfer functions w.r.t. particular signals in the system without the need to rebuild the model in order to assess one particular point of interest. The linear plant model of the SAGITTA Demonstrator is equipped with loop switches at all inputs and outputs, which significantly simplifies later stability and PIO analyses. Furthermore, the "User Data" field of the generalized model object is used for storage of data such as trim values and aircraft parameters, thereby incorporating all relevant information for controller design and verification, so that the generalized state-space model becomes the single source of information for controller design and verification.

In the following section, the linear state-space model described above is evaluated w.r.t. its dynamic characteristics.

3.10. Dynamic Modes

The linear state-space model developed provides a thorough insight into the dynamics of the system and offers extensive analysis options in time and frequency domain. In what follows, the focus is on the dynamic characteristics of the system. The analysis is based mainly on evaluation of absolute and relative locations of the poles and zeros of the linear system in the complex plane. The definition of the respective terms can be found in [78].

A conventional aircraft typically exhibits three lateral dynamic modes. The first is the so-called Dutch-roll oscillation, which is characterized by a pair of conjugate complex poles; the second and third are the roll subsidence and the spiral mode, which are described by two real aperiodic poles. Unconventional aircraft configurations may not necessarily show the previously described dynamic modes. Such aircraft often have a degenerated pole configuration. One reference describing a particular degradation of roll and spiral modes is [27]. Such unconventional dynamic characteristics are often attributed to adverse flying qualities and thus, are difficult to deal with during control design. Hence, one of the first questions to be answered during analysis of the dynamics of unconventional configurations like the SAGITTA Demonstrator, is whether or not the system is subject to a typical distribution of poles and zeros.

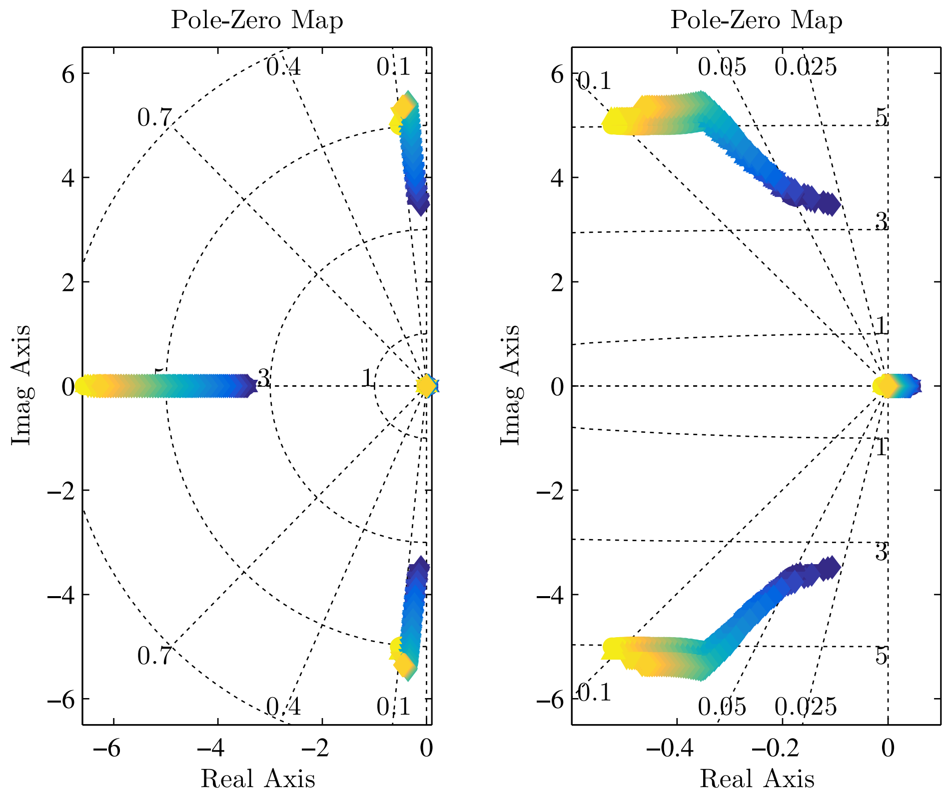

Figure 3.17.: Open Loop Poles of Lateral Motion

In order to analyze the dynamic characteristics of the SAGITTA Demonstrator, the 6-DoF nonlinear model is trimmed and linearized over multiple operating points. The envelope is defined by the following grid:

Variable	**Unit**	**Breakpoints**
V	[m/s]	$32 - 62$ in $1\,\mathrm{m/s}$ steps
h	[m]	$50, 150, 250$
m_{fuel}	[kg]	$0, 3, 11, 21$

Table 3.8.: Trim and Linearization Grid

An initial evaluation of the pole locations shows, that these typical attributes of conventional aircraft also exist in the nominal dynamics of the SAGITTA Demonstrator. The poles that characterize the respective modes are shown in figure 3.17 for the entire envelope from low (blue/dark) to high speeds (yellow/bright). The time constants, and the damping and frequency of the aircraft modes at $h = 50\,\mathrm{m}$ are provided in figure 3.18. The characteristics at other altitudes are essentially the same, and are omitted here.

By examining the plots it can be seen that the Dutch-roll is stable throughout the envelope. It is weakly damped, and the damping decreases from higher to lower speeds and therefore from lower to higher AoA. This may be attributed to a rapid collapse of efficiency of the vertical tail with increasing AoA. The sharp bend in the frequency plot of the Dutch-roll is clearly visible. Contrary to what is more commonly observed, the $\omega_{0,DR}$ of the SAGITTA Demonstrator is nearly constant at high speeds or small AoAs. Whether this can be traced to real aerodynamic effects or if it is caused by measurement errors from the wind tunnel campaign cannot be explained at present. It can be seen

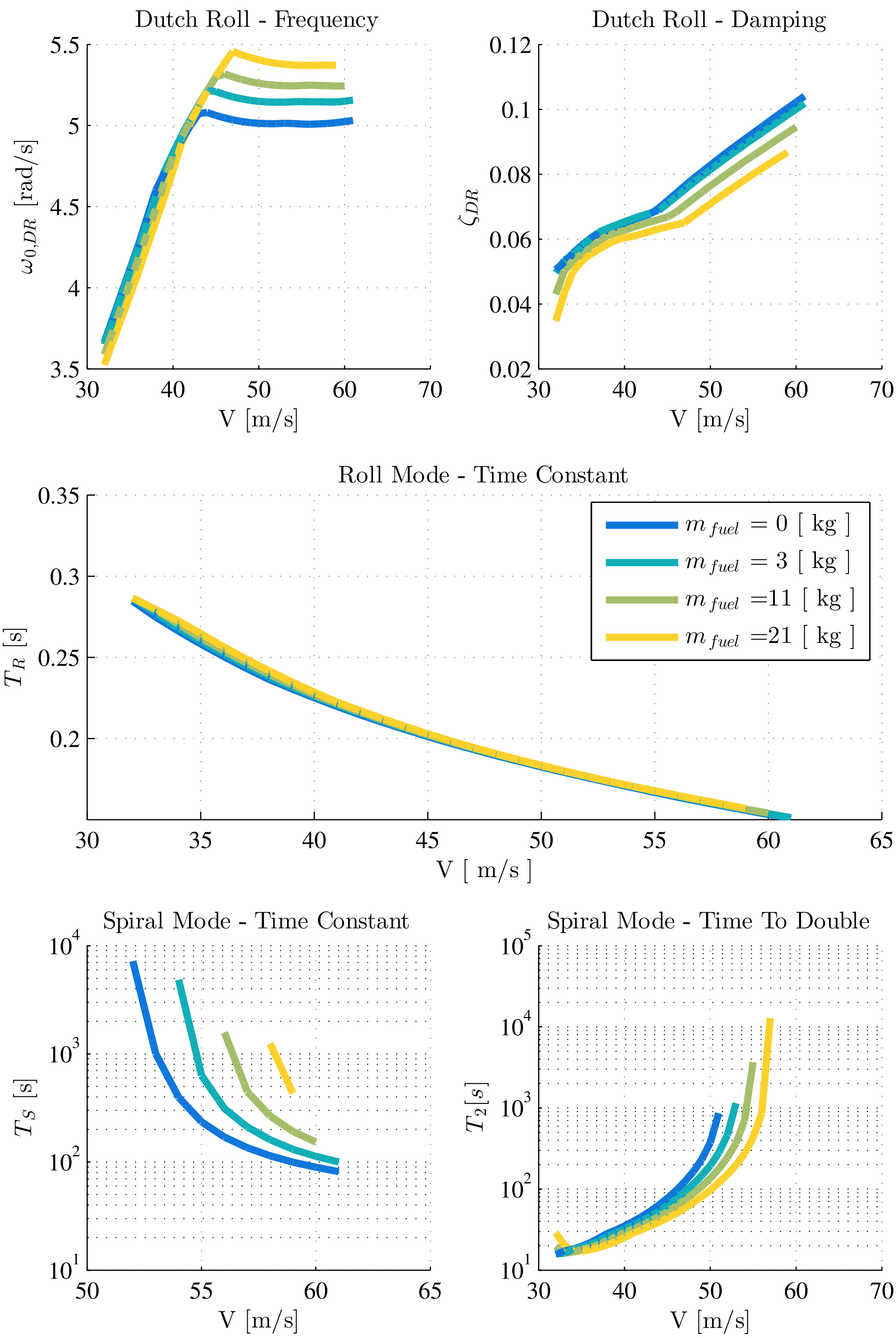

Figure 3.18.: Open loop dynamic characteristics of lateral motion

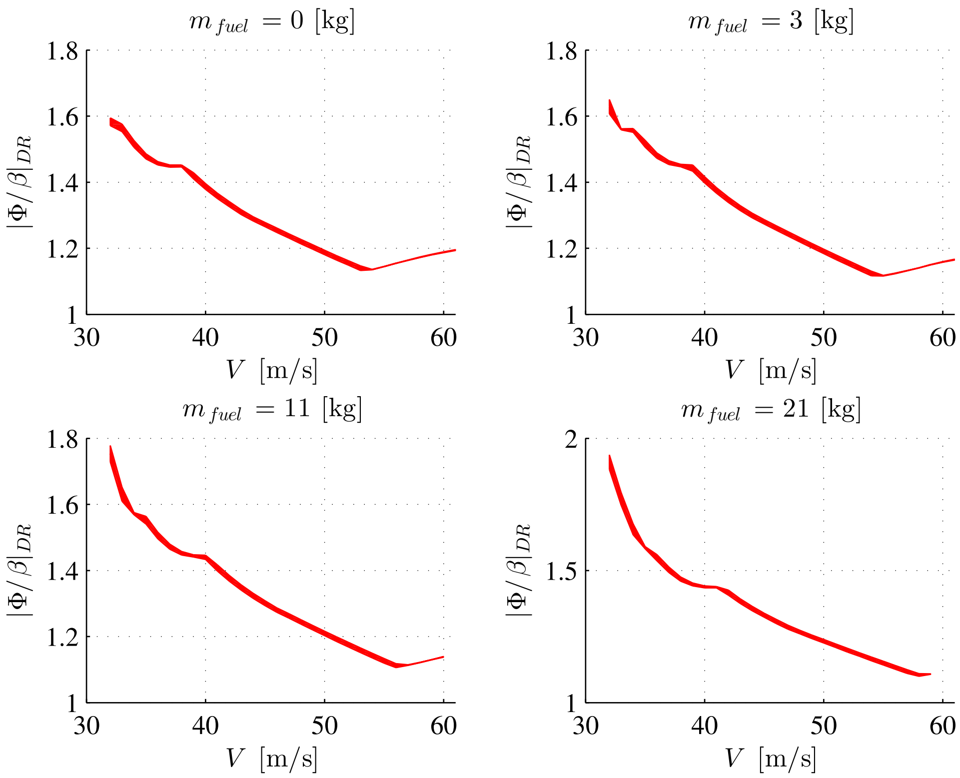

Figure 3.19.: $|\Phi/\beta|_{DR}$ of the inherent aircraft

that, for almost the entire envelope, the spiral mode is unstable. The spiral pole is moving from the right complex half-plane at low speed towards the imaginary axis and becomes stable for higher speeds. The roll subsidence is stable and well damped. It is characterized by the fast real pole that is located in the left half plane, and shows a fairly large variation over the speed envelope.

Figure 3.20 shows the phasor diagrams and the corresponding eigenvectors for two extreme operating points of SAGITTA Demonstrator's envelope. The diagrams illustrate the relationship of amplitude and phase of the eigenvector entries [74]. Thus, they provide an insight into the contribution of the lateral-directional states to particular modes, and therefore provide information on the extent of couplings present between the states.

From the phasor diagrams on the left-hand side is can be seen, that at high AoA the Dutch-roll is dominated by the entry related to roll rate (p), and in this situation sideslip angle (β) and yaw rate (r) are less dominant, the situation at low AoA is more balanced with p and r providing approximately equal contributions to the Dutch-roll. A further important characteristic, that is evident from the phasor diagram of the Dutch-roll is the roll-to-sideslip ratio $|\Phi/\beta|_{DR}$ of the system. It describes the ratio of amplitudes of the bank angle (Φ) and AoS (β) in the Dutch-roll oscillation and is an important measure of the Flying Qualities of an aircraft. The evaluation of $|\Phi/\beta|_{DR}$ across the envelope is depicted in figure 3.19. The values vary in the range $1.1 \leq |\Phi/\beta|_{DR} \leq 2$. The eigenvector of the roll subsidence is dominated by roll rate. For high AoA a small amount of r is visible in the eigenvector. Similarly, the increasing influence of yaw rate with AoA is observed with the spiral pole, where the largest entry of the eigenvector is associated with bank angle (Φ), which matches the conventional flight dynamics theory.

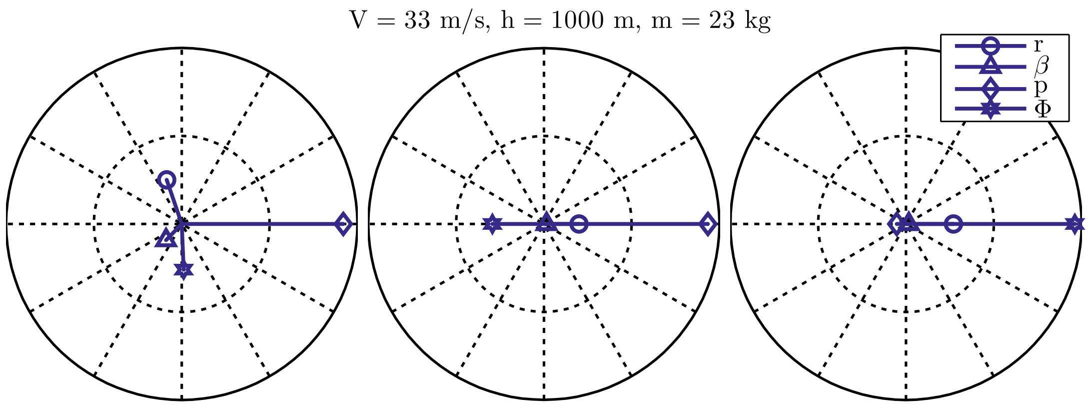

	Dutch Roll	Roll Mode	Spiral Mode
r	-0.086+0.25i	0.2	0.27
β	-0.089-0.092i	0.015	0.016
p	0.92	0.935	-0.05
Φ	0.011-0.26i	-0.29	0.96

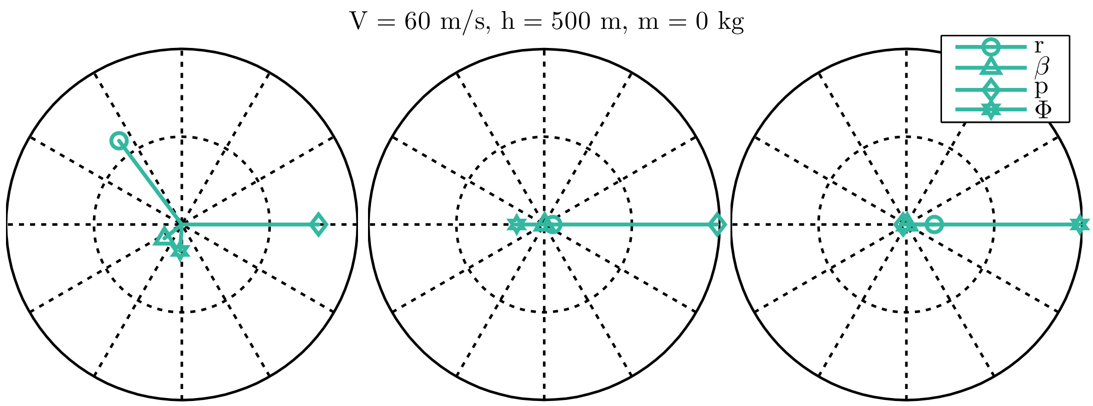

	Dutch Roll	Roll Mode	Spiral Mode
r	-0.358+0.48i	0.05	0.16
β	-0.1-0.08i	0.0036	0.004
p	0.78	0.99	-0.018
Φ	-0.01-0.15i	-0.16	0.99

Figure 3.20.: Open Loop Eigenvectors of Lateral Motion

To summarize the first dynamics analysis of the SAGITTA Demonstrator, it can be stated that, although the geometric configuration of the aircraft is unconventional, its dynamic characteristics, in terms of inherent dynamic modes, are thankfully comparable to those of conventional aircraft configurations. Nevertheless, it should be emphasized, that the configuration under study has two attached vertical fins. The aircraft without these stabilizing surfaces is expected to be substantially different in terms of inherent dynamics.

In order to obtain a more thorough insight into the dynamics of the SAGITTA Demonstrator and to find uncertain parameters having the greatest influence, an attempt is made to determine literal expressions for the characteristics of the aircraft, and to investigate them in terms of entries in the state-space model. Several methods exist for obtaining such approximations for natural frequency and damping of modes of the lateral

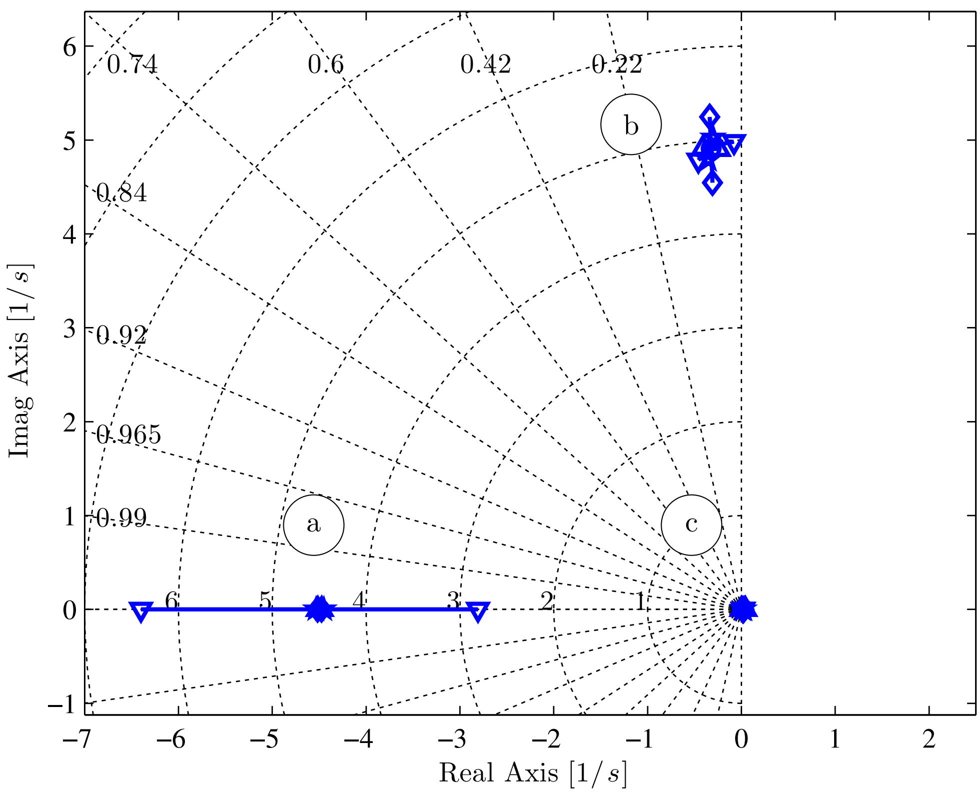

Figure 3.21.: Influence of single parameter variations on pole location

motion. One of these which leads to the best results is described by Mengali in [50] and is briefly outlined in appendix A.2. The results of the literal approximations allow attention to be focused on a few stability derivatives, that contribute significantly to certain flight dynamic characteristics. By application of uncertainties to these stability derivatives, and subsequent visualization of their influence on the pole locations in the pole-zero map, the most critical uncertain parameters become apparent.

Figure 3.21 provides an overview, of how a perturbation of a single uncertain stability derivative in the range specified in table 3.1 affects the pole locations of the aircraft trimmed and linearized at medium speed. Figure 3.22 shows certain enlargement of the pole-zero diagram, affording further details on roll subsidence (a), the Dutch-roll (b), and the spiral mode (c) variation due to uncertainties. The Dutch-roll's damping is strongly influenced by C_{lp}. Furthermore, as expected, the Dutch-roll frequency is influenced by $C_{n\beta}$. The uncertainties in the two stability derivatives C_{nr} and $C_{l\beta}$ also alter the Dutch-roll location, but their influence is significantly less prominent compared to $C_{n\beta}$ and C_{lp}. The pole location of the roll subsidence mainly depends on roll damping C_{lp}. The spiral mode's pole location is mainly influenced by the yaw damping uncertainty. From the observations described above, one can conclude, that there are two uncertain parameters which have the most influence on the uncertainty regions that describe the possible pole locations of the system. Those parameters are C_{lp} and $C_{n\beta}$. Hence, in a future system identification phase, it would be worthwhile to focus on precise determination of these parameters.

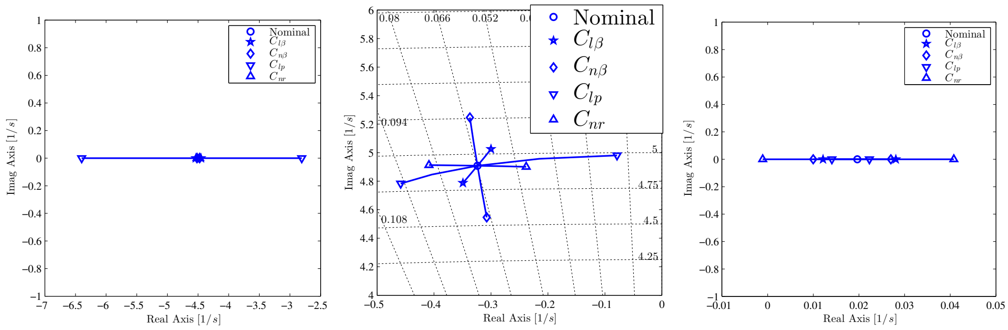

(a) roll subsidence (b) Dutch-roll (c) spiral mode

Figure 3.22.: Influence of single parameter variations on pole location | details

3.11. Inherent Gust Reaction

The SAGITTA Demonstrator operates at relatively low airspeed. This makes the aircraft vulnerable to atmospheric disturbances. Due to the low airspeed, even a light lateral gust results in relatively large β_W and thus a significantly larger stimulation of lateral-directional states compared to full-scale aircraft, which typically operate at higher airspeeds. Hence, one specific challenge of the SAGITTA Demonstrator control is the improvement of gust rejection properties.

Figure 3.23 shows the system's reaction to light and moderate lateral gusts. The colors of the lines represent different gust lengths and different operating points. Table 3.9 provides a corresponding color map.

The analysis of the gust reaction in time domain highlights some previously raised deficiencies of the inherent dynamics. From the plots provided, a weakly damped oscillation with a relatively long decay time can be observed in lateral states. Furthermore, the expected couplings of lateral-directional variables are visible. This is manifested in (e.g.) the bank angle and AoS time series. The disturbance in bank angle due to a lateral gust reaches values of up to 8° at high AoA. As will be seen during the discussion of requirements in chapter 3, this is beyond the bank angle limit for landing.

Nr.	V [m/s]	h [m]	m_{fuel} [kg]	Gust 1	Gust 2	Gust 3	Gust 4
1	36	50	0				
2	36	250	21				
3	45	150	3				
4	45	150	11				
5	59	50	0				
6	59	250	21				

Table 3.9.: Gust Color Map

3.12. Control Characteristics

In section 3.1 the analysis of yaw characteristics due to control surface deflections was preliminary in nature, since it did not consider the trim deflections at the particular operating points. The trim deflections of the inboard flaps have only minor impact on

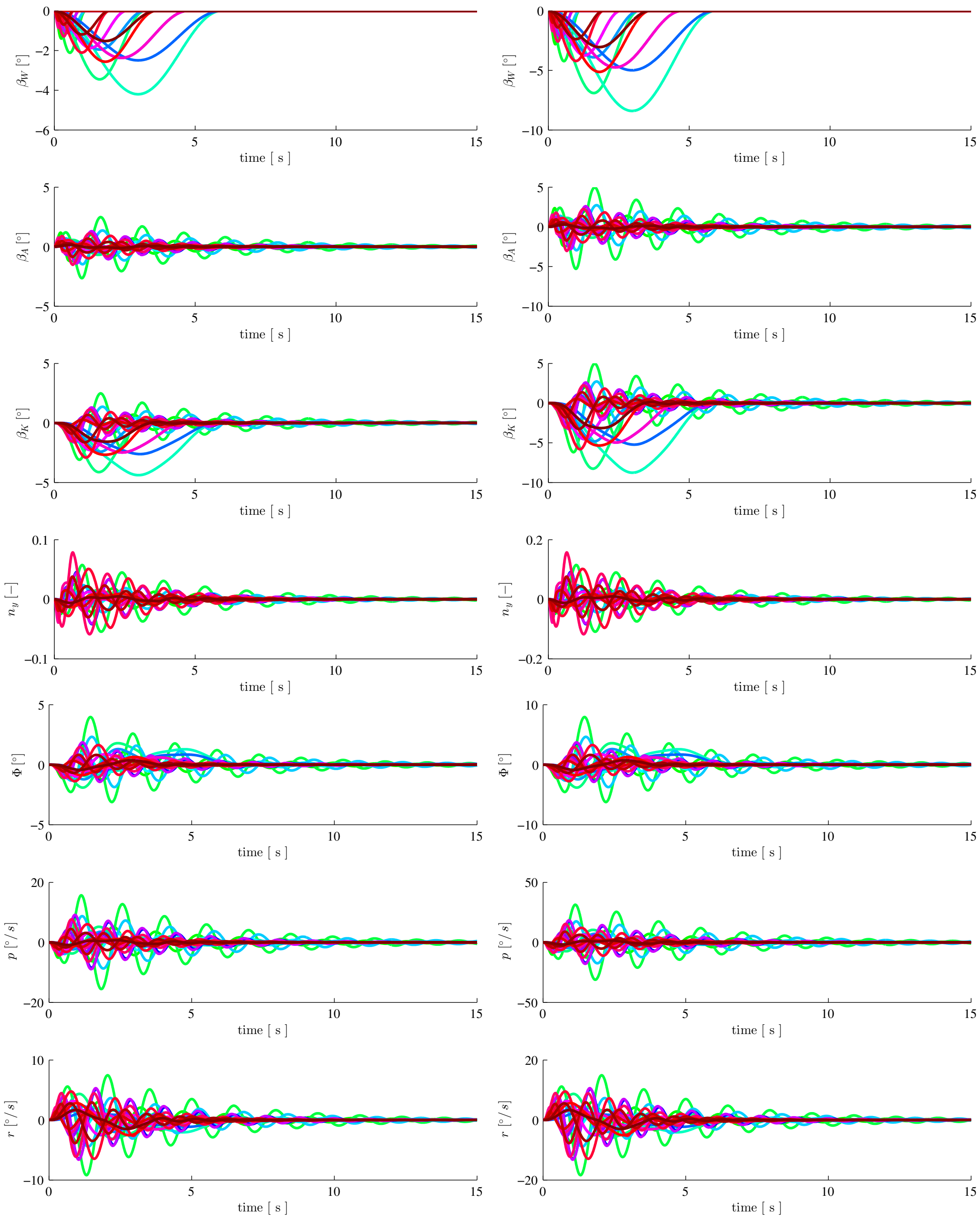

(a) light (b) moderate

Figure 3.23.: Inherent Gust Reaction - (nominal system, without uncertainties)

the effectiveness of the aileron control linkage (as mentioned previously, the aerodynamic model does not take into account flap interference effects between inboard and midboard flaps). In contrast to the aileron linkage, the elevon linkage is heavily influenced by trim deflections of the control surfaces, since trimming in the longitudinal plane significantly shifts the initial position of the control surfaces that are linked to the equivalent aileron, thereby leading to different aerodynamic conditions.

At this stage of development, trimming of the aircraft has been performed and the subsequent linearization already takes into account the trim results. Thus, having obtained the linearized dynamics of the lateral motion, the statement on proverse/adverse yaw

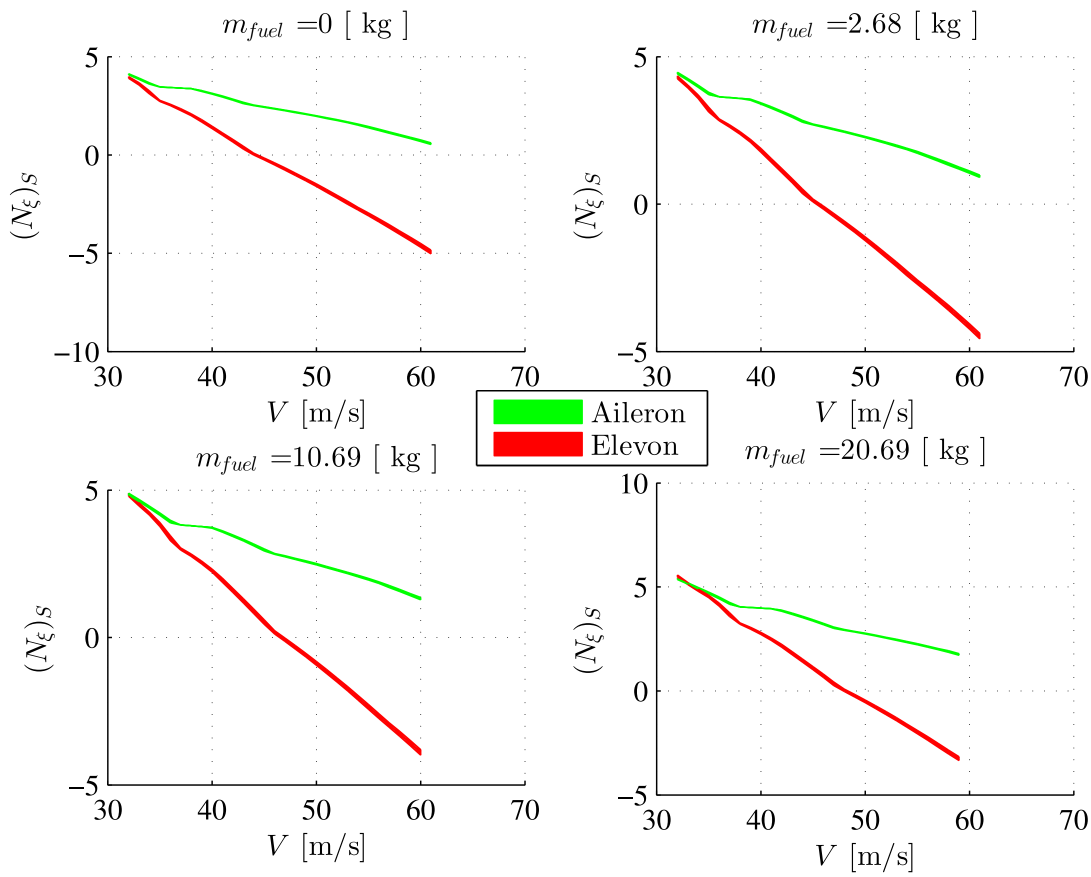

Figure 3.24.: Ratio of control moment due to equivalent aileron deflection

characteristics can now be updated. In order to do this, the yaw moment due to equivalent aileron deflection, thus the $(N_\xi)_S$ in stability axes, as specified in equation (3.5), must be determined. The result of this evaluation for aileron and elevon control linkages in shown in figure 3.24. As anticipated during the work on control linkage, the aileron linkage shows significant adverse yaw over the entire speed envelope. The elevon linkage shows adverse yaw at low speeds and proverse yaw at high speed. The change of the characteristics using elevon linkage takes place in the middle of the trimmable speed envelope. Hence, the decision made in section 3.1 to use the aileron or simple control linkage can be confirmed.

A further common analysis of control characteristics is based on the evaluation of the relative locations of Dutch-roll poles and the zeros of the transfer function from aileron to bank angle. This not only considers the initial direction of the yaw moment generated by the control surfaces, but also takes aircraft dynamics into account. The analysis is performed below for the implemented "simple" control linkage type, whereby the characteristics of midboard flaps and outboard flaps are analyzed w.r.t. their effect on roll control.

The starting point for further analysis is the response function Φ/ξ provided in [14]:

$$\frac{\Phi}{\xi} = \frac{K_\Phi\left(s^2 + 2\zeta_\Phi\omega_\Phi s + \omega_\Phi^2\right)}{\left(s^2 + 2\zeta_{DR}\omega_{0,DR}s + \omega_{0,DR}^2\right)\left(s + 1/T_R\right)\left(s + 1/T_S\right)}. \tag{3.70}$$

The ratio of $\omega_\Phi/\omega_{0,DR}$, namely the ratio of the radial distance of the transfer function's poles and zeros from the origin of the pole-zero map, is frequently used as an indicator of whether a proverse or adverse yaw is induced by the aileron during initiation of turns. By taking a look at the following approximation

$$\frac{(\omega_{\Phi})^2}{(\omega_{0,DR})^2} \approx 1 - \frac{N_{\xi} L_{\beta}}{L_{\xi} N_{\beta}} \tag{3.71}$$

given in [14], one can see, that depending on the sign of N_{ξ}, and assuming operations at a small AoA, the system shows the following behavior:

$$\text{proverse yaw: } N_{\xi} < 0 \Rightarrow \frac{\omega_{\Phi}}{\omega_{0,DR}} > 1 \qquad \text{adverse yaw: } N_{\xi} > 0 \Rightarrow \frac{\omega_{\Phi}}{\omega_{0,DR}} < 1. \tag{3.72}$$

Figure 3.25 shows the pole-zero maps of lateral motion for two extreme points in the SAGITTA Demonstrator's flight envelope. In these maps, circles indicate zeros and crosses indicate poles of the system. Since theoretically all flaps can be used for initiation of roll, the figure shows the situation for midboard flaps on the left-hand side ($G_{\Phi\xi}$) and for outboard flaps ($G_{\Phi\zeta}$) on the right-hand side. In the plot on the left, the zeros are located closer to the plot's origin. From this, it can be concluded, that a roll initiated by the midboard flap, especially at high AoAs, shows adverse yaw behavior ($\omega_{\Phi}/\omega_{0,DR} < 1$). This is consistent with the previously derived results on yaw characteristics for the aileron control linkage. In contrast to the control characteristics observed for midboard flaps, roll motion that is induced by outboard flaps leads to proverse yaw (pole-zero map on the right in figure 3.25).

In addition to the proverse/adverse yaw characteristics, the transfer function presented above provides an insight into the contribution of the Dutch-roll to roll motion: if the complex poles of the transfer function are canceled by the zeros of $G_{\Phi\xi}$, the Dutch-roll is not noticeable in the bank angle response to aileron command. The further apart the poles and zeros are, the more the Dutch-roll is visible in the response to aileron command. The pole-zero map on the left shows a large variation in the undesired contribution of the Dutch-roll to the rolling motion. Although at low AoA the Dutch-roll poles are nearly canceled by the zeros of $G_{\Phi\xi}$ and consequently almost no Dutch-roll is present during rolling, if it is initiated by midboard flaps, the situation becomes worse at high AoA, where poles and zeros are far away from each other, and hence, a high amount of adverse yaw is observable in rolling motion. If the turn is initiated by outboard flaps the ratio of $\omega_{\Phi}/\omega_{0,DR} > 1$.

Early in the history of studies into flying qualities it was realized that the relative location of poles and zeros is more significant than the ratio of their radial distance from the origin. It was observed, that the pilot's opinion on flying qualities in roll greatly depends upon the phase of the Dutch-roll component in roll rate response Ψ_{β}, and this is linked to the relative location of complex poles and zeros of the corresponding transfer function according to figure 3.26 [1]. Depending on Ψ_{β}, the pilot evaluates the same amount of oscillation in roll rate response differently. This can be understood from the root locus of $G_{\Phi\xi}$. When the pilot is controlling the bank attitude, he is closing the loop by feeding back the bank angle to the roll input. Depending on his internal feedback gain, he thereby drives the poles of the Dutch-roll towards the complex zeros. In cases where the zeros are located above and to the right of the pole in the pole-zero map, the loop closure leads to a reduction in Dutch-roll damping. Thus, for some feedback gains the Dutch-roll may even become unstable. In such cases the pilot tolerates only a small amount of oscillation in the roll rate. In other situations, where the pilot is increasing the Dutch-roll damping by loop closure, he is prepared to tolerate more oscillations in

[1] The figure only shows the relation between Ψ_1 and Ψ_{β} for positive dihedral ($L_{\beta} < 0$). A second scale exists for aircraft with $L_{\beta} > 0$ and can be found in [14].

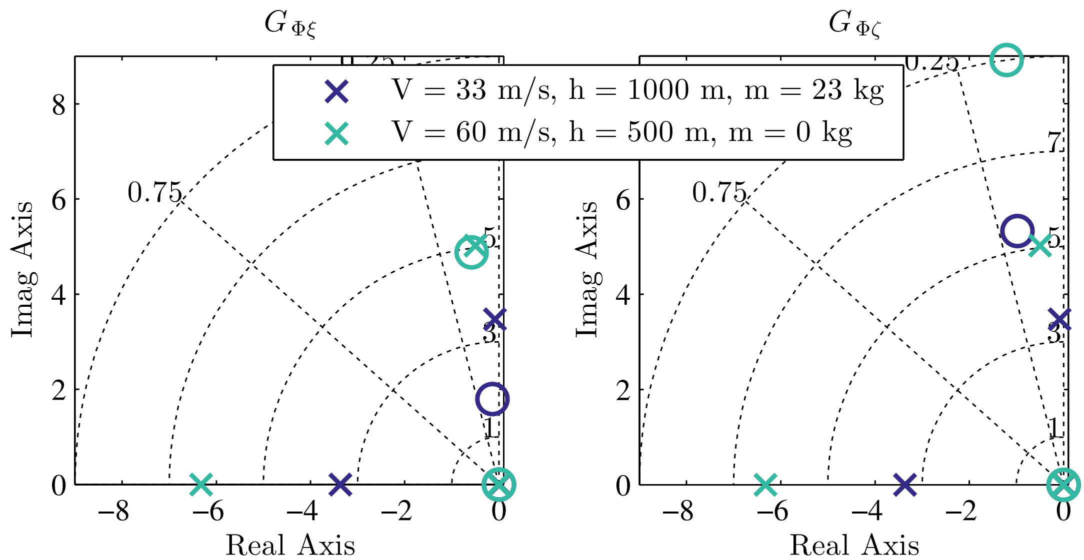

Figure 3.25.: Location of the transmission zeros in lateral motion

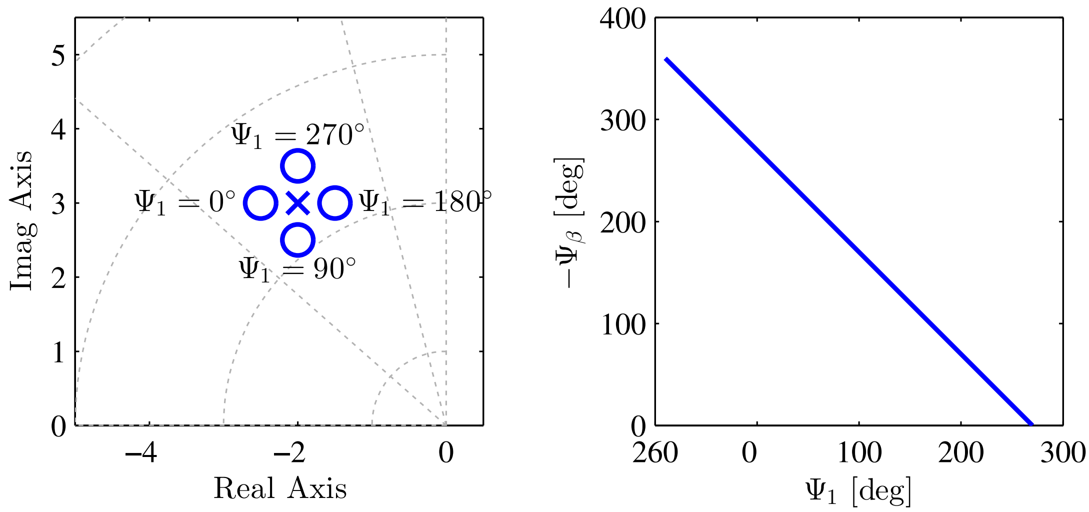

Figure 3.26.: Relation of location of poles and zeros with phase of Dutch-roll component for positive dihedral ($L_\beta < 0$) [14]

roll response . This is usually the case when the zero lies below and to the left of the pole in the pole-zero map [14]. The same arguments are valid for loop closure by automatic control. Another method for the assessment of flying qualities w.r.t. oscillations during rolling is the evaluation of p_{osc}/p_{av} versus Ψ_β. Thereby, p_{osc}/p_{av} describes the ratio of the oscillation in roll rate to the average roll rate during the roll maneuver. In order to obtain the p_{osc}/p_{av} ratio, a time domain simulation is performed on the transfer-function $G_{p\xi}$. The calculation method for determination of the ratio is specified in [14] as

$$\frac{p_{osc}}{p_{av}} = \frac{P_1 + P_3 - 2P_2}{P_1 + P_3 + 2P_2} \quad \text{for} \quad \zeta_{DR} \leq 0.2 \qquad \frac{p_{osc}}{p_{av}} = \frac{P_1 - P_2}{P_1 + P_2} \quad \text{for} \quad \zeta_{DR} > 0.2 \tag{3.73}$$

where P_1 and P_3 are the first two maxima and P_2 the first minimum in the time response of the roll rate to positive roll command.

Figure 3.27 shows the p_{osc}/p_{av} ratio for the two extreme flight conditions analyzed in figure 3.25. Here, the p_{osc}/p_{av} is calculated for $G_{p\xi}$ and $G_{p\zeta}$ in order to assess the

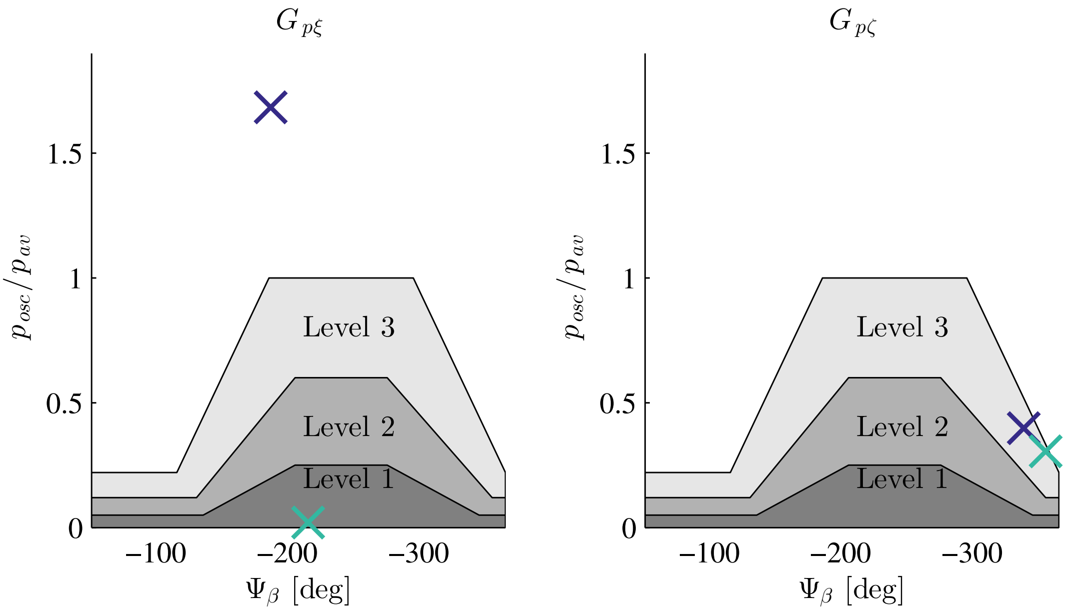

Figure 3.27.: Roll rate oscillations in the open loop system

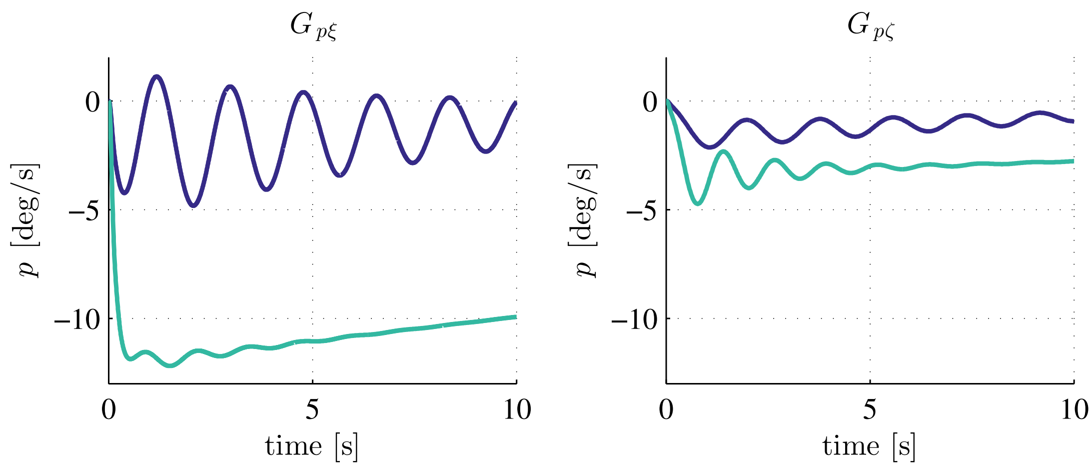

Figure 3.28.: Roll rate response to 1° equivalent flap deflection

suitability of both, midboard and outboard flaps for initiating roll. The assessment is based on so-called Flying Qualities Levels from [57]. Figure 3.27 shows the Flying Qualities Level 1 (best) to Level 3 (worst) for p_{osc}/p_{av}. In this figure, the dark area indicates Level 1 and the light area Level 3 Flying Qualities. The plot confirms the strong couplings indicated in figure 3.25. The extent to which Flying Qualities vary in roll becomes even more obvious from this analysis. Particularly notable in the left-hand plot is the ratio of p_{osc}/p_{av} at high AoA (dark cross), which lies outside the range of Level 3 Flying Qualities. The control problem at this operating point becomes apparent when evaluating the corresponding time response to flap inputs. Figure 3.28 indicates a violent oscillation in the response for the point under investigation. This is due to the previously identified undesired contribution of the Dutch-roll oscillation. Furthermore, the so-called roll rate reversal, i.e. changing sign of roll rate, appears. In addition, while the characteristics of roll with midboard flaps dramatically change across the speed envelope, roll control using outboard flaps seems to be more consistent, although due to their proverse characteristics, a bank angle feedback to outboard flaps tends to reduce the stability of the Dutch-roll.

3.13. Validation of Linearization Results in Particular Trim Conditions

In order to validate the linearization results, time domain simulations are performed using the linearized state-space model and the nonlinear 6-DoF simulation model. During the simulation runs, lateral motion is excited with velocity and altitude held constant. The time response of four different model variants are compared:

A Linearized model with actuators specified per column "PT_2" of table 3.5

B Linearized model without actuators

C Nonlinear model with nonlinear actuators as presented in section 3.4

D Nonlinear model without actuators

Pure time delays that are implemented in the actuator model are omitted from the following study to simplify the analysis. A frequency sweep is commanded as a control input ξ_{equiv}. The amplitude is chosen to be 1° and frequency lies in the range $f = 0 - 5$ Hz.

Figure 3.29 shows the comparison of frequency responses of A to D, that are determined by the quotient of the fast Fourier transform of input and output signals. A near-perfect match of both systems without actuators is observed over the entire frequency range of interest. A good correlation is also achieved between linear and nonlinear models with actuators. However, some noticeable deviations are still apparent for low and high frequencies. For high frequencies the deviations in phase indicate the differences in natural frequency between the nonlinear actuator model and the linear approximation at $V_{DC} = 26\,\mathrm{V}$ given in table 3.5. Marginal deviations in magnitude between the linear and nonlinear model at low frequencies can be traced to actuator stiffness, which leads to stationary offsets between targeted and achieved control surface position.

In conclusion, the linearized model yields a fairly good match with the nonlinear model in terms of rigid body states. Some minor deficiencies have to be accepted when the nonlinear actuator model is replaced by the approximation given in table 3.5.

Although the controller design is based on state-space models representing the aircraft in level flight, in order to gain more confidence in the validity of this approach, linearization results from level flight are compared below with quasi-steady state push-over and pull-up maneuvers ($\dot{\alpha} = 0$ and small $q = \dot{\Theta}$). Figure 3.30 shows a comparison of lateral-directional modes for the three particular trim conditions. One can see that dynamic modes of the systems in pull-up and push-over conditions deviate significantly from level flight. This is inter alia due to the large AoA range spanned by the two extreme flight conditions. Despite the limited applicability of linear stability analysis to systems in non-steady-state (especially regarding the long term dynamics), it is meaningful to perform the stability analysis on closed-loop systems representing push-over and pull-up flight conditions as a means of risk reduction.

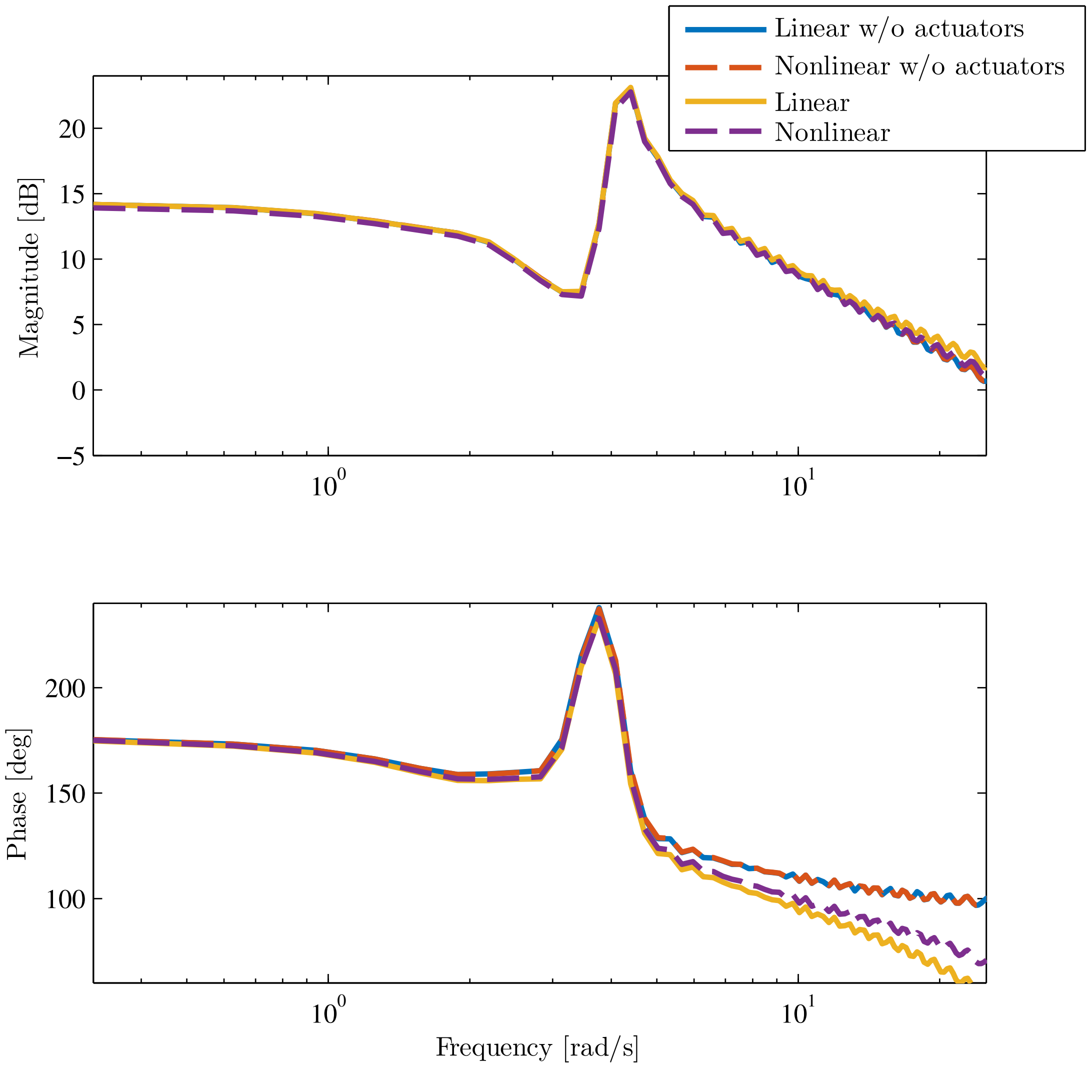

Figure 3.29.: Comparison of Frequency Response of Linear and Nonlinear Model $G_{\omega_x \xi}$

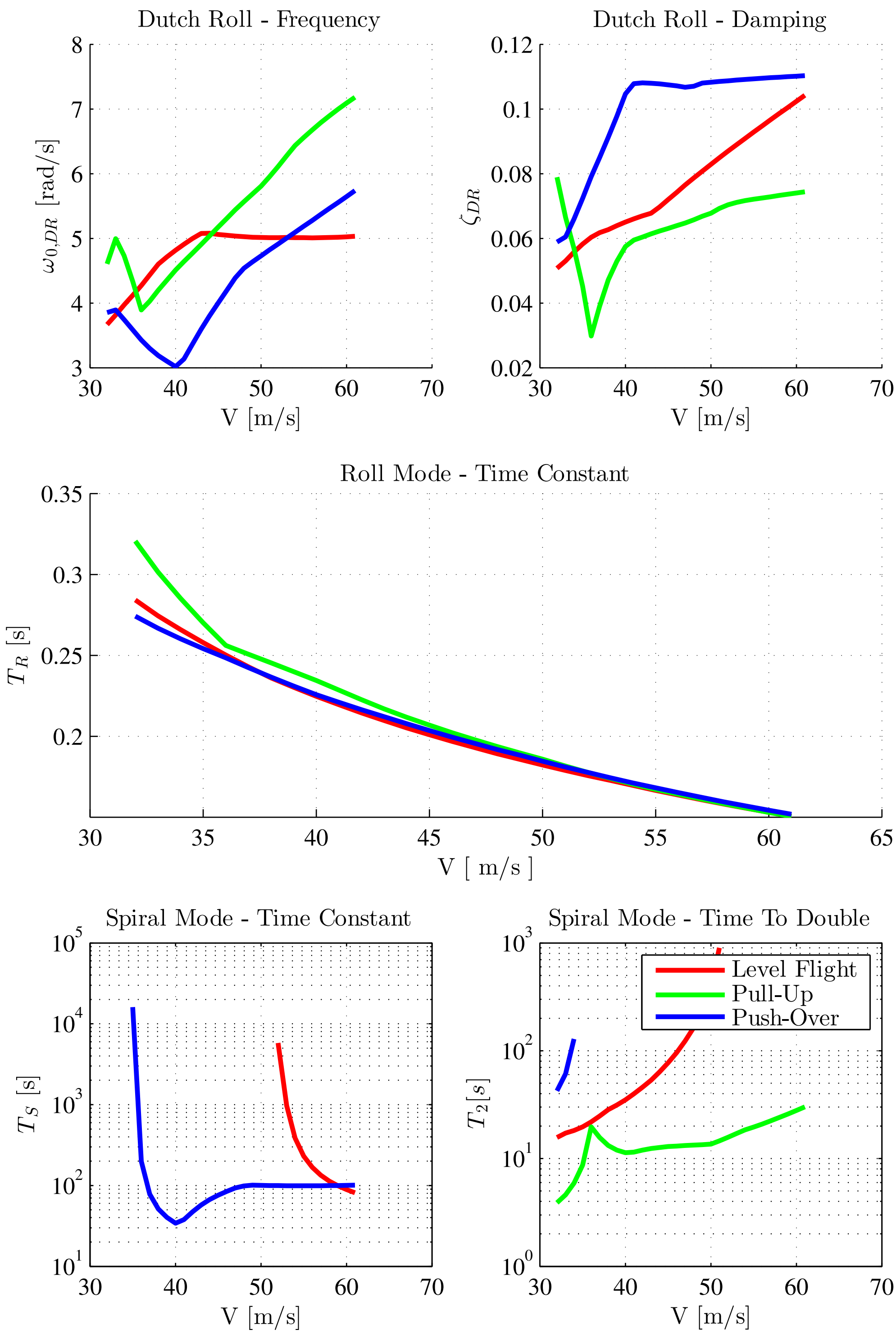

Figure 3.30.: Open Loop Mode details of lateral motion at particular trim conditions

4. Flying Qualities of Remotely Piloted Aircraft

In recent decades Flying Qualities requirements for unmanned aircraft have been subject of fierce controversial debate. Due to the significant differences in size and operational concepts, the applicability of Flying Qualities for manned aircraft to unmanned systems has been questioned by several researchers.

The need to adapt existing requirements to RPAs was identified very early on. The Air Force Flight Dynamics Laboratory published RPV Flying Qualities Design Criteria [68] in 1976. In this publication, the emphasis is on the classification of unmanned systems. Four Remotely Piloted Vehicle (RPV) classes are proposed and definitions are provided for levels of Flying Qualities for automated and manual flight. Furthermore, this publication addresses the specifics of remote control namely the control station and data link. Unfortunately, due to lack of data, the document reproduces the values of quantitative requirements from MIL-8785B and MIL-F-9490D and does not provide any guidance on adjusting such values to RPA.

More recently, the topic of Flying Qualities of unmanned aircraft has continued to be the focus of several studies, but still to this day the results are rather incomplete [18, 22]. A broad data-base that would enable the derivation of a comprehensive Flying Qualities standard to be developed, is still not available.

The present work is not able to fill this gap, but aims to provide an extensive Flying Qualities standards review, customization and application of Flying Qualities to the lateral motion of a particular RPA. Specifically, this chapter presents firstly the project requirements of the inner-loop controller, then reviews the Flying Qualities of lateral motion, and finally derives a customized Flying Qualities requirement set applicable to the SAGITTA project.

4.1. Concept of Remote Aircraft Steering

Before starting the derivation of project requirements, the different concepts of aircraft steering are introduced and their implications on Flying Qualities are discussed in qualitative terms.

According to [26], a pilot sitting in an aircraft experiences the following cues:

motion cues e.g. linear and angular accelerations

visual cues e.g. aircraft attitude, movement of external environment

aural cues e.g. turbine sound, stall warning

control force e.g. resulting from aerodynamic forces at the control surface.

These cues are the primary means by which a pilot sitting in the cockpit of an aircraft senses and evaluates Flying Qualities.

When considering remote aircraft steering the situation changes significantly, and two operating scenarios must be differentiated, namely Line Of Sight (LOS) and Beyond Line Of Sight (BLOS) operations. Whereas in LOS operations the aircraft is permanently visible from the ground and can be tracked by the remote pilot without the need for vision aids, BLOS operation does not require direct visual contact from the ground to the aircraft. Although aircraft are considered remotely controlled when employing either of these steering concepts, a distinction between the two must be made, since the cues available to the pilot could differ significantly and might therefore lead the pilot to assess the situation differently.

Control stations for manual control in BLOS operations usually provide a Human Machine Interface comparable to aircraft cockpits. In such control stations visual cues are the main source of information for the pilot. Besides the obligatory moving map, control stations often provide a First Person View (FPV) to the pilot. Sounds and force feedback can be simulated, if needed. Nevertheless, the pilot's perception is more limited that it would be inside the aircraft. This is mainly due the absence of motion cues and a visual perception which is restricted by the camera's field of view.

At first sight, the cues available in LOS are comparable to those in BLOS. Here too, there are no motion cues, and the pilot relies on visual cues. However, since the visual cues depend on direct eye contact with the aircraft they tend to weaken as the distance between pilot and aircraft increases, making the attitude determination difficult at long distances. Along with weather conditions, the shape of the aircraft also plays an important role: the attitude of conventional aircraft with pronounced wings is easier to determine than the attitude of a diamond-shaped aircraft. This fact not only has to be taken into account when designing control systems of RPA, but it is also expected to influence the evaluation of Flying Qualities. The understanding of how the amount of visual information available to the pilot impacts Flying Qualities is embodied in the so-called Usable Cue Environment (UCE) parameter [4]. It is therefore particularly important when evaluating Flying Qualities of unmanned aircraft, or when comparing the information obtained from different systems to keep in mind that the information available to the pilot could significantly influence the conclusion reached.

One aspect of LOS which represents a major advantage compared to BLOS is the relatively small delay in the data link communication between aircraft and control station: while BLOS operations are capable of spanning continents by means of e.g. satellite communication, and can thus involve large feed-forward delays (via command) and feedback delays (via sensors and displays) that may adversely affect manual control, LOS operation is characterized by the proximity of pilot and aircraft.

From simulation studies it is understood that large time delays of multiple hundreds of milliseconds, which are not uncommon in satellite communication [88], have a significant effect on a pilot's judgment regarding Flying Qualities. For BLOS operations therefore, time delay compensation techniques are used to facilitate steering from afar. Such techniques are not mandatory for LOS operations, since the delays introduced by the radio data link are usually significantly smaller. Nevertheless, when considering Flying Qualities of RPA, special attention must be paid to time delays and their effects.

The SAGITTA Demonstrator can be controlled in different ways. In automated flight, it is steered by means of a control station when in BLOS operation, but when in vicinity to the pilot (within LOS) it is possible to control the aircraft manually.

Interface requirements

- I-1 the system shall provide an interface to the External Pilot.
- I-2 the system shall provide an interface to outer loops (autopilot and trajectory control).
- I-3 the inner loop shall provide lateral control of the aircraft using aerodynamic control surfaces.

Functional requirements

- II-1 the system shall provide stability and adequate lateral control characteristics throughout the flight envelope in all phases in flight.
- II-2 the system shall support manual landing via the External Pilot.
- II-3 the system shall support automatic takeoff and landing.
- II-4 the command inputs to the lateral inner-loop shall be limited to $|\Phi| = 30°$.

Performance and robustness requirements

- III-1 The aircraft shall be capable of being controlled by a skilled RC pilot.
- III-2 Takeoff and landing shall be possible with a tail wind of 15 knots or a cross wind of 10 knots. The aircraft shall be operable in light turbulence conditions.
- III-3 The system shall be robust with respect to analyses defined by the clearance road map.
- III-4 The system shall provide stability and lateral control in the event GNSS is unavailable.

Table 4.1.: Project requirements to CSAS

4.2. Project requirements concerning CSAS

Table 4.1 lists the project requirements of the CSAS. These are discussed in detail below.

The interface requirements I-1 and I-2 are primarily motivated by the three operational scenarios, namely: control of the aircraft by the Flight Operator using either medium level or high level commands, and control by the External Pilot using low level commands. Consequently, the inner loop (CSAS) has to provide an interface to the outer loops of the controller (e.g. autopilot) as well as to the External Pilot's commands from the EPCS. The outputs of the CSAS are the commanded deflections of the aerodynamic control surfaces (I-3). Thrust is directly controlled by the External Pilot during flight using low level commands, whereas with medium and high level commands thrust is

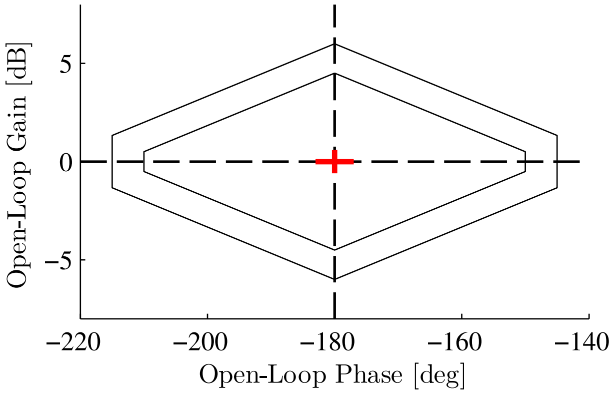

Figure 4.1.: Visualization of Nichols Diamonds

controlled by the outer loops of the Flight Control System. Thrust control is therefore not included in the CSAS.

Requirement II-1 states the main functionality of a CSAS. In this requirement the scope of the stabilization functionality is limited to flight phases only and excludes stabilization and control on the ground. However, requirements II-2 and II-3 explicitly include operation on the ground as well as the transition phases from and to the airborne state. Since flight via low level commands is a backup feature of the system, support for manual takeoff is not required. The next functional requirement listed in table 4.1 relates to the Global Navigation Satellite System (GNSS) signal reception. In order to increase the availability of automatic modes that depend on satellite navigation, the bank angle is limited to a fairly small value of $|\Phi_{cmd,lim}| = 30°$, so that shadowing effects of the GNSS antenna are minimized. If the GNSS is unavailable, the aircraft shall continue its operation using medium level commands. To enable this, the CSAS shall provide appropriate means of stabilization and control without the need for valid GNSS data (III-4).

Although no official certification requirements have been imposed on the flight control system by civil or military certification authorities, a clearance road map has been established by the project team (III-3). The clearance road map includes the validation of stability margin requirements by means of Nichols plots. For this, two so-called Nichols Diamonds are defined. These describe areas in the Nichols diagram that shall not be violated by the open-loop frequency responses of the inner loop controller. Each Nichols Diamond is defined by two points (phase/magnitude) in the Nichols chart relative to the critical point (-180°/0 dB). The coordinates are provided in table 4.2. A

Diamond	**Phase** [deg]	**Magnitude** [dB]
Nominal	0	±6
	±35	±1.33
Reduced	0	±4.5
	±30	±0.5

Table 4.2.: Definition of Nichols Diamonds for Clearance

visualization of the Nichols Diamonds is provided in figure 4.1, thereby the red cross indicates the so-called critical point. According to the clearance road map, the Nichols Diamonds shall be applied to the linear models that represent level flight, pull-up and push-over maneuvers and shall take into consideration the uncertainties in aerodynamic characteristics (see table 3.1), actuator supply voltage and time delays of feedbacks. Table 4.3 shows the relevant uncertainty combinations and the applicable diamonds evaluated for the clearance. As can be seen, the clearance road map addresses the nominal case as well as single and multi tolerance cases. Multi tolerance cases are those where a combination of at least two uncertain parameters (e.g. aerodynamic tolerances, actuator supply voltage or feedback delays) are changed from nominal or expected values to ones specifying reduced performance. When multi tolerance cases are analyzed, all aerodynamic uncertainty entries are reduced using a scale factor of $s = 0.62$ when incorporating two tolerances, and a factor of $s = 0.46$ when incorporating three tolerances. The motivation for doing this is to provide clearance cases which have comparable probabilities of occurrence.

Diamond	**Delay** [ms]	**Aero - Tolerances** [%]	**Act. Supply Voltage** [V]
Nominal	Ideal (0)	0%	Nominal (26)
Nominal	Nominal (50)	0%	Nominal (26)
Reduced	Ideal (0)	100%	Nominal (26)
Reduced	Nominal (50)	100%	Nominal (26)
Reduced	Nominal (50)	62%	Reduced (22)
Reduced	Increased (70)	62%	Nominal (26)
Reduced	Increased (70)	46%	Reduced (22)

Table 4.3.: Clearance Matrix

The most vague requirement from table 4.1 is given in the III-1. The validation of requirement III-1 is conducted by asking experienced pilots to evaluate a landing task in simulated (virtual) flight tests. The requirement is fulfilled if one of three External Pilots rates the Flying Qualities as acceptable or adequate with reference to Cooper-Harper rating scale (for the Cooper-Harper rating scale see [8]). Evaluation by External Pilots is not included in this work, and instead Flying Qualities of manned aircraft are adopted to the SAGITTA aircraft and used to validate compliance with requirement III-1.

Requirements discussion and further refinement

The project requirements have been presented in the section. From this list, further requirements for the CSAS are derived and several design decisions are made. Among other things, the bank angle Φ is selected as the command variable for lateral motion. Whilst not common for manned aircraft, the bank angle command provides multiple advantages to the pilot of a remotely controlled aircraft. The so-called Attitude-Command/Attitude-Hold system simplifies the pilot's control task, especially in cases where the aircraft's attitude is difficult to determine. Due to the unconventional shape of the SAGITTA Demonstrator, the pilot can easily be confused since no pronounced wing or other features are present which would assist in clearly identifying the aircraft's current situation. With an AC/AH system the external pilot can estimate the current attitude of the aircraft simply by reading the position of the control sticks of the radio transmitter. This is possible as the stick position represents the commanded steady-state attitude of the aircraft. If, in addition, the system includes a command limiter, a full stick deflection provides the pilot with the largest possible command which does not lead to a dangerous condition and provides suitable safety margins. Releasing the stick automatically leads to wings leveling - a built-in safety feature which can be of great benefit in case the pilot becomes disoriented. On the other hand, due to this characteristic a permanent stick deflection is required in long steady turns which imposes a higher workload on the pilot. Since typical missions of the SAGITTA Demonstrator are fairly short and are mainly performed using medium or high level commands, the higher workload during the short time an external pilot is controlling the aircraft is expected to be manageable. The bank angle is also suitable for use as the command variable for the autopilot and the trajectory control system, and so the selection of an AC/AH system for lateral-directional motion complies with the interface requirements defined in table 4.1.

In order to satisfy requirement II-1, it can be expected to have some form of scheduling of controller gains throughout the flight envelope. To make the system as robust to system failures as possible, the design should depend on as few scheduling variables as possible. For this reason only those measurements shall be used, which are expected to be highly available throughout the flight.

Requirements II-3 and II-4 lead to an expansion of the controller system by adding a ground mode and transition functionality from ground to air and vice versa. A description of the implementation of this functionality is not included in this work. In addition to implementation of transition functionality, for compliance with requirements II-3 and II-4 structural landing gear limits need to be considered. These are: the maximum bank angle at landing ($\Phi_{land,lim} \leq \pm 4.5°$), the maximum crab angle ($\beta_{land,lim} \leq \pm 4.5°$) and the maximum vertical speed at touchdown. The landing gear limits on bank angle and crab angle, in combination with the cross wind requirement specified in III-2 potentially impact the controller design as they might necessitate the implementation of a decrab functionality. If this is the case for the SAGITTA Demonstrator will be revealed later in this work.

Since reconfiguration of the control laws to counteract loss of GNSS would introduce unnecessary complexity into the system, requirement III-4 motivates the designer to avoid using any signals in the inner loop that originate from the GNSS receiver. Moreover, in order to further increase the robustness of the controller w.r.t. potential sensor malfunctions, the system developer has extended the list of requirements to include an optional fixed gain, non-scheduled emergency controller. Since the fixed gain controller is not expected to provide satisfactory stabilization and performance across the entire envelope, the controller with scheduled gains will be used in nominal conditions, with the fixed gain controller being engaged only in adverse conditions.

The ill-defined requirement in III-1 raises the question of Flying Qualities of a remotely piloted, unmanned aircraft. The evaluation of Flying Qualities is an important element in the validation of a Flight Control System, but unfortunately to date no consolidated universal reference for evaluation of Flying Qualities of unmanned systems exists. Due to the overall lack of experience in the field of Flying Qualities of unmanned systems; the scarcity of publicly accessible data-bases; and huge variety of aircraft configurations (in terms of control concepts, weight and size) the issue of Flying Qualities evaluation for unmanned aircraft is still at the research stage. By thoroughly reviewing the Flying Qualities of manned aircraft and adapting specific, requirements that are applicable to the SAGITTA aircraft, this work aims to provide a contribution to this research.

4.3. Review of Flying Qualities of manned aircraft

The clearance road map presented above mainly addresses the stability and robustness properties of the closed-loop system. and does not provide any guidelines for controller performance characteristics. In order to overcome the lack of controller performance requirements for manual control via radio transmitter, a brief review of relevant documents from manned aviation is performed, and the methods that have been found for Flying Qualities analysis together with the related requirements are presented and complemented by a discussion of their applicability to evaluation of unmanned aircraft performance. The goal is to identify requirements that are potentially relevant to the radio-piloted SAGITTA Demonstrator taking into account the unconventional response characteristics of an AC/AH system.

The focus of the review is MIL-HDBK 1797 as this provides the most comprehensive set of Flying Qualities requirements and also delivers background information and verification guidelines. This standard is supplemented by MIL-DTL-9490E and by SAE ARP94910 for manned and unmanned aircraft respectively, these being the main sources for autopilot requirements that incorporate performance and accuracy of attitude control. In this context it should be noted that, whereas with the SAGITTA Demonstrator attitude control is used by the External Pilot for manual steering by means of continuously adjusted commands, in the standards mentioned above attitude control is used as an autopilot mode, in an open-loop manner and therefore by means of discrete (non-continuous) commands. Since both standards, MIL-DTL-9490E and SAE ARP94910, provide identical wording for the requirements, this document will cite only [55]. Finally, the rotorcraft standard ADS-33E-PRF is incorporated into the review since many helicopters employ an AC/AH system for manual control and consequently an extensive knowledge base exists for this class of flying platform.

Preliminary notes on applicability of manned aircraft handling qualities to radio piloted aircraft

One of the main concerns when applying manned aircraft handling qualities requirements to Remotely Piloted Aircraft (RPA) is the fact that, compared to their manned counterparts, most RPA are significantly smaller and lighter, therefore have lower moments of inertia and consequently exhibit much faster dynamic characteristics. As shown in [22], this property might produce misleading results from Flying Qualities evaluations when the Flying Qualities level boundaries from e.g. [57] are applied to small-scale aircraft. In order to make small-scale aircraft comparable to full-size, manned aircraft in terms of Flying Qualities, so-called dynamic scaling must be applied. Dynamic scaling is a method for defining the relationship between full-size and small model aircraft in a form of a scaling number. Dynamic similarity is a related concept provided in [15] using the following definition:

> *When a geometrically similar model of an aircraft reacts to external forces and moves in such a manner that the relative positions of its components are geometrically similar to those of a full-scale airplane after a proportional period of time, the model and airplane are referred to as dynamically similar.*

The approach of dynamic scaling has been applied extensively in the evaluation of manned aircraft Flying Qualities by the use of "dynamically similar" free-flying models (e.g. by NASA: see [15]).To achieve similitude under conditions of incompressible flow, so-called Froude dynamic scaling (table 4.4) is typically applied, which provides a relationship between the full-scale aircraft, hereafter indicated by the subscript f, and the scaled model indexed by the subscript m with σ being the ratio of air density ρ_m/ρ_f and N being the geometric scale factor (compare [15]). By keeping the Froude number of the full scale and the model aircraft identical, similar inertial and gravity effects on both are established. The Froude number is defined according to [89] as

$$N_F = \frac{V^2}{gl} \tag{4.1}$$

with V being the velocity, g being the gravitational constant, and l being the characteristic length.

Lengths:	l_m	$= \frac{l_f}{N}$
Time Constants:	T_m	$= \frac{T_f}{\sqrt{N}}$
Mass:	m_m	$= \sigma \frac{m_f}{N^3}$
Linear Velocities:	V_m	$= \frac{V_f}{\sqrt{N}}$
Moments of inertia:	I_m	$= \sigma \frac{I_f}{N^5}$
Frequencies:	ω_m	$= \omega_f \sqrt{N}$

Table 4.4.: Froude dynamic scaling relation

The main relationships listed in table 4.4 are derived below using basic flight dynamics relationships.

First of all, geometric similarity is achieved in accordance with the definition given above by scaling all lengths by a predefined value N; areas by N^2; and volumes by N^3. With the aid of the level flight condition

$$C_L \bar{q} S = mg, \tag{4.2}$$

and constraining the lift coefficients C_L of the small- and full-scale aircraft to be identical in comparable flight situations (e.g. level flight), it is possible to derive the dynamic pressure ratio:

$$\frac{(\bar{q})_m}{(\bar{q})_f} = \frac{(m)_m}{(m)_f} \frac{(S)_f}{(S)_m}. \tag{4.3}$$

Using the following approximation for the natural frequency of (e.g.) the short period dynamic mode:

$$\omega_{0,SP}^2 = -M_\alpha = \frac{\bar{q} S \bar{c}}{I_{yy}}, \tag{4.4}$$

the frequency ratio between the model and the full-scale aircraft can be expressed as:

$$\frac{(\omega_0^2)_m}{(\omega_0^2)_f} = \frac{(\bar{q})_m}{(\bar{q})_f} \frac{(I_{yy})_f}{(I_{yy})_m} \frac{(S)_m}{(S)_f} \frac{(\bar{c})_m}{(\bar{c})_f} \tag{4.5}$$

By substituting the pressure ratio in equation (4.5) by the expression in equation (4.3), and assuming the radius of gyration to be correctly scaled geometrically, the following relationship between the full-scale and the model frequencies is derived:

$$\frac{(\omega_0)_m}{(\omega_0)_f} = \sqrt{N}. \tag{4.6}$$

The equivalent relationship for time can be derived directly from equation (4.6):

$$\frac{(T)_m}{(T)_f} = \frac{1}{\sqrt{N}}. \tag{4.7}$$

Using the approximation of the roll time constant

$$T_R = -\frac{1}{L_p}, \tag{4.8}$$

the ratio of the time constants can be expressed as

$$\frac{(T_R)_m}{(T_R)_f} = \frac{(L_p)_f}{(L_p)_m} = \frac{(\bar{q})_f}{(\bar{q})_m} \frac{(I_{xx})_m}{(I_{xx})_f} \frac{(S)_f}{(S)_m} \frac{(s)_f^2}{(s)_m^2} \frac{V_m}{V_f} = \frac{V_m}{V_f}, \tag{4.9}$$

in which use is made of the requirement on similarity requirement regarding the non-dimensional roll moment derivative w.r.t roll rate (equation (4.10)).

$$(C_{lp})_f = (C_{lp})_m \tag{4.10}$$

Taking into account the dynamic pressure ratio given in equation (4.3), equation (4.9) becomes

$$\frac{(T_R)_m}{(T_R)_f} = \sqrt{\frac{(m)_m}{(m)_f} \frac{(S)_f}{(S)_m}} \tag{4.11}$$

which, in cases where mass is correctly scaled geometrically, directly leads to

$$\frac{(T_R)_m}{(T_R)_f} = \frac{1}{\sqrt{N}} \tag{4.12}$$

and is thus consistent with the dynamic scaling requirement of proportionality of time.

$$C_l = C_{lp}\left(\frac{sp}{V}\right) + C_{l\beta}\beta + C_{l\xi}\xi + +C_{l\zeta}\zeta \tag{4.13}$$

The similarity requirement on non-dimensional rates given in equation (4.14) can easily be derived from the roll moment equation (4.13).

$$\left(\frac{sp}{V}\right)_f = \left(\frac{sp}{V}\right)_m \tag{4.14}$$

From this, and by making use of the relationship between length and velocity, the dynamic scaling of rotation rates can be calculated as follows:

$$\frac{(\omega)_m}{(\omega)_f} = \sqrt{N} \tag{4.15}$$

The relationship between angular accelerations can consequently be derived from (e.g.) the first-order roll dynamics:

$$\frac{(\dot{p})_m}{(\dot{p})_f} = \frac{(L_p)_m}{(L_p)_p} \frac{(p)_m}{(p)_p} \tag{4.16}$$

which leads to

$$\frac{(\dot{\omega})_m}{(\dot{\omega})_f} = N. \tag{4.17}$$

In cases where mass is not geometrically scaled, or it is not possible the model aircraft to be operated at the same altitude as the full-scale aircraft, similarity is achieved by using the ratio of densities, which leads to:

$$\frac{(m)_m}{(m)_f} = \frac{(\rho)_m}{(\rho)_f}\frac{1}{N^3} \tag{4.18}$$

and for the moment of inertia this results in:

$$\frac{(I)_m}{(I)_f} = \frac{(\rho)_m}{(\rho)_f}\frac{1}{N^5}. \tag{4.19}$$

Application of dynamic scaling to the SAGITTA Demonstrator requires there to be a full-scale counterpart for determination of the scale factor N in table 4.4. Little information is available concerning the full-scale SAGITTA aircraft. One known value is the wing span which is $b_f = 12$m. Since the wing span of the SAGITTA Demonstrator is $b_m = 3$m, a scaling factor of $N = 4$ is assumed. To be consistent with this, the scaling of all time-related requirements is $1/\sqrt{N} = 0.5$, while the frequency-related requirements are scaled by $\sqrt{N} = 2$. Assuming $(\rho)_m / (\rho)_f = 1$, the demonstrator, with a mass of between 112 kg and 144 kg, is able to provide results comparable to the full scale aircraft if its mass is between 7168 kg and 9216 kg, which is a realistic scenario for landing. Hence, the dynamic scaling using $N = 4$ provides a relationship between the SAGITTA Demonstrator and the future full-scale aircraft which is consistent with data currently available.

Aircraft Class and Flight Phase Category

When quantifying Flying Qualities requirements, MIL-HDBK 1797 differentiates between aircraft types that are organized into classes, and between flight phases that are organized into categories [57]. The aircraft classes are mainly characterized by the aircraft size and weight, as well as by the required amount of maneuverability in terms of load factor (n_z) (which is defined by the mission profile of the particular aircraft). The SAGITTA mission profile requires low-to-medium maneuverability, which is common for Class II aircraft. The full-scale aircraft with a Take Off Weight (TOW) of up to 17 160 kg, is well within the bounds for Class II specified in [14]. Therefore, the SAGITTA full-scale aircraft, as well as the scaled demonstrator, fall into Class II category. Since manual control is only a backup means of steering the aircraft, it is intended to be used only for safe landing in the event of an emergency. Therefore, the work on Flying Qualities deals only with the requirements applicable to the landing phase. Consequently, all values stated hereafter relate to the flight phase Category C.

Low-Order Equivalent Systems

Most of requirements in MIL-HDBK 1797 [57] are defined in terms of equivalent parameters that are obtained from so-called Low Order Equivalent Systems (LOESs) which are approximated from higher order dynamics of the aircraft. The concept of approximation of High Order Systems (HOSs) using LOESs for analyzing the dynamics of controller-augmented aircraft was introduced in the late 1960s. Since then it has found its way into the main Flying Qualities specification standards. Today, the derivation of LOESs is the basis for evaluation of a large variety of Flying Qualities criteria. The idea behind this approach is to make aircraft with higher order dynamics (e.g. resulting from introduction of higher order controllers) comparable to "conventional" aircraft, whose dynamics are well understood and for which the notion of "excellent Flying Qualities" has been refined and quantified through flight tests. In [57], the LOESs describing lateral-directional dynamics are assumed to have the following structure:

$$\frac{\Phi}{\delta_{pilot}} = \frac{K_\Phi \cdot (s^2 + 2\zeta_\Phi \omega_\Phi s + \omega_\Phi^2)e^{-\tau_{e_p} s}}{(s + 1/T_S)(s + 1/T_R)(s^2 + 2\zeta_{DR}\omega_{0,DR} s + \omega_{0,DR}^2)} \tag{4.20}$$

$$\frac{\beta}{\delta_{pilot}} = \frac{(A_3 s^3 + A_2 s^2 + A_1 s + A_0)e^{-\tau_{e_\beta} s}}{(s + 1/T_S)(s + 1/T_R)(s^2 + 2\zeta_{DR}\omega_{0,DR} s + \omega_{0,DR}^2)}. \tag{4.21}$$

where

K_Φ	: static loop sensitivity
ζ_Φ	: equivalent relative damping of the transmission zeros
ω_Φ	: equivalent natural frequency of the transmission zeros
τ_{p_e} and τ_β	: equivalent time delays resulting from higher order elements of the control chain (e.g filters)
T_S	: equivalent spiral mode time constant
ζ_{DR}	: equivalent relative damping of the dutch roll
$\omega_{0,DR}$	: equivalent natural frequency of the dutch roll

The acquisition of particular parameters for lateral and directional LOES is achieved by making the LOES frequency responses equal those of the HOS. For this, the following cost function in [57] is minimized in an optimization process:

$$J = \frac{20}{n}\sum_{i=1}^{n}(Gain_{HOS} - Gain_{LOES})^2 + 0.02 \cdot (Phase_{HOS} - Phase_{LOES})^2. \tag{4.22}$$

The lateral and directional transfer functions are fitted simultaneously over the frequency range from $0.1\,\mathrm{rad\,s^{-1}}$ to $10\,\mathrm{rad\,s^{-1}}$, whereby common parameters are constrained to have the same values. Whether or not the mismatch between the HOS and the LOES is acceptable is determined by so-called mismatch envelopes for the gain and the phase. These envelopes can be found in e.g. [57].

In principle, the concept of LOES approximation is valid for all types of aircraft. Nevertheless, since the Flying Qualities requirements in [57] were expressed with conventional aircraft behavior in mind, the validity of using LOESs with structures in equation (4.20) and equation (4.21) might be inappropriate for aircraft having non-conventional response types. Indeed, in [52], Mitchell states that the LOES approach "...shall never be applied to an airplane with attitude-command dynamics". However, in his justification of this statement he mainly addresses longitudinal dynamics. Whether or not an LOES representation is applicable to a certain response-type has to be analyzed on a case-by-case basis and, by way of example, this is done for the SAGITTA Demonstrator as follows.

A closed-loop system of the SAGITTA Demonstrator at medium speed and altitude is selected as the higher order system to be matched by the equivalent low-order representation. At this stage of development, the characteristics of the closed-loop system are anticipated to be of the AC/AH type in both Φ and β control variables. The higher order closed-loop system comprises the rigid body aircraft including actuator dynamics, two controller integrators, one command filter and two sensor filters. When equalizing the matching of the transfer functions the lower limit of the frequency range to be matched has been extended to $\omega = 0.004\,\mathrm{rad\,s^{-1}}$ to permit a better assessment

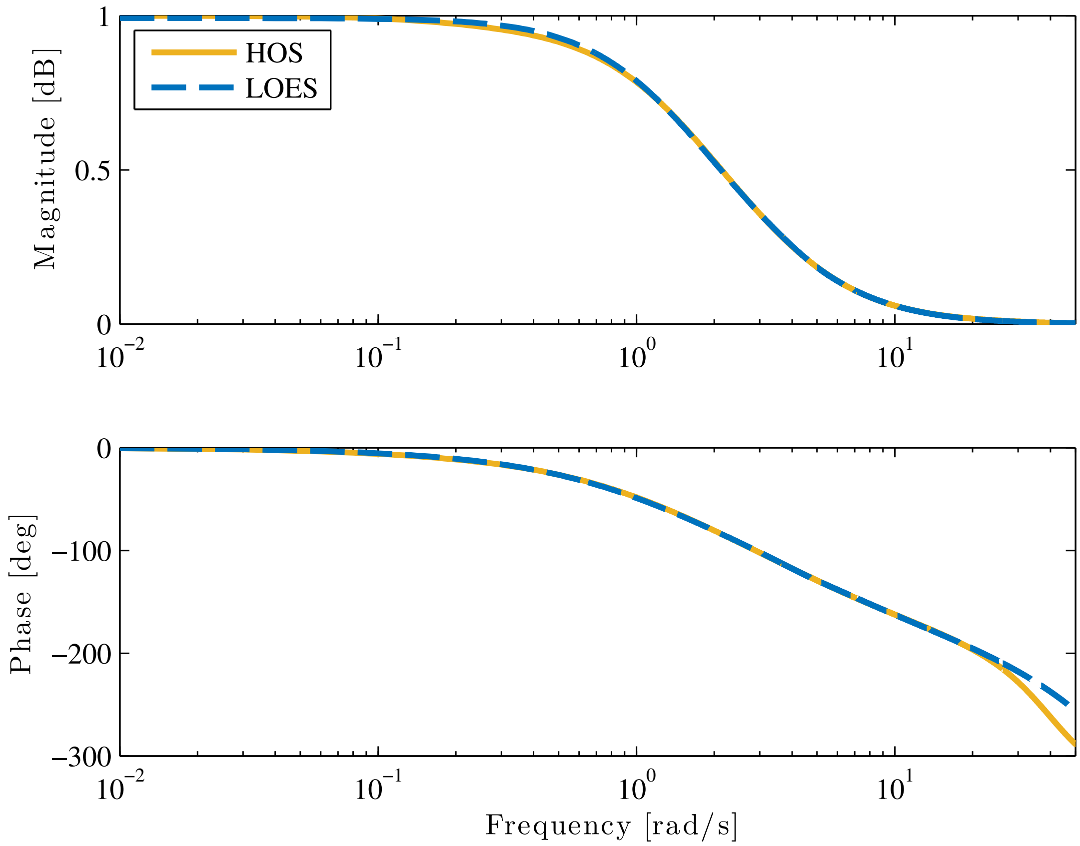

Figure 4.2.: Comparison of HOS and LOES | Frequency response of $G_{\Phi\Phi_{cmd}}$

of steady-state behavior. The result of the simultaneous matching of equations (4.20) and (4.21) with all parameters being unconstrained is shown in figures 4.2, 4.3 and 4.4 in terms of frequency response, the pole zero map, and the time histories of the system's response respectively. From these figures, it can be seen, that a good match is achieved with the resulting equivalent time delays $\tau_{e_p} = 0.029\,\mathrm{s}$ and $\tau_{e_\beta} = 0.0231\,\mathrm{s}$ being of reasonable magnitude.

Comparison of the roots (or poles) of the LOES with the dominant roots of the HOS reveals that the roll subsidence poles exhibit the largest difference, while the spiral poles are located relatively close to each other, and the Dutch-roll poles align almost perfectly. This good match is a result of the careful definition of the dominant poles of the closed-loop system, which are chosen with the pole distribution of a conventional aircraft in mind. Additionally, the good match between closed-loop LOES and HOS is achieved by introduction of (e.g.) a feed-forward controller element, which cancels out the integrators introduced by the feedback controller. A detailed description on the design of the feed-forward controller will be provided in chapter 5.

The excellent match between HOS and LOES suggests, that the LOES is applicable to AC/AH-type systems as long as the higher-order closed-loop system provides dominant roots that can be attributed to "conventional" aircraft modes, and as long as the controller-introduced poles in the region of rigid body modes are canceled out by additional controller elements. In the present case, however, it has also been shown that derivation of the equivalent system's parameters from dominant roots of the higher order AC/AH system is also valid. Although this approach is explicitly rejected by [57], it will be used in this work as it provides satisfactory results in terms of LOES and HOS

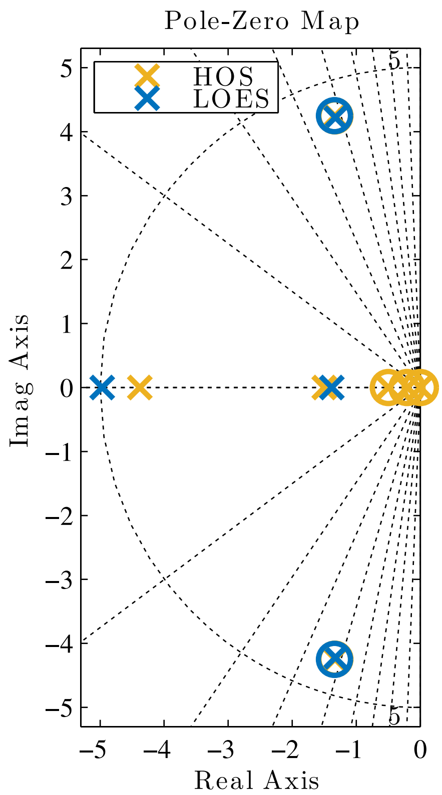

Figure 4.3.: Comparison of HOS and LOES | Pole-Zero Map of ACAH System

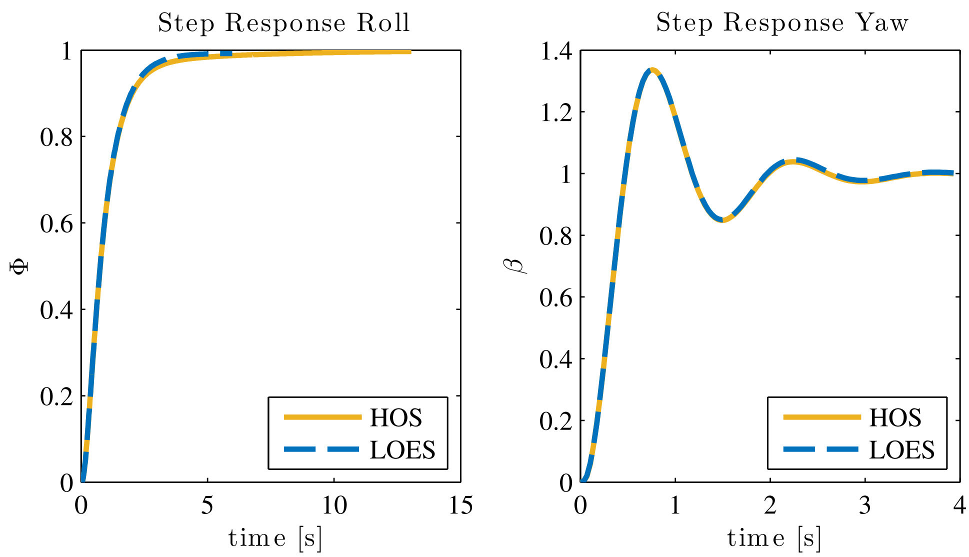

Figure 4.4.: Comparison of HOS and LOES | Step response in roll and yaw

matching. Furthermore, this approach is both intuitive and simple to apply, and once accepted for the task at hand, it enables the application of numerous Flying Qualities requirements to the SAGITTA Demonstrator. These, as well as other requirements arising from relevant documents, are discussed in detail in subsequent sections.

Roll subsidence time constant

The roll subsidence time constant T_R is the faster of the two aperiodic modes of the lateral motion of a conventional aircraft and is mainly related to the aircraft roll damping. It is typically obtained from the LOES. In table 4.5 the upper boundary for the roll subsidence time constant is reproduced from [57]. In addition, a lower boundary of $T_R <= 0.33$s is proposed in [57]. This lower boundary is motivated by the risk of roll ratcheting, which is attributed to high roll damping. Roll ratcheting is a pilot-vehicle coupling phenomenon characterized by roll oscillations. It is often observed in high performance aircraft during rapid rolling maneuvers and is associated with an abrupt roll recovery. In [30] Hess attributes the effect to the pilot's inappropriate use of vestibular feedback of angular and linear acceleration during aggressive rolling, which, in combination with the dynamic characteristics of the neuromuscular system and the control stick, leads to a lightly damped oscillation. This hypothesis can also be found in [13]. Since the vestibular apparatus of a pilot controlling an RPA is not stimulated by the motion of the aircraft, it is assumed that for RPA there is therefore no lower limit on T_R.

Spiral stability time to double

The spiral mode is described by the slower of the two aperiodic modes and is related to the spiral mode time constant T_S or the time to double T_2. The pilot prefers a neutral spiral mode, but accepts a spiral mode that is slowly divergent in its nature. The requirements for class II aircraft are reproduced in table 4.5. Furthermore, [57] provides a reference which indicates that, in some scenarios a highly stable spiral might be acceptable to the pilot.

When working on RPAs it should be kept in mind that most comments with regard to adverse Flying Qualities of aircraft having a highly stable spiral are related to the amount of force that needs to be applied by the pilot during turns. Such force is not required when controlling radio piloted aircraft using e.g. standard model airplane radio transmitters as these do not provide a force feedback to the pilot. With RPAs therefore the spiral mode requirements of AC/AH systems in particular might differ significantly from their conventional, manned counterparts.

Coupled Roll-Spiral oscillation

The coupled roll-spiral oscillation is a union of the poles combining the roll subsidence and the spiral mode into a conjugated complex pair of poles. The corresponding roll-spiral mode is unconventional and is typically not desired. It is associated with poor lateral path dynamics. Nevertheless, a roll-spiral mode can provide Level 1 Flying Qualities for Category C flight phases as long as $\zeta_{RS}\omega_{0,RS} \leq 0.5$. In [14], Chalk states that when adverse Flying Qualities were attributed to the appearance of roll-spiral oscillations, these were always accompanied by stability derivatives of "unusual values", while "satisfactory Flying Qualities" could still result in the case of a roll-spiral oscillation induced by bank angle feedback. This is worth noting, since it indicates, that the roll-spiral oscillation does not necessarily result in adverse Flying Qualities. MIL-1797 [57] states that sometimes a roll-spiral coupling might even be "desirable: for example for attitude command on landing approach, where fine tracking but no rapid, gross maneuvering is required". Unfortunately the accuracy of this quote cannot be verified since the relevant reference document was not available at the time this paper was prepared.

Roll oscillations

The roll oscillations requirement is stated in [60] and [57] and is related to the roll-yaw coupling of aircraft configurations with high $|\Phi/\beta|_{DR}$. In such configurations the roll response is contaminated by the Dutch-roll which is apparent in oscillations stimulated by an impulse in roll command. Such oscillations reduce the pilot's ability to control the rolling motion of the aircraft precisely, and therefore the requirement establishes limits for the parameters p_{osc}/p_{av} and Φ_{osc}/Φ_{av} which have been defined previously in equation (3.73). The roll oscillation requirement is extended to AC/AH systems in the rotorcraft standard [4]. Instead of an impulse excitation of the rolling motion, the standard proposes for AC/AH systems a step input and subsequent evaluation of the ratio Φ_{osc}/Φ_{av}.

The roll oscillation requirement only needs to be applied in cases where $|\Phi/\beta|_{DR} \geq 1.5$ (see MIL-1797 [57]). Since a requirement on the phi-to-beta ratio is easier to incorporate in the controller design process, in this work the roll oscillation requirement is replaced by the requirement $|\Phi/\beta|_{DR} \leq 1.5$ within the entire flight envelope.

Roll Time Delay

This requirement defines an upper limit for the parameter τ_{e_p} in the LOES representation of the roll rate response to a pilot's input. This parameter can either be extracted by a laborious process of matching the corresponding LOES, or set equal to the so-called effective time delay, which can be extracted from the time response as described in Appendix A of MIL-HDBK-1797 [57]. Instead of the roll time delay requirement, the bandwidth criterion presented later will be used as this provides an equivalent to the roll time delay requirement.

Roll axis response to roll control inputs

This section defines the requirement on the quickness of response of the aircraft to high amplitude commands. More specifically the roll axis response requirement defines an upper limit on the time taken to achieve a specified change in bank angle. A class II aircraft in flight phase C is considered to have Level 1 Flying Qualities if the time to achieve a bank angle of $\Phi = 30°$ is $T_{\Phi=30} \leq 1.8$s. Since this requirement has been defined with a conventional rate response type system in mind, the standard suggests applying a constant control input in order to roll through the desired bank angle when performing verification of the requirement on the assumption that the aircraft will respond to such input with a constant roll rate and hence yield consistent results that are independent of piloting techniques. With unconventional response types, this requirement becomes more challenging since the aircraft response in such cases is significantly different. For an AC/AH system, a constant input in roll axis leads to a specific desired bank angle.

During the maneuver the roll rate is permanently changing and becomes smaller as the difference between the commanded and the actual bank angles reduces. This behavior typically leads to a larger time-to-target compared to a rate command system since the rotation slows as the bank angle nears the desired value. In some aircraft this problem can be overcome by commanding a much larger bank angle than the one stated in the requirement in order to obtain a rate response comparable to the one of aircraft with rate response type. For aircraft where the maximum achievable bank angle is close to the targeted value, the above-mentioned technique will not help and the requirement will remain more challenging than for conventional aircraft. Nevertheless, the requirement itself seems to be suitable for AC/AH systems.

In order to account for the special nature of the command type, this requirement is replaced by the attitude hold requirement taken from autopilot specifications of manned aircraft.

Dynamic lateral-directional response

The main requirement on the dynamics of yaw motion is related to the two parameters describing the Dutch-roll, namely its frequency $\omega_{0,DR}$ and damping ζ_{DR}. The values for class II aircraft are defined in [57] and are reproduced in table 4.6.

Yaw axis response to roll controller

The requirement on yaw axis response to roll controller defines an upper limit on AoS when a pure roll command is applied. It primarily aims to enable turn coordination by the pilot. Depending on the pro/adverse yaw characteristics of the AoS response to roll command, two values for maximum AoS are defined (table 4.6).

In the case of the SAGITTA Demonstrator this requirement is replaced by the requirement for automatic coordination during turn initiation. The maximum allowed sideslip value during turn initiation is set to equal the maximum allowed sideslip in flight, which is defined later in the context of the sideslip limit requirement.

Control-Margin Increments due to Sensor Noise and Turbulence

MIL-HDBK 1797 [57] provides a recommendation concerning the control margin w.r.t. sensor noise and turbulence in terms of variance of the control surface deflection and deflection rate. Since the formulation of the recommendation leaves some room for interpretation, the term "control margin" is used here as a synonym for the available maximum control deflection or rate. From the recommendation in [57] the following requirement is extracted:

$$|\delta_{max}| \overset{!}{\geq} 3\sigma_{\delta,turb} \qquad |\dot{\delta}_{max}| \overset{!}{\geq} 3\sigma_{\dot{\delta},turb}, \tag{4.23}$$

with δ_{max} and $\dot{\delta}_{max}$ being the maximum available control surface deflection and deflection rate respectively, and σ_{δ} and $\sigma_{\dot{\delta}}$ being the respective standard deviations in severe turbulence. An analogous requirement formulated for the reaction of control surfaces to sensor noise is given in equation (4.24).

$$|\delta_{max}| \overset{!}{\geq} 3\sigma_{\delta,sens} \qquad |\dot{\delta}_{max}| \overset{!}{\geq} 3\sigma_{\dot{\delta},sens} \tag{4.24}$$

Requirement		Level		
MIL Ch.		Level 1	Level 2	Level 3
4.5.1.1	Roll mode time constant $T_{R,min}$ [s]	1.4	3	10
4.5.1.2	Spiral stability: time to double $T_{2,min}$ [s]	12	8	4
4.5.1.3	Coupled roll-spiral oscillation $(\zeta_{RS}\omega_{0,RS})_{min}$ [$\mathrm{rad\,s^{-1}}$]	0.5	0.3	0.15
4.5.1.4	Roll oscillations $(p_{av}/p_{osc})_{max}$ [%]		figure 3.27	
4.5.1.5	Roll time delay $\tau_{e_p,max}$ [s]	0.1	0.2	0.25
4.5.8.1	Roll axis response to roll control inputs of $\Phi = 30°, T_{\Phi=30,min}$ [s]	1.8	2.5	3.6

Table 4.5.: Roll Axis Requirements, Class II Aircraft, Flight Phase C [57]

As will be shown later, the formulation of control margin requirements in terms of limits on standard deviation encourages the use of spectral power analysis, a powerful tool for assessment of actuator activity and sensor filter design.

Attitude hold

The standards [56] and [55] provide guidance on the accuracy and performance of aircraft in attitude hold and other autopilot modes. According to [55] "attitudes should be maintained in smooth air with a static accuracy... of ±1°". In turbulent conditions the Root Mean Square (RMS) should not exceed 10° in roll. "Accuracy requirements shall be achieved and maintained ... within 5 seconds of mode engagement for a 5 degree attitude disturbance."

Coordination in steady banked turns

A further requirement which is typically applied to autopilot modes of aircraft, but which is also applicable to a Control and Stability Augmentation System (CSAS) implementing AC/AH, is the requirement on coordinated turns: "The incremental sideslip angle should not exceed 2 degrees from the trimmed value, and lateral acceleration should not exceed 0.03g, while at steady bank angles up to the maneuver bank angle limit reached in normal maneuvers." (from [55]).

Coordination in straight and level flight

The following requirement provides guidance on the accuracy of directional control in level flight: "The accuracy while the aircraft is in straight and level flight should be maintained with an incremental sideslip angle of ±1° from the trimmed value or a lateral acceleration of ±0.02g at the c.g., whichever is lower." (from [55]).

Sideslip limits

The sideslip limit is determined by subtracting a predefined safety margin of 4° from the available data range provided by the ADM. For the SAGITTA Demonstrator the absolute maximum sideslip limit is $\beta_{max} = \pm 10°$.

Requirement		Level		
MIL Ch.		Level 1	Level 2	Level 3
4.6.1.1	Dynamic lateral-directional response $\zeta_{DR,min}$	0.08	0.02	0
4.6.1.1	Dynamic lateral-directional response $(\zeta_{DR}\omega_{0,DR})_{min}$	0.1	0.05	-
4.6.1.1	Dynamic lateral-directional response $(\omega_{0,DR})_{min}$	0.4	0.4	0.4
4.6.2	Yaw axis response to roll controller β_{max}[deg] proverse yaw	2	4	-
4.6.2	Yaw axis response to roll controller β_{max}[deg] adverse yaw	6	15	-

Note regarding (4.6.1.1): for cases $\omega_{0,DR}^2|\Phi/\beta|_{DR} > 20\,\mathrm{rad\,s^{-1}}$ the minimum $\zeta_{DR}\omega_{0,DR}$ shall be increased by:

$$\text{Level 1}: \quad \Delta\zeta_{DR}\omega_{0,DR} = 0.014\left(\omega_{0,DR}^2|\Phi/\beta|_{DR} - 20\right)$$
$$\text{Level 2}: \quad \Delta\zeta_{DR}\omega_{0,DR} = 0.009\left(\omega_{0,DR}^2|\Phi/\beta|_{DR} - 20\right)$$

Table 4.6.: Yaw Axis Requirements, Class II Aircraft, Flight Phase C [57]

Pilot-in-the-loop oscillation

A requirement which plays an important role in manned aviation, but which has barely been studied in the case of RPA, is the requirement on the PIO tendency (see section 4.1.11.6 in [57]). It addresses the pilot-vehicle coupling and the stability properties of the pilot-vehicle closed-loop dynamics. According to [3], PIOs can be classified by three types as follows:

Type I Linear pilot-vehicle coupling

Type II Limit cycles due to one or more nonlinear elements in series in the primary control loop

Type III Limit cycles due to one or more nonlinear elements in vehicle motion feedback paths subsidiary to the primary control loop

In lateral-directional motion, Type I PIOs are mainly linked to the relative position of poles and zeros of the lateral transfer function, while Type II PIOs may occur in the event of (e.g.) actuator rate saturation which lead to a reduction in phase margin. Type III PIOs are related to nonlinearities in the feedback path (e.g. changes in controlled elements [3, 31]).

Several techniques exist for analyzing Type I PIOs. The two most important are the Neal-Smith Criteria and the Bandwidth Criteria by Hoh. These are presented in sections 4.4 and 4.5 respectively, where their applicability to the present work is discussed. Subsequently, in section 4.6, the Open Loop Onset Point (OLOP) criterion, which can be used to analyze an aircraft's susceptibility to Type II PIOs is also described briefly.

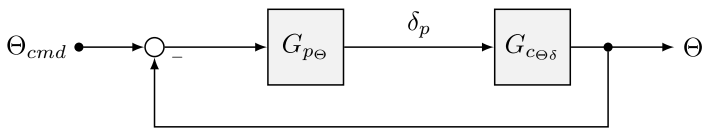

Figure 4.5.: Attitude loop closure via pilot according to Neal-Smith criteria

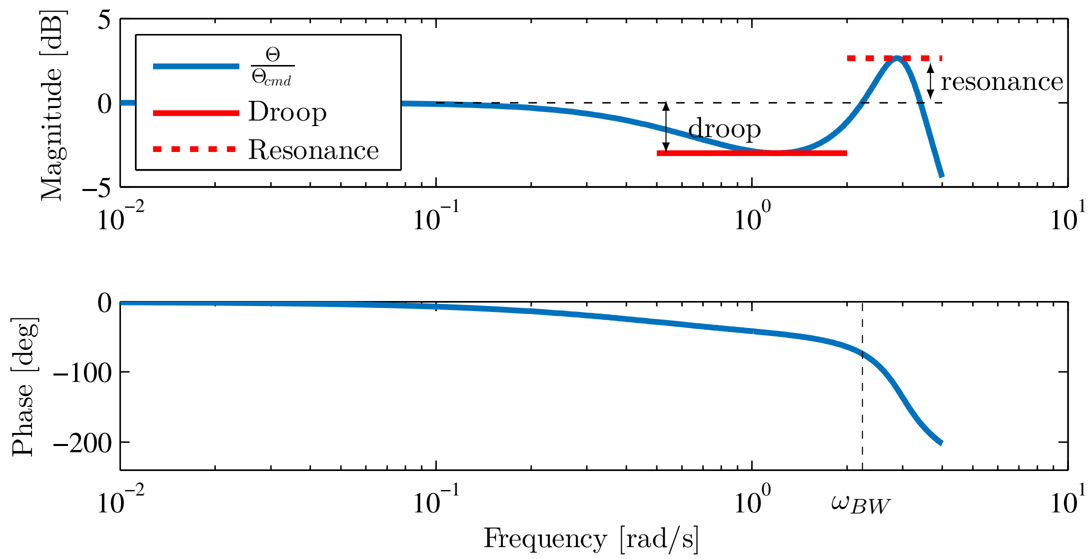

Figure 4.6.: Closed-loop frequency response in context of Neal-Smith Criterion

4.4. Neal-Smith criteria

One of the best-known methods for predicting Flying Qualities and PIOs is to apply the Neal-Smith criteria which were originally derived from the HOS data-base for fighter aircraft in the combat phase (see [62]). It is especially useful in situations where the LOES approach fails, since the Neal-Smith criteria can be applied to transfer functions of any dynamic order and form. The method considers the performance of the closed-loop pilot-vehicle system shown in figure 4.5 when tracking a desired pitch attitude, and is based on transforming the pilot's opinion of good tracking performance into a mathematical formulation. The pilot tries to achieve a fast and predictable steady-state tracking of attitude which in terms of frequency response, means a closed-loop magnitude close to 0 dB for frequencies up to the maximum required for the task under consideration. Since oscillations and overshoots are highly undesirable when tracking attitude, a frequency response beyond the task's maximum frequency must show minimal resonance. The pilot's opinion culminates in two variables which can be determined from either the open-loop or closed-loop transfer functions of pilot and vehicle. A graphical representation of the variables that are relevant to evaluation of the Neal-Smith criteria is provided in figure 4.6. This shows a Bode plot of a sample closed-loop response of pilot and vehicle and two quantities, namely droop and resonance, which the pilot is trying to minimize while keeping the system's bandwidth at a particular value suitable for the task at hand (where the bandwidth is defined as the range up to the frequency ω_{BW} when the phase of the closed-loop system is at $\phi = -90°$).

Based on flight tests Neal and Smith defined the required bandwidth for attitude tracking tasks in combat as $\omega_{BW} = 3.5\,\mathrm{rad\,s^{-1}}$, with maximum droop required to be $|\frac{\Theta}{\Theta_{cmd}}| \geq -3\,\mathrm{dB}$ within the range $\omega \leq \omega_{BW}$ [61].

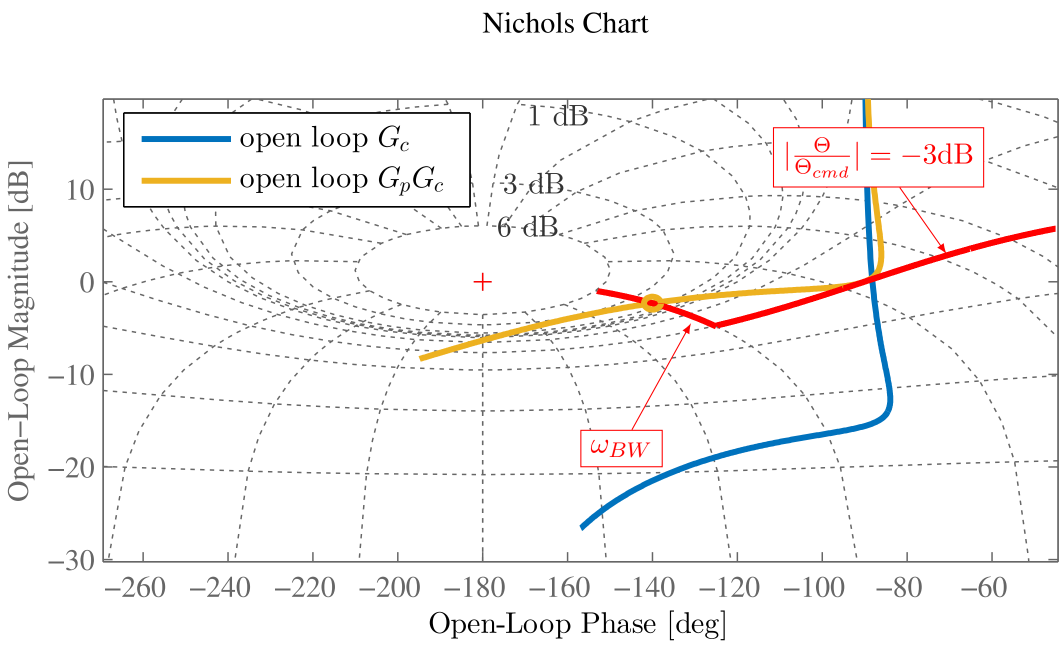

Figure 4.7.: Neal-Smith performance bounds

These two requirements are denoted by two red boundaries in the Nichols Chart in figure 4.7. One of these represents the closed-loop magnitude of $-3\,\mathrm{dB}$: the open-loop transfer function representing the pilot and vehicle is not allowed to cross this boundary from above for $\omega <= \omega_{BW}$. The other is located at the closed-loop phase of $\phi = -90°$ and thereby represents the closed-loop bandwidth that is specified for the task under study. Consequently, the open-loop of pilot and vehicle (G_pG_c) must cross this boundary exactly at the task specific ω_{BW} (the location of the crossing is marked in the plot by the yellow circle).

For the purpose of modeling, Neal and Smith assume the dynamics of the pilot are described adequately by the simplified precision model (SPM) given in equation (4.25).

$$G_p = K_p \frac{T_L s + 1}{T_I s + 1} e^{-\tau_{e_p} s} \tag{4.25}$$

where K_p represents the pilot's static gain, and T_L and T_I are the lead time and lag time constants respectively. According to this model, the pilot has three means of adjusting the shape of pilot-vehicle response, namely: the gain K_p, which is used to shift the open-loop frequency response in the Nichols Chart either upwards by increasing the gain or and downwards by decreasing the gain: and the two time constants of the lead-lag element, which can be used to modify the curvature and phase of the frequency response. The time delay τ_{e_p} is set to $0.3\,\mathrm{s}$. Figure 4.7 shows a sample transfer function of the plant G_c and the open-loop plant-vehicle transfer function G_pG_c after the pilot model has been adjusted to a task-specific bandwidth (here a task with a bandwidth of $\omega_{BW} = 2.5\mathrm{rad\,s^{-1}}$ is chosen). After adjustment of the pilot model in such a way that the overall system complies with the Neal-Smith criteria, the resulting closed-loop resonance can be determined from the Nichols Chart. This value is plotted against the phase angle ϕ that is calculated from the lead-lag element of the pilot model. The result is used to predict the Flying Qualities level and susceptibility to PIO. Figure 4.8 shows the evaluation of the sample transfer function from figure 4.7 in the context of the Flying Qualities Level boundaries defined in [61].

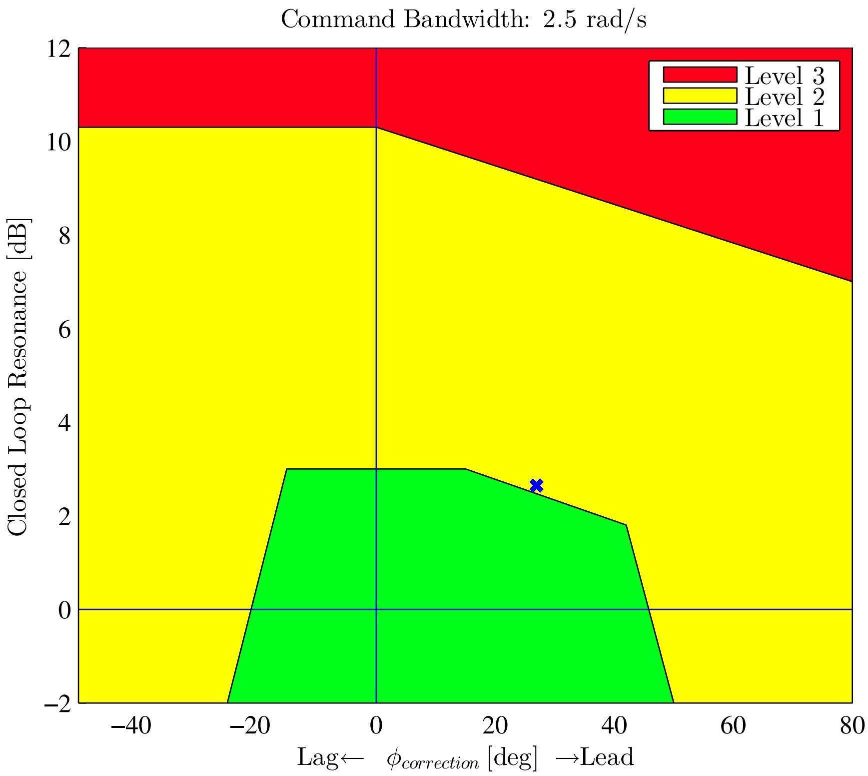

Figure 4.8.: Original Neal-Smith Flying Quality Levels

The original Neal-Smith criteria were revised and extended in [69] for the landing task based on the Landing Approach Higher Order System (LAHOS) data. Radford adjusted the parameters for landing to

$$\omega_{BW} = 3\,\mathrm{rad\,s^{-1}} \qquad \tau_e = 0.2\,\mathrm{s}.$$

Furthermore, he relaxed the "droop" requirement for systems with a closed-loop resonance of $\leq 2\,\mathrm{dB}$ and made minor adjustments to the Flying Qualities boundaries initially defined. Later, in [53] Mooij also extended the criteria to include the approach and landing task for transport aircraft and changed the minimum bandwidth to $\omega_{BW} = 1.2\,\mathrm{rad\,s^{-1}}$.

The multiple adjustments to boundaries and task bandwidths in the past highlight the main problem of the Neal-Smith criteria. The Neal-Smith criteria were already found early on to be very sensitive to the selection of the task bandwidth and resonance. Based on the observations that were made regarding sensitivity, Radford proposed in [69] the so-called adaptability criteria which try to capture the degree of change of compensation the pilot needs to apply in case when changing tasks. Since these adaptability criteria have not been studied to any great depth, they are not taken into consideration in the course of this work. Besides the adaptability criteria, a "carpet plot" was introduced into the Flying Qualities map to indicate the sensitivity of a closed-loop system to variations in parameters. The "carpet plot" provides a useful tool for detection of systems with rapidly changing Flying Qualities - so-called Flying Qualities cliffs.

Application of the Neal-Smith criteria assumes tight compensatory attitude control by the pilot. Using an AC/AH system the pilot is no longer required to close the attitude loop in a tight manner and is likely to control the attitude far more loosely. Consequently, without further analysis and adjustments, the basic Neal-Smith criteria

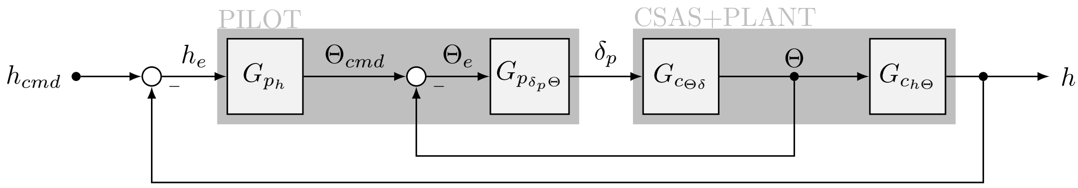

Figure 4.9.: Attitude and Altitude loop closure via pilot

do not seem to be suitable for AC/AH systems. One possible approach to evaluating an AC/AH system, could be to customize the extension of the Neal-Smith criteria that has been proposed by Sarrafian [73] for flight path control in landing. Based on pilot comments which support the opinion that rate of change in altitude is highly relevant when evaluating the landing performance, Sarrafian derived a multi-loop closure technique according the following principles: After closing the attitude loop with a fixed attitude lead compensation of $\phi_{lead} = 25°$ according to the Neal-Smith method, an outer altitude loop is closed with a pilot model that is represented by a pure gain. The corresponding block diagram is shown in figure 4.9 in which the pilot outer loop transfer function G_{p_h} is a pure gain. The altitude bandwidth is defined by selecting the gain of G_{p_h} such that at the closed-loop phase $\phi = 90°$ a closed-loop amplification of $2 - 3$dB is achieved.

The multi-loop approach presented here could be used for evaluation of Flying Qualities of an AC/AH system w.r.t. (for example) altitude control. By replacing the inner control element $G_{p\delta_p\Theta}$ in figure 4.9 by the AC/AH controller and subsequently closing the altitude loop by the pilot (G_{p_h}), the evaluation of the Flying Qualities by means presented in [73] can be performed. The approach seems promising, and thus worth to be investigated in the future.

While the Neal-Smith criteria have been proven to provide useful results for longitudinal motion, their application to lateral control is not entirely conclusive. In [5] an attempt was made to apply the Neal-Smith Criteria to lateral motion. Based on the LATHOS data the Flying Qualities levels that have been derived from longitudinal experiments were found to be inappropriate for lateral control. New lateral Flying Qualities boundaries have been proposed, but even with the proposed modifications several anomalies were discovered which led to a poor correlation between the pilot's Flying Qualities and the predicted levels.

To summarize, it seems that the Neal-Smith criteria provide a good insight into the pilot-vehicle interaction and resulting Flying Qualities. Unfortunately, no study has yet been completed regarding their application to AC/AH systems. Furthermore, no Flying Qualities level boundaries for lateral motion are available that would provide a solid basis for correlation with pilot ratings. Hence, after analysis of the Neal-Smith method it is deemed to be unsuitable for application to lateral control of the SAGITTA Demonstrator - at least for the time being. Nevertheless, the outer-loop closure by Sarrafian derived from the multi-loop technique does seem to be applicable to AC/AH in both longitudinal and lateral-directional motion. In respect of lateral-directional motion the corresponding multi-loop pilot-aircraft transfer-function can be set up as per figure 4.9 and in accordance with [1] by replacing the altitude variable by heading, and the pitch angle by bank angle signals. The derivation of valid Flying Qualities boundaries for the Neal-Smith criteria is an open issue to be resolved in future.

4.5. Bandwidth Criterion

The Bandwidth Criterion was developed for highly augmented fighter aircraft to account for unconventional aircraft behavior introduced by Flight Control Systems. It can be applied to transfer functions of any form without the need for LOES approximation. As with Neal-Smith criteria, the Bandwidth Criterion focuses on the attitude response to pilot input and assumes a tight closed-loop compensatory high frequency tracking task with small amplitudes.

The Bandwidth Criterion uses the concept of the crossover model introduced by McRuer (see [49]), which is also the basis of the Neal-Smith Criteria, but in contrast to Neal-Smith, the bandwidth method eliminates the need for selecting either a task bandwidth or pilot model parameters in order to conduct the analysis. Instead, it defines two measures, namely bandwidth and phase delay, which are used for evaluation of Flying Qualities. Again, as with Neal-Smith, these parameters can be associated with the well-known equivalent parameters from LOES, namely the natural frequency and the equivalent time delay of the closed attitude loop transfer function.

For evaluation of the bandwidth criterion, the bandwidth frequency is defined as the lowest frequency of the open-loop transfer function where: the gain margin is at least 6 dB w.r.t. to the open-loop gain at ω_{180} ($\omega_{BW,gain}$); and the phase margin is at least 45° ($\omega_{BW,phase}$). The gain margin of 6 dB allows the pilot to double the gain in order to e.g. increase the bandwidth ω_{BW} without compromising the stability. The phase margin value is derived from a desired closed-loop damping of $\zeta = 0.35$ which approximately corresponds to a phase margin of $\phi = 45°$ [33]. A high bandwidth generally indicates good Flying Qualities in terms of fast reaction to pilot inputs. The reaction of an aircraft having a low bandwidth is often called "sluggish" by pilots [33].

The phase delay describes the change in stability margins related to phase when the pilot increases the crossover frequency ω_c (frequency, where the open loop gain is 0 dB) beyond the bandwidth frequency, and is thus a measure of the sensitivity to changes in frequency. Small values indicate a flat phase roll-off, and large values a steep roll-off. According to [57], the value of phase delay (τ_p) is calculated as follows:

$$\tau_p = \frac{\Delta\phi_{2\omega_{180}}}{57.3(2\omega_{180})} \tag{4.26}$$

where ω_{180} describes the frequency where the transfer function has a phase of $\phi = -180°$ and

$$\Delta\phi_{2\omega_{180}} = -\left(\phi(2\omega_{180}) + \phi(\omega_{180})\right). \tag{4.27}$$

Besides their use in evaluation of Flying Qualities levels, the two parameters ω_{BW} and τ_p determined by the Bandwidth Criterion also provide a prediction of PIO susceptibility. The corresponding boundaries for pitch control can be found in [51].

The Bandwidth Criterion is the primary means of evaluating Flying Qualities in the case of small-amplitude-high-frequency maneuvers for rotorcraft (see[4]). However, the Bandwidth Criterion is also applied for evaluation of fixed-wing aircraft. The MIL-HDBK-1797 [57] proposes use of the criterion in situations where LOES matching is not possible or is providing misleading results. The standard establishes longitudinal Flying Qualities levels but does not provide any guidance concerning its application to the analysis of rolling motion. Mitchell discusses application of the Bandwidth criterion to roll attitude in [52]. Based on evaluation of the Lateral Higher Order System (LATHOS) data-base, he proposes the Flying Qualities level boundaries that are reproduced in

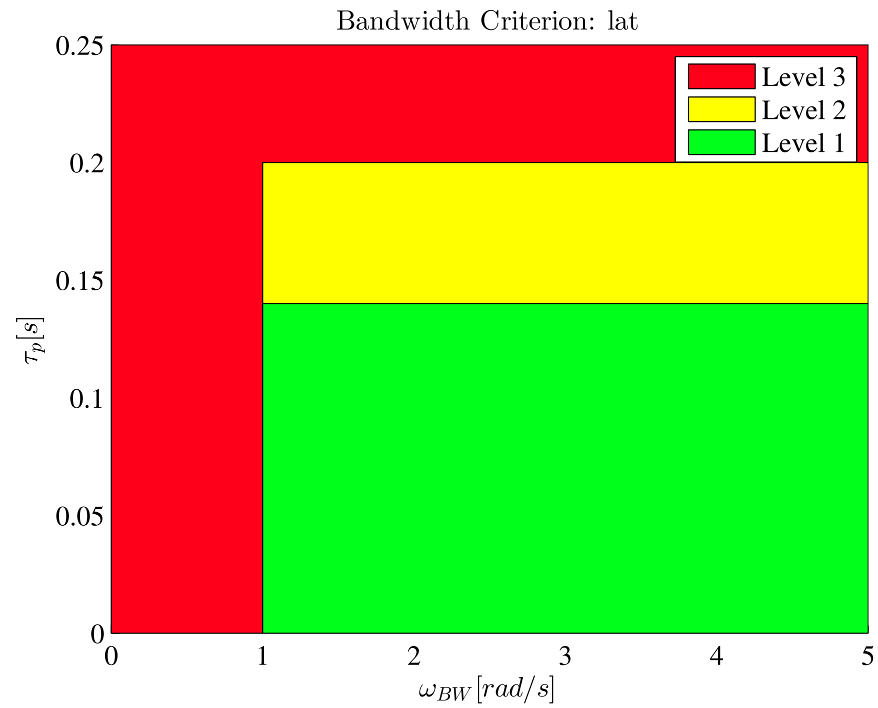

Figure 4.10.: Roll Bandwidth Boundaries

figure 4.10. As can be seen, the key factor in evaluation of Flying Qualities with regard to Bandwidth criterion in roll is the phase delay τ_p, since the categorization does not depend on the bandwidth, given that this is $\omega_{BW} \geq 1\,\mathrm{rad\,s^{-1}}$.

It should be noted that the above definitions of bandwidth are applicable for systems having a rate-response type (see [33]), but not usable for analysis of AC/AH systems. For AC/AH systems Mitchell proposes in [52] to determine the bandwidth frequency by analyzing only the phase response. In cases where $\omega_{BW,gain} < \omega_{BW,phase}$ or in situations where $\omega_{BW,gain}$ is indeterminate, Mitchell postulates that the aircraft may be prone to PIO during super-precision tasks or when subject to aggressive pilot techniques.

4.6. Open Loop Onset Point

The OLOP criterion was developed by Duda for prediction of Type 2 PIOs and as such it covers, among other nonlinearities, cases of PIOs due to actuator rate or position saturation. Although the OLOP criterion is relatively new and therefore cannot be found in any of the de facto Flying Qualities standards, very detailed discussions on OLOP can be found in [25, 66]. The key points are summarized briefly as follows.

It is well known that an active rate limit introduces an additional phase delay and modifies the amplitude of the frequency response of a dynamic system. This becomes apparent by comparing system responses in time domain of rate unlimited systems with those of rate limited systems when subject to e.g. sinusoidal inputs. The behavior of such systems can be divided into three modes of operation, which occur according to the amplitude and frequency of the input signal to the system:

1. inactive rate limiter (linear behavior)
2. rate limiter not continuously active

3. rate limiter continuously active

In order to analyze the behavior of a system operating with a continuously active rate limiter (Mode 3) a so-called "describing function" can be used, which approximates the nonlinear behavior by a quasi-linear transfer function that depends on the input amplitude. The derivation of such describing function for Mode 3 can be found in [66].The behavior in the Mode 2 is approximated by interpolating the frequency and phase response between the linear transfer function in Mode 1 and the describing function in Mode 3. Transitions between the modes occur at frequencies which vary according to the input amplitude.

The OLOP criterion provide means to determine the impact of actuator rate or position saturation on closed-loop stability by application of a simple procedure and without the need of derivation of a describing function. Assuming a sinusoidal signal at the input of the rate limiter of the form shown in equation (4.28)

$$u = \hat{u} \sin(\omega t) \tag{4.28}$$

where $\hat{u}$ is the maximum amplitude, and ω is the frequency of the input signal, the maximum rate of change of this signal can be determined by differentiating u with respect to time and then calculating the maximum value of the function obtained by differentiation. This leads to the following expression for the maximum rate of change:

$$(\dot{u})_{max} = \hat{u}\omega. \tag{4.29}$$

The rate limit R fed by this sinusoidal signal is activated when the following condition is true:

$$(\dot{u})_{max} = \hat{u}\omega \stackrel{!}{=} R. \tag{4.30}$$

This relationship can be used to determine the frequency at which the rate limiter is activated, and thus the frequency at which the transition between linear behavior and activation of the rate limiter occurs. The corresponding procedure is presented below.

Given a closed-loop system with a rate limiter in the feedback path as shown in figure 4.11a, the first step is to remove the limiter from the closed-loop dynamics. The resulting linear closed-loop system is shown in figure 4.11b. In the next step, the frequency response $G_{u\delta_{cmd}}(s)$, where u represents the signal at the rate limiter, that has been removed, is determined. This frequency response is scaled by the maximum command input $(\delta_{cmd})_{max}$ which leads to

$$\hat{U}(s) = G_{u\delta_{cmd}}(s)\,(\delta_{cmd})_{max}\,. \tag{4.31}$$

In addition, the function representing the frequency dependent activation of the rate limiter is derived from equation (4.30) as

$$\hat{u} = \frac{R}{\omega}. \tag{4.32}$$

The rate saturation is considered to appear at the frequency where the two frequency responses from equations (4.31) and (4.32) intersect. This leads to the following condition for activation of the rate limiter:

$$\left|G_{u\delta_{cmd}}(s)\,(\delta_{cmd})_{max}\right| \stackrel{!}{=} \frac{R}{\omega}, \tag{4.33}$$

One practical way of determining the intersection of the two frequency responses is by graphical means using the Bode plot. The frequency at which the two amplitude

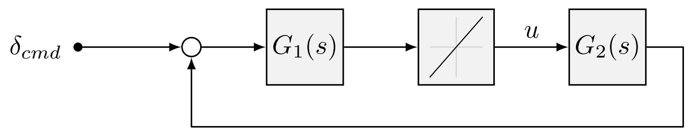

(a) system with rate limiter in feedback path

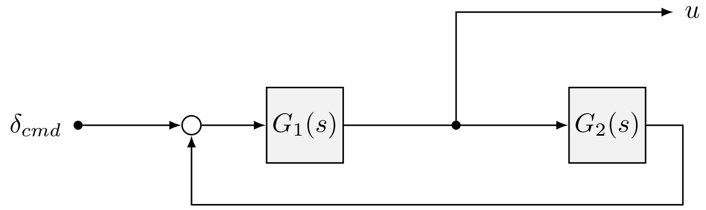

(b) system without rate limiter in feedback path

Figure 4.11.: Model representation for determination of onset frequency

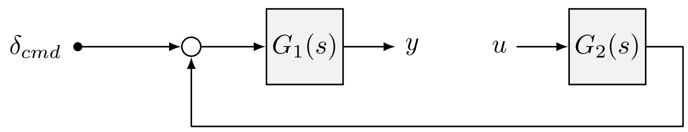

Figure 4.12.: Open loop G_{yu} for evaluation of OLOP criterion

responses intersect is called the onset frequency (ω_{onset}) and identifies the transition from linear to nonlinear system behavior. If in addition to the rate limit, a limit on the amplitude of the signal u is imposed (e.g. an actuator position limit), a further condition for transition from linear to nonlinear system behavior can be established:

$$|G_{u\delta_{cmd}}(s)\,(\delta_{cmd})_{max}| \stackrel{!}{=} (u)_{lim}\,. \tag{4.34}$$

In this case, the onset frequency (ω_{onset}) is determined by both conditions given by equations (4.33) and (4.34): the condition that is satisfied first (in terms of frequency) defines the ω_{onset}.

Once the onset frequency has been determined, the next step is to analyze the impact that rate limiter activation has on closed-loop stability. For this, the open-loop transfer function G_{yu} (figure 4.12) is evaluated at ω_{onset}. The resulting open-loop amplitude and phase at the onset frequency (the so-called OLOP parameter) can be visualized in the Nichols diagram. Figure 4.13 shows two exemplary locations of the OLOP parameter in the Nichols diagram (blue circles). In addition, the figure shows the effect of rate limiter activation at these locations. The arrows portrait qualitatively the increase in open-loop phase and the reduction in open-loop amplitude resulting from operation at the actuator's rate limits. Whilst in the case of $\omega 1_{onset}$, this leads to a significant increase in closed-loop amplitude and thus the frequency response is driven towards the critical point, the phase shift for $\omega 2_{onset}$ barely alters the closed-loop amplitude and therefore does not compromise the closed-loop stability. Hence the situation for $\omega 1_{onset}$ is more critical. From this example it can be seen that the location of the onset frequency in the Nichols chart determines how critical activation of a rate limit might be. Based on simulation studies, an OLOP boundary has been derived by Duda which separates non-critical areas of the Nichols chart (below the red line in figure 4.13) from

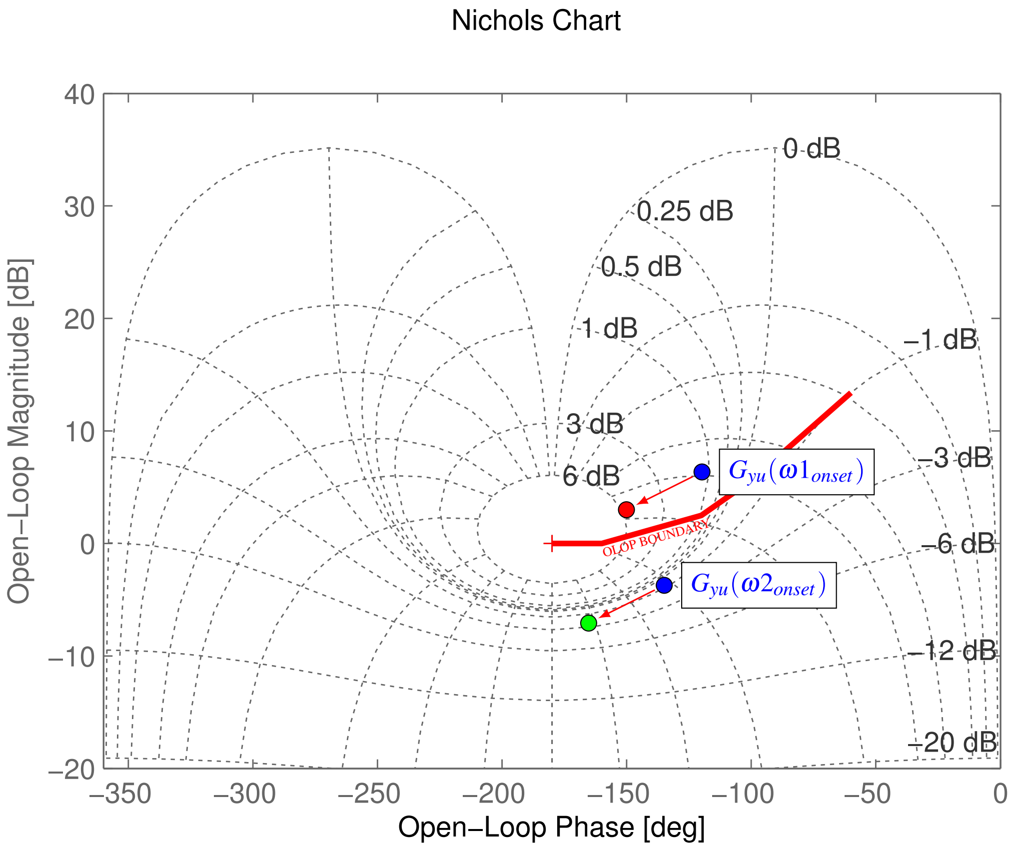

Figure 4.13.: Influence of rate saturation on stability (adopted from [66])

those in which the activation of nonlinearities has a negative impact on closed-loop stability. The application of the boundary enables evaluation of the vulnerability of the system to nonlinearities such as rate limits by analyzing the linear open-loop transfer function G_{yu} and without the need to derive a describing function. This simplifies enormously the analysis of the impact that nonlinear elements have on the control system.

The procedure described above for determination of closed-loop stability for when rate limiters are active can be extended to the analysis of pilot-vehicle systems. For this purpose, a pilot model consisting of a pure gain is introduced into the control loop. The amplification of the pilot is chosen such that a certain phase margin of ϕ_d is achieved at an open-loop magnitude of 0 dB by the pilot-vehicle system. In order to cover different pilot behavior, a range for ϕ_d is defined. When analyzing lateral motion, the range for the phase margin is $\phi_d = -135° \pm 25°$. After selecting the pilot gain, the open-loop G_{yu} (now consisting of the pilot and the controller-augmented plant) is once more evaluated at ω_{onset} w.r.t. the OLOP boundary. Finally, the PIO prediction from the OLOP analysis is validated by means of nonlinear time-domain simulation.

In summary, the OLOP method is a valuable extension of the PIO analysis, that, by means of linear analysis techniques and with little effort, provides a good insight into the reaction of the system to activation of actuator deflection rate or position limits. It is applicable to manned as well as to remotely piloted aircraft.

4.7. Application of requirements to SAGITTA Demonstrator

In the section above, the applicability of Flying Qualities requirements to RPAs has been discussed. From this, a comprehensive set of requirements relevant to the SAGITTA Demonstrator has been compiled, whereby the dynamic scalability is taken into account to derive requirement boundaries adjusted to the specifics of the SAGITTA system.

Due to the experimental nature of the system and because of the short mission duration, for all requirements that are related to Flying Qualities, a Level 2 rating is considered acceptable for flights operating in a failure free state. The failure free state is defined here by an actuator supply voltage of $V = 26\,\mathrm{V}$ and a feedback time delay of $t_d = 50\,\mathrm{ms}$ with aerodynamic uncertainties also being taken fully into account. To all other cases, including reduced actuator supply voltage and increased feedback time delays, the Flying Qualities requirements are not applicable. Nevertheless, in order to describe the specifics of these cases in some depth, they are analyzed and presented in chapter 6.

The stability requirements are some of the few mandatory requirements imposed on the SAGITTA Demonstrator's Flight Control System. As has been shown in the previous chapter, these requirements need to be evaluated for different flight conditions such as Level Flight, Pull-Up and Push-Over maneuvers. All further requirements, which are soft in their nature, and are thus considered "should" requirements, apply to Level Flight conditions only.

Stability requirements

Stability properties are evaluated in terms of so-called "bottleneck" cuts in the Nichols Chart, whereby the clearance matrix specified in table 4.3 applies to all operating points in Level Flight, Pull-Up and Push-Over maneuvers, thereby variations in actuator supply voltage, aerodynamic uncertainties and worst-case time delays in the feedback path have to be taken into account.

Damping, frequency and pole locations

The following requirements are assigned to the Dutch-roll:

$$\zeta_{DR,min} = 0.02, \quad (\omega_{0,DR})_{min} = 0.8\,\mathrm{rad\,s^{-1}}, \quad (\zeta_{DR}\omega_{0,DR})_{min} = 0.1315\,\mathrm{rad\,s^{-1}}. \quad (4.35)$$

For the calculation of $(\zeta_{DR}\omega_{0,DR})_{min}$, the expression $\omega_{0,DR}^2|\Phi/\beta|_{DR}$ is evaluated according to the note in table 4.6, thereby the inherent frequency of $\omega_{0,DR} = 5\,\mathrm{rad\,s^{-1}}$ and a $|\Phi/\beta|$ ratio of 1.5 are assumed.

The requirement on roll pole location is derived from the maximum roll time constant T_R and is

$$\lambda_{R,max} = -0.66\,\mathrm{rad\,s^{-1}}. \quad (4.36)$$

The spiral pole must reside in the left-hand complex plane, its exact location being determined by application of the attitude hold requirement.

$|\Phi/\beta|$ ratio

The closed-loop $|\Phi/\beta|$ ratio of the SAGITTA Demonstrator should be

$$|\Phi/\beta|_{max} = 1.5 \tag{4.37}$$

and remain throughout the envelope at or below the value of the corresponding ratio of the inherent plant.

Step response characteristics

The step response characteristics should comply with the attitude hold requirement described earlier and have a settling time of

$$t_{s,max} = 2.5\,\mathrm{s} \tag{4.38}$$

Note: The settling time specification should take into account the accuracy requirement, that is a part of the attitude hold requirement.

Coordination in steady banked turns

The requirement on coordination of sideslip and lateral accelerations applies to the CSAS of the SAGITTA Demonstrator.

Turbulence rejection requirements

The turbulence rejection requirements of the SAGITTA Demonstrator include the requirement on the maximum standard deviation of bank angle in turbulence, which is derived from the attitude hold requirement:

$$\sigma_{\Phi,max} = 10°. \tag{4.39}$$

Control margins associated with the reaction of control surfaces to turbulence constitute further requirements, which are represented by

$$\sigma_{\xi,max} = \frac{30°}{3} \qquad \sigma_{\dot{\xi},max} = \frac{100°}{3} \tag{4.40}$$

and

$$\sigma_{\zeta,max} = \frac{25°}{3} \qquad \sigma_{\dot{\zeta},max} = \frac{100°}{3}. \tag{4.41}$$

Noise rejection requirements

All control-margin increments resulting from noise that have been defined earlier apply to the SAGITTA Demonstrator.

Bandwidth

The bandwidth requirements for lateral motion are applicable to the SAGITTA Demonstrator. It is assumed for this purpose that the boundaries for ω_{BW} need to be scaled according to the dynamic scaling factor derived previously, though the boundaries for τ_p are not altered.

PIO characteristics

A PIO analysis should be demonstrated by means of the OLOP method.

4.8. Inherent Flying Qualities Evaluation

After specifying the relevant Flying Qualities requirements and related analysis methods, the study of Flying Qualities is concluded with an evaluation of the inherent dynamic characteristics.

Figure 4.14 shows the nominal characteristics for the configuration having a fuel mass of $m_{fuel} = 2.68$ [kg] and the relevant Level 1 Flying Qualities boundaries scaled by the factor $N = 2$ as determined by the dynamic scaling considerations covered in section 4.3. It can be seen, that the nominal inherent dynamics comply with the previously stated requirements w.r.t. the natural frequency of the Dutch-roll, as well as the roll pole's location. The Dutch-roll damping complies with the requirements in the upper regions of the speed envelope. At low speeds however, the boundary is violated and the damping falls below the line indicating the minimum damping for Level 1 Flying Qualities. Consequently, the flight controller has to increase the Dutch-roll's damping in order to make it comply with the specified requirement. The spiral pole is unstable in regions of the envelope corresponding to low speeds, but still exhibits acceptable time to double amplitude T_2. Nevertheless, since a bank angle AC/AH system with zero steady-state error is to be designed, the spiral mode must be stable for the entire envelope and thus needs to be adjusted using the control algorithm.

The lateral dynamics of the Demon aircraft from the FLAVIIR project [9] is also shown in figure 4.14 (denoted blue lines). The Demon is an aircraft which is particularly suitable for comparison with the SAGITTA Demonstrator, since it is of comparable size (wing span of 2 [m]) and weight (90 [kg]). Furthermore, its flight envelope closely matches the envelope of the SAGITTA Demonstrator. As with the SAGITTA Demonstrator, the Demon features a diamond-shaped wing, but in contrast to SAGITTA, the Demon aircraft has a pronounced fuselage that is expected to have a significant impact on lateral dynamics. The Dutch-roll frequency of the SAGITTA Demonstrator and the Dutch-roll frequency of the Demon are comparable at low speeds. As speed increases however, a deflection in the slope of the SAGITTA Demonstrator's Dutch-roll frequency can be clearly seen. The damping of the Dutch-roll of the SAGITTA Demonstrator is significantly lower than that of the Demon. The reason for this may be the effect of the Demon's pronounced fuselage and its larger vertical tail. The Demon has, due to its lower roll moment inertia, a significantly smaller roll time constant than the SAGITTA Demonstrator. The Demon's spiral mode is stable throughout the envelope, while the SAGITTA Demonstrator's spiral pole is unstable in the range of lower speeds.

The inherent $|\Phi/\beta|_{DR}$ ratio for the SAGITTA Demonstrator over the entire flight envelope and the corresponding requirement $|\Phi/\beta| \leq 1.5$ are depicted in figure 4.15. For much of the envelope the ratio complies with the requirement. At low speed, and consequently at high AoA the couplings become larger and increase in value as high as $|\Phi/\beta| = 2$ when the aircraft is operated at $m_{fuel} = 20.69$ [kg]. Although the inherent $|\Phi/\beta|_{DR}$ ratio is still moderate, it is desirable to reduce the couplings in order to improve the reaction to roll disturbances during lateral gusts. An increase in the phi-to-beta ratio as a result of implementing the Control and Stability Augmentation System (CSAS) should be avoided.

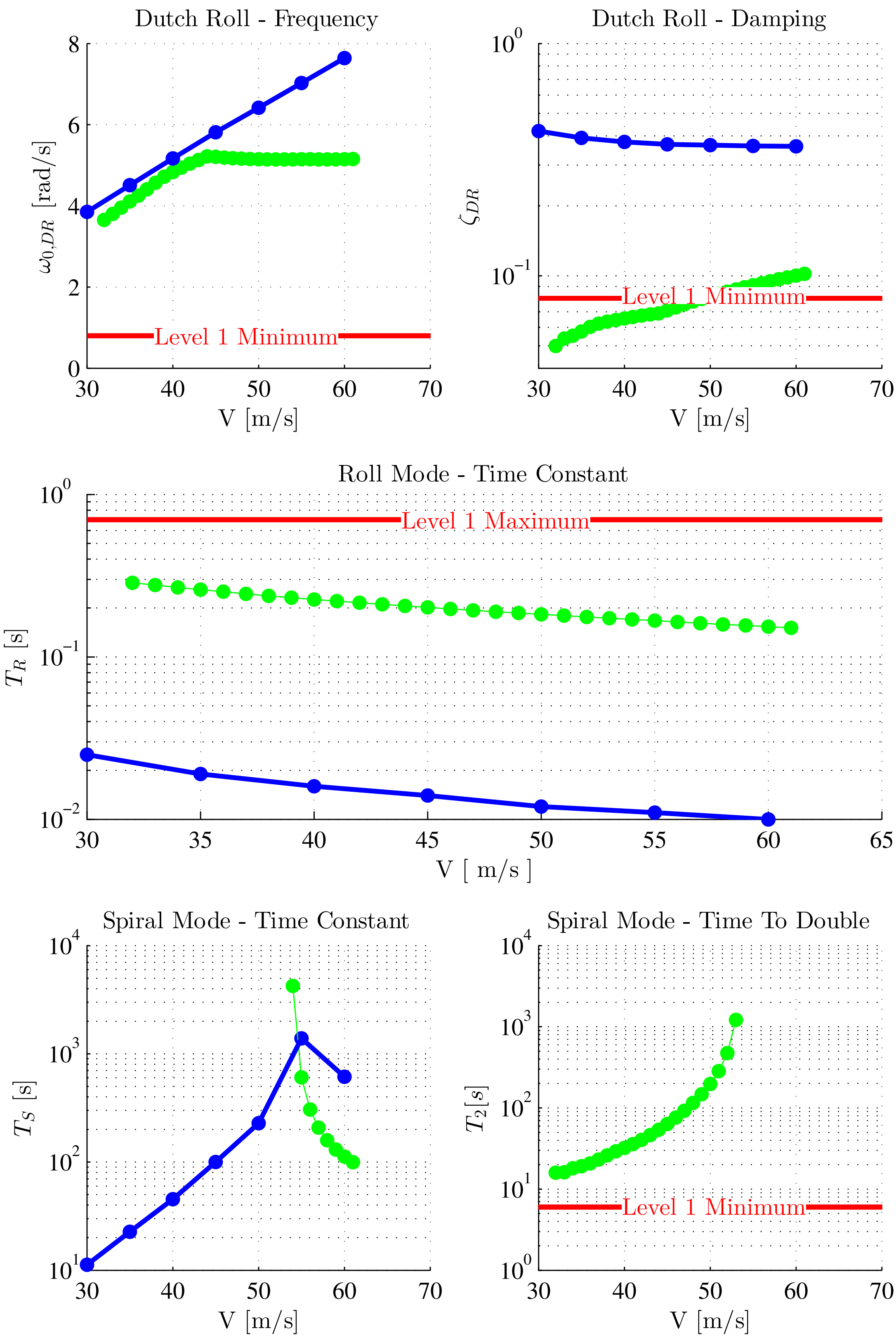

Figure 4.14.: Evaluation of lateral dynamics w.r.t. Flying Qualities: SAGITTA at $m_{fuel} = 3\,\mathrm{kg}$ (green) and Demon (blue)

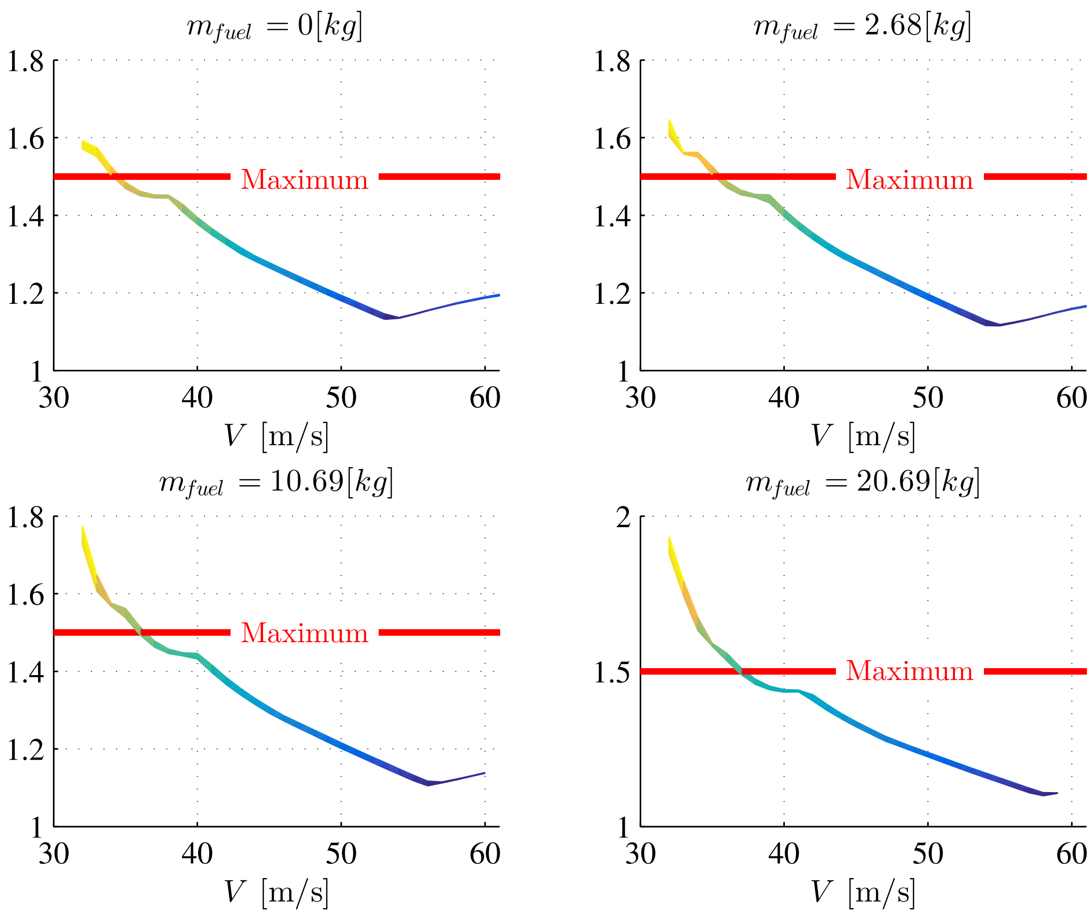

Figure 4.15.: Inherent $|\Phi/\beta|$ coupling with requirement boundary

Another interesting, and important, aspect of the aircraft dynamics is the effect of uncertainties on the system's pole locations. Figure 4.16 shows for the entire flight envelope, the locations of poles of the lateral motion of the SAGITTA Demonstrator when subject to aerodynamic uncertainties. To produce this diagram, thirty random samples are taken from each uncertain state-space model describing the lateral aircraft dynamics at a particular operating point and plotted into the pole-zero map. The colors in the plot indicate the density of the poles in a certain area: a bright color signifies few poles, while a dark color signifies a dense population in a given area. The figure shows variations in the location of the roll pole between $\lambda_R = 2$ and 10, with most of the samples concentrated around $\lambda_R = 4$. The spiral pole varies between being stable and unstable. The Dutch-roll is stable in most cases, but also some uncertainty combinations exist which may drive the inherent Dutch-roll into instability. Since an unstable Dutch-roll must be avoided at all costs, special attention must be paid to ensure that the closed-loop system is always stable - even when uncertainties are present.

In this chapter the requirements on the lateral CSAS of the SAGITTA Demonstrator have been presented. In order to evaluate the Flying Qualities of the SAGITTA Demonstrator, the approach of dynamic scaling the Flying Qualities boundaries was investigated and applied. Additionally, an extensive study of the lateral Flying Qualities of manned aircraft, and their applicability to unmanned aircraft with an AC/AH response type, has been performed. In contrast to other publications in this field, this study takes into account not only the well-known de facto standards for fixed-wing aircraft, but also standards for rotorcraft as well as less well-known publications. The study is completed

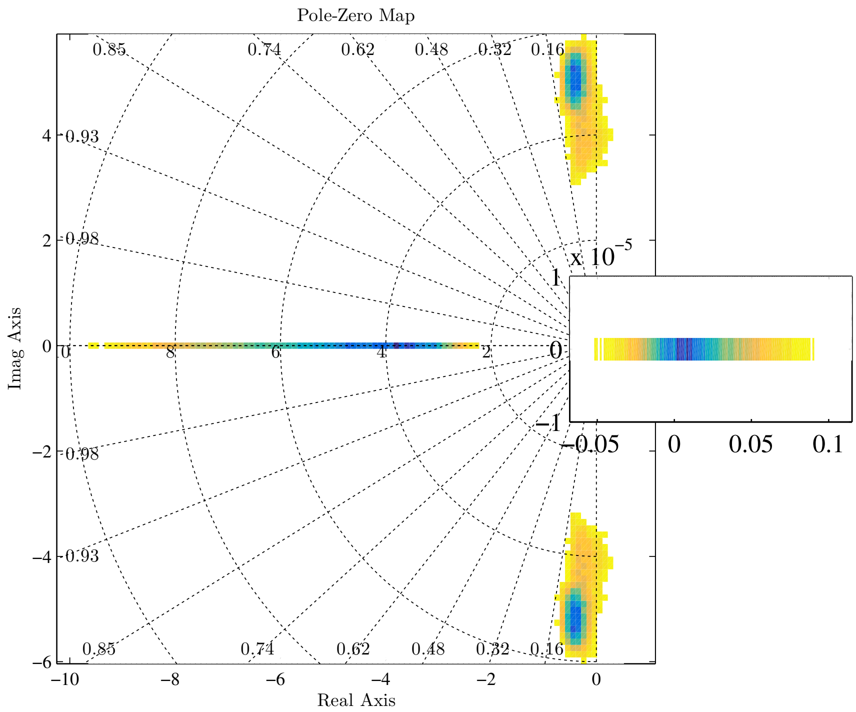

Figure 4.16.: Effect of uncertainties on the inherent lateral dynamics

by description of the OLOP method for analysis of the aircraft's susceptibility to PIOs. The study on Flying Qualities resulted in a number of methods which will be used for validation of the Flight Control System of the SAGITTA Demonstrator. This chapter concludes with an initial evaluation of the inherent lateral dynamics of the SAGITTA Demonstrator w.r.t. stability requirements and applicable Flying Qualities measures.

5. Controller Design

Before starting the design of a control system for a new aircraft, it is crucial to perform an in-depth analysis of the inherent aircraft dynamics, to determine its system constraints and to get an idea of the major challenges in control design. The major challenges of the present configuration arise from the large uncertainties in the dynamics; the novel control surface design with significant cross-axis couplings; and also the poor quality of sensor measurements, which creates serious limitations on their usability in feedback design. These considerations turn out to be the driving factors in controller design. In order to develop a suitable solution for the first flight, four different architectures have been developed. They are characterized as follows:

Version 1 Full output feedback design with full decoupling of roll and yaw motion ($|\Phi/\beta| = 0$)

Version 2 Full output feedback design with reduced decoupling of roll and yaw motion ($|\Phi/\beta| \leq 1.5$)

Version 3 Output feedback design with planned coupling of roll and yaw motion of $|\Phi/\beta| \leq 1.5$ and suppressed integrator cross feed gains $k_{I\dot{p}\beta}$ and $k_{I\dot{r}\Phi}$

Version 4 Output feedback design with decoupling of roll and yaw motion of $|\Phi/\beta| \leq 1.5$ without utilization of AoS feedback

The process of controller design for the lateral motion of the SAGITTA Demonstrator is outlined. It describes the architecture selection, subsequent analyses and modifications resulting from this analyses, and presents the principles that underpin the design decisions. The stepwise assembly of the controller (consisting of control allocation, rate and attitude feedback, and feed-forward design) is also described, and possibilities for extension of the controller are proposed for consideration in future project phases.

5.1. Control Allocation

In chapter 3, a control assignment scheme is introduced which provides a correlation of equivalent surface commands to physical control surfaces. This reduces the number of control inputs and provides comparability with conventional aircraft, and thereby, simplifies the analysis of the inherent dynamic properties of the aircraft. The control mechanization is based on the steering of conventional unaugmented aircraft. It provides commands that mimic aileron and rudder and is sometimes referred to as "Explicit Ganging".

Besides Explicit Ganging, many other approaches to control allocation have been developed in recent years. Most of the approaches involve mixing of control effectors of over-actuated systems in order to achieve a commanded moment that is optimal in a given sense (e.g. minimum deflections or minimum resulting control error) accomplishing this by simultaneously taking system limitations (e.g. deflection limits) into account.

In this regard, the aim of the control allocation is often to maximize the Attainable Moment Subset (AMS).

In this application, the control assignment scheme, and thus the clustering of control effectors has already been established in earlier design steps. The remaining degree of freedom available to the designer is the distribution of the commands from the controller to the equivalent control surfaces. These commands are often referred to as pseudo controls and are typically related to moments or angular accelerations. The pseudo controls constitute the interface between the control law and the control allocation. Carefully selected pseudo controls and the corresponding control allocation can greatly reduce cross-axis couplings and thereby simplify significantly the controller structure. By selecting physically meaningful pseudo controls, a deeper physical insight into the control algorithm can be obtained. Several possible approaches to this exist. One straight-forward solution is to align the pseudo controls with the moments around the body axes of the aircraft. This can be done, for example, by inverting the matrix $\boldsymbol{B}_{MOM}$ representing the control effectiveness of the aircraft w.r.t. body axes moments. For the lateral-directional motion (and hence the equivalent control surface deflection ξ, ζ and corresponding roll and yaw moments L, N) the resulting matrix is

$$\boldsymbol{B}_{MOM} = \begin{bmatrix} L_\xi & L_\zeta \\ N_\xi & N_\zeta \end{bmatrix}. \tag{5.1}$$

When the state-space model does not incorporate actuator dynamics, $\boldsymbol{B}_{MOM}$ is formed from entries of the input matrix $\boldsymbol{B}$. In cases, where the actuator dynamics is part of the state-space model, the corresponding entries of $\boldsymbol{B}_{MOM}$ can be found in the system matrix $\boldsymbol{A}$.

The control allocation matrix $\boldsymbol{F}$ is obtained from $\boldsymbol{B}_{MOM}$ as follows:

$$\boldsymbol{F} = \boldsymbol{B}_{MOM}{}^{-1} = \begin{bmatrix} k_{\xi_{cmd}\dot{p}_{cmd}} & k_{\xi_{cmd}\dot{r}_{cmd}} \\ k_{\zeta_{cmd}\dot{p}_{cmd}} & k_{\zeta_{cmd}\dot{r}_{cmd}} \end{bmatrix}, \tag{5.2}$$

Application of the control allocation matrix $\boldsymbol{F}$ to the input matrix $\boldsymbol{B}$ results in the following effective control input matrix w.r.t. the body axes moments:

$$\boldsymbol{B}_{eff} = \begin{bmatrix} L_\xi & L_\zeta \\ N_\xi & N_\zeta \end{bmatrix} \begin{bmatrix} G_{\xi\xi_{cmd}}(0) & 0 \\ 0 & G_{\zeta\zeta_{cmd}}(0) \end{bmatrix} \begin{bmatrix} k_{\xi_{cmd}\dot{p}_{cmd}} & k_{\xi_{cmd}\dot{r}_{cmd}} \\ k_{\zeta_{cmd}\dot{p}_{cmd}} & k_{\zeta_{cmd}\dot{r}_{cmd}} \end{bmatrix} = \begin{bmatrix} 1 & 0 \\ 0 & 1 \end{bmatrix} \tag{5.3}$$

where $G_{\xi\xi_{cmd}}(0)$ and $G_{\zeta\zeta_{cmd}}(0)$ represent the DC-gains (steady-state amplification) of the respective actuator including the surface command-to-actuator and actuator-to-surface deflection transmission ratios. The DC-gains are assumed to be unity. The control allocation described here leads to normalization and alignment of the input directions with the body axes moments. The related pseudo controls can be interpreted as angular acceleration commands $\dot{p}_{B_{cmd}}$ and $\dot{r}_{B_{cmd}}$, where the subscript B denotes the body coordinate system.

The advantage of aligning the pseudo inputs with body axes moments lies in the ease of interpretation of such inputs. But, in terms of flight physics, the initiation of a rotation by means of a pure roll around the body axes is not efficient. A turn by means of a pure roll around the x-axis of the body at AoA $\neq 0$ due to kinematic coupling leads to an exchange between AoA and AoS, such that for the extreme situation of $\Phi = 90°$ the AoA is completely migrated into an adverse AoS and the AoA becomes zero. In this way the Dutch-roll is excited and a yawing moment is introduced by the effect of $C_{n\beta}\beta$. At the same time, the AoA must be reestablished and increased in order to maintain altitude during the turn. This is why aircraft that are operating at high AoAs often perform the so-called velocity vector roll in order to initiate turns. That is, the aircraft is rotated around its current velocity vector so that the AoA is not altered and the AoS is kept near zero.

A velocity vector roll can be performed either by coordinated mixing of body-axes pseudo controls $\dot{p}_{B_{cmd}}$ and $\dot{r}_{B_{cmd}}$ or by implementation of a control allocation that provides pseudo controls, where one input is aligned with the velocity vector. When implementing a velocity vector roll, assuming steady-state aerodynamic speed and non changing AoA during the maneuver, the velocity vector can be assumed to coincide with the x-axis of the stability-axes coordinate system (S). With this assumption, the actual AoA in the transformation from body to velocity roll is replaced by the angle of attack α_0 at the particular trim point, this being a function of the measured impact pressure. Hence, for the approximate velocity vector roll, the pseudo controls can be aligned with the stability axes of the aircraft ($\dot{p}_S$ and $\dot{r}_S$). In order to accomplish this, the control allocation with respect to body axes can be extended by the transformation matrix between body and stability coordinate systems $\boldsymbol{M}_{BS}$ according to equation (5.4).

$$\boldsymbol{F}_S = \boldsymbol{B}_{MOM}{}^{-1}\boldsymbol{M}_{BS} = \begin{bmatrix} k_{\xi_{cmd}\dot{p}_{S_{cmd}}} & k_{\xi_{cmd}\dot{r}_{S_{cmd}}} \\ k_{\zeta_{cmd}\dot{p}_{S_{cmd}}} & k_{\zeta_{cmd}\dot{r}_{S_{cmd}}} \end{bmatrix} \tag{5.4}$$

Apart from its advantages, it should be noted that the velocity vector or stability-axes roll stimulates the effect of inertia coupling, and thereby injects an additional moment into the longitudinal motion. This might lead to pitch departure, which is especially a problem for agile fighter configurations in rapid rolling maneuvers [86]. Such couplings can be taken into account by explicit introduction of a nonlinear compensation term into the controller structure. Alternatively, as here, inertia coupling is treated as a disturbance and is handled by the feedback controller.

Lallman introduced the idea of pseudo controls in [44]. His initial idea was, to align pseudo control inputs to particular dynamic modes of the aircraft. With the aid of state transformation of the plant dynamics using the following relation

$$\boldsymbol{x} = \boldsymbol{V}\tilde{\boldsymbol{x}} \tag{5.5}$$

with $\boldsymbol{V}$ being the eigenvector matrix, he obtained the state space representation in the modal form as given in equation (5.6)

$$\dot{\tilde{\boldsymbol{x}}} = \boldsymbol{V}^{-1}\boldsymbol{A}\boldsymbol{V}\tilde{\boldsymbol{x}} + \boldsymbol{V}^{-1}\boldsymbol{B}\boldsymbol{u} = \boldsymbol{\Lambda}\tilde{\boldsymbol{x}} + \boldsymbol{\Gamma}\boldsymbol{u} \tag{5.6}$$

with $\boldsymbol{\Lambda}$ having a block-diagonal form and $\boldsymbol{\Gamma}$ being the modal input matrix representing the influence of the system inputs to the particular modes. For derivation of the control allocation matrix $\boldsymbol{F}$ optimization is used in [44]. The following cost function penalizes the excitation of non-desired (ND) modes and rewards excitation of desired (D) modes by a particular pseudo input ν_j:

$$J = \boldsymbol{f}_j^T \sum_D \gamma_i \gamma_i^T \boldsymbol{f}_j - \boldsymbol{f}_j^T \sum_{ND} \gamma_i \gamma_i^T \boldsymbol{f}_j \tag{5.7}$$

with $\boldsymbol{\gamma}_i^T$ being the i-th row of $\boldsymbol{\Gamma}$ and $\boldsymbol{f}_j$ being the control allocation for the pseudo input ν_j. By maximizing the cost function a control allocation matrix $\boldsymbol{F}$ can be derived, where, for example, the first pseudo input ν_1 is assigned to control of roll and spiral modes, while the second ν_2 is mainly used for control of the Dutch-roll.

In order to evaluate this approach, it is applied to the lateral-directional motion of the SAGITTA Demonstrator. The pseudo controls are selected in such a way that one

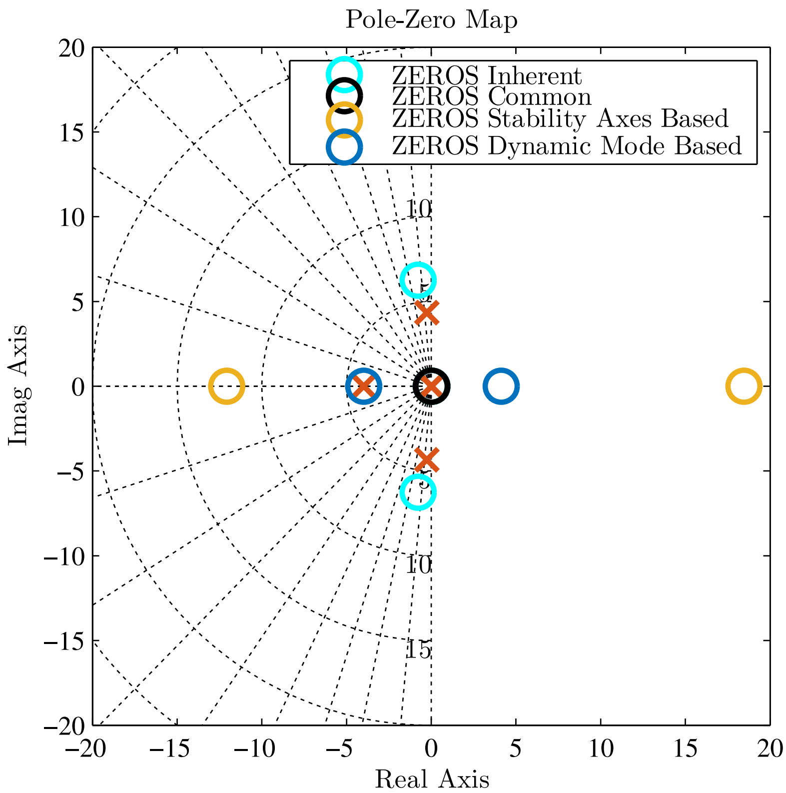

Figure 5.1.: Example Pole-Zero Map resulting from different control allocation approaches

of these contributes mainly to the roll (R) mode and does not excite the Dutch-roll, while the other is allocated to the Dutch-roll (DR) and does not influence the roll mode. Figure 5.1 shows the comparison of dynamic-mode-based control allocation with the previously introduced stability axes control allocation in terms of poles and zeros of the corresponding transfer functions. This figure shows the poles (indicated by red crosses) and the zeros of the transfer function $G_{p\dot{r}_{S_{cmd}}}$ (labeled as zeros stability-axes-based) resulting from application of stability-axes-based control allocation, and the poles and zeros of $G_{pDR_{cmd}}$ (labeled as zeros dynamic-mode-based) showing the influence of the Dutch-roll pseudo input (DR) on roll rate resulting from dynamic-mode-based control allocation. In addition, the zeros of the inherent plant's transfer function $G_{p\zeta}$ (labeled as zeros inherent) are plotted for comparison. Furthermore, zeros that are common to all transfer functions are indicated by black circles. One can see the effect of dynamic-mode-based control allocation, which is moving the open-loop zeros towards the poles that should not be excited and away from those that should be controlled by the particular pseudo input. In the present case, since pseudo input related to Dutch-roll is considered, the control allocation is selected such that one of the open loop zeros almost exactly cancels the roll pole. The main advantage of this approach is in the decoupling of inputs w.r.t. the dynamic modes. This enables independent and isolated control design for particular modes.

The pseudo control strategy has been developed further by Sobel and Lallman in [83], whereby singular value decomposition of the input matrix is used for determination of main input directions, and the small singular values are then discarded. With this procedure, inputs that have only a small influence on the dynamics of the system are not used in the controller design. In this way, the resulting feedback gains can be reduced

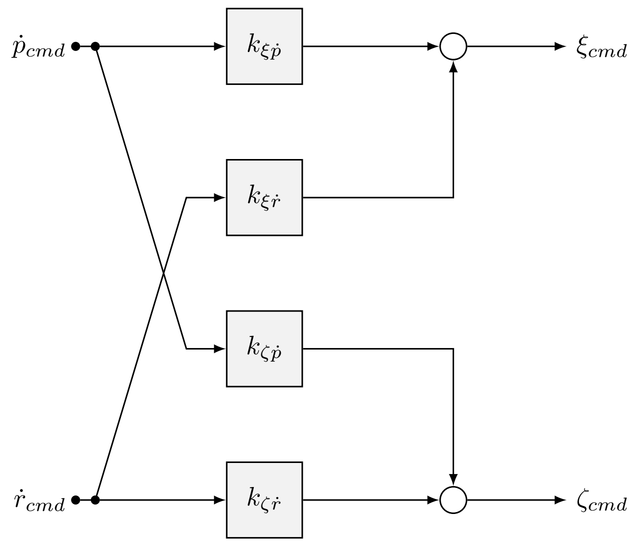

Figure 5.2.: Block diagram showing the Control Allocation

significantly [81]. For over-actuated systems this is a viable approach. In the case at hand, however, having reduced the input dimensions by the previously introduced explicit ganging, the approach is no longer applicable due to the lack of redundancy in the inputs.

The approach for control allocation adopted here is the one with pseudo controls aligned with the stability coordinate system's x and z-axes, whereby the entries of the control allocation are adjusted during the flight based on the current flight condition using measurements of the impact pressure. The resulting block diagram is shown in figure 5.2.

5.2. Introduction to Eigenstructure Assignment

The lateral motion of an aircraft represents a typical problem of Multiple Input Multiple Output (MIMO) controller design. In recent decades many methods have been proposed to solve this problem. A large number of publications exist which explore the application of optimization based control. In [86], Stevens and Lewis apply in the Linear-Quadratic regulator (LQR) method using output feedback to the lateral dynamics of the F-16 aircraft. A Linear-Quadratic-Gaussian (LQG) based design of a turn coordinator control system can be found in [45]. Further approaches consider the optimization of the H_2 and H_∞ norms and their combinations. A design method that is not based on optimization and which is widely used for control of MIMO systems is Eigenstructure Assignment (EA) which makes it possible to explicitly shape the eigenvalues and eigenvectors of the closed-loop system. The present work focuses on this design method. A summary of the historical development of Eigenstructure Assignment can be found in [46]. For a comprehensive overview of the alternative methods and their application to aircraft control the reader is referred to [71].

Use of Eigenstructure Assignment in the work at hand is mainly motivated by the valuable physical insight, that the method provides to the control designer. The strength of the methodology lies in the possibility to incorporate a great number of flight dynamics requirements into the design process. Since many flying qualities requirements are formulated in the frequency domain, and are often related to particular aircraft modes, a design methodology which provides direct control over the closed-loop pole locations and eigenvector characteristics is preferable to designs using LQR or H_∞, where the locations of the poles can be specified only implicitly. The drawback of an EA based approach, however, is that the resultant designs are often vulnerable to uncertainties and, in case of partial EA, may even lead to unstable closed-loop systems. The selection of the desired eigenvalues and eigenvectors requires a good understanding of the plant characteristics. Inconsistent or unachievable specifications may result in large controller gains. The application of Eigenstructure Assignment in a preliminary study related to the SAGITTA Demonstrator [7] has shown promising results. A brief summary of the standard EA using output feedback is given below. The standard EA is complemented by a Constrained Eigenstructure Assignment (CEA) that is based on the work of Shapiro and Andry (see [2, 77]).

Starting from the linear state-space model in equation (5.8)

$$\begin{aligned} \dot{\boldsymbol{x}} &= \boldsymbol{A}\boldsymbol{x} + \boldsymbol{B}\boldsymbol{u} \\ \boldsymbol{y} &= \boldsymbol{C}\boldsymbol{x} + \boldsymbol{D}\boldsymbol{u}, \end{aligned} \tag{5.8}$$

with $\boldsymbol{x} \in \mathbb{R}^n$, $\boldsymbol{y} \in \mathbb{R}^r$ and $\boldsymbol{u} \in \mathbb{R}^m$ the definition of the eigenvalue λ_i and corresponding eigenvector $\boldsymbol{v}_i$ is given by equation (5.9)

$$\boldsymbol{A}\boldsymbol{v}_i = \lambda_i \boldsymbol{v}_i \tag{5.9}$$

which after reordering leads to

$$[\lambda_i \boldsymbol{I} - \boldsymbol{A}]\, \boldsymbol{v}_i = \boldsymbol{0}, \tag{5.10}$$

where $\boldsymbol{I}$, is a unity matrix. The control law for the output feedback is described by

$$\boldsymbol{u} = -\boldsymbol{K}\boldsymbol{y}, \tag{5.11}$$

where $\boldsymbol{K}$ represents the feedback matrix and $\boldsymbol{y}$ the output vector of the system. By assuming the feed-through matrix of the system to be zero ($\boldsymbol{D} = 0$), and by inserting the expression for the output feedback into the state equation in equation (5.8), the closed-loop system matrix $\tilde{\boldsymbol{A}}$ can be written as

$$\tilde{\boldsymbol{A}} = \boldsymbol{A} - \boldsymbol{B}\boldsymbol{K}\boldsymbol{C}. \tag{5.12}$$

and the expression in equation (5.10) for the closed-loop system becomes

$$\left[\tilde{\lambda}_i \boldsymbol{I} - \boldsymbol{A} + \boldsymbol{B}\boldsymbol{K}\boldsymbol{C}\right] \tilde{\boldsymbol{v}}_i = \boldsymbol{0}. \tag{5.13}$$

with $\tilde{\lambda}_i$ being the closed-loop eigenvalue and $\tilde{\boldsymbol{v}}_i$ the closed-loop eigenvector. This equation can be reordered as follows

$$\begin{bmatrix} \tilde{\lambda}_i \boldsymbol{I} - \boldsymbol{A} & \boldsymbol{B} \end{bmatrix} \begin{bmatrix} \tilde{\boldsymbol{v}}_i \\ \tilde{\boldsymbol{w}}_i \end{bmatrix} = \boldsymbol{0} \tag{5.14}$$

with

$$\tilde{\boldsymbol{w}}_i = \boldsymbol{K}\boldsymbol{C}\tilde{\boldsymbol{v}}_i. \tag{5.15}$$

Equation (5.14) is the basic equation for eigenstructure assignment. In order to fulfill this equation the vector $\begin{bmatrix} \tilde{\boldsymbol{v}}_i & \tilde{\boldsymbol{w}}_i \end{bmatrix}^T$ must reside in the null space of $\begin{bmatrix} \tilde{\lambda}_i \boldsymbol{I} - \boldsymbol{A} & \boldsymbol{B} \end{bmatrix}$. Therefore, the following must be true:

$$\begin{bmatrix} \tilde{\boldsymbol{v}}_i \\ \tilde{\boldsymbol{w}}_i \end{bmatrix} \in \operatorname{Ker}\left(\begin{bmatrix} \tilde{\lambda}_i \boldsymbol{I} - \boldsymbol{A} & \boldsymbol{B} \end{bmatrix}\right). \tag{5.16}$$

Thus, for particular $\tilde{\lambda}_i$ the achievable closed-loop eigenvector $\tilde{\boldsymbol{v}}_i$ satisfies the following equation

$$\begin{bmatrix} \tilde{\boldsymbol{v}}_i \\ \tilde{\boldsymbol{w}}_i \end{bmatrix} = \bar{\boldsymbol{N}}_i \boldsymbol{l}_i, \tag{5.17}$$

where $\bar{\boldsymbol{N}}_i$ is a matrix consisting of base vectors $\bar{\boldsymbol{n}}_1, ..., \bar{\boldsymbol{n}}_m$ that span the kernel of $\begin{bmatrix} \tilde{\lambda}_i \boldsymbol{I} - \boldsymbol{A} & \boldsymbol{B} \end{bmatrix}$ and $\boldsymbol{l}_i \in \mathbb{C}$ is a scaling vector.

The matrix $\bar{\boldsymbol{N}}_i$ can be separated further into the basis that is related to the eigenvector $\tilde{\boldsymbol{v}}_i$ and a basis that is related to the input direction $\tilde{\boldsymbol{w}}_i$ as follows

$$\bar{\boldsymbol{N}}_{\boldsymbol{i}} = \begin{bmatrix} \boldsymbol{N}_i \\ \hat{\boldsymbol{N}}_i \end{bmatrix} = \begin{bmatrix} \boldsymbol{n}_1 & ... & \boldsymbol{n}_m \\ \hat{\boldsymbol{n}}_1 & ... & \hat{\boldsymbol{n}}_m \end{bmatrix} \tag{5.18}$$

and consequently equation (5.17) can be expanded to

$$\begin{bmatrix} \tilde{\boldsymbol{v}}_i \\ \tilde{\boldsymbol{w}}_i \end{bmatrix} = \begin{bmatrix} \boldsymbol{N}_i \\ \hat{\boldsymbol{N}}_i \end{bmatrix} \boldsymbol{l}_i. \tag{5.19}$$

Since in most cases the designer is only interested in specifying of some entries of the eigenvectors, each desired closed-loop eigenvector $(\tilde{\boldsymbol{v}}_i)_{des}$ can be defined in terms of specified entries $(\tilde{\boldsymbol{v}}_i^s)_{des}$ and unspecified entries $(\tilde{\boldsymbol{v}}_i^u)_{des}$ and can be reordered using a reordering matrix $\boldsymbol{P}_i$ according to:

$$\begin{bmatrix} (\tilde{\boldsymbol{v}}_i^s)_{des} \\ (\tilde{\boldsymbol{v}}_i^u)_{des} \end{bmatrix} = \boldsymbol{P}_i \left(\tilde{\boldsymbol{v}}_i\right)_{des} = \begin{bmatrix} \boldsymbol{P}_i^s \\ \boldsymbol{P}_i^u \end{bmatrix} \left(\tilde{\boldsymbol{v}}_i\right)_{des}. \tag{5.20}$$

which leads to the following expression for the specified elements of the desired closed-loop eigenvector:

$$(\tilde{\boldsymbol{v}}_i^s)_{des} = \boldsymbol{P}_i^s \boldsymbol{N}_i \boldsymbol{l}_i = \boldsymbol{N}_i^s \boldsymbol{l}_i. \tag{5.21}$$

When the number of specified elements (s) equals the number of system inputs (m), the scaling vector can be calculated as

$$\boldsymbol{l}_i = \left(\boldsymbol{N}_i^s\right)^{-1} \left(\tilde{\boldsymbol{v}}_i^s\right)_{des}. \tag{5.22}$$

and with the resulting $\boldsymbol{l}_i$, the achievable closed-loop eigenvector is

$$(\tilde{\boldsymbol{v}}_i^s)_{ach} = \left(\boldsymbol{N}_i^s\right) \boldsymbol{l}_i. \tag{5.23}$$

In this case, the achievable eigenvector $(\tilde{\boldsymbol{v}}_i^s)_{ach}$ equals the desired one. When $s > m$, $\boldsymbol{l}_i$ is calculated as follows:

$$\boldsymbol{l}_i = \left(\boldsymbol{N}_i^s\right)^{+} \left(\tilde{\boldsymbol{v}}_i^s\right)_{des}. \tag{5.24}$$

Here, $(\boldsymbol{N}_i^s)^+$ is the Moore-Penrose pseudo inverse of $\boldsymbol{N}_i^s$. In this case, the achievable eigenvector is a projection of the desired one into the null space $\boldsymbol{N}_i^s$.

Once the scaling vectors, and hence the achievable vectors $\tilde{\boldsymbol{v}}_i$ and $\tilde{\boldsymbol{w}}_i$ for $i = 1, .., r$ have been found, the feedback matrix $\boldsymbol{K}$ can be calculated from equation (5.15), resulting in

$$\boldsymbol{K} = \tilde{\boldsymbol{W}}(\boldsymbol{C}\tilde{\boldsymbol{V}})^{-1}, \tag{5.25}$$

where $\tilde{\boldsymbol{V}}$ and $\tilde{\boldsymbol{W}}$, shown in equation (5.26) are the matrices that are comprised of achievable closed-loop eigenvectors and the input direction vectors respectively, and which correspond to r desired eigenvalues, where r is the number of outputs used for feedback. The resultant feedback matrix $\boldsymbol{K}$ is fully populated.

$$\tilde{\boldsymbol{V}} = \begin{bmatrix} (\tilde{\boldsymbol{v}}_1)_{ach} & ... & (\tilde{\boldsymbol{v}}_r)_{ach} \end{bmatrix} \quad ; \quad \tilde{\boldsymbol{W}} = \begin{bmatrix} (\tilde{\boldsymbol{w}}_1)_{ach} & ... & (\tilde{\boldsymbol{w}}_r)_{ach} \end{bmatrix} \tag{5.26}$$

An effective and very useful extensions of the EA is the Constrained Eigenstructure Assignment (CEA). The CEA enables the designer to suppress undesired entries of the feedback matrix $\boldsymbol{K}$ and consequently to introduce structural constraints into the feedback design. The extension of EA is briefly presented below. For convenience, the matrix multiplication $\boldsymbol{CV}$ in equation (5.25) is renamed

$$\boldsymbol{\Omega} = \boldsymbol{CV} \tag{5.27}$$

and the input direction matrix $\boldsymbol{W}$ as well as the feedback matrix $\boldsymbol{K}$ are divided into particular rows

$$\boldsymbol{W} = \begin{bmatrix} \boldsymbol{w}_1^T \\ \vdots \\ \boldsymbol{w}_m^T \end{bmatrix} \qquad \boldsymbol{K} = \begin{bmatrix} \boldsymbol{k}_1^T \\ \vdots \\ \boldsymbol{k}_m^T \end{bmatrix}. \tag{5.28}$$

By introduction of the Kronecker multiplication $\otimes$, the expression in equation (5.25) can be split into m separate equations as follows:

$$\begin{bmatrix} \boldsymbol{k}_1^T \\ \vdots \\ \boldsymbol{k}_m^T \end{bmatrix} = \begin{bmatrix} \boldsymbol{w}_1^T \\ \vdots \\ \boldsymbol{w}_m^T \end{bmatrix} \left[\boldsymbol{I}_m \otimes \boldsymbol{\Omega}^{-1} \right] \tag{5.29}$$

Now, if the designer requires the feedback gain k_{ij} to be suppressed, (i.e.) the entry standing in i-th row and j-th column of the feedback matrix, he needs to consider the i-th row in equation (5.29):

$$\boldsymbol{k}_i^T = \boldsymbol{w}_i^T \boldsymbol{\Omega}^{-1}. \tag{5.30}$$

Here, the j-th row of $\boldsymbol{\Omega}$ is removed in order to yield $\hat{\boldsymbol{\Omega}}$. Since as a result, the matrix $\hat{\boldsymbol{\Omega}}$ becomes non-square, the pseudo-inverse $\hat{\boldsymbol{\Omega}}^+$ is used to calculate the remaining entries of the i-th row of $\boldsymbol{K}$ according to:

$$\hat{\boldsymbol{k}}_i^T = \boldsymbol{w}_i^T \hat{\boldsymbol{\Omega}}^+, \tag{5.31}$$

where $\hat{\boldsymbol{\Omega}}$ is the matrix $\boldsymbol{\Omega}$ reduced by the j-th row, and $\hat{\boldsymbol{k}}_i^T$ is a $1 \times (r - c)$ row vector with c being the number of suppressed elements in the i-th row of $\boldsymbol{K}$. For the case of suppressing a single entry k_{ij}, $c = 1$. The procedure of calculating $\hat{\boldsymbol{k}}_i^T$ is applied to all rows of the feedback matrix. The resulting rows $\hat{\boldsymbol{k}}_i^T$ are complemented by zeros in the corresponding columns j that were suppressed. Subsequently, these rows $\hat{\boldsymbol{k}}_i^T$ are stacked to form the feedback matrix $\boldsymbol{K}$. The result is a feedback matrix with a predefined structure which, if the entries to be suppressed are selected appropriately, provides approximately the desired closed-loop eigenstructure. In what follows, the appropriate selection of gains to be suppressed is investigated, thereby the structure of the feedback is indicated by $*$ and 0 in the matrix $\boldsymbol{K}$. Asterisks ($*$) indicate feedback entries that are determined by the CEA algorithm, while zeros (0) indicate suppressed entries.

5.3. Initial Controller Design: *V1*

One of the first and most important steps in controller design is the selection of sensor measurements for feedback. The selection is typically driven by multiple aspects like availability, characteristics and reliability of sensor signals as well as by its necessity or meaning for a particular controller functionality. Each sensor system used in the controller introduces new failure conditions that need to be taken into account and may introduce unnecessary complexity into the system. It is therefore extremely important to explore carefully the available sensor measurements, not only in terms of their meaning for the control algorithm, but also w.r.t. aspects of systems engineering. Table 5.1 shows the main sensor measurements of the NAV and ADS of the SAGITTA Demonstrator.

Source	**Variable**	**Description**
NAV	p, q, r	rotation rates in body axes
	f_x, f_y, f_z	specific forces in body axes
	Φ, Θ, Ψ	attitude in Euler angles
	$(u_K, v_K, w_K)_{NED}$	kinematic velocity in NED coordinate system
	$(\lambda, \mu, h)_{WGS84}$	position in WGS84 coordinate system
ADS	$p_s, p_t - p_s \approx \bar{q}$	static and impact pressure
	α, β_F	angle of attack and flank angle

Table 5.1.: Available Sensor Measurements

As described in chapter 2, the NAV includes an IMU and a DGPS receiver. The measurements provided by these two elements differ w.r.t. their availability. The sensor measurements from accelerometers and gyroscopes, as well as derived quantities such as attitude angles, are assumed to have a high availability. The reception of the GNSS service depends on the number of visible satellites, which in turn depends on aircraft location and orientation as well as the time of day. Further effects like multi-path or atmospheric disturbances can negatively influence the quality of GNSS reception. Hence, compared to signals described previously, measurements provided by the DGPS module are expected to have a lower availability. Thus, position and kinematic velocity information from the GNSS are expected to be temporarily unavailable during some periods of the flight mission, and consequently these sensor measurements are omitted in further CSAS design.

The ADS is one of the basic sensor systems of an aircraft. Since the flight dynamics characteristics depend on dynamic pressure to a significant extent, its use is indispensable for a sound CSAS design. For example, it is expected, that the impact pressure measurement $(p_t - p_s)$ will be required for scheduling of the gains over the flight envelope. In addition, in the first iteration of controller design, the measurement of AoS are considered as feasible feedback variables. In line with considerations on sensor measurements, the feedbacks of p, r, Φ and β are used for the design of the controller.

A controller can typically be divided into feedback and feed-forward paths. The first design of the feedback controller is described as follows. The two control variables of the system are Φ and β. In order to achieve steady-state accuracy in these variables, two integrators are included in the controller structure. During the gain design the two integrators of the feedback controller can be considered part of the plant (i.e. dynamics of the aircraft) representing the lateral-directional motion. Hence, the two integrators are added to the aircraft model's outputs. The resultant so-called augmented plant is shown in figure 5.3. In addition to the system outputs r, β, p and Φ, it has two outputs representing the integrated measurements of Φ and β. Later in the process, after gain design is performed, these integrators become part of the CSAS.

After selecting the measurements for feedback design, an initial specification of desired eigenvalues is formulated based on the requirements in chapter 4.

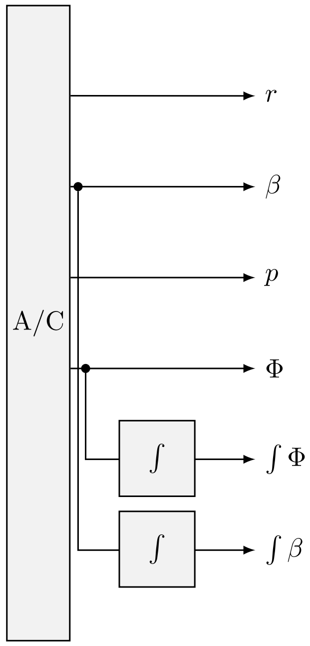

Figure 5.3.: Plant for feedback gain design

Since the inherent Dutch-roll frequency is compliant with the requirements, it is chosen for the specification of the closed-loop's Dutch-roll frequency. Thus, for every point in the envelope the following applies:

$$(\omega_{0,DR})_{des} = (\omega_{0,DR})_{inh}\,, \tag{5.32}$$

where $(\omega_{0,DR})_{inh}$ represents the inherent frequency of the Dutch-roll. In addition, the desired Dutch-roll damping is set to

$$(\zeta_{DR})_{des} = 0.3 \tag{5.33}$$

which is well within the limits for Level 1 flying qualities. The inherent roll subsidence pole location complies with its requirements. Nevertheless, in order to avoid a singular matrix $\left[\tilde{\lambda}_i \boldsymbol{I} - \boldsymbol{A} \quad \boldsymbol{B}\right]$ in equation (5.16), the desired roll subsidence poll is slightly adjusted to

$$(\lambda_R)_{des} = 1.05\,(\lambda_R)_{inh}\,. \tag{5.34}$$

For the specification of the closed-loop spiral pole, the attitude hold requirement described in section 4.3 is taken into consideration. This can be expressed as a settling time of $t_s \approx 5\,\mathrm{s}$ following a 5° disturbance of the bank angle, with the settling time threshold adjusted to ±20% of the desired value in order to reflect the accuracy statement of the attitude hold requirement. Taking the dynamic scaling into account, the limit for the settling time is adjusted to $t_s \approx 2.5\,\mathrm{s}$. The following transfer function

$$G_{\Phi\Phi_{cmd}} = \frac{1}{(T_R s + 1)\,(T_S s + 1)} \tag{5.35}$$

describing the second-order closed-loop dynamics in the roll-axis can be used for determination of the permissible spiral mode time constants. This is done by substitution of $T_R = -1/\,(\lambda_R)_{des}$ and subsequent evaluation of the settling time of equation (5.35) for a grid of potential T_S. The result of this evaluation is presented in figure 5.4. The green area encompasses the possible combinations of spiral- and roll subsidence time constants that lead to compliance of the roll dynamics with the attitude hold

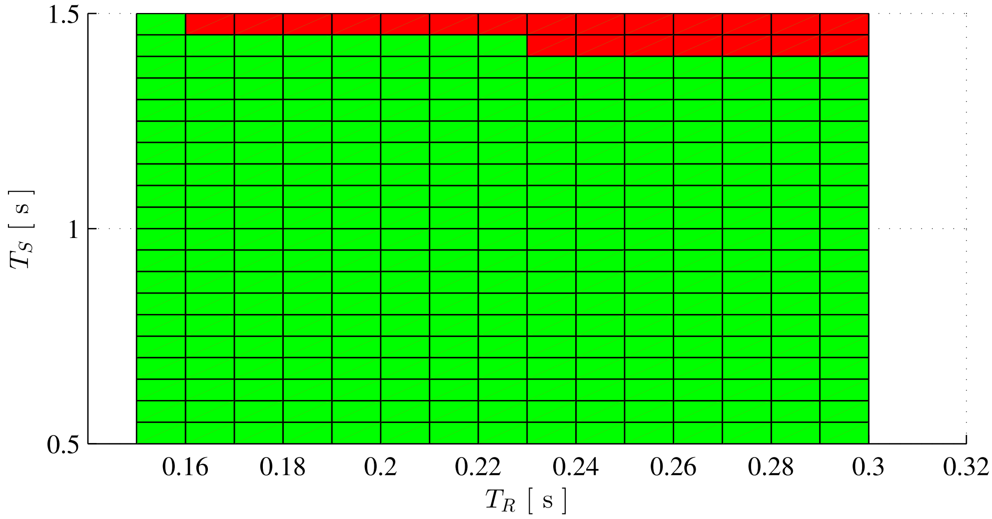

Figure 5.4.: Permissible spiral time constants

performance requirement. From this figure, it is concluded that the desired spiral time constant is

$$T_S \leq 1.35. \tag{5.36}$$

After definition of the desired eigenvalues has been completed, the desired eigenvectors of the closed-loop system can be specified. The eigenvector representing the roll subsidence mode is defined as follows:

$$\begin{array}{c} r \\ \beta \\ p \\ \Phi \\ \int \Phi \\ \int \beta \end{array} \begin{bmatrix} * \\ 0 \\ 1 \\ * \\ * \\ * \end{bmatrix}, \tag{5.37}$$

in which asterisks ($*$) stand for arbitrary values. By setting the entry in the β - row to zero, the Dutch-roll is canceled from the roll response. At the same time, this selection aligns the roll motion with the x-axis of the stability coordinate system, and thus contributes to the rolling around the velocity vector.

The eigenvector of the spiral mode is selected such that turn coordination is achieved. For this, the influence of the spiral mode on AoS needs to be eliminated. The entries r and p of the spiral mode's eigenvector are not specified but are obtained automatically from further kinematic relationships [19].

$$\begin{array}{c} r \\ \beta \\ p \\ \Phi \\ \int \Phi \\ \int \beta \end{array} \begin{bmatrix} * \\ 0 \\ * \\ 1 \\ * \\ * \end{bmatrix} \tag{5.38}$$

The ratio of $|\Phi/\beta|$ is initially set to zero for the Dutch-roll in order to realize a complete decoupling. The rotation rates are again not defined explicitly, but result from kinematics.

$$\begin{array}{c} r \\ \beta \\ p \\ \Phi \\ \int\Phi \\ \int\beta \end{array} \begin{bmatrix} * \\ 1 \\ * \\ 0 \\ * \\ * \end{bmatrix} \tag{5.39}$$

The integrator eigenvectors are set to be decoupled from each other

$$\begin{array}{c} \\ r \\ \beta \\ p \\ \Phi \\ \int\Phi \\ \int\beta \end{array} \begin{array}{c} \begin{array}{cc} \int\Phi & \int\beta \end{array} \\ \begin{bmatrix} * & * \\ * & * \\ * & * \\ * & * \\ 1 & 0 \\ 0 & 1 \end{bmatrix} \end{array}. \tag{5.40}$$

Following the definition of the desired eigenvalues and eigenvectors, the next step is to define the feedback controller structure. According to equation (5.11), the control law is given by the system outputs $\boldsymbol{y}$ (which in our case are $r, \beta, p, \Phi, \int\Phi, \int\beta$) and the feedback matrix $\boldsymbol{K}$. The feedback structure is modified by suppression of entries in the matrix $\boldsymbol{K}$. The initial feedback matrix $\boldsymbol{K}_1$ is shown below in equation (5.41), in which the suppressed feedback gains are indicated by zero-entries, while allowed gains are marked by asterisks:

$$\boldsymbol{K}_1 = \begin{array}{c} \\ \dot{p} \\ \dot{r} \end{array} \begin{array}{c} \begin{array}{cccccc} r & \beta & p & \Phi & \int\Phi & \int\beta \end{array} \\ \begin{bmatrix} * & * & * & * & * & * \\ * & * & * & * & * & * \end{bmatrix} \end{array}. \tag{5.41}$$

This feedback matrix defines the first controller variant *V1*. In equation (5.41), the particular matrix entries are denoted by the respective designators of rows and columns. Hence, for example, the entry in the first row and second column is designated $k_{\dot{p}\beta}$. For implementation in the software of the control system, the feedback matrix is split into single gains which are organized in multiple feedback cascades. The resulting block diagram is provided in figure 5.5. Due to the cascaded structure, the gains upstream (to the left) of p_{cmd} and r_{cmd} do not directly represent gains of $\boldsymbol{K}_1$, but are obtained from entries of the feedback matrix by dividing by $k_{\dot{p}p}$ and $k_{\dot{r}r}$ respectively. For example, the gains $k_{p\beta}$ and $k_{Ir\Phi}$ are calculated as follows:

$$k_{p\beta} = \frac{k_{\dot{p}\beta}}{k_{\dot{p}p}} \qquad k_{Ir\Phi} = \frac{k_{I\dot{r}\Phi}}{k_{\dot{r}r}}. \tag{5.42}$$

Since the *V1* - controller structure does not include any structural constraints, the gain design can be performed using standard Output Eigenstructure Assignment. The resulting feedback gains are depicted in figure 5.6 for $m_{fuel} = 3\,\mathrm{kg}$. Taking a closer look at the gains, it can be seen that some of them show sharp deflections over the speed envelope, which can be associated with the bends in the Dutch-roll's natural frequency and damping. Furthermore, the large entries in the gain $k_{\dot{p}\Phi}$, and hence the bank angle feedback to $\dot{p}_{cmd}$, as well as in the gain $k_{\dot{p}\beta}$ are especially noticeable. The magnitude of the latter is the result of the challenging Dutch-roll eigenvector specification required to achieve a full roll-yaw decoupling, since it leads inevitably to cancellation of the L_β entry in the state-space model.

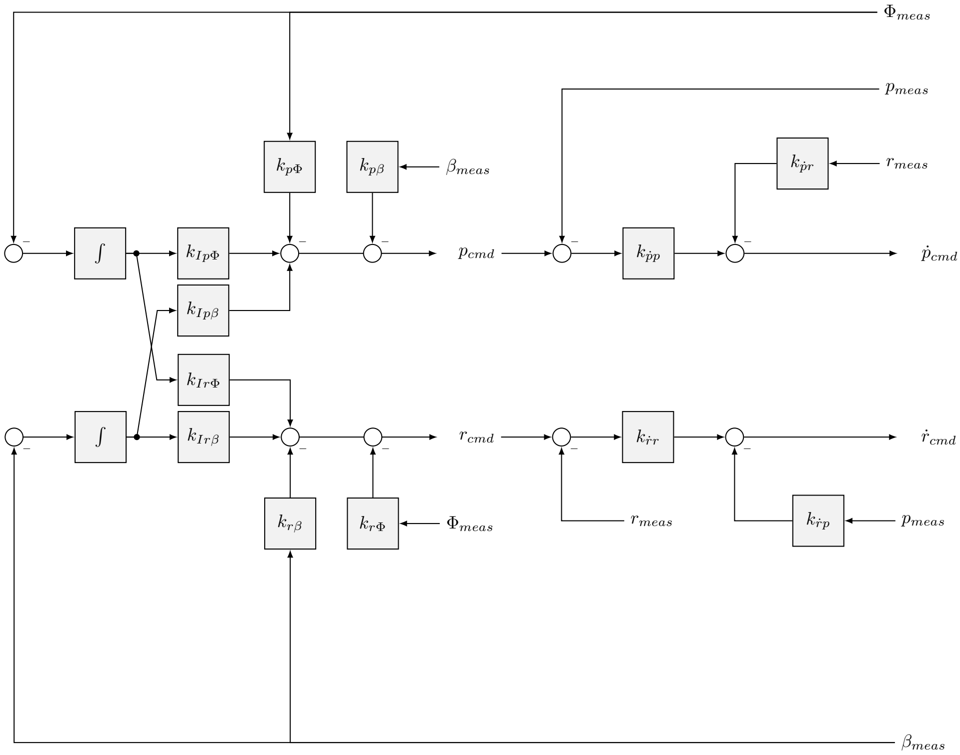

Figure 5.5.: Initial feedback controller structure

High gain feedbacks typically increase the system's sensitivity to sensor noise. Such controllers in combination with a noisy measurement, as is the case for the AoS sensor of the SAGITTA Demonstrator, adversely affect the performance of the closed-loop system. Besides reduction of the actuator's service life due to permanently high demand for actuating energy, a high gain feedback of noisy signals could degrade the stability properties of the system if the actuators are driven to their rate or position limits. Furthermore, high gain feedbacks reduce the robustness of the closed-loop system to uncertainties.

In order to analyze the effect of sensor noise on the actuators, to begin with, a time domain simulation of the closed-loop system with $\boldsymbol{K}_1$ feedback in level flight and calm atmospheric conditions is performed over the entire envelope with sensor noise being activated for all feedback measurements. The simulation is evaluated w.r.t. the noise requirements stated in equations (4.23) and (4.24). For this, the standard deviations of actuator rates and position are calculated from simulation results and compared to the corresponding requirements. An overview of the results of this evaluation across the flight envelope is shown in table 5.2. The fields colored green indicate that the particular requirement has been passed, while those in red indicate violations. The entries in the red fields are the variables, whose limits have been violated. Examination of the table reveals violations at low velocities, which indicates a problem in the feedback design. Moreover, it shows that the requirement is violated as a result of exceeding the limit on standard deviation of actuator rate of the equivalent rudder $\dot{\zeta}_{equiv}$, whereas the requirement on actuator position is not violated.

As a means of obtaining information on the contribution of the various feedbacks to the overall actuator activity, and thereby to identify the critical feedback variables that mostly lead to requirements violations, PSD analysis in frequency domain is a useful technique. According to [10], a signal can be related to the signal's standard deviation

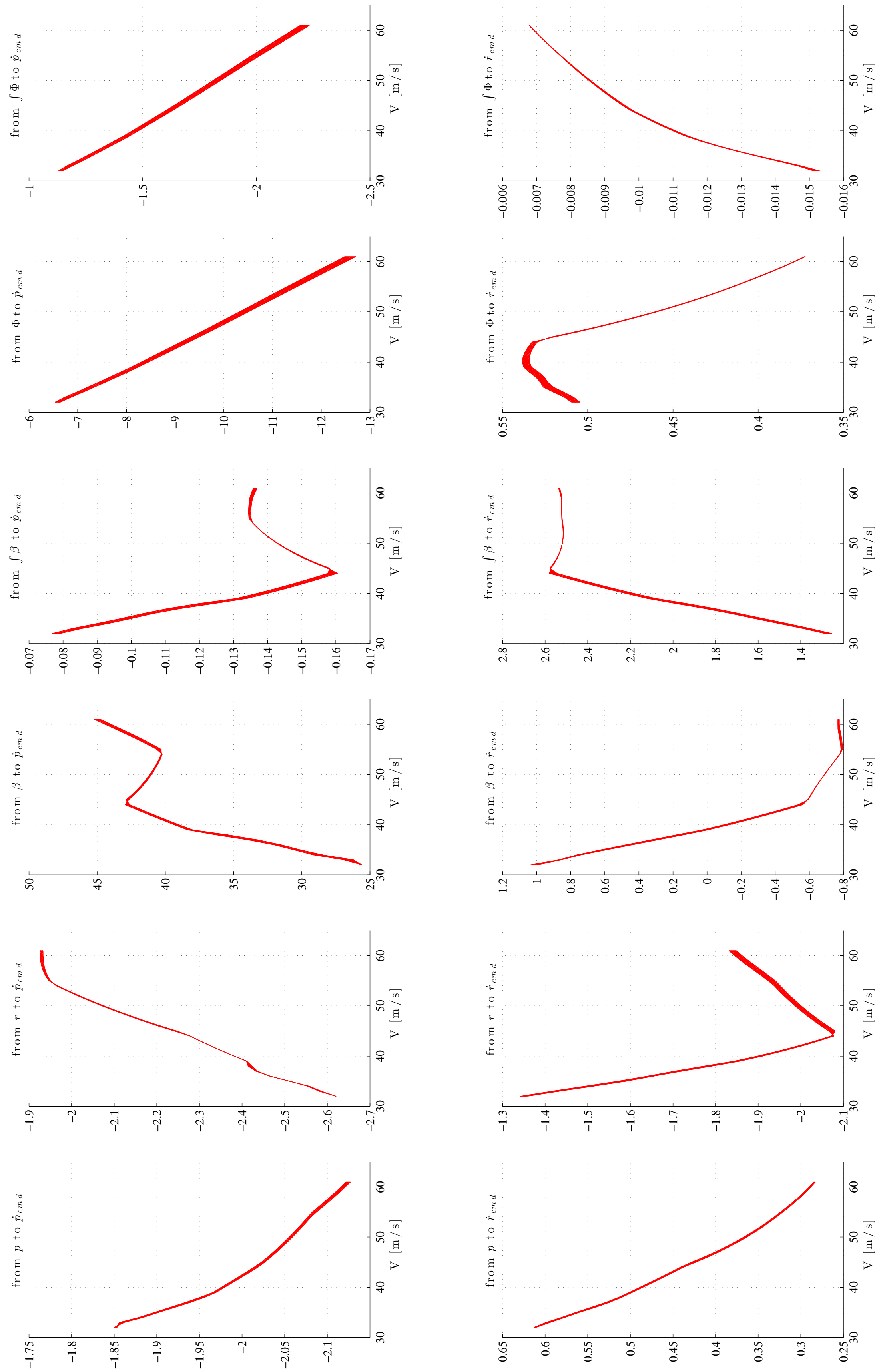

Figure 5.6.: Variant 1: Feedback Gains of $\boldsymbol{K}_1$

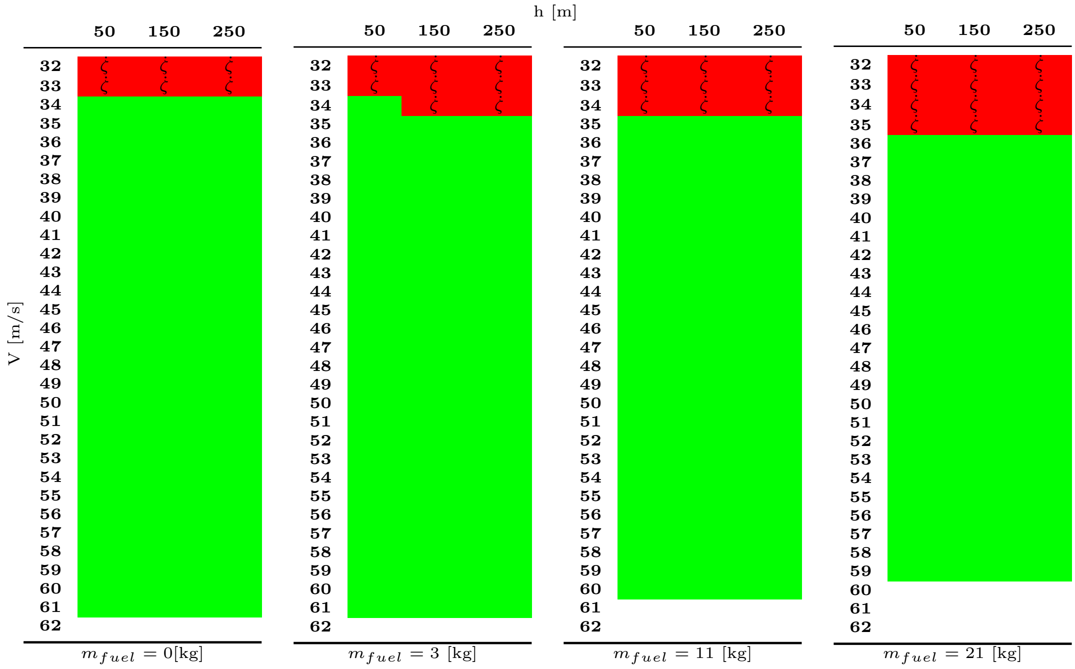

Table 5.2.: Variant 1: Sensor noise requirement evaluation overview

or variance and its average power P_{xx} as stated in equation (5.43),

$$P_{xx} = \sigma_x^2 = \lim_{T\to\infty} \frac{1}{2T} \int_{-T}^{T} |x(t)|^2 dt = \int_{-\infty}^{\infty} S_{xx}(f)df = \frac{1}{2\pi} \int_{-\infty}^{\infty} S_{xx}(\omega)d\omega \tag{5.43}$$

where $S_{xx}(\omega)$ is the Power Spectral Density of $x(t)$ which can be interpreted as the "...breakdown of variance with respect to frequency"[80]. The double subscript xx here indicates the auto correlation of a signal. From this, and equations (4.23) and (4.24), the requirements on maximum actuator activity can be expressed as follows:

$$P_{\delta\delta} = \sigma_\delta^2 \leq \frac{\delta_{max}^2}{9} \tag{5.44}$$

$$P_{\dot{\delta}\dot{\delta}} = \sigma_{\dot{\delta}}^2 \leq \frac{\dot{\delta}_{max}^2}{9}, \tag{5.45}$$

where δ_{max} and $\dot{\delta}_{max}$ are the maximum available control surface deflection and rate respectively. The following equation describes the relation of input and output signal PSDs of a Linear Time Invariant (LTI) system [16]:

$$S_{yy}(\omega) = |G_{yu}(\omega)|^2 S_{uu}(\omega), \tag{5.46}$$

where S_{uu} represents the PSD of the input signal, S_{yy} the PSD at the output of the system, and $|G_{yu}(j\omega)|^2$ is the power transfer function from input to output. By using the relationship in equation (5.46), the effect of sensor noise on the actuator can be obtained without the need for time domain simulation. All that is required for the analysis are the closed-loop transfer functions from the particular sensor noise input to the actuator output (i.e. the noise sensitivity transfer function $G_{\delta n}$ with subscript δ being the deflection of the control surface under consideration, here ζ_{equiv}) and n, the noise of a particular sensor measurement. Then, with $S_{nn}(\omega)$ being the PSD of the noise signal, the PSD at the actuator can be calculated as

$$S_{\delta\delta}(\omega) = |G_{\delta n}(\omega)|^2 S_{nn}(\omega). \tag{5.47}$$

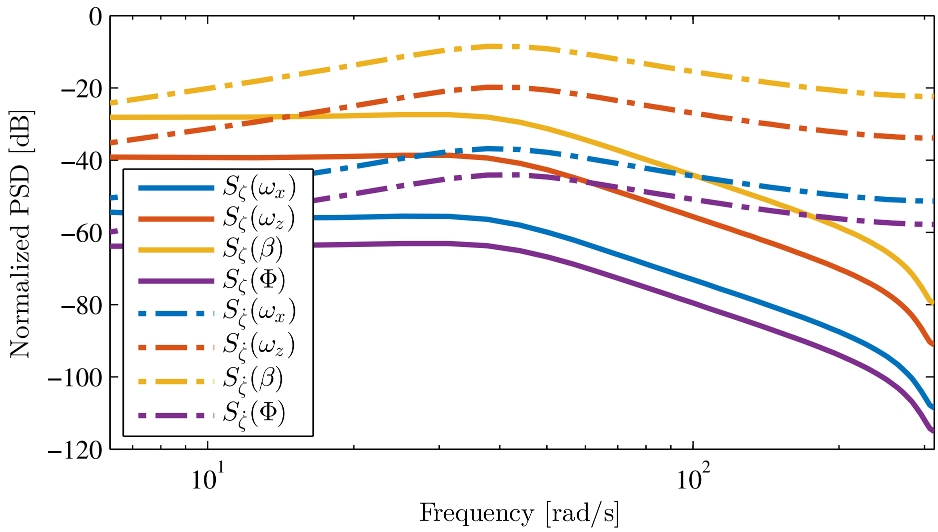

Figure 5.7.: *V1* - Noise Power Spectral Density at the actuator output

Band limited white noise is known to have a flat PSD. That means, all frequencies within the band defined by ω_{BW} contribute equally to the power of the overall signal. According to the Shannon Theorem, the bandwidth ω_{BW} equals to 1/2 of the system's sampling frequency. The following applies to the average power of band limited white noise:

$$P_{nn} = \sigma_n^2 = \frac{1}{\pi}\int_0^{\omega_{BW}} S_{nn}(\omega)d\omega = \frac{\omega_{BW}}{\pi}S_{nn} \tag{5.48}$$

Consequently, the PSD S_{nn} of the noise signal can be calculated from the standard deviation of the noise (σ_n) as follows:

$$S_{nn} = \frac{\pi P_{nn}}{\omega_{BW}} = \frac{\pi\sigma_n^2}{\omega_{BW}}. \tag{5.49}$$

By exploiting these relationships, the noise power transfer function scaled by the noise power spectral density can be used to estimate the contribution of sensor noise to the overall noise amplitude at the actuator. This is done for the actuators related to ζ below. Here, each sensor used in the *V1* - controller is considered separately. To obtain the impact of sensor noise on the rudder actuator rate ($S_{\dot\zeta\dot\zeta,sens}$), the noise of a particular sensor (S_{nn}) is sent through the power transfer function $|sG_{\zeta n}|^2$. Accordingly, the PSD of the rudder actuator deflection is calculated as follows:

$$S_{\zeta\zeta,sens} = |G_{\zeta n}|^2 S_{nn}. \tag{5.50}$$

The results of the evaluation are shown in figure 5.7 in which solid lines are the PSDs describing the actuator deflections $S_{\zeta\zeta,sens}$, and dashed lines are the corresponding PSDs $S_{\dot\zeta\dot\zeta,sens}$ for the actuator rate. The particular sensor measurements are indicated in the legend by arguments in round brackets. Also, the double subscripts, denoting auto-correlation are replaced by single subscripts in order to aid readability. (Note: To obtain a complete picture the PSDs of the individual feedbacks should be superimposed though this has not been done here).

In order to evaluate the impact of sensor noise w.r.t. the corresponding requirement at the actuator output, the PSDs depicted in figure 5.7 must be integrated to determine the average actuator power $P_{\delta\delta}$. This is done here by utilization of the left-hand rectangle

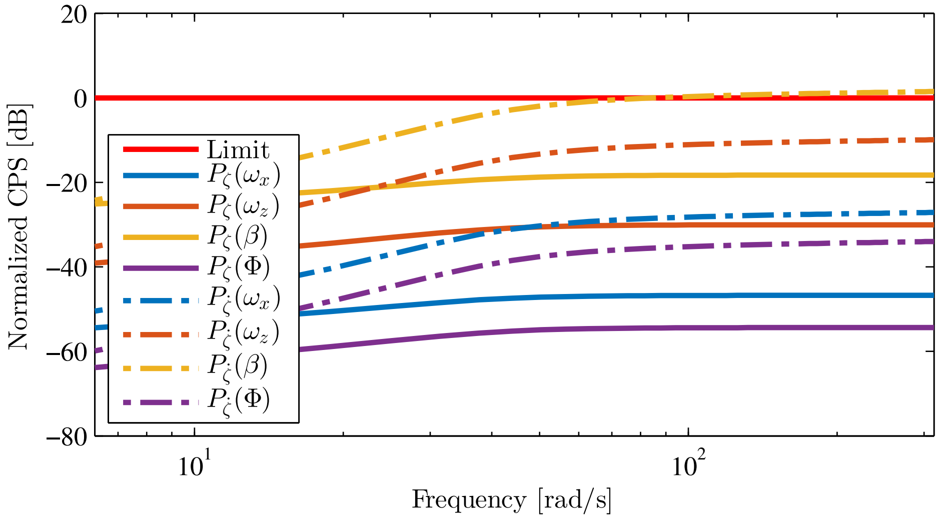

Figure 5.8.: *V1* - Cumulative Noise Power Spectrum at the actuator output

integration method. The integration result of the PSD up to a particular frequency is the so-called Cumulative Power Spectrum (CPS). Figure 5.8 shows the CPS of the actuator rate and deflection subject to sensor noise. The data is normalized with the value of variance stated in the requirements, namely

$$\frac{P_{\delta\delta}}{\sigma^2_{\delta,req}} \quad \text{and} \quad \frac{P_{\dot\delta\dot\delta}}{\sigma^2_{\dot\delta,req}} \tag{5.51}$$

with

$$\sigma^2_{\delta,req} = \frac{\delta^2_{max}}{9} \quad \text{and} \quad \sigma^2_{\dot\delta,req} = \frac{\dot\delta^2_{max}}{9} \tag{5.52}$$

Also shown on the graph is a line (labeled "Limit") indicating the maximum tolerated σ^2 and which therefore denotes the requirement limit. If the CPS curve intersects with this line it indicates that the requirement on actuator activity has been violated due to the noise of the corresponding feedback. The plot in figure 5.8 shows a violation of actuator rate due to the noise of the AoS feedback. This means that the noise level of the AoS measurement alone is such that the requirement on actuator activity has not been fulfilled, even when all other sensors are assumed to be free of noise. This analysis therefore confirms the initial presumption that the high gain AoS feedback might present a problem.

Typically, noise amplification through the controller can be addressed by implementation of a low-pass filter in the feedback path to reduce the noise content in the signal at high frequencies. The analysis above can be used for design of such a filter. The following describes an example of filter design for attenuation of noise in the AoS feedback. For better readability, the double subscript indicating auto-correlation is dropped and replaced by a single subscript.

From equation (4.24), the condition for compliance with the requirement on actuator rate activity due to noise is given by

$$P_{\dot\delta} = \frac{1}{\pi}\sum_{i=0}^{n-1} S_{\dot\delta}(i\Delta\omega)\Delta\omega \overset{!}{\leq} \sigma^2_{\dot\delta,req} = \frac{\dot\delta^2_{max}}{9}. \tag{5.53}$$

Here, the continuous integration is substituted by its discrete realization using the sum of rectangles, where $\Delta\omega$ is the discretization step size of angular frequency, n is $\omega_{BW}/\Delta\omega$ and $S_{\dot\delta}$ the PSD of the actuator rate.

When a filter is introduced into the controller's feedback path, the PSD $S_{\dot{\delta}_f}$ of the filtered actuator rate can be expressed in terms of the filter transfer function G_f and the PSD of the unfiltered actuator signal as follows:

$$S_{\dot{\delta}_f}(\omega) = |G_f(\omega)|^2 S_{\dot{\delta}}(\omega) \tag{5.54}$$

which allows the condition in equation (5.53) to be rewritten as

$$P_{\dot{\delta}_f} = \frac{1}{\pi} \sum_{i=1}^{n} |G_f(i\Delta\omega)|^2 S_{\dot{\delta}}(i\Delta\omega)\Delta\omega \overset{!}{\leq} \sigma^2_{\dot{\delta},req} = \frac{\dot{\delta}^2_{max}}{9}. \tag{5.55}$$

and which finally leads to

$$\sum_{i=1}^{n} |G_f(i\Delta\omega)|^2 S_{\dot{\delta}}(i\Delta\omega)\Delta\omega \overset{!}{\leq} \pi\sigma^2_{\dot{\delta},req}. \tag{5.56}$$

Since all feedbacks contribute to the overall power $P_{\dot{\delta}}$ at the actuator, each feedback signal must be assigned a budget from $\sigma^2_{\dot{\delta},req}$. In the case of the controller *V1*, the budget for the AoS feedback is obtained by reducing the overall $\sigma^2_{\dot{\delta},req}$ by the sum of contributions to the actuator rate activity of all further feedbacks as shown in equation (5.57).

$$P_{\dot{\delta}_\beta} = \sigma^2_{\dot{\delta},req} - \left(P_{\dot{\delta}_{\omega_x}} + P_{\dot{\delta}_{\omega_z}} + P_{\dot{\delta}_\Phi}\right) \tag{5.57}$$

In this case, to keep the example as simple as possible, the requirement is changed to $P_{\dot{\delta}_\beta} \leq \sigma^2_{\dot{\delta},req}$.

Assuming that the filter structure and parametrization are known, equation (5.56) can be evaluated for a parameters grid and subsequently the suitable filter parameter combination can be determined by graphical means.

For the problem at hand, a second order low-pass filter of the form in equation (5.58) with a damping of $\zeta = 0.707$ for the AoS feedback is adopted in order to achieve the desired performance w.r.t. to actuator rate.

$$G_f(s) = \frac{\omega_0^2}{s^2 + 2\zeta\omega_0 s + \omega_0^2} \tag{5.58}$$

Figure 5.9 shows the normalized cumulative power spectrum $P_{\dot{\delta}_f}$ of the filtered actuator rate signal $\dot{\delta}_f$ for different settings of the AoS filter's natural frequency (ω_0). From this figure, it can be seen that for $\omega_0 \leq 75\,\mathrm{rad\,s^{-1}}$ the curve of the cumulative power spectrum remains below the line representing limit for actuation power $\sigma^2_{\dot{\delta},req}$. Consequently, a low-pass filter with the appropriate natural frequency provides enough signal attenuation for the AoS feedback to comply with the corresponding noise requirement. The drawback of employing such a filter in the control system is the introduction of additional delay in the feedback path. In the case of a filter with $\omega_0 = 75\,\mathrm{rad\,s^{-1}}$, the effective time delay is $\tau_{eff} = 0.0044\,\mathrm{s}$. If the stability margins of the controller allow the introduction of an additional delay of such amount, the low-pass filter offers a very effective means of noise attenuation. Other options for solving the problem of noise amplification are: to reduce the corresponding feedback gain; to replace the feedback of AoS by other quantities; or to omit the feedback without any replacement. Several publications can be found that consider replacement of AoS measurement with an estimate e.g. using lateral acceleration. Most of the approaches rely strongly on aerodynamic coefficients. Since the ADM of the SAGITTA Demonstrator provides highly uncertain data, it has been decided not to pursue the approach of AoS estimation.

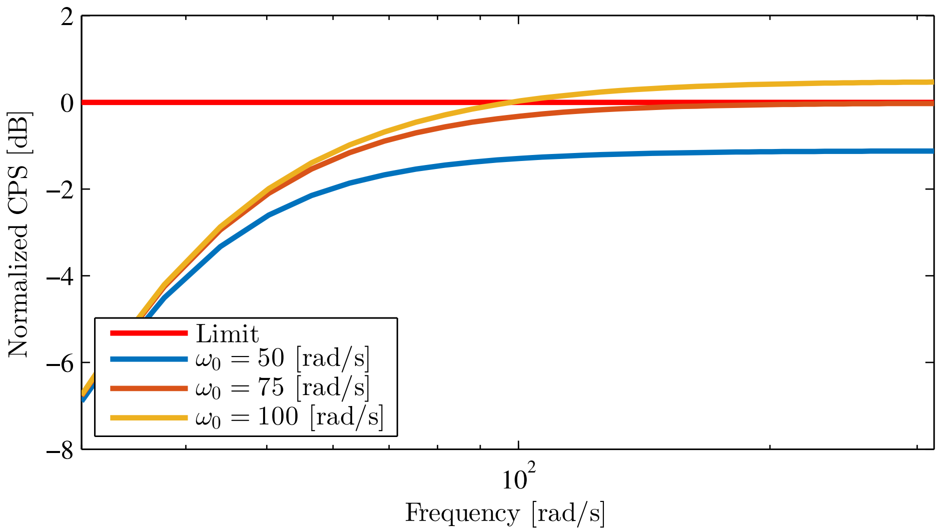

Figure 5.9.: *V1* - Impact of variation of natural frequency of the AoS feedback low-pass filter on the CPS of actuator rate

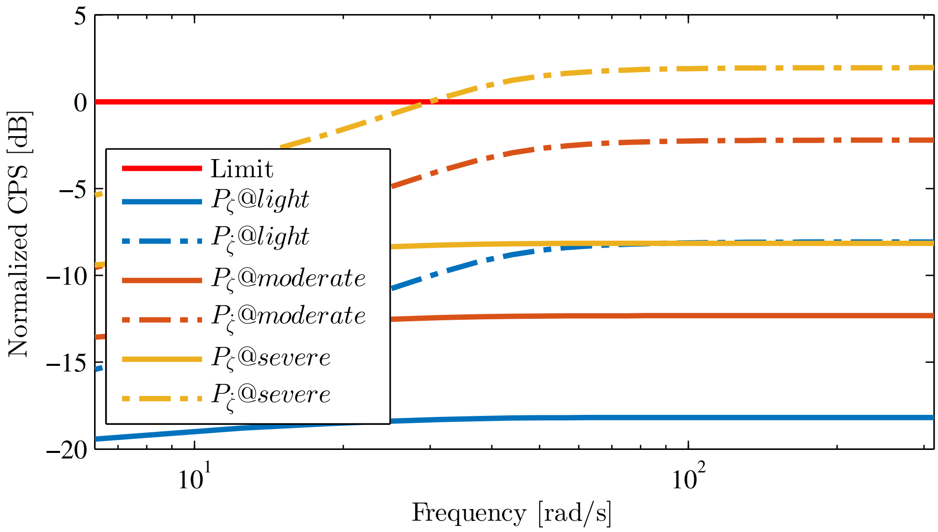

Figure 5.10.: *V1* - Cumulative Power Spectrum of actuators during turbulence

Another useful evaluation of the feedback controller w.r.t. gain magnitude, is the assessment of the requirement on maximum amount of actuator activity caused by turbulence. The approach to this analysis is similar to the one that is applied to noise. The main work in preparation for such analysis has already been done in chapter 3, since the state-space model of the aircraft already includes a linear filter, that represents the Dryden turbulence model. Consequently, the power transfer function from the turbulence filter input to the actuator output can be obtained easily. For evaluation this function is scaled with unity white noise. The CPS curves representing the rate and position of the actuator for the three turbulence intensities (light, moderate and severe) are presented in figure 5.10. The resulting diagram nicely illustrates the present situation. The CPS curves for rate and position for both light and moderate turbulence are below the line denoting the actuation power limit. Consequently, for those conditions the requirements on actuator activity are met. For severe turbulence intensity, however, the CPS representing the actuator rate exceeds the limit, meaning that the actuator rate activity requirement is violated. The outcome of the analysis of actuator activity resulting from turbulence is a further affirmation of a high-gain feedback design. Furthermore, the critical turbulence frequency spectrum which yields $\dot{\zeta}$ beyond the specified limits, lies well within the actuator bandwidth. Consequently, any low-pass filter that is intended to reduce actuator activity in order to assure compliance with the requirements, would lower the bandwidth of the overall system. In this case it is preferable to perform a gain redesign.

In this section a novel method of evaluating the impact of turbulence and noise on actuators used for primary control has been presented. The two analyses reveal the shortcomings of the *V1* feedback controller design. It has been shown that a controller design providing full roll-yaw decoupling of the SAGITTA Demonstrator results in high actuator rates due to sensor noise and high turbulence amplification at the actuator. Such a design leads to unacceptable actuator rate saturations and consequently has a negative impact on the overall stability of the closed-loop system. In addition, the section illustrates some challenges in control of the SAGITTA Demonstrator have been illustrated, namely: low quality sensors; strong inherent dynamic couplings of the aircraft; and challenging requirements. Also, in this section, power spectrum analysis is used to design a low-pass filter, which resolves the problem of noise amplification in the AoS feedback, but lowers the bandwidth of the overall system. In what follows, the problem of noise and turbulence amplification at the actuator is addressed by lessening the decoupling requirement and thereby reducing the feedback gains.

5.4. Moderate decoupling controller design: *V2*

In order to overcome the problems of *V1* design, first of all the requirement for perfect roll-yaw decoupling is discarded. In its place an attempt is made to achieve the requirement of $|\Phi/\beta|_{DR} \leq 1.5$ without changing the controller structure. The inherent phi-to-beta ratio $r_{DR,inh}$ is given in equation (5.59) by the open loop Dutch-roll eigenvector entries $(v_\Phi)_{DR}$ and $(v_\beta))_{DR}$, which are related to the states Φ and β, respectively.

$$r_{DR,inh} = \frac{|\,(v_\Phi)_{DR}\,|}{|\,(v_\beta)_{DR}\,|} \tag{5.59}$$

Using the inherent phi-to-beta-ratio, the specification of the closed-loop Dutch-roll eigenvector can be adjusted for the next controller version (*V2*) as follows:

$$\boldsymbol{v}_{DR,des} = \begin{array}{c} r \\ \beta \\ p \\ \Phi \\ \int\Phi \\ \int\beta \end{array} \begin{bmatrix} * \\ (v_\beta)_{DR} \\ * \\ c_{DR}\,(v_\Phi)_{DR} \\ * \\ * \end{bmatrix} \tag{5.60}$$

where

$$c_{DR} = \begin{cases} 1 & \text{for } r_{DR,inh} \leq r_{DR,des} \\ \frac{r_{DR,des}}{r_{DR,inh}} & \text{for } r_{DR,inh} > r_{DR,des} \end{cases} \tag{5.61}$$

is the scaling factor of the Φ - entry of the Dutch-roll eigenvectors $\boldsymbol{v}_{DR}$ and $r_{DR,des}$ is the desired closed-loop phi-to-beta ratio. The remaining specifications for controller design as well as for the feedback structure are taken from the specification of the *V1* - controller.

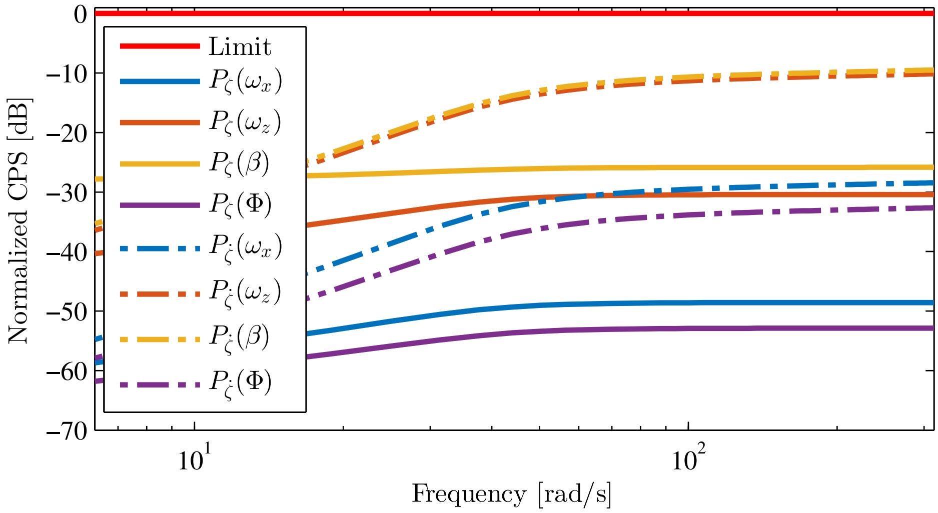

Figure 5.11.: *V2* - Cumulative Noise Power Spectrum

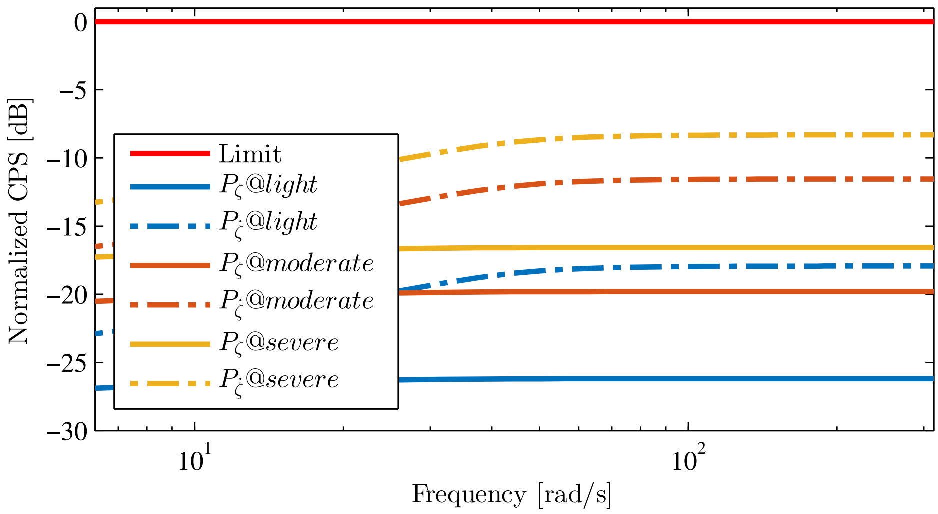

Figure 5.12.: *V2* - Cumulative Turbulence Power Spectrum

The gain design (*V2*) with the adjusted requirement on roll-yaw coupling is realized using the standard EA algorithm. It results in significantly smaller gains, as can be seen in figure 5.20. The analysis of the *V2* - controller w.r.t. sensor noise (figure 5.11) and turbulence (figure 5.12) shows that the specified requirements are met and, compared to the *V1* - controller, a better design is achieved in terms of actuator activity. Hence, due to the reduced stress of the actuators during flight, their service life is significantly extended and their power consumption is reduced.

An important lesson that can be learned from the discoveries made during developing the *V1* and *V2* controllers is that a single adverse decision made on flight dynamics requirements, in this case asking for e.g. full decoupling of rolling and yaw motion, may jeopardize the entire control system design.

5.5. Reduction of ineffective gains: *V3*

A good controller design is one that establishes the required functionality and performance with the simplest possible structure. The benefits of a simple controller structure are better system understanding; ease of implementation; and an increase in computational and memory efficiency. Thus, it is good practice to review the controller structure w.r.t. possible simplifications. In this case the review is performed as follows.

Referring again to figure 5.6 which shows the gains for the *V1* - controller, it can be seen that the magnitudes of feedbacks $k_{I\dot{p}\beta}$ and $k_{I\dot{r}\Phi}$ are significantly smaller than those of other entries. This is an indication of the ineffectiveness of the these feedbacks and results from the specification of decoupling the integrator eigenvectors. Consequently, the question arises whether these feedbacks can be removed from the controller design. As a first step towards answering this question, a structured approach to identifying irrelevant feedbacks is required.

As a means for determination of gains in the feedback matrix that have less effect, Calvo-Ramon proposes in [11] the calculation of a decision matrix $\boldsymbol{D}^{\lambda}$. The decision matrix consists of entries which describe the influence of a feedback gain k_{ij} on locations of eigenvalues in the pole-zero map. The corresponding entries of $\boldsymbol{D}^{\lambda}$ are calculated according to

$$d_{ij} = \frac{1}{n}\sqrt{\sum_{h=1}^{n}\left(s_{ij}^{h}\right)^{2}} \tag{5.62}$$

or in case of complex eigenvalues

$$d_{ij} = \frac{1}{n}\sqrt{\sum_{h=1}^{n}\left(s_{ij}^{h}\right)\left(\overline{s_{ij}^{h}}\right)}, \tag{5.63}$$

where n denotes the number of eigenvalues and $\left(\overline{s_{ij}^{h}}\right)$ denotes the conjugate complex of $\left(s_{ij}^{h}\right)$, whereby $\left(s_{ij}^{h}\right)$ is the shift of the h-th eigenvalue λ^{h} due to the feedback gain k_{ij}, and is calculated as follows:

$$s_{ij}^{h} = \frac{\partial\lambda^{h}}{\partial k_{ij}}k_{ij}. \tag{5.64}$$

The partial derivative $\partial\lambda^{h}/\partial k_{ij}$ can be calculated starting with the matrix equality for closed-loop eigenvalues and eigenvectors:

$$\left(\boldsymbol{A}-\boldsymbol{BKC}\right)\boldsymbol{v}^{h} = \lambda^{h}\boldsymbol{v}^{h}. \tag{5.65}$$

By multiplying equation (5.65) with the system's left eigenvector $\left(\boldsymbol{w}^{h}\right)^{T}$ and the following derivative of the closed-loop system matrix w.r.t the gain k_{ij}

$$\frac{\partial\left(\boldsymbol{A}-\boldsymbol{BKC}\right)}{\partial k_{ij}} = -\boldsymbol{B}\frac{\partial\boldsymbol{K}}{\partial k_{ij}}\boldsymbol{C} = -\boldsymbol{b}_{i}\boldsymbol{c}_{j}^{T} \tag{5.66}$$

the expression in equation (5.67) is derived,

$$-\left(\boldsymbol{w}^{h}\right)^{T}\boldsymbol{b}_{i}\boldsymbol{c}_{j}^{T}\boldsymbol{v}^{h} = \left(\boldsymbol{w}^{h}\right)^{T}\frac{\partial\lambda^{h}}{\partial k_{ij}}\boldsymbol{v}^{h} \tag{5.67}$$

which finally leads to

$$\frac{\partial\lambda^{h}}{\partial k_{ij}} = -\frac{1}{\left(\boldsymbol{w}^{h}\right)^{T}\boldsymbol{v}^{h}}\left(\boldsymbol{w}^{h}\right)^{T}\boldsymbol{b}_{i}\boldsymbol{c}_{j}^{T}\boldsymbol{v}^{h} \tag{5.68}$$

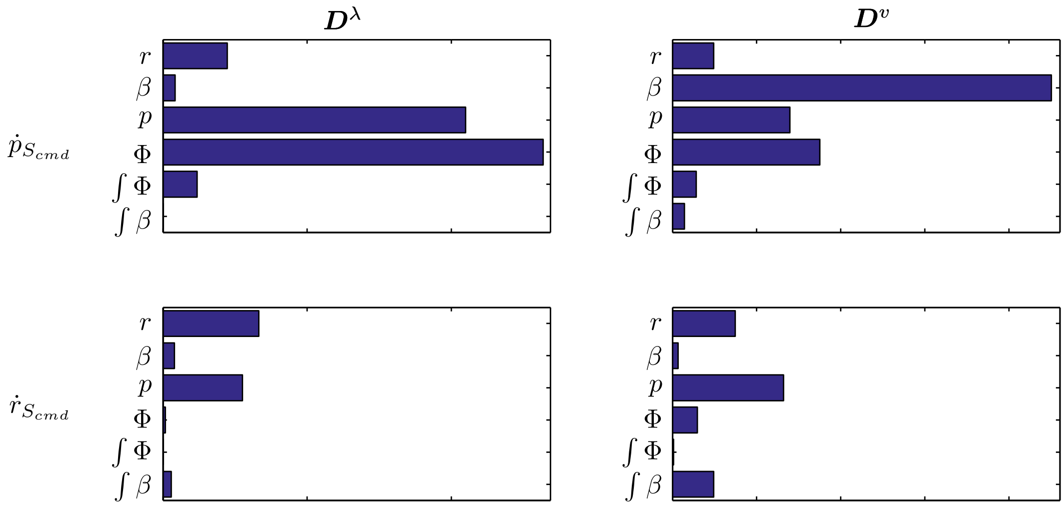

Figure 5.13.: *V1* - Decision Matrices

with $\boldsymbol{b}_i$ being the i-th column of the input matrix $\boldsymbol{B}$ and $\boldsymbol{c}_j^T$ the j-th row of the output matrix $\boldsymbol{C}$.

In [82], Sobel et. al. extended the concept of decision matrix by calculating of the corresponding decision matrix $\boldsymbol{D^v}$, which describes the influence of feedback gains on closed-loop eigenvectors. The shift in h-th eigenvector is formulated as:

$$p_{ij}^h = \frac{\partial \boldsymbol{v}^h}{\partial k_{ij}} k_{ij}. \tag{5.69}$$

with

$$\frac{\partial \boldsymbol{v}^h}{\partial k_{ij}} = \sum_{m=1}^{n} \alpha_{ijhm} \boldsymbol{v}^m \tag{5.70}$$

where the coefficient α is calculated as

$$\alpha_{ijhq} = \frac{1}{(\lambda^q - \lambda^h) (\boldsymbol{w}^q)^T \boldsymbol{v}^q} \left((\boldsymbol{w}^q)^T \boldsymbol{b}_i \boldsymbol{c}_j^T \boldsymbol{v}^h \right) \text{ for } q \neq h \tag{5.71}$$

and

$$\alpha_{ijhh} = -\frac{1}{(\boldsymbol{v}^h)^T \boldsymbol{v}^h} \sum_{\substack{m=1 \\ m\neq h}}^{n} \alpha_{ijhm} (\boldsymbol{v}^m)^T \boldsymbol{v}^h \text{ for } q = h. \tag{5.72}$$

The entries d_{ij} of the eigenvector decision matrix $\boldsymbol{D^v}$ are calculated using the same procedure as in equations (5.62) and (5.63) substituting s_{ij}^h with p_{ij}^h.

The calculation of $\boldsymbol{D}^\lambda$ and $\boldsymbol{D^v}$ is performed using the algorithm provided in [21]. For the *V1* feedback design, the eigenvalue and eigenvector decision matrices for an arbitrary (mid-envelope) flight condition are depicted as bar charts in figure 5.13. The two bar plots on the left represent the first and second rows of the eigenvalue decision matrix, which has the same form as the feedback matrix $\boldsymbol{K}$. The two diagrams on the right are the first and second rows of the eigenvector decision matrix. The variable symbols to the left of each bar denote the particular feedback variables, and hence the columns of the matrices, the pseudo inputs corresponding to the rows of the feedback matrix, are shown on the far left.

It can be determined from the decision matrices that the obvious choice for suppression are the cross-axis integrator gains $k_{I\dot{p}\beta}$ and $k_{I\dot{r}\Phi}$. Their suppression has almost no effect

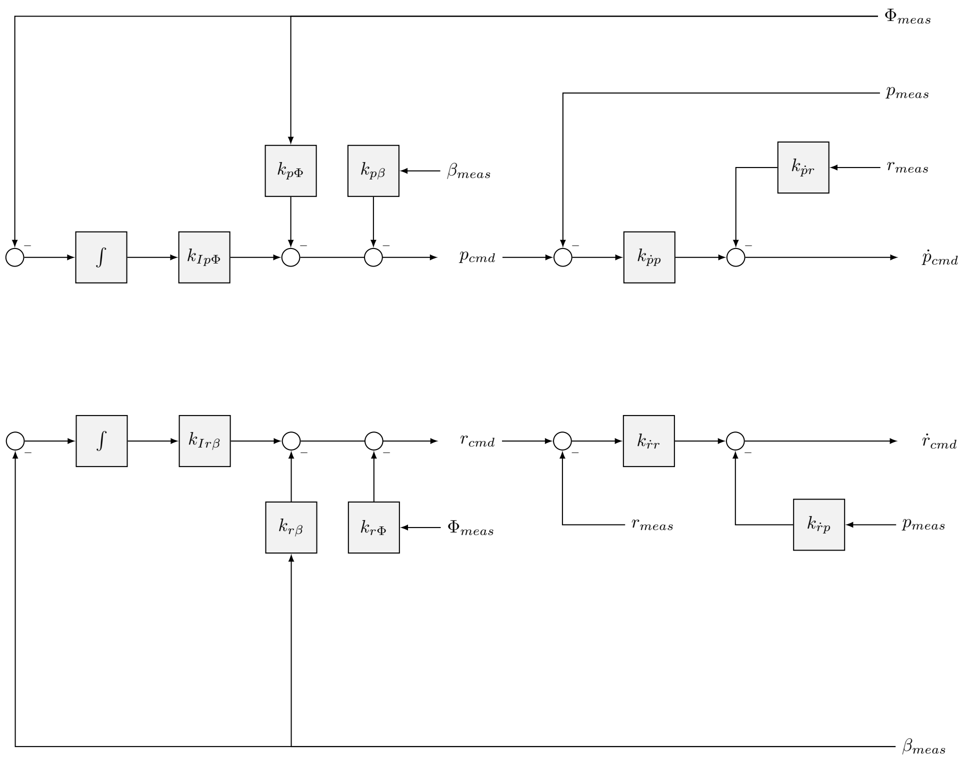

Figure 5.14.: Feedback controller structure after suppression of negligible gains

on the eigenvalues of the closed-loop system and only marginal effect on the eigenvectors. The suppression of these gains leads to a simpler controller structure by decoupling the roll and yaw paths. Figure 5.14 shows the corresponding block diagram, and in equation (5.73) the structure of the resulting feedback matrix $\boldsymbol{K}_3$ is given.

$$\boldsymbol{K}_3 = \begin{array}{c} \begin{array}{cccccc} r & \beta & p & \Phi & \int\Phi & \int\beta \end{array} \\ \left[\begin{array}{cccccc} * & * & * & * & * & 0 \\ * & * & * & * & 0 & * \end{array}\right] \end{array} \tag{5.73}$$

The situation is different when applying the decision matrices to the *V2* - controller. The previously negligible gain $k_{I\dot{p}\beta}$ has significantly more influence on the eigenvectors than is the case with the *V1* - controller. This fact is illustrated by the eigenvector decision matrix $\boldsymbol{D}^{\boldsymbol{v}}$ in figure 5.15. As a result, the applicable feedback gain cannot be suppressed without consequences for the eigenvectors of the closed-loop system. The following analyzes those consequences in detail. For this purpose, the entries of the above-mentioned decision matrices are split into the influences on particular eigenvalues and eigenvectors. These matrices are referred to as eigenvalue shift matrix $\boldsymbol{S}^{\boldsymbol{\lambda}}$ and eigenvector shift matrix $\boldsymbol{S}^{\boldsymbol{v}}$. Figure 5.16 shows the resulting shifts for the *V2* - controller. The two diagrams on the left represent the two rows of the eigenvalue shift matrix. The applicable feedback variables are listed to the left of these diagrams, i.e. along the y-axis, while the columns, representing the applicable eigenmodes are labeled underneath, i.e. along the x-axis. The two diagrams on the right represent the corresponding eigenvector shift matrix. The upper two diagrams pertain to the pseudo input $\dot{p}_{S_{cmd}}$ and those below to $\dot{r}_{S_{cmd}}$.

In the diagrams of eigenvalue shift matrices and eigenvector shift matrices the magnitudes of the quantities $\sqrt{\left(s_{ij}^h\right)\left(\overline{s_{ij}^h}\right)}$ and $\sqrt{\left(p_{ij}^h\right)\left(\overline{p_{ij}^h}\right)}$ are represented by a light color for large

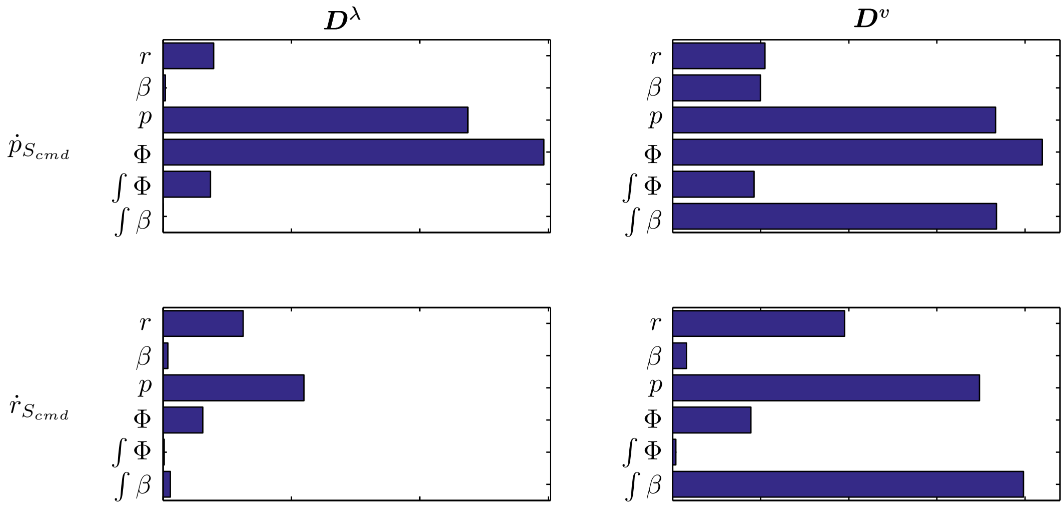

Figure 5.15.: *V2* - Decision Matrices - details

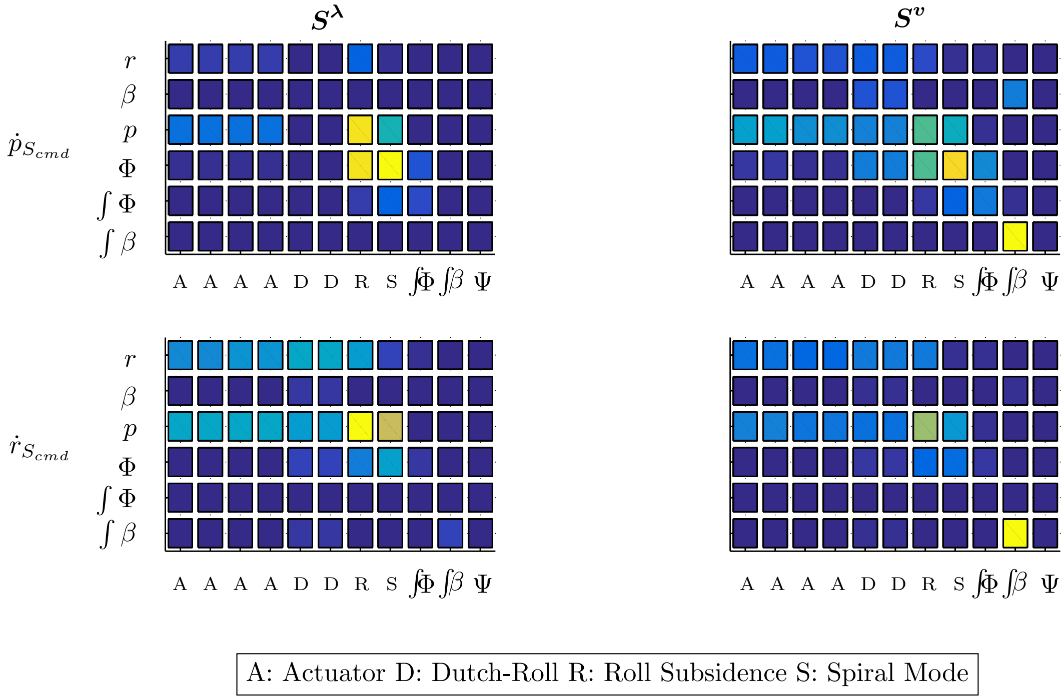

Figure 5.16.: *V2* - Eigenvalue and eigenvector shift matrices

entries and by a dark color for small entries. By examining the entries of the resultant matrices $\boldsymbol{S}^{\lambda}$ for eigenvalues and $\boldsymbol{S}^{v}$ for eigenvectors, the sensitivity of the eigenmodes to feedbacks can be identified and familiar relationships of eigenmodes and rigid body states can be seen.

By examining figure 5.16, the question of how the feedback gain $k_{I\dot{p}\beta}$ influences the eigenvectors of the closed-loop system can be partially addressed. The analysis shows, that the influence of the β- integrator feedback on the set of eigenvectors is limited to the eigenvector that is related to the β-integrator eigenmode itself. This can be seen in the upper eigenvector shift matrix ($\boldsymbol{S}^{v}(\dot{p}_{S_{cmd}})$) diagram, where the row related to the $\int \beta$ feedback has a single large entry (yellow) in the column related to the $\int \beta$ eigenvector. From this, it can be concluded, firstly, that the particular feedback gain

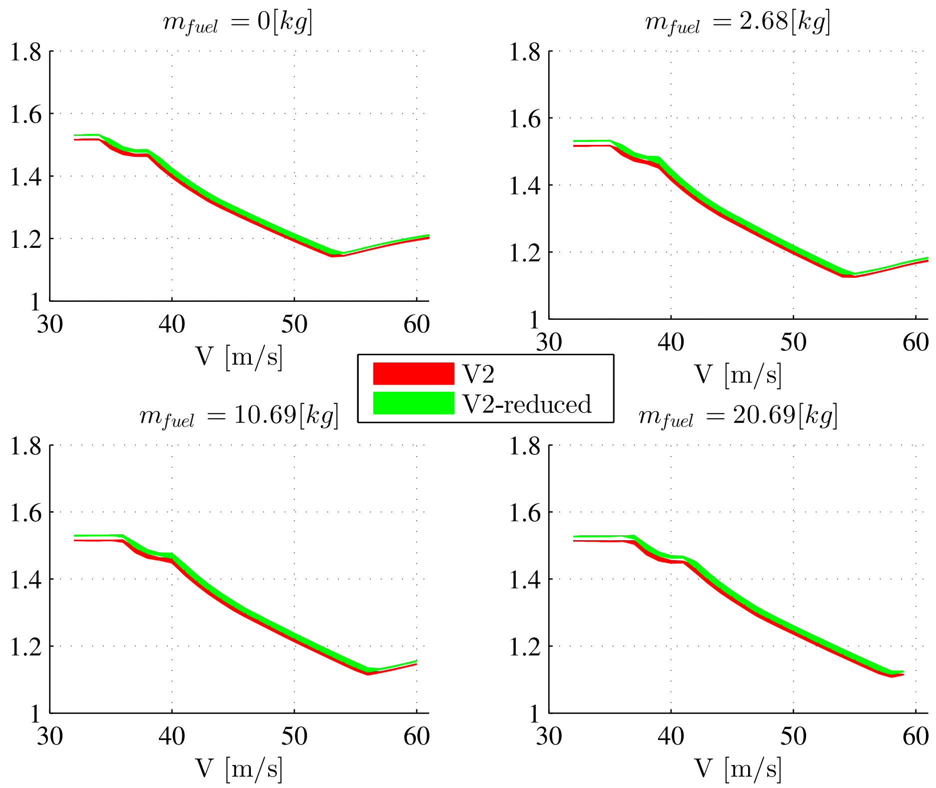

Figure 5.17.: Comparison of $|\Phi/\beta|$ ratio of *V2* and *V2* with $k_{I\dot{p}\beta} = 0$ (reduced)

$k_{I\dot{p}\beta}$ can be set to zero without altering the eigenmodes related to the rigid body states and, secondly that the suppression of this gain has no influence on the $|\Phi/\beta|$ ratio of the closed-loop system. In order to verify this, the feedback gain $k_{I\dot{p}\beta}$ of the *V2* - controller is set to zero by post-processing (i.e. after completing the gain design, and without altering the remaining structure and gains of the controller). The new controller variant created in this way is called *V2 - reduced*. Comparison of the $|\Phi/\beta|$ ratio of the original *V2* - controller and *V2 - reduced* - controller with $k_{I\dot{p}\beta} = 0$ is shown in figure 5.17. As anticipated, only marginal differences in the $|\Phi/\beta|$ ratio can be detected in this diagram, which confirms that the β - integrator feedback to $\dot{p}_{S_{cmd}}$ has only marginal impact on the $|\Phi/\beta|$ ratio and therefore can be suppressed in the controller design without a major impact on the closed-loop system dynamics.

The question now arises, whether the suppression can be taken into account during gain design instead of applying it in post-processing. In a first attempt to answer this question, the Constrained Eigenstructure Assignment algorithm with the corresponding structural constraint (suppression of $k_{I\dot{p}\beta}$) is applied to the system without altering the desired eigenvalues and eigenvectors, i.e using the eigenvalue and eigenvector specifications from the *V2* - controller design. This gain design results in a significant change in the feedback entry $k_{\dot{p}\beta}$. This can be understood by reference to the eigenvector shift matrix $\boldsymbol{S^v}$ in figure 5.16. The two variables which, through feedback to $\dot{p}_{S_{cmd}}$, have the most influence on the β - integrator eigenvector are the β feedback and the β integrator feedback. Since one of these two feedbacks is suppressed by the structural constraint, the other partially compensates for this in order to yield the desired eigenvector. This leads to an increase in the gain magnitude, which threatens the initial aim of reducing the impact of noise and turbulence on the actuation. The relationship between the made observations of the eigenvector shift matrix and the resulting feedbacks leads to the idea of adjusting the eigenvector specifications with the objective of reducing

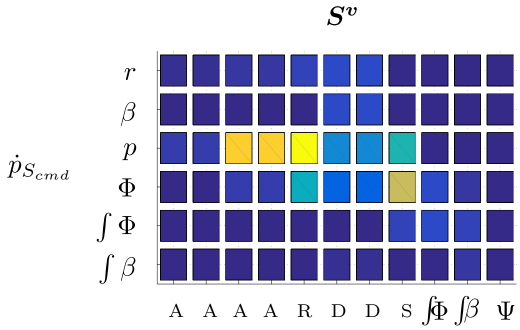

Figure 5.18.: *V2* - Eigenvector shift matrix for $v_{\beta=0}$

the impact of the feedback that is to be suppressed. This idea is applied below with the aim of suppressing the two integrator cross axes gains $k_{I\dot{p}\beta}$ and $k_{I\dot{r}\Phi}$. First of all several eigenvector candidates are defined, and for each of the these an Eigenstructure Assignment is performed. The resultant closed-loop system is used to calculate new eigenvalue- and eigenshift-matrices, which are subsequently analyzed w.r.t. to the magnitude of entries in the rows representing feedbacks to be suppressed, namely for the $k_{I\dot{p}\beta}$ the $\int \beta$ row of the $\boldsymbol{S^v}(\dot{p}_{S_{cmd}})$ and for $k_{I\dot{r}\Phi}$ the $\int \Phi$ row of $\boldsymbol{S^v}(\dot{r}_{S_{cmd}})$. It is found that the following specification for the integrator provides the best results, and hence the smallest entries in the eigenvector shift matrix:

$$\begin{array}{c} \\ r \\ \beta \\ p \\ \Phi \\ \int\Phi \\ \int\beta \end{array} \begin{array}{c} v_{\beta=0} \\ \begin{bmatrix} * \\ 0 \\ * \\ * \\ 1 \\ * \end{bmatrix} \end{array} . \tag{5.74}$$

The matrix $\boldsymbol{S^v}(\dot{p}_{S_{cmd}})$ which shows the influence of feedbacks to $\dot{p}_{S_{cmd}}$ is depicted in figure 5.18. From the eigenvector shift matrix it can be concluded that the eigenvector specification $v_{\beta=0}$ provides smaller entries in the $\int \beta$ row compared to the initial design. This means that the eigenvectors of the system will alter least if it is the feedback gain $k_{I\dot{p}\beta}$ which is suppressed.

A controller redesign matching the structure given in equation (5.73) and using an adjusted specification for the β-integrator eigenvector according to equation (5.74) leads to the controller version *V3*. The resulting feedback gains of the *V3* - controller are shown in figure 5.20. The *V3* - controller is slightly superior to the *V2* - *reduced* in terms of being closer to the desired Dutch-roll coupling, as can be seen in figure 5.19.

Stimulated by the work of Calvo-Ramon and Sobel, it has been demonstrated in this section, how gains that have no effect can be detected and suppressed. The method was applied to the *V2* - controller of the SAGITTA Demonstrator. In the present work the concept of decision matrices has been extended, and eigenvalue and eigenvector shift matrices have been introduced providing a thorough insight into the contribution of feedbacks to particular modes. It has been shown, how these matrices can be used to detect whether or not an entry, that has initially been identified as "relevant" by the decision matrices can nevertheless be suppressed without altering the eigenstructure of the rigid body system. In addition, it has been shown how eigenvalue and eigenvector shift matrices can be applied to adjust eigenvector specifications in such a way, that feedback entries can be suppressed with little impact on closed-loop dynamics.

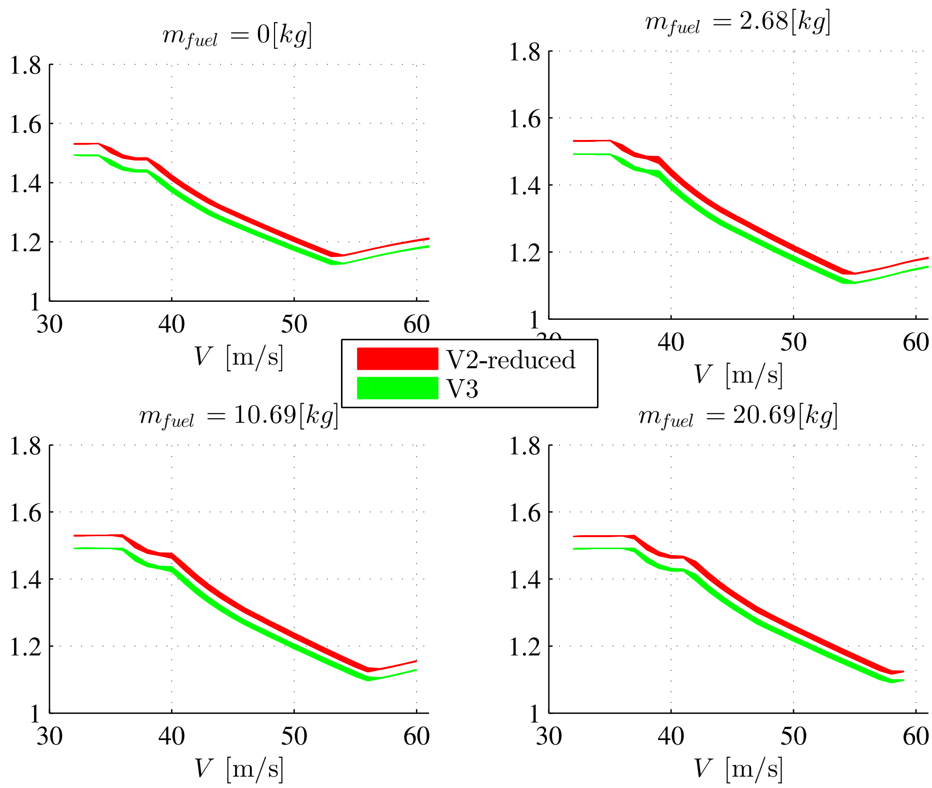

Figure 5.19.: Comparison of $|\Phi/\beta|$ ratio of *V2-reduced* and *V3*

5.6. Design of the controller without AoS feedback: *V4*

There are several reasons why feedbacks of aerodynamic flow angles are often avoided in controller design. One example is "...the difficulty of getting an accurate, rapidly responding, noise-free measurement..." and another: their "...vulnerability...to mechanical damage"[86]. In order to overcome vulnerability to mechanical damage, most modern commercial aircraft are equipped with multiple redundant sensors. Considerable effort is put into their precise design and assembly as well as the extensive calibration and testing required. The result is a complex and expensive system. Whether the designer can forgo the use of aerodynamic flow angles is often a question of reaching a compromise between the system's performance and robustness.

In the case at hand, where the performance is secondary to robustness, and where serious doubts exist whether AoS measurements with the assumed characteristics are suitable for use in feedback design, the elimination of AoS measurement can reduce the risk significantly and can become the key attribute of a robust design. For this reason, an attempt is made to eliminate AoS feedback from the gain design.

The starting point for these structural modifications is the feedback structure of the *V3* - controller. In addition to the less effective suppressed gains, which were considered in the *V3* - controller structure, all entries related to the AoS feedback, namely $k_{\dot{p}\beta}$, $k_{\dot{r}\beta}$, $k_{I\dot{r}\beta}$ are set to zero. Consequently, the β-integrator is removed from the plant model shown in figure 5.3. The resulting structure of the *V4* - controller is given in equation (5.75).

$$\boldsymbol{K}_4 = \begin{array}{c} \begin{array}{cccc} r & p & \Phi & \int\Phi \end{array} \\ \begin{bmatrix} * & * & * & * \\ * & * & * & 0 \end{bmatrix} \end{array}. \tag{5.75}$$

Since the feedback of this controller is composed of four variables, the number of eigenvalues that can be specified is limited to $r = 4$. Thus, having two system input channels via $\dot{p}_{cmd}$ and $\dot{r}_{cmd}$, two entries of the corresponding eigenvectors can be specified without restrictions. For the design of *V4* - controller, two Dutch-roll eigenvalues are specified, the third pole is given by roll subsidence and the forth by the spiral mode. Consequently, one eigenmode of the lateral rigid-body closed-loop system is left unspecified. The subsequent application of the Constrained Eigenstructure Assignment (CEA) provides a good match between desired and achieved eigenmodes. Unfortunately this is accomplished at the expense of incurring unstable aperiodic pole, which is provoked by a destabilizing feedback gain $k_{I\dot{p}\Phi}$.

In order to overcome the problem of this unstable integrator pole, inspired by control optimization using eigenstructure assignment as described in [79], a search algorithm is implemented, whereby the CEA is applied to a grid of eigenvalue specification candidates for roll subsidence, spiral mode and Dutch-roll mode. The resulting closed-loop systems are then checked w.r.t. stability and the $|\Phi/\beta|_{DR}$ ratio. Subsequently, the control effort of each controller candidate is calculated based on the approach given in [79] and in which control effort is defined by the following cost function J.

$$J = \sum_{i=1}^{r} ||\boldsymbol{m}_i||. \tag{5.76}$$

with

$$\boldsymbol{m}_i = \boldsymbol{KC}\boldsymbol{v}_{i,ach} \tag{5.77}$$

being the modal control vector corresponding to a particular eigenvalue. Finally, the controller selected for loop closure is the one which satisfies the requirements on stability and $|\Phi/\beta|_{DR}$ coupling at the same time is minimizing the cost function, and which therefore yields a system with minimum control energy.

A comparison of the feedback gains which result from conventional Eigenstructure Assignment for the *V2* - controller with those resulting from CEA for the *V3* and *V4* - controllers is shown in figure 5.20. Here, the spread of gains over altitude is projected into the two-dimensional plane of the paper. The spread is a result of applying the above-mentioned search algorithm, which focuses on stability, the roll yaw ratio and minimization of the control effort, but which does not take into account the variation of gains. Future gain design shall consider a minimization algorithm that penalizes the rate of change in the gains.

5.7. Turn Coordination

The functionality of turn coordination is an essential element of a controller design for lateral motion. It ensures that the yaw rate required for coordinated turns is established and maintained by the controller.

The expression for the yaw rate in coordinated turns is given below. It is revealed, that the implemented feedback controller already implicitly provides the desired functionality of turn coordination. In addition, it is explained how the controller structure can be modified to explicitly take into account the turn coordination and how it can be included in the eigenstructure assignment-based gain design procedure.

The condition for coordinated flight is achieved when the acceleration during a turn is aligned with the x-z plane of the aircraft. In coordinated turn the lateral acceleration

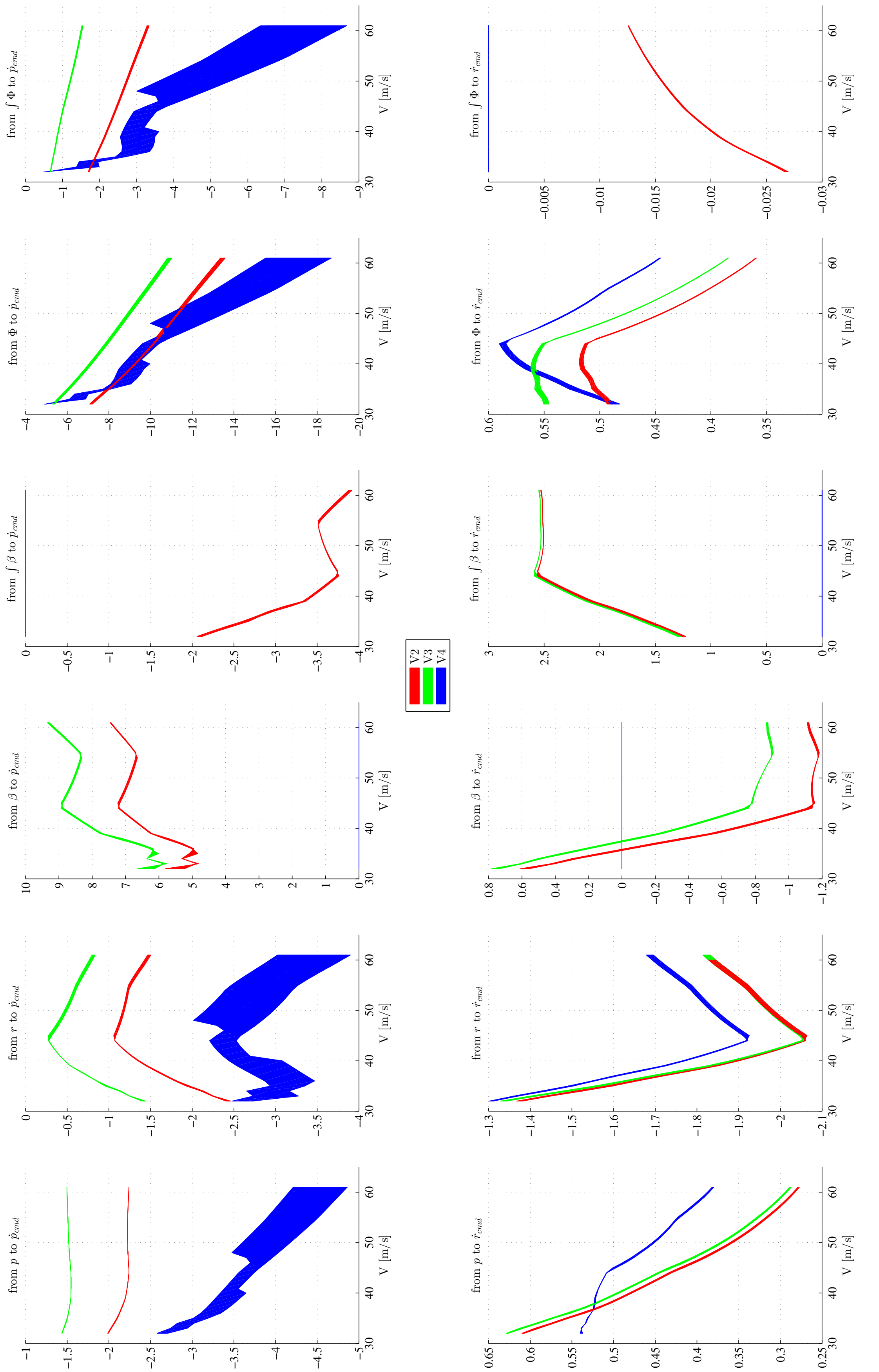

Figure 5.20.: Comparison of feedback gains of *V2*, *V3* and *V4*

in body axes is therefore zero. For a flight path angle $\mu_K = \mu_A$ (assuming no wind and a small AoS), this results in the following simplified condition:

$$\dot{\chi} = \frac{g}{V} \tan \Phi. \tag{5.78}$$

This condition can be achieved by establishing the appropriate rotation rates $\left(\boldsymbol{\omega}^{OB}\right)$ of the aircraft relative to the NED-frame (see appendix A.1.2). The rotation rates can be divided into the rotation between NED-frame and flight path $\left(\boldsymbol{\omega}^{OK}\right)$, and between flight path and body $\left(\boldsymbol{\omega}^{KB}\right)$ as follows:

$$\left(\boldsymbol{\omega}^{OB}\right) = \left(\boldsymbol{\omega}^{OK}\right) + \left(\boldsymbol{\omega}^{KB}\right). \tag{5.79}$$

In steady-state flight condition $\left(\boldsymbol{\omega}^{KB}\right) = 0$, the expression in equation (5.79) can be simplified to:

$$\left(\boldsymbol{\omega}^{OB}\right)_B = \begin{bmatrix} p \\ q \\ r \end{bmatrix} = \boldsymbol{M}_{BO} \left(\boldsymbol{\omega}^{OK}\right)_O \tag{5.80}$$

Considering the third row of this equation, and assuming level flight turn with $\dot{\gamma} = 0$, the following relation for the yaw rate can be derived:

$$r = \cos\Theta \cos\Phi \dot{\chi}. \tag{5.81}$$

After substitution of $\dot{\chi}$ in equation (5.81) using equation (5.78), the expression for the yaw rate in coordinated flight is obtained:

$$r = \frac{g}{V} \cos\Theta \sin\Phi. \tag{5.82}$$

Linearization of the expression in equation (5.82) leads to:

$$\delta r = \frac{g}{V_0} \left(\cos\Theta_0 \cos\Phi_0 \delta\Phi - \sin\Phi_0 \sin\Theta_0 \delta\Theta\right), \tag{5.83}$$

in which the index 0 denotes the reference operating point. With $\Phi_0 = 0$, that is, linearization in level flight, the equation collapses to

$$\delta r = \frac{g}{V_0} \cos\Theta_0 \delta\Phi. \tag{5.84}$$

Turn coordination is thereby expressed as a function of velocity and pitch attitude at a reference operating point 0 and the current bank angle.

As presented in [8], for example, there are several possibilities for incorporating turn coordination into the flight control system. One suitable approach is to introduce a yaw rate command that is equivalent to the turn coordination term presented above. Other options exist, for example, those which involve feedback of lateral acceleration or AoS. Such approaches are not considered in this work since they introduce sensor measurements which would otherwise not be required, and which would add further complexity and therefore higher risk to the system.

In the work up to this point, coordination has been implicitly taken into account by the Eigenstructure Assignment. It is implemented in the feedback $k_{\dot{r}\Phi}\Phi$ and is enforced by specification of roll and spiral mode eigenvectors.

The turn coordination can also be explicitly integrated in the controller by introducing into the augmented plant a new feedback variable $\tilde{r}$ which combines the yaw rate measurement and the turn coordination command:

$$\tilde{r} = r_{meas} - \frac{g}{V_0} \cos\Theta_0 \Phi_{meas}. \tag{5.85}$$

The resulting feedback matrix $\boldsymbol{K}$ has the following structure:

$$\boldsymbol{K} = \begin{array}{c} \begin{array}{ccccc} r & \tilde{r} & p & \Phi & \int\Phi \end{array} \\ \begin{bmatrix} * & 0 & * & * & * \\ 0 & * & * & 0 & 0 \end{bmatrix} \end{array}. \tag{5.86}$$

In this way, the two gains $k_{\dot{r}\Phi}$ and $k_{\dot{r}r}$ are replaced by $k_{\dot{r}\tilde{r}}$. The CEA can now be applied to the augmented plant which includes $\tilde{r}$. The eigenvalue and eigenstructure specifications remain unchanged compared to the *V4* - controller.

While V_0 and $\cos\Theta_0$ in the gain design are constant values obtained from trimming the aircraft at the operating point of interest, in the final controller, the nonlinear relationship in equation (5.82) is implemented, where V and Θ are feedback variables.

In cases where the turn coordination is implicitly taken into account in the gain design process, the feedback from Φ to $\dot{r}_{cmd}$ may provide further functionalities and thus, cannot be assigned to one single feature. Incorporation of the coordination term into the linear feedback design assigns a physical meaning and a dedicated, single functionality to the feedback from Φ to $\dot{r}$ which increases the physical insight into the controller structure.

The block diagram of the resulting rate loop is depicted in figure 5.21. Since the feedback gains from Φ and $\int\Phi$ to p_{cmd} are organized in the attitude loop, they are omitted in this diagram. The *V4* - controller represents the final solution for feedback design. All further considerations regarding feed-forward design and additional controller elements are based on this result.

5.8. Feed-Forward Design

The feed-forward element of the controller provides the possibility of shaping the tracking dynamics of the closed-loop system without altering the disturbance reaction [8] and stability margins. It is used to obtain a desired transient response to a command, and to achieve steady-state tracking accuracy. Furthermore, a well-designed feed-forward controller can improve the Flying Qualities and can help to reduce the system's susceptibility to PIOs.

Based on the experience gained during the "preliminary controller design and manual landing study" [7] it is decided to implement an AC/AH response type controller for lateral motion. Due to the unconventional aircraft form without pronounced wings and the large operating range, the task of manually controlling the aircraft is very complicated. Therefore, by choosing an AC/AH behavior for the CSAS, the External Pilot's task of manually controlling the aircraft is simplified. By anticipating the attitude of the diamond wing based on the stick position on the transmitter, the External Pilot is able to control the aircraft in an extended range without direct visual contact. Furthermore, by using a AC/AH system the pilot changes the manner of controlling the flight path of the aircraft. The input bandwidth to the CSAS is expected to decrease and the pilot is expected to control the attitude more or less in an open-loop

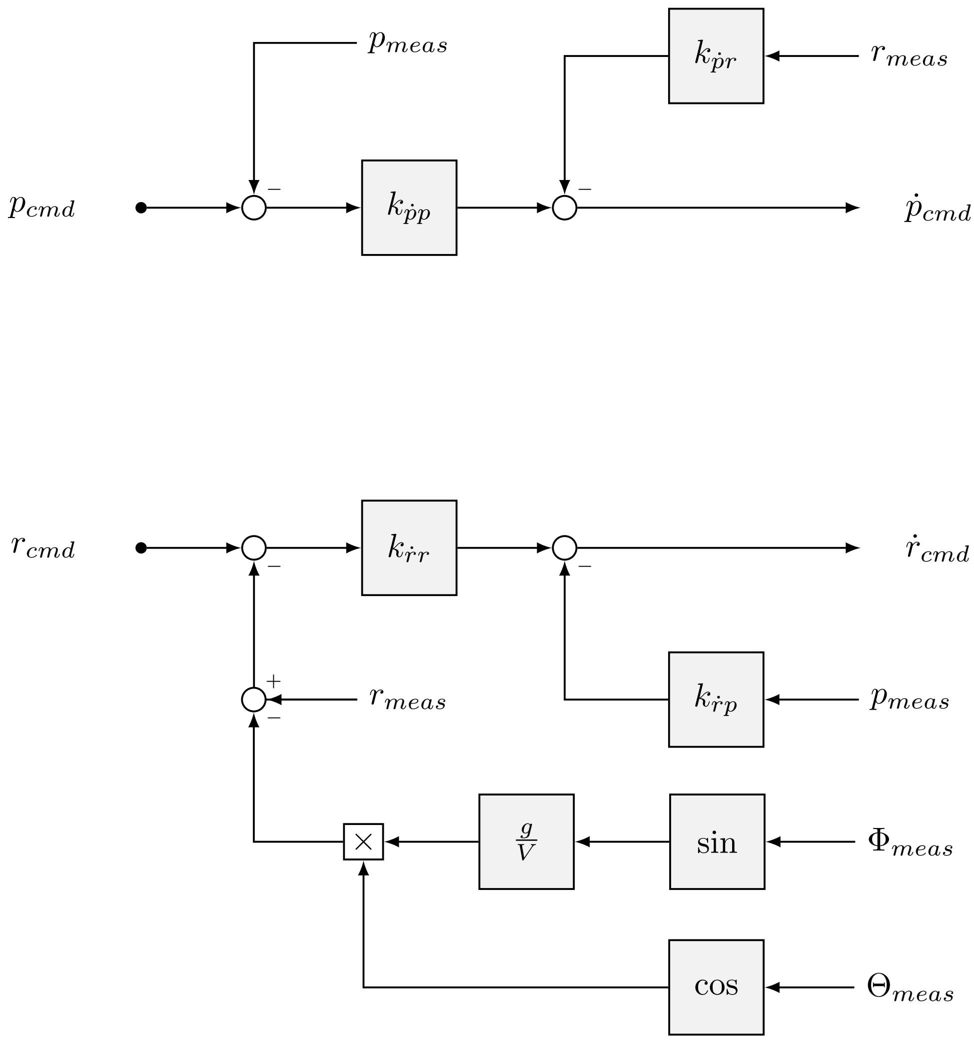

Figure 5.21.: Rate loop with turn coordination

manner. It must be noted that the use of an unconventional response type in the CSAS represents a particular challenge for analysis of Flying Qualities and PIOs, since many well-established evaluation methods do not apply to this kind of system. In order to address this topic, this work includes an extensive study on Flying Qualities analyses in chapter 4, and presents analyses applicable on AC/AH that are utilized in chapter 6.

The proposed feed-forward design consists of a pure gain fed by the bank angle command Φ_{cmd}. The corresponding block diagram is shown in figure 5.22. The advantage of this structure lies in the additional degree of freedom that is introduced by the direct feed-through proportional gain $h_{p\Phi}$, which can be selected to, for example, satisfy tracking requirements.

Several guidelines for how to select the feed-forward gain can be found in the literature. One of the approaches is to select the gain in such a way that steady-state accuracy is achieved, thereby limiting the integrator's functionality to rejection of stationary disturbances. During development of the controller, it was observed, that this approach may lead to considerable amplification of the command and often results in high overshoot of the tracking variable. Consequently, another approach has been selected for the lateral CSAS of the SAGITTA Demonstrator. It is comparable to the one in [28]. Here, the additional degree of freedom is utilized to cancel the integrator pole of the controller in the feed-forward path. In this way the integrator is "hidden" from the pilot

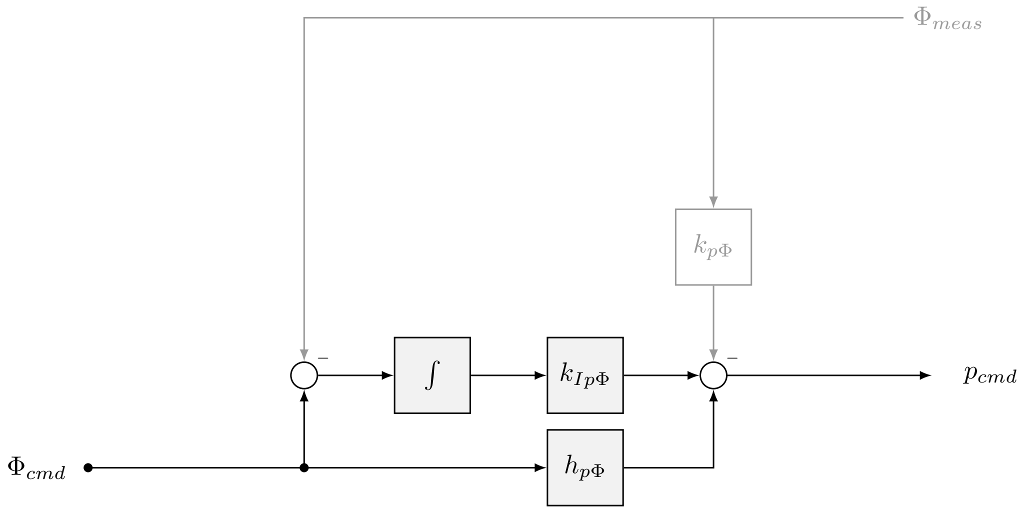

Figure 5.22.: Feed-forward design

in order to achieve an aircraft reaction that the pilot is accustomed to, and consequently to obtain better Flying Qualities. The cancellation is achieved by calculation of the feed-forward gain $h_{p\Phi}$ according to

$$h_{p\Phi} = -\frac{k_{Ip\Phi}}{\lambda_I}, \tag{5.87}$$

where λ_I represents the integrator pole of the controller.

5.9. Command Filter Design

To reduce the vulnerability of the system to PIOs, some control systems are equipped with a command rate limiter, to prevent actuator limits from being reached as a result of aggressive commands from the pilot. By limiting the rate of command, the phase shift that is associated with operating at the actuator limits is avoided, and there is therefore no negative impact on closed-loop stability of the aircraft system. Nevertheless, this approach has its drawbacks. When the pilot closes the control loop by, for example, performing a tracking task, the rate limiter in the command path of the controller becomes part of the closed-loop system and as a result may negatively affect the overall stability margins of the pilot-aircraft system. Consequently, when a nonlinear command element is introduced into the feed-forward path of the controller, a PIO analysis must be performed to confirm resistance of the pilot-aircraft system to PIO .

Instead of adding a rate limiting element into the system, and subsequently to perform a PIO analysis on the pilot-aircraft system, another approach to solve the actuator rate limit issue is proposed below, one which does not introduce an additional nonlinear element (command rate limiter), but instead a linear filter and which therefore does not require further pilot-vehicle analysis. The approach is based on the OLOP analysis. It uses the method of determination of the ω_{onset} as means of command filter design. The idea is to shape this filter in such a way that the actuator limit under consideration cannot be reached through sinusoidal pilot commands of any particular frequency. To achieve this, the closed-loop transfer function from pilot command input to the relevant actuator deflection δ is employed:

$$G_{\delta\Phi_{cmd}}(s). \tag{5.88}$$

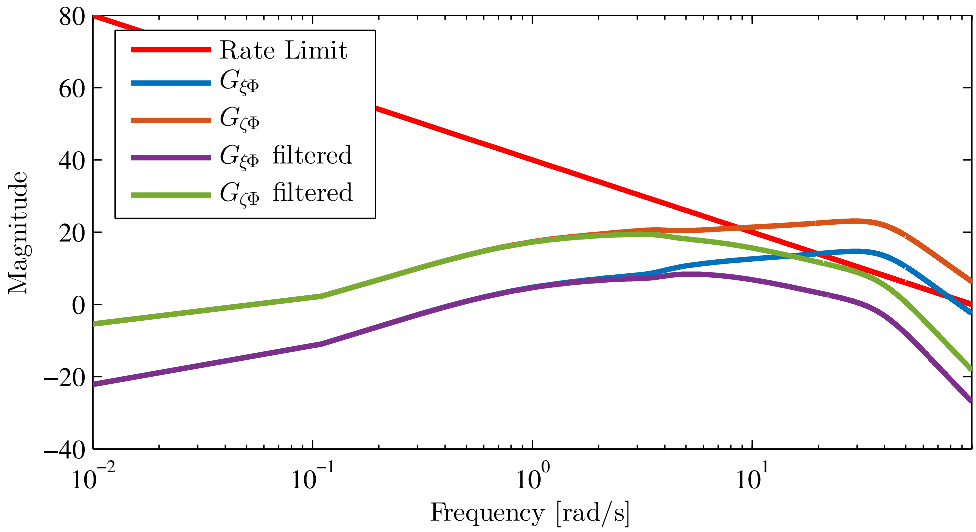

Figure 5.23.: Influence of the command filter on the closed-loop transfer function to actuator

This transfer function is supplemented by a linear command filter (e.g. first order):

$$H_{hq}(s) = \frac{1}{T_{hq}s + 1}. \tag{5.89}$$

The filtered transfer function

$$G_{\delta\Phi_{cmd,hq}} = G_{\delta\Phi_{cmd}}(s)H_{hq}(s), \tag{5.90}$$

scaled by the maximum command input ($\Phi_{cmd} = 30°$), is tuned so that the overall magnitude of the frequency response from command to actuator remains below the rate limit. This is done by adjusting the filter's time constant T_{hq}. For closed-loop systems with multiple actuators, as is the case for lateral motion of the SAGITTA Demonstrator, the OLOP analysis must be performed for all applicable actuators and the command filter shall be adjusted in such a way, that the rate limitation cannot be triggered in ξ_{equiv} and in ζ_{equiv} by pilot's inputs. Figure 5.23 shows the scaled frequency responses $G_{\xi\Phi}$ and $G_{\zeta\Phi}$ of the closed-loop system before and after application of the filter. It can be seen that the unfiltered command drives the ζ_{equiv} and ξ_{equiv} actuators into their limits at $\omega \approx 8\,\mathrm{rad\,s^{-1}}$ and $\omega \approx 18\,\mathrm{rad\,s^{-1}}$ respectively. This is not necessarily a sign that the closed-loop system is susceptible to PIOs, since the ω_{onset} might occur in a frequency region which is "safe" according to OLOP. In order to access how critical the rate limitation is at ω_{onset}, the closed-loop system must be cut at the actuator, and the location of ω_{onset} in the frequency response of the transfer function $G_{\delta\delta}(s)$ in the Nichols Chart must be analyzed. This step is omitted here. Instead, by inserting the filter $H_{hq}(s)$, the transfer function from command input to the actuator is modified so that it does not intersect with the line representing the rate limit. This ensures that there is no onset frequency that could lead to PIOs. Obviously, the filter design can also be completed using any higher order filter, if more control over the shape of the frequency response is desired.

5.10. Reduction of Scheduling Variables

Up to this point, the controller design has been completed for all operating points in the envelope. The result is a gain set, where the gains vary with speed, altitude and fuel mass. While speed and altitude can be obtained easily from the ADS, a direct measurement of the fuel mass is not available. The information concerning the fuel mass is based on the initialization before the engine start and integration of the fuel flow over the period of operation.

To make the closed-loop system as robust as possible, it is desirable to reduce the number of scheduling variables and thus the dependence on sensors and other system components. When considering which scheduling variables may be excluded from the controller design, the prime candidate is the fuel mass, since, as explained above, this is a highly uncertain, and therefore untrustworthy quantity due to the free integration of inaccurate fuel flow information. Moreover, by taking fuel mass out of the controller design, the Utility Control Electronics providing the fuel flow information, would be removed from the list of flight critical components, which is an additional reason for pursuing this course of action.

Several approaches are available to eliminate the dependency of the flight controller on aircraft fuel mass. One straight-forward solution is to perform the gain design for one fixed fuel mass and subsequently to apply the resulting gains to all operating points without taking the changing mass into account: in other words to omit the variation of fuel mass in the controller design. The value of the fixed fuel mass could be selected such that it equates to the most critical aircraft configuration (for instance w.r.t. stability). In this way, when the aircraft is operating in such conditions, the control system would have appropriate gains to ensure the desired stability margins. With this approach, it is necessary to investigate, whether the closed-loop system provides satisfactory solution in all operating points and therefore stable closed-loop systems with acceptable stability margins. Ignoring the variation of mass during gain design is a simple, yet effective approach for configurations where the influence of mass variation on aircraft dynamics is less pronounced.

Another effective means of reducing the number of scheduling parameters is the Multi-Model Eigenstructure Assignment, which was successfully applied in [27] to lateral control of an aircraft. The concept behind this approach is to select multiple plant models for gain design, where the selection of the plants is made based on particular unfavorable characteristics, for example, minimum stability margins. In the case of lateral motion one can select three plants, with the first being the most critical in terms of Dutch-roll; the second corresponding to the most unfavorable roll subsidence characteristics; and the third having the spiral pole with the smallest time-to-double. The goal of the gain synthesis is to obtain a single feedback matrix which offers a compromise that leads to acceptable characteristics at all operating points. This approach can be used in combination with Constrained Eigenstructure Assignment.

Since both approaches, disregarding the mass variation or applying the Multi-Model Constrained Eigenstructure Assignment (MMCEA), lead to acceptable results for the applicable flight envelope, the approach which is simpler to implement (i.e. gain design using a fixed fuel mass) is chosen. In order to achieve the best results for the landing phase, $m_{fuel} = 3\,\mathrm{kg}$ is selected as the reference mass for gain design.

5.11. Overall Controller Design - Summary

The evolution of the controller structure and gain design for lateral control of the SAGITTA Demonstrator are presented in this chapter. A description is given as to how particular aspects of aircraft configuration, such as dynamic couplings; sensor characteristics; as well as the concept of control via an External Pilot are taken into account during the development.

The resulting design consists of a control allocation that distributes the stability-axes roll and yaw moments to equivalent surfaces. A rate controller incorporating turn coordination is built upon the control allocation. Finally, an attitude feedback controller and corresponding feed-forward controller are designed for precise bank angle control. The feed-forward design is augmented by a command filter, which prevents actuators being driven into their limits as a result of aggressive pilot or outer-loop commands. The overall controller assembly is depicted in figure 5.24.

The architecture presented is characterized by use of a minimum number of feedback variables and gains. This saves resources in terms of memory and computational load. It forgoes any utilization of air flow angle measurements, GNSS data, or fuel mass information, making the controller robust to many potential system failures. It provides a level of $|\Phi/\beta|_{DR}$ decoupling that is comparable to that of a full output feedback design.

Although not presented in this thesis, it is worth mentioning that based on the *V3* - version of the feedback controller, a Φ and β - command system has been developed in parallel to the first flight controller. This can be used as a substitute for the latter, as soon as the ADS characteristics are shown to be better in flight than is suggested by the wind tunnel results.

In addition to the controller design, this chapter also describes novel methods for analyzing actuator activity resulting from either sensor noise or atmospheric disturbances such as turbulence. Furthermore, the gain sensitivity analysis from Calvo-Ramon and Sobel is extended and applied to the feedback controller of the SAGITTA Demonstrator. This method provides a more complete insight into the influence of particular feedback gains on the dynamic modes of the system.

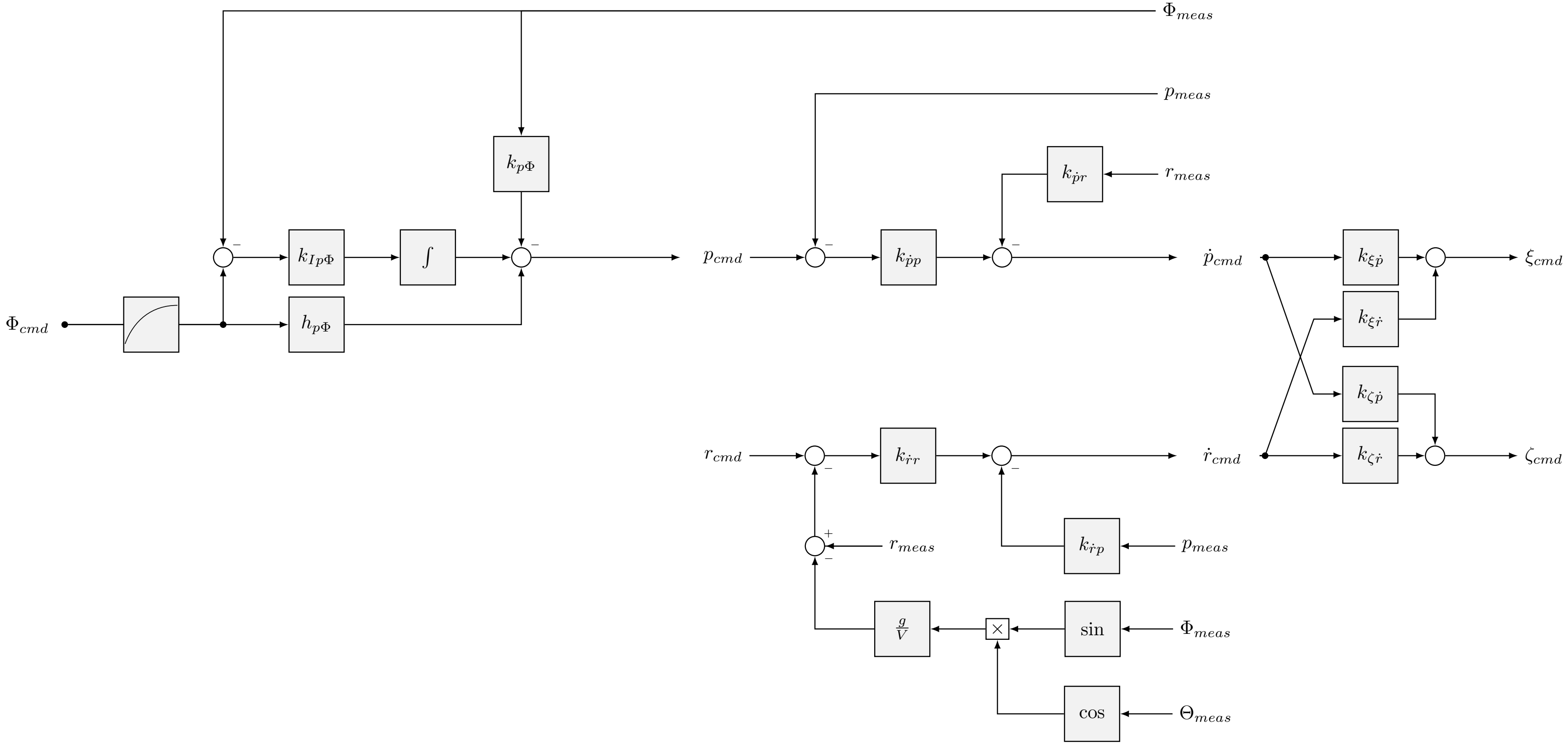

Figure 5.24.: Controller architecture assembly

6. Analysis of the Closed-Loop System

The FMS of the SAGITTA Demonstrator has undergone an extensive requirements-based verification process which was built into an industrial development life cycle. This process included the verification of hardware (e.g. sensor time delays and Electromagnetic Compatibility (EMC) testing), carry flight tests of sensors, system architecture reviews and system safety analyses.

As mentioned earlier, the work at hand focuses on the flight dynamics aspects of FMS design. Consequently, all other aspects of FMS verification are disregarded here.

In this chapter the gain design results are compared with the expected outcome through which the gain design method is validated. Subsequently, an incremental analysis of the closed-loop system's behavior is performed. Particular effects are analyzed both, individually and in relevant combinations. The objective of this exercise is to assess the controller design w.r.t. the requirements given in section 4.7. Finally, this chapter aims to provide evidence of safe closed-loop system behavior throughout the specified envelope taking into account the changes in system characteristics over the envelope; the specified system uncertainties; and a range of atmospheric conditions. In the case of the SAGITTA Demonstrator, safety is not aimed at safeguarding human life, but rather, the aim of quality assurance using so-called clearance process is to maximize the probability of a successful first flight of the SAGITTA Demonstrator and hence to minimize the probability of aircraft loss due to controller design errors.

The issues which are subject to flight controller clearance are, inter alia, verification of the plant model; review of the control algorithm; and evaluation of the behavior of the closed-loop system. For this purpose, the system is assessed in frequency domain, for example by means of stability analysis, and in linear and nonlinear time domain simulations using Model-In-The-Loop (MIL) testing. The outcome of the clearance process is the confirmation of the suitability of the control algorithm and gain design for the intended flight mission together with flight permission from the clearance authorities.

The final step in validation of an FMS is demonstration of its functionality in flight. The V&V activities are therefore concluded in chapter 7 by presenting the results of the first flight to reveal the outcome of the work outlined in this thesis.

6.1. Envelope

One of the major end results of the flight control analysis is the determination of an envelope in which safe flight operations are possible. MIL-HDBK-1797A specifies three envelopes for manned aircraft: The "Operational Flight Envelope" defines the conditions, under which the aircraft in nominal (failure-free) state provides Level 1 Flying Qualities. Within this envelope, system failures are allowed to lead to a degradation to Level 2 or Level 3 Flying Qualities once per 100 flights[85]. The "Service Flight Envelope" is derived from aircraft limits such as maximum speed or service ceiling. The "Permissible

Flight Envelope" encompasses all flight conditions that are allowable and reachable and from which the aircraft can safely return to the Service Flight Envelope [57]. In this work the concept of a "Design Envelope" is introduced. This is defined as the speed, altitude and fuel mass range for which the aircraft can be trimmed in steady-state straight level flight. The trim results defining the Design Envelope are given in table 6.1. The controller design and analysis are performed for each point in this envelope. The

	Range	**Unit**
$\boldsymbol{V}$	$32 - 59$	$\mathrm{m\,s^{-1}}$
$\boldsymbol{h}$	$50 - 150$	m
$\boldsymbol{m_{fuel}}$	$0 - 21$	kg

Table 6.1.: Design Envelope

Design Envelope is used as the basis for determining the Operational Flight Envelope. By introducing a constraint on maximum AoA in level flight, the lower speed threshold of the Design Envelope is obtained. For this, the maximum allowed trim Angle-of-Attack ($\alpha_{trim,max}$) is selected such that a margin of 6° is present at all operating points between $\alpha_{trim,max}$ and the absolute maximum AoA for which aerodynamic measurements are available from wind tunnel tests. This margin takes into account maneuvering (e.g. pull-up, push-over or turns), sensor uncertainties and atmospheric disturbances. The resulting envelope is the initial Operational Flight Envelope which is subject to further analyses below and is shown in table 6.2, where red fields indicate invalid envelope points, corresponding to $\alpha_{trim} > \alpha_{trim,max}$. In order to simplify further analysis, as well as the clearance process, the initial Operational Flight Envelope is made rectangular and the minimum speed for all fuel mass configurations is set to $V_{min} = 35\,\mathrm{m\,s^{-1}}$.

6.2. Analysis of Nominal Feedback Design

Due to the structural constraints imposed on the controller, application of the CEA produces results that constitute an approximation of the exact Eigenstructure Assign-

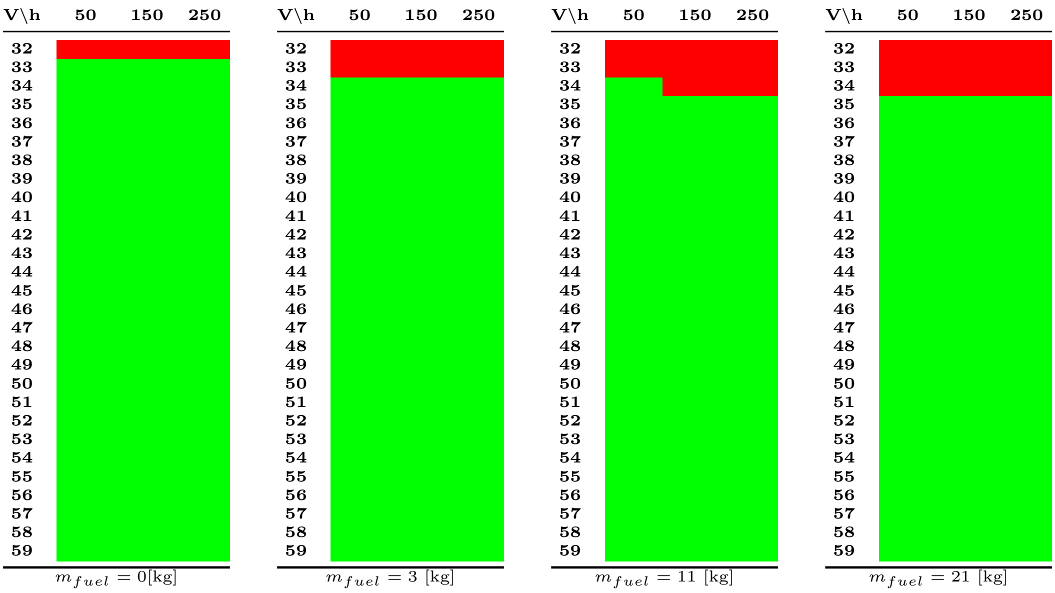

Table 6.2.: Initial Operational Flight Envelope

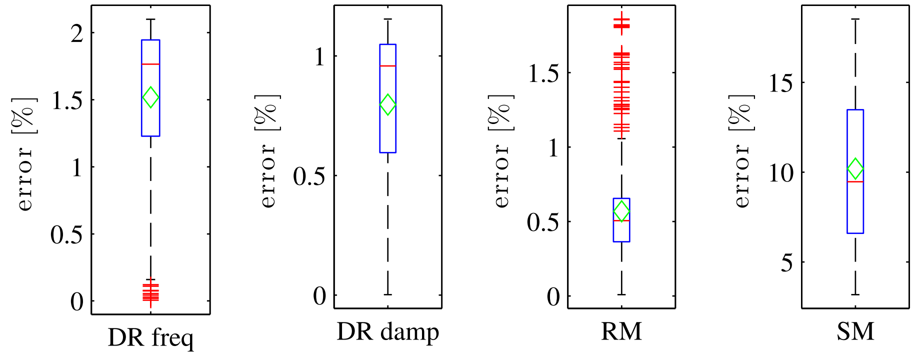

Figure 6.1.: Comparison of desired and achieved closed-loop eigenvalues

ment. As a consequence, the achieved eigenstructure differs from the target specification. In order to obtain a quantitative measure of the difference between the exact and approximate EA, the gain design method is evaluated in the first step of closed-loop system analysis. For this purpose, the achieved closed-loop pole locations are compared with the desired ones for each point in the Design Envelope. Figure 6.1 shows the relative error between the achieved and the desired pole locations over the entire envelope. The red line indicates the median value of the error between desired and achieved pole locations. The box around the red line represents 50 % of the errors and the black vertical lines indicate 150 % of the blue box size in each direction. All other points beyond the black lines are depicted as red crosses and indicate outliers. Furthermore, green diamonds have been added to the box plots to denote the mean values for particular quantities. These diamonds can be interpreted as the magnitude of the error that may be expected. The results for Dutch-roll (DR) and the Roll subsidence (R) show a fairly good correlation between desired and achieved pole locations. The spiral pole (SM) shows sizable deviations of up to $\approx 18\,\%$. The reason for this is mainly the small but present sensitivity of the eigenvalues of the closed-loop system to changes in the entry $k_{I\dot{r}\Phi}$. Since this entry is suppressed in the gain design, the differences between desired and achieved closed-loop eigenvalues can be attributed to the chosen structure of the feedback matrix. It should be noted that the spiral pole's absolute error is fairly small due to its location close to the origin of the complex plane and hence, its small eigenvalue. For this reason, the disparity between the desired and achieved spiral poles is tolerated in favor of a simpler controller structure.

After assessing the eigenvalues of the closed-loop system, the roll-yaw couplings are analyzed. These are depicted in figure 6.2 in terms of the $|\Phi/\beta|_{DR}$ ratio of the Dutch-roll eigenvector. The first abnormality that can be seen is the absence of the closed-loop values at high AoAs i.e. at high mass and low speeds. At these operating points no feedback that would fulfill the stated requirements was found during the search performed as described in section 5.6. Specifically, in this area of the envelope the desired $|\Phi/\beta| \leq 1.5$ was not achieved by the selected architecture. This does not represent an issue, as the points of concern are located outside the clearance envelope, which is defined by the maximum of $\alpha_0 = 12°$. However, for the sake of robustness, the gain set is extended for these particular points by clipping the gain values at the level pertaining to the last valid point in the speed envelope and holding these constant across the problematic speed range. The resulting $|\Phi/\beta|_{DR}$ ratio of the closed-loop system with the gains held constant at low speed is provided in figure A.3 in the appendix A. Apart from the problem at the edges of the envelope described above, the closed-loop system yields a satisfactory result in terms of roll-yaw couplings: the $|\Phi/\beta|_{DR}$ ratio of the closed-loop system remains below that of the inherent dynamics and never exceeds the

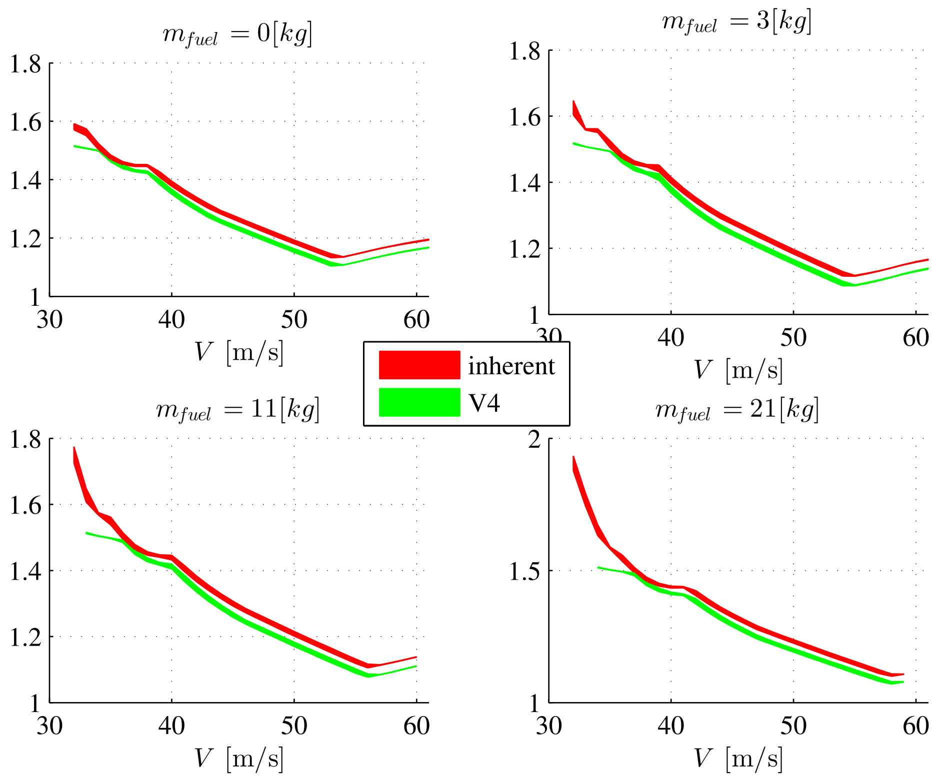

Figure 6.2.: Comparison of inherent and *V4* - controller $|\Phi/\beta|$ ratio

value of $(1 + \Delta_{tol})|\Phi/\beta|_{des}$, where $\Delta_{tol} = 0.05$. In summary, it can be said that based on the analyses completed to this point, the gain design exhibits satisfactory results.

In the next step, the stability and robustness of the nominal closed-loop system are assessed in the Nichols Chart w.r.t the stability diamonds that have been specified in figure 4.1. Besides diamonds in figure 4.1 representing nominal and tolerated conditions, the conventional diamond from [8] is for reference also included in the figure as a dashed line. For the analysis the closed-loop system is cut at the locations that are subject to stability analysis. This is done for each location separately. While the signal under study is cut, all other connections in the controller remain closed. It is common practice to perform the analysis only on the so-called "bottleneck" cuts in order to limit the stability analysis to few pertinent signals. It is reasonable to define the "bottlenecks" as those locations in the system at which the resulting gain and phase margins can be attributed to particular physical properties of the system. The actuator inputs are often chosen as such "bottlenecks" and in this case the resulting gain margin at the actuator inputs can be interpreted as the amount of additional uncertainty in the particular control surface's efficiency that would lead to instability. By analyzing the time delay margins at these locations, it is possible to anticipate a transport delay between the FCC and the control surface deflection that would drive the system to instability. Furthermore, by cutting the loop at the actuator input, it is also possible to analyze the effect of actuator loss on the overall stability by, for example, evaluation of the open-loop poles. Figures 6.3a and 6.3b show the "bottleneck" cuts at the actuator inputs for ξ_{equiv} and ζ_{equiv} respectively in terms of frequency response in the Nichols Chart and the corresponding gain-, phase- and time delay margins. The gray area represents the hull curve for the entire Design Envelope, whereas the colored lines denote specific points highlighted within the envelope corresponding to the combinations given in table 6.3. It can be seen in both frequency responses that the nominal diamonds

Nr.	V [m/s]	h [m]	m_{fuel} [kg]	Color
1	36	50	0	
2	36	250	21	
3	45	150	3	
4	45	150	11	
5	59	50	0	
6	59	250	21	

Table 6.3.: Prominent points of the Design Envelope

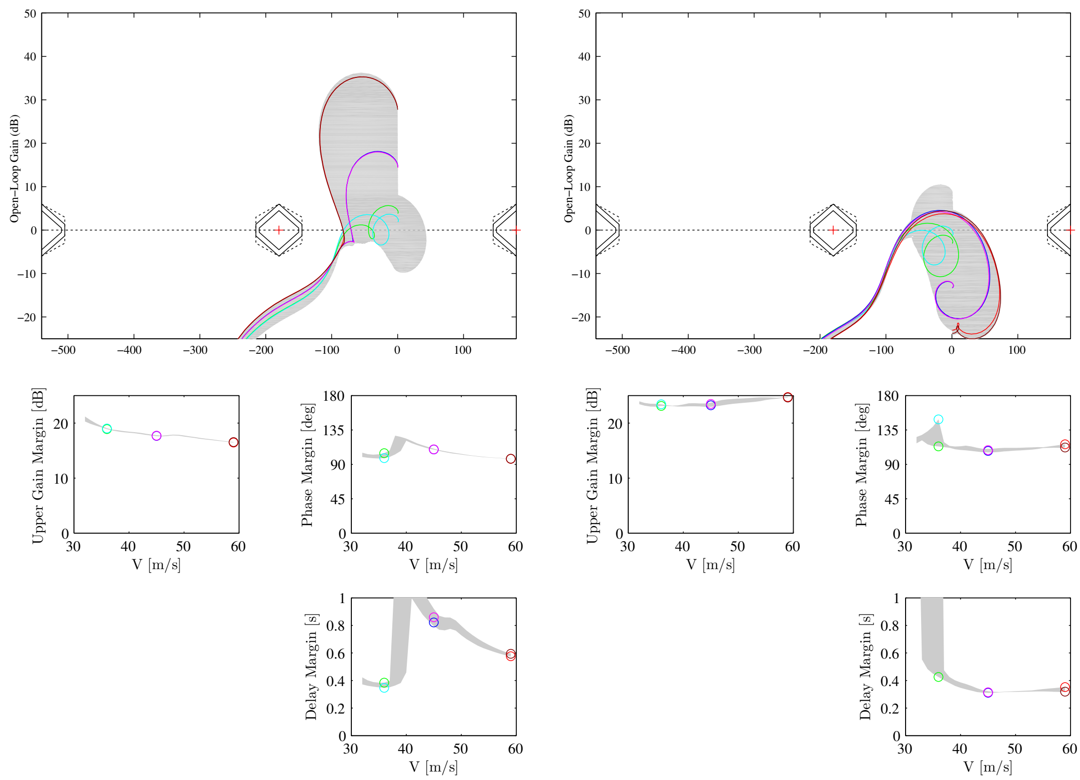

(a) ξ_{equiv} - cut (b) ζ_{equiv} - cut

Figure 6.3.: Stability - (nominal, without delays)

around the critical point, given by the red cross, are not violated. Thus, it is concluded that the nominal system without delays complies with the stability requirements.

A large scatter is noticeable in the hull curve of the delay margin at small speeds. This can be explained by taking a closer look at the course of the frequency responses. It can be seen that the frequency responses representing the system at low speeds exhibit loops which may cross the open-loop gain line $A = 0\,\text{dB}$ one or more times at different frequencies. In such cases, final intersection with the $0\,\text{dB}$ line determines the phase and delay margins. The loops in the frequency response plots reflect the sensitivity to uncertainties since, for these loops, only slight variations in the open loop gain may result in significant changes to the delay margin. Consequently, uncertainties affecting the gains of open loop transfer function only marginally, may lead to large variations in the delay margins. In situations such as this, uncertain systems must therefore be analyzed carefully w.r.t. delay margins.

It might be concluded from the two Nichols Diagrams presented above that the controller could be amplified more strongly, since the distance between the frequency response and the diamond is fairly large. However, it will be shown later that by introducing the expected time delays and uncertainties, the frequency responses of the bottleneck cuts will move close to the diamond and consequently stronger amplification of the controller would result in violations of the stability boundaries.

Although the analysis of "bottleneck" cuts is often sufficient for stability clearance, analysis of loop cuts at other locations of a MIMO system may provide important additional information to the designer. Cuts at sensor outputs give an idea of how much additional gain and time delay are acceptable for a particular feedback and thus give an estimate of the required sensor characteristics. Furthermore, a cut at the sensor output provides an insight into the impact a sensor loss would have on the system's stability. For a deeper insight into the stability characteristics of the closed-loop system more information can be found in appendix A.4, where the sensor cuts for undelayed systems without uncertainties are described.

Having discussed the stability characteristics, the disturbance rejection properties of the nominal closed-loop system without time delays are now analyzed. For this purpose, lateral gust, as specified in section 3.8, is injected into the β_W input of the closed-loop system. Typically, the gust is tuned so that particular eigenmodes of the aircraft are excited. However, in this work, instead of tuning the gust to the eigenmodes of the system, light and moderate gusts of four different lengths are applied: an approach which is accepted by the clearance authorities. Figures 6.4 and 6.5 show the reaction of the closed-loop system to such disturbance for the operating points shown in table 6.3. The mapping of gust length to color can be found in table 3.9. As stated in section 3.11, the β_W resulting from light and moderate gusts is relatively large compared to that of manned aircraft which operate at higher speeds. Consequently, the SAGITTA Demonstrator is stimulated significantly by such gust inputs. The reaction of the closed-loop system shows an obvious improvement compared to the inherent reaction of the aircraft. The system is more strongly damped, and therefore, oscillations decay very fast. Furthermore, an improvement in the $|\Phi/\beta|_{DR}$ ratio at low speeds is apparent. This is illustrated by the smaller disturbance in Φ, which is almost halved compared to the reaction of the uncontrolled aircraft. The actuator activity portrayed in figure 6.5 shows small to moderate deflections of the control surfaces and actuator rates which stay well below the specified limits. It can be seen that the activity of the outboard flaps is more pronounced than that of the midboard flaps, but remains within a reasonable range.

In summary, it can be concluded that the feedback design for the nominal system without delays provides a significant improvement w.r.t. stability and disturbance rejection.

6.3. Tracking Behavior

After analysis of the feedback design, the tracking behavior of the nominal system without delays is evaluated w.r.t. conventional performance criteria such as rise time, settling time, overshoot and undershoot. Standard definitions for the first three of these quantities are provided in [78]; the last can be derived in the same manner as the definition of overshoot.

Before starting the analysis, a custom definition of the settling time is established. This is based on the attitude hold requirement introduced in chapter 4, where it is specified that, after a 5° bank angle disturbance, the aircraft returns to wings level and achieves

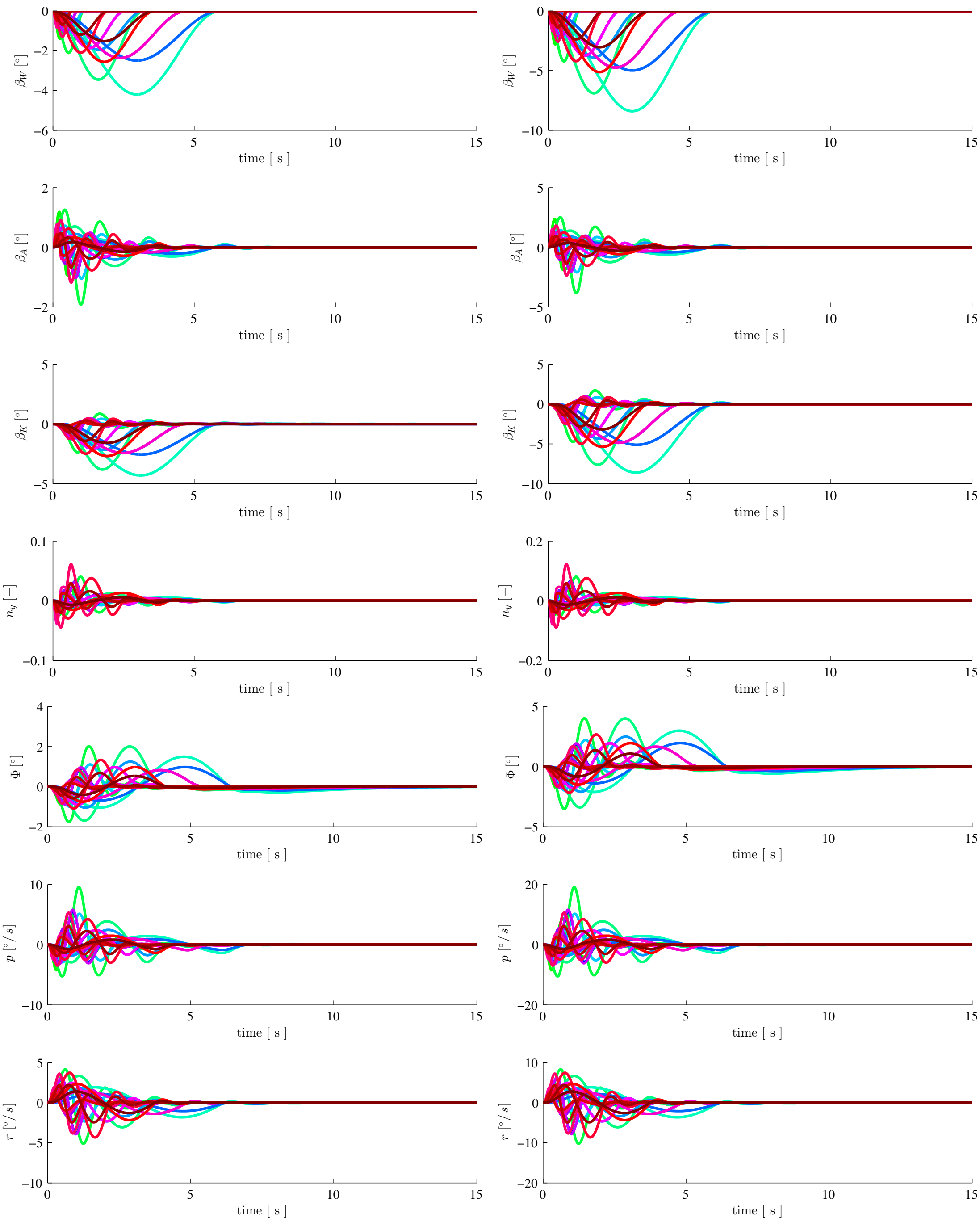

(a) light (b) moderate

Figure 6.4.: Gust Rejection - system states and outputs - (nominal, without time delays)

and maintains an accuracy of $\pm 1°$ (and thus $\pm 20\%$ of the initial disturbance) within a defined amount of time. From this, the common specification of settling time ($\pm 5\,\%$ of the steady-state value) is modified such that it is measured up to the point in time where the signal enters and remains in the band of $\pm 20\%$ around the steady-state value.

Figure 6.6 shows the step response characteristics for $m_{fuel} = 0\,\text{kg}$. Plots for other values of mass can be found in appendix A.5. All step response characteristics show only marginal variations with altitude. Both the rise time and settling time are decreasing slightly with increasing speed. This behavior is consistent with the characteristics of aircraft having no control augmentation, and is therefore well known to pilots. The

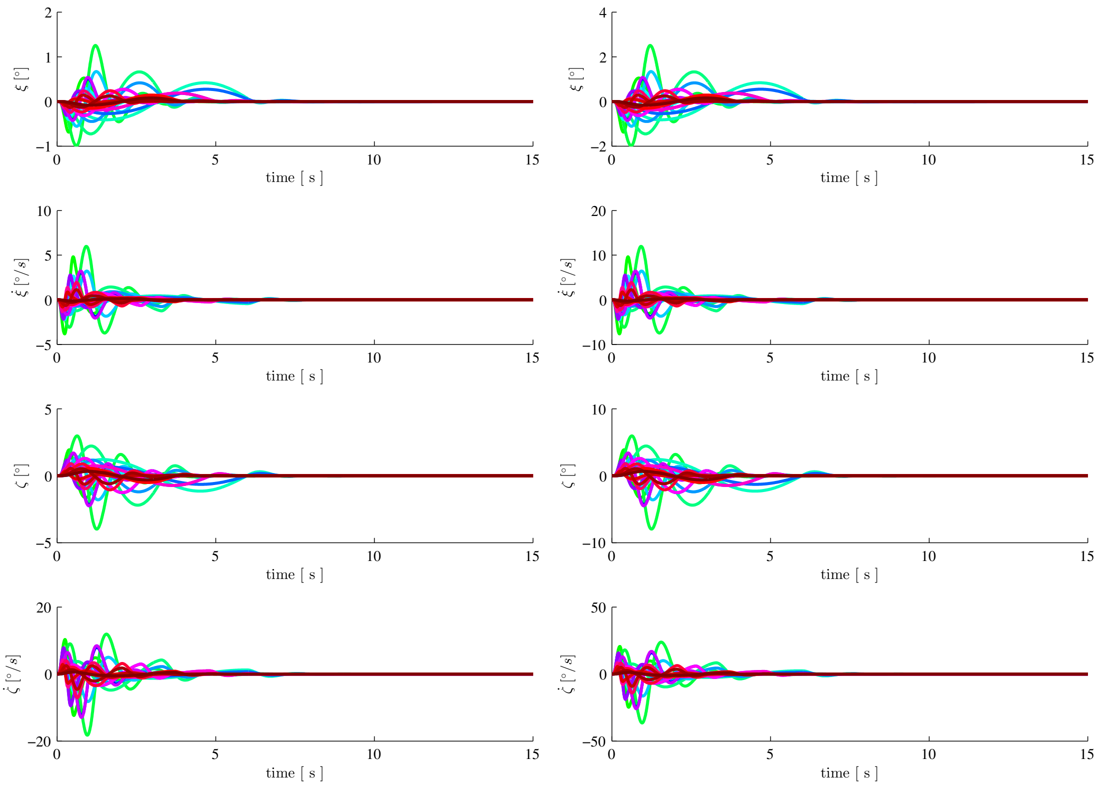

(a) light (b) moderate

Figure 6.5.: Gust Rejection - control surfaces - (nominal, without time delays)

step response shows neither overshoot nor undershoot. By studying the buildup of the bank angle in response to a step command (depicted by the black line) in figure 6.7a for the selected points in the envelope, it can be seen that the slight variation of step response characteristics seen in figure 6.6 has a barely visible impact on the time history of the bank angle, which means that the step characteristics are fairly consistent over the envelope. In addition to the response of the control variable, figure 6.7a also shows the tracking error e_Φ, the normalized lateral specific force f_y/g and $e_{\beta_A} = 0 - \beta_A$. From this it can be seen that during rolling at low speeds an AoS of $\approx 0.5°$ is developed, reducing to $\approx 0.3°$ during steady turn phases. Hence, the aircraft performs a near-perfect velocity vector roll. The resulting lateral acceleration remains small during the entire maneuver. Note that the acceleration's time history shape differs significantly from the time history shape of AoS. In particular, the initial reaction of the acceleration is dominated by the contribution of the control surfaces. Hence, estimation of AoS by means of lateral acceleration requires precise knowledge of actual control surface deflection and efficiency, and thus relies heavily on model and sensor information which is subject to large uncertainties and errors. As such, it is not well suited for the SAGITTA Demonstrator application. The control surface deflections and deflection rates are shown in figure 6.7b. The maximum equivalent deflections of the midboard flaps ξ_{equiv} during roll initiation, as well as the corresponding midboard flaps' deflection rates remain relatively small. The outboard flaps exhibit more activity compared to the midboard flaps, and at low flight speeds the outboard flaps deflection rates reach values up to 5/6 of the specified maximum. In summary, the resulting control surface activity can be considered satisfactory since the goal of non-saturating control is achieved during the tracking task.

The plot in figure 6.8 shows the results of evaluating the closed-loop system at the

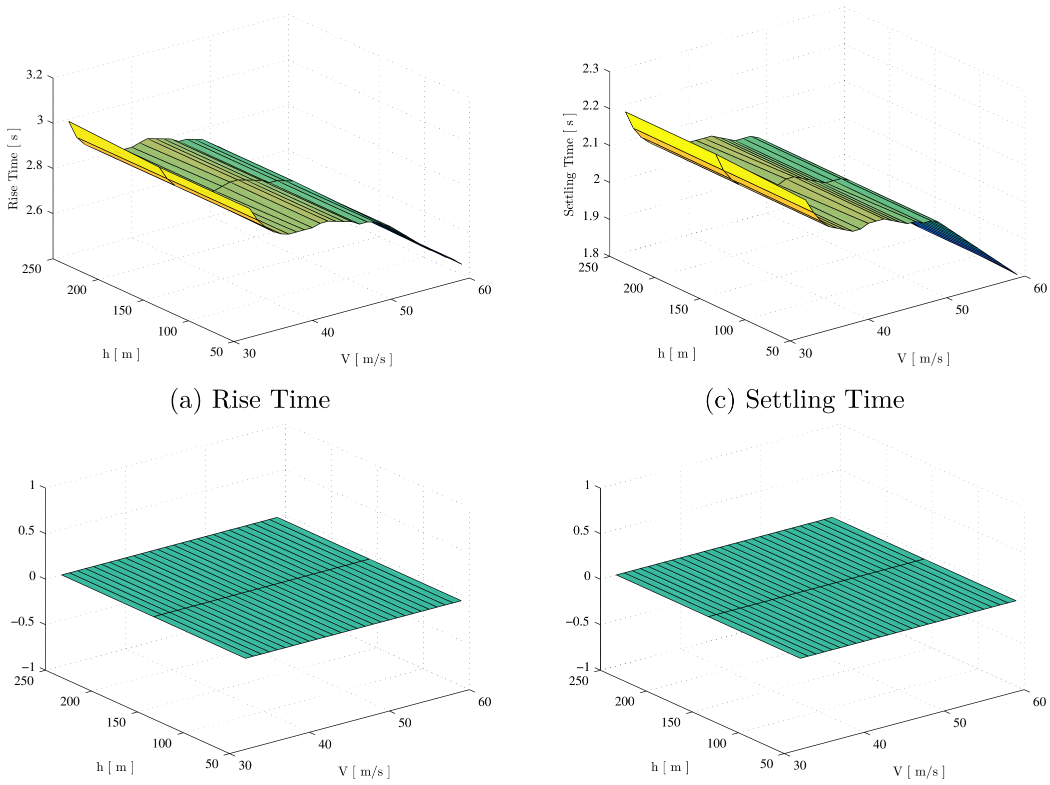

(a) Rise Time

(c) Settling Time

(b) Overshoot

(d) Undershoot

Figure 6.6.: Step response characteristics at $m_{fuel} = 0\,\mathrm{kg}$ - (nominal, without time delays)

selected operating points w.r.t. the bandwidth criterion that is closely related to tracking. For evaluation of this criterion, a feed-forward time delay of $\tau_{d,ff} = 50\,\mathrm{ms}$ is input into the system, this being an approximation of the worst case communication delay from the command input of the EP to the input of the FCC. The figure depicts the Flying Quality boundaries for the full scale aircraft. According to this the closed-loop system provides Level 1 Flying Qualities in terms of bandwidth. This is still true, if it is assumed that for small unmanned systems the requirement on bandwidth ω_{BW} needs to be multiplied by the dynamic scaling factor (N), whilst the τ_p is assumed to be not affected by the dynamic scaling. The phase delay is not scaled, since it is not considered to be a quantity that is related to time, but is regarded as a sensitivity measure which is unaffected by scaling. Whether or not the assumption is valid requires further analysis outside the scope of this project.

Detailed evaluation of the bandwidth criterion reveals that the closed-loop system at low speeds up to $38\,\mathrm{m\,s^{-1}}$ tends to show the following characteristics:

$$\omega_{BW,gain} < \omega_{BW,phase}, \tag{6.1}$$

which is, as stated in chapter 4, an indication that the aircraft might become prone to PIO when performing super-precision tasks that could be required in situation such as a dogfight. These characteristics are acceptable to the designer of the system, since it is not intended that the aircraft performs any tasks that would require super-precision maneuvering.

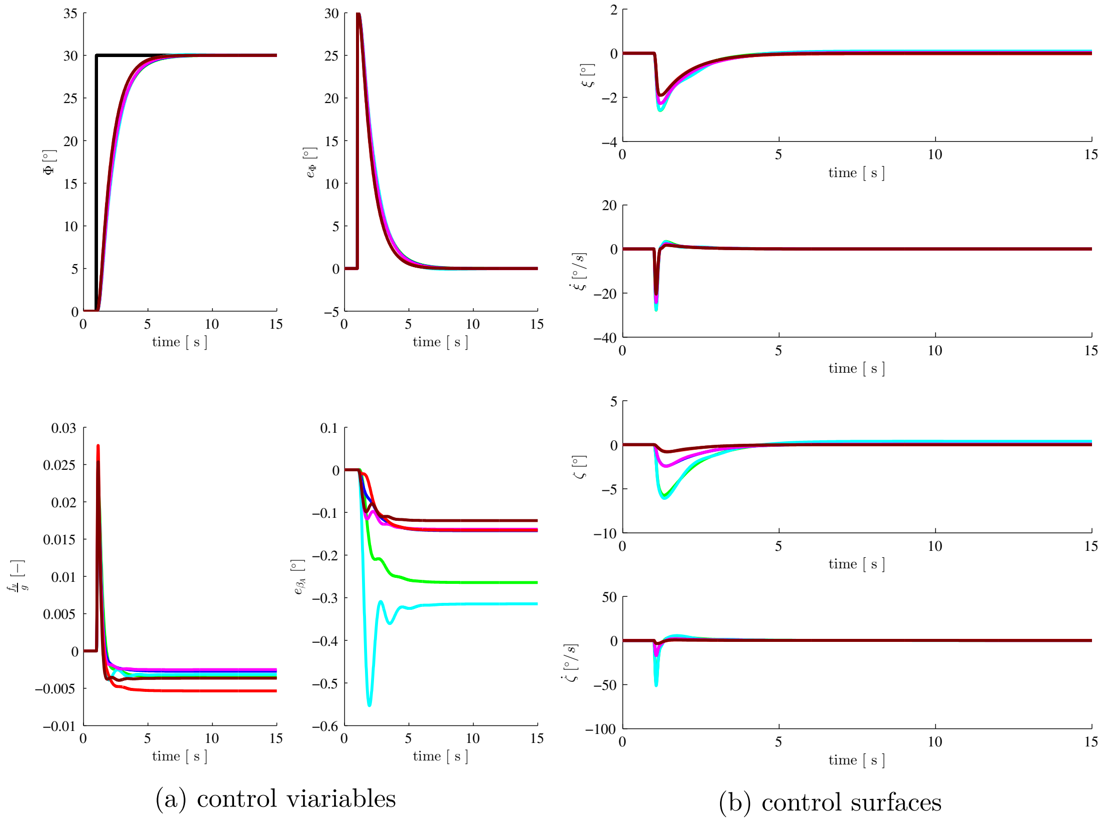

Figure 6.7.: Tracking - step response - (nominal, without delays)

6.4. Impact of Uncertainties and System Degradations on Closed-Loop Dynamics

In this section, the influence of aerodynamic uncertainties on stability and tracking performance is analyzed. In addition, the impact on closed-loop stability of a reduction in the actuators' natural frequency due to a reduced supply voltage, is briefly discussed.

In order to evaluate the impact of aerodynamic uncertainties, thirty random samples are selected from the uncertain state-space model [1]. The resulting closed-loop systems are first evaluated w.r.t. their pole locations. Subsequently, the influence of the uncertainties on closed-loop stability is demonstrated for the previously selected operating points in the envelope. Finally, the effect uncertainties have on tracking behavior and the reaction to gusts is discussed.

Figure 6.9 shows the density plot of the poles of the closed-loop Dutch-roll; the roll subsidence pole location; the spiral pole; and the bank angle integrator of the controller, after taking the aerodynamic uncertainties into account. Here, the darker areas indicate a higher density of poles, while lighter colors indicate areas that are more thinly populated. The figure reveals a broad scattering of the closed-loop roll subsidence pole. Nevertheless, compared to the location of the inherent roll subsidence pole, the closed-loop pole is more strongly damped at all points in the envelope. The locations of the closed-loop system's Dutch-roll vary greatly, but for all evaluated uncertainty combinations, the closed-loop Dutch-roll remains stable. With the minimum closed-loop damping of $\zeta_{min} = 0.13$, the system provides Level 1 Flying Qualities even in the

[1] Although, a greater number of uncertainty samples would be required in order to be statistically significant, the number was limited to thirty due to limitations on computer memory.

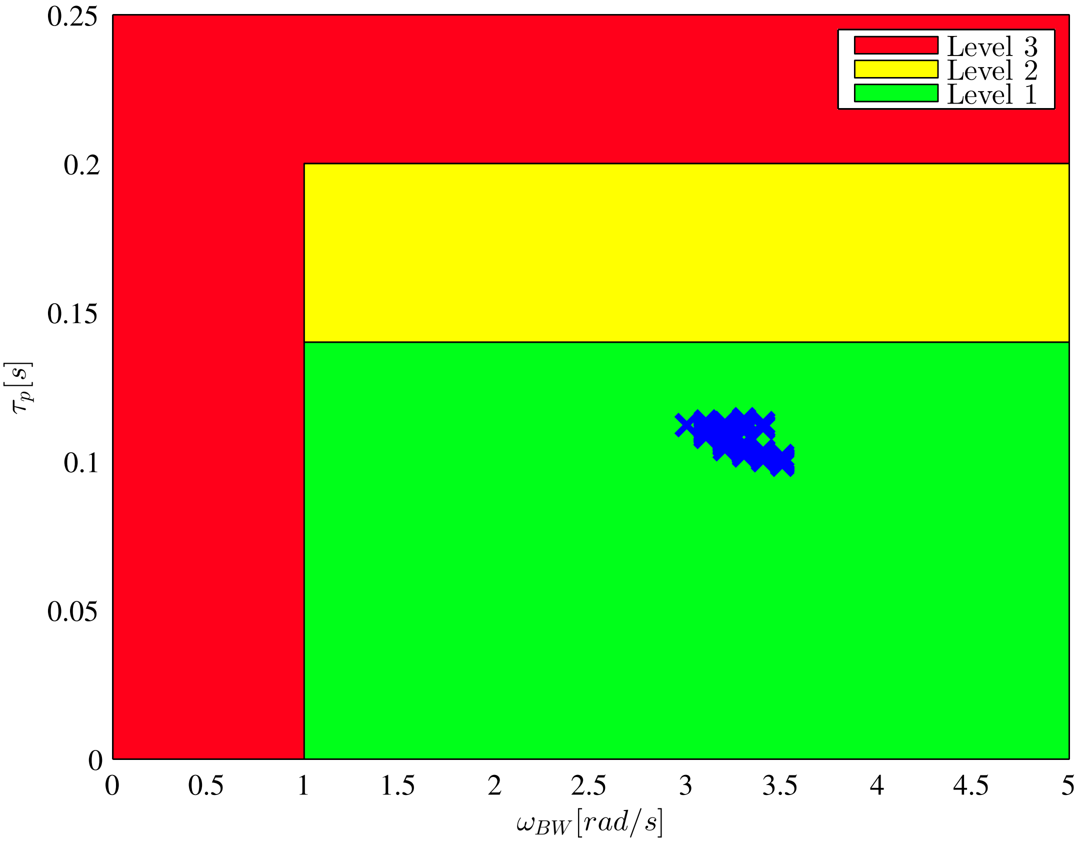

Figure 6.8.: Bandwidth Criterion Evaluation - (nominal, without delays)

case of present aerodynamic uncertainties. A further observation worthy of note is made w.r.t. the spiral pole: it can be seen that the spiral pole and the bank angle integrator move towards each other as the speed increases and eventually merge to form a strongly damped, conjugated complex pole pair. This leads to development of a new, unconventional motion form in some areas of the envelope. Since this motion form is well damped, it is not expected to be critical.

Within the trimmed envelope, the $|\Phi/\beta|_{DR}$ ratio of the closed-loop system being subject to aerodynamic uncertainties varies in the range $0.6 - 2.6$, which is, according to [19], in the band between low ($|\Phi/\beta| \approx 1.5$) and moderate ($|\Phi/\beta| \approx 5$).

In figure 6.10 the Nichols Plots of the bottleneck cuts at ξ and ζ are shown for selected systems after applying uncertainties. Lines and circles of the same color denote various realizations of aerodynamic uncertainty for the same operating point in the envelope. It can be clearly seen how the uncertainties affect the stability characteristics of the closed-loop. The gain margins span a band of up to $\Delta A = 5\,\mathrm{dB}$, while the variations in the delay margin add up to several hundreds of milliseconds. Despite the large variations in the delay margins, their absolute value never falls below 200 ms. Thus, the nominal delay in the feedback path of $t_d = 50\,\mathrm{ms}$ (which is not taken into account at this stage of the analysis) is not expected to drive the system into instability. The extent to which this expectation can be confirmed will be shown later in this chapter.

In the next step, the influence of uncertainties on the step response is analyzed. The only step response characteristics for which requirements are specified is the settling time. Although no requirements are specified for other characteristics the corresponding figures are helpful in understanding the reaction of the aircraft to aerodynamic uncertainties.

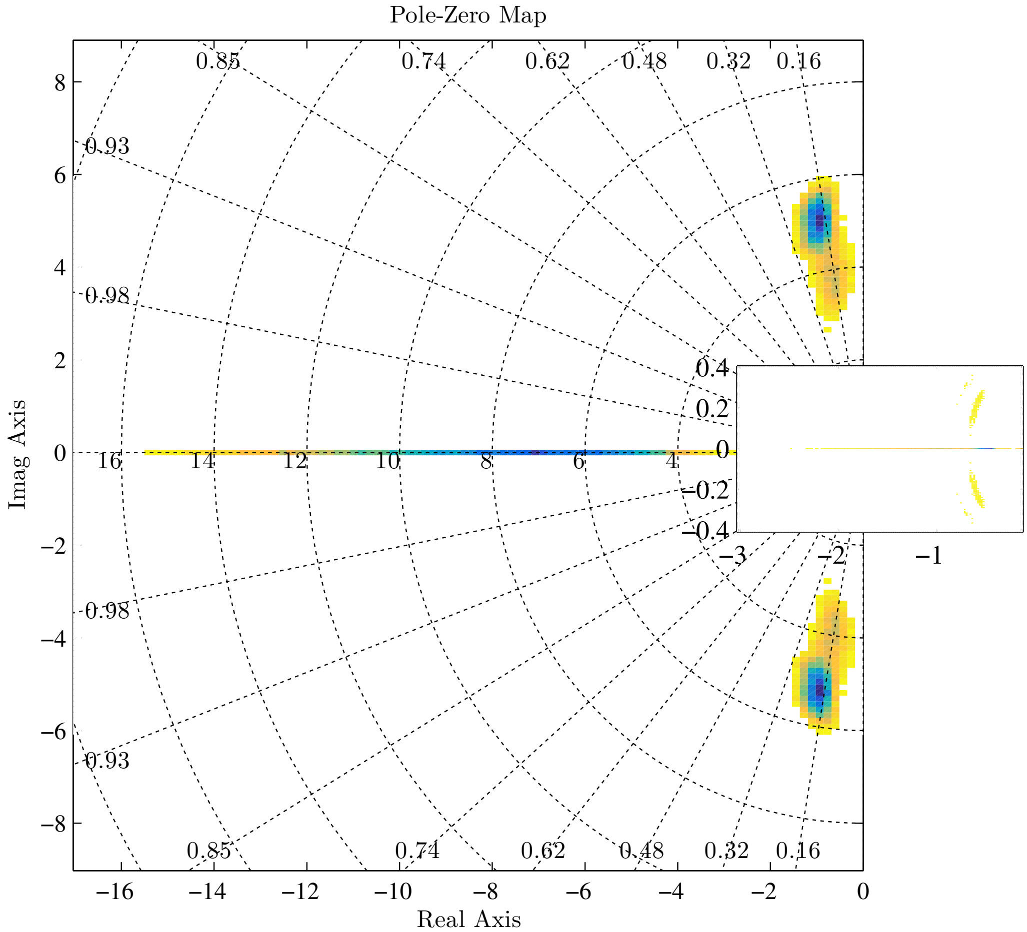

Figure 6.9.: Effect of uncertainties on the closed-loop lateral dynamics

The step response characteristics over the speed envelope are provided in figure 6.11. From figure 6.11c it can be seen that the settling time requirement is fulfilled for all points in the Design Envelope being below $t_s = 5\,\mathrm{s}$ for all combinations of uncertainty analyzed. The rise time in figure 6.11a remains below 3.2 s. It is noticeable that the difference between rise time and settling time is relatively large. This means that the initial response to a step command is quick compared to the time that the tracking variable requires to finally settle. It is expected that, as long as the system is not subject to overshoots, the rise time is more important to the EP than the settling time, since, for low precision tasks, the EP is less interested in achieving a certain exact value than in achieving a fast and predictable initial reaction to a given input. The overshoot in figure 6.11b varies between zero and $\approx 4.7\,\%$. The variation is a result of the relative migration of the Dutch-roll poles and zeros of the transfer function $G_{\Phi\Phi_{cmd}}$ when subject to uncertainties. The amount of overshoot remains very small for all combinations of uncertainties studied.

In order to demonstrate the influence of the actuator supply voltage on closed-loop stability, the Nichols diagram for the ξ_{equiv}-cut and the corresponding stability margins are plotted in figure 6.12 for two relevant actuator supply voltages. It can be seen, that the reduction of the actuator's supply voltage, which is directly linked to actuator's natural frequency, leads to a slightly smaller upper gain margin and a decrease in the delay margin of $\Delta\tau_d \approx 5\,\mathrm{ms}$. Thus, the reduction of the power supply from 26 V to 22 V produces marginally reduced stability margins.

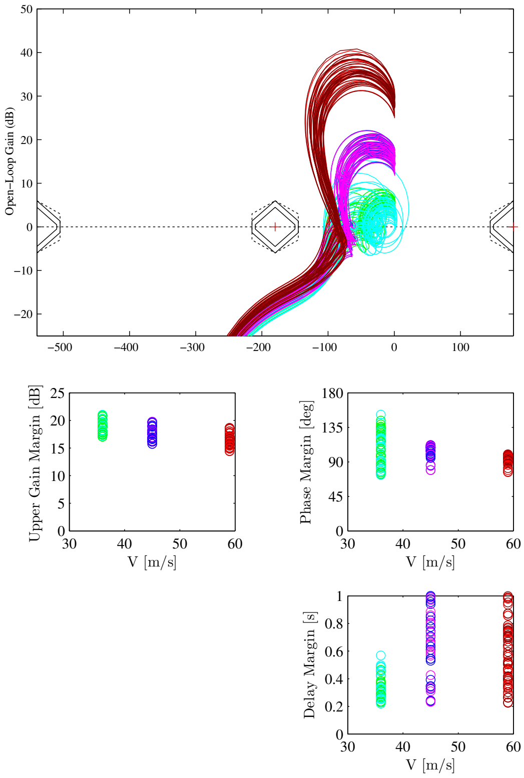

(a) ξ_{equiv} - cut

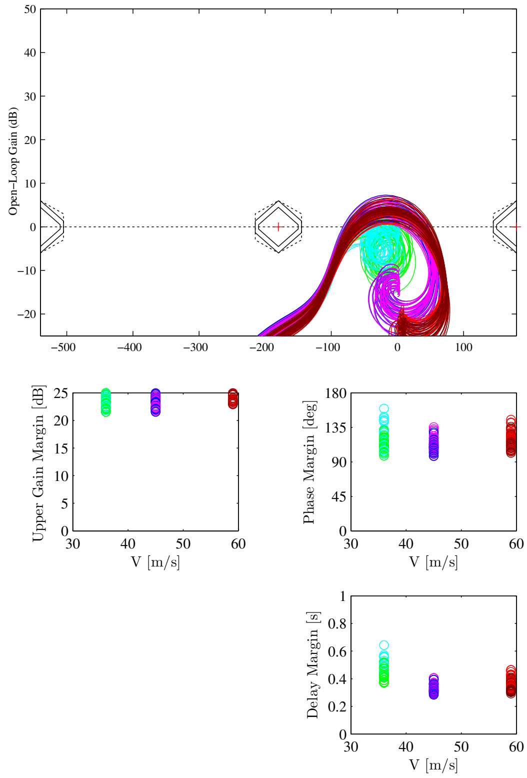

(b) ζ_{equiv} - cut

Figure 6.10.: Stability - (uncertain, without delays)

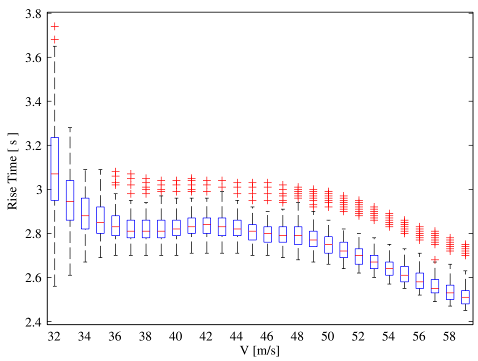

(a) Rise Time

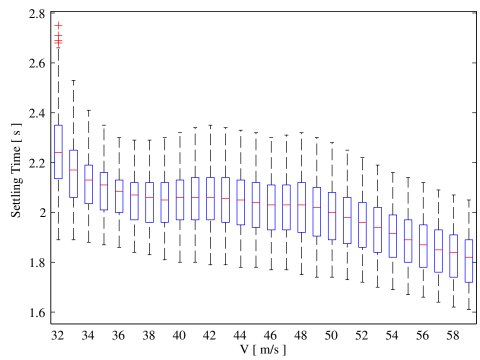

(c) Settling Time

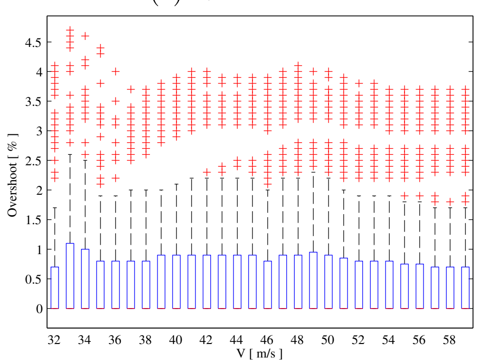

(b) Overshoot

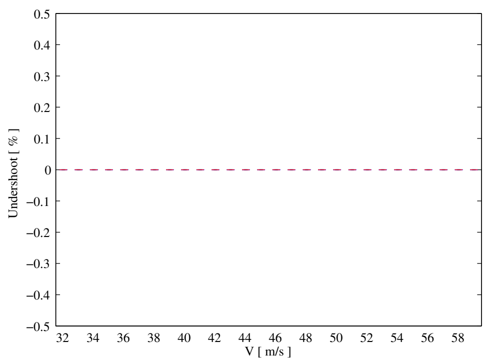

(d) Undershoot

Figure 6.11.: Tracking - (uncertain, without delays)

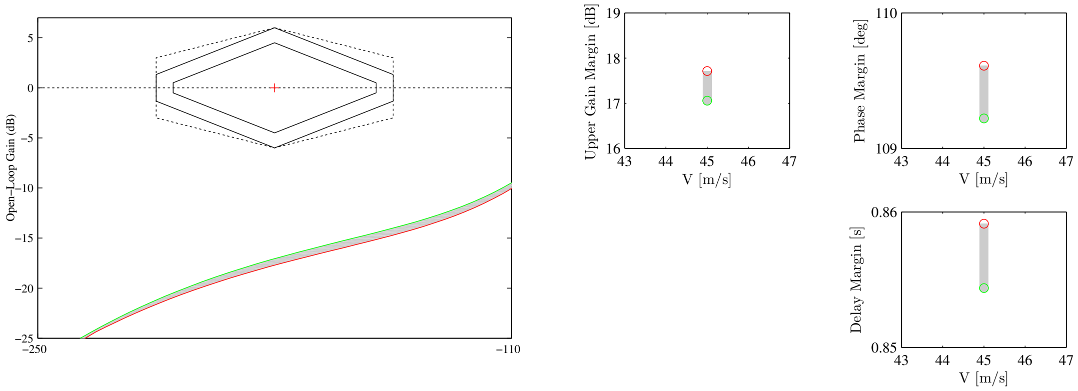

Figure 6.12.: Stability - (nominal, without delays) - 22 V(green) vs. 26 V(red) actuator

It should be noted that the analysis that has been performed on the impact of uncertainties on the closed-loop system does not provide a definitive conclusion, since it is based on randomly selected samples of the uncertain system and, as such, does not necessarily reflect a worst-case scenario. Nevertheless, it provides a good insight into the sensitivity of the stability and performance properties of the system when subject to uncertainties.

6.5. Impact of Time Delays

In this work, two types of time delay are considered. The first is in the communication chain from the External Pilot to the aircraft. This comprises the processing time in the radio transmitter, the Radio Modem Interface Ground (RMIG) and the RMIA, and includes transport delay from RMIA to the FCC. The total time delay in this communication chain is approximated to $\tau_{d,ff} = 0.05\,\text{s}$. This value derives from measurements of the communication chain between the radio transmitter and the Radio Modem Interface Air and includes an additional buffer to cover a worst case scenario. The second type of delay is found in the feedback path. It comprises sensor processing delays, sensor transport delays, the processing time of the FCC and ACEs, as well as internal actuator delays. The nominal feedback delay is estimated to be $\tau_{d,fb} = 0.05\,\text{s}$, but to cover uncertainties in time delay measurements, for the sensitivity analysis this figure is increased to $\tau_{d,fb} = 0.07\,\text{s}$. The feed-forward delay has no direct influence on the closed-loop stability of the aircraft. Nevertheless, when the control loop is closed by the External Pilot or the Operator it can affect significantly the overall stability and even lead to PIOs and an unstable pilot-vehicle system. Since the feedback time delay directly affects the stability margins of the augmented aircraft it is fundamentally important for it to be analyzed.

Figure 6.13 shows the influence of the feedback delay on the frequency response and therefore on the stability margins of the closed-loop system. The ξ_{equiv} cut for three different amounts of delay is shown. It can be seen clearly, how the gain margin is reduced by introduction of a time delay. While the system with a delay of $\tau_d = 0\,\text{ms}$ shows a gain margin of 16.6 dB, this is reduced to 11.6 dB when a 50 ms delay is introduced, and reduces further to 10.4 dB with a delay of 70 ms. The corresponding variations in ζ_{equiv} cut are even larger. The open loop gain at phase $\varphi = -180°$ varies between $-16.9\,\text{dB}$ and $-24.7\,\text{dB}$. Similarly, the phase margin is between $\varphi = 97°$ and $\varphi = 86°$

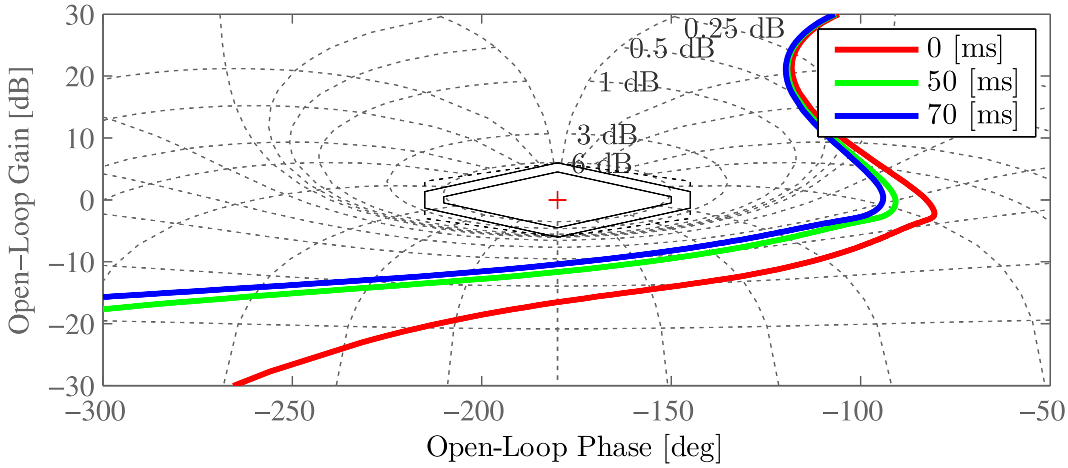

Figure 6.13.: Impact of Feedback Delays

for ξ_{equiv} and between $\varphi = 113°$ and $\varphi = 91°$ for ζ_{equiv}. Thus, the impact of time delay is associated with increasing the gain by a factor of 2 to 3 at $\varphi = -180°$.

By influencing the closed-loop stability characteristics, feedback delays also influence significantly the Flying Qualities of the system. This is clearly visible in figure 6.14, where the bandwidth criterion for the closed-loop system with a feed-forward delay of $\tau_{d,ff} = 50\,\text{ms}$ is evaluated with feedback delays of $\tau_{d,fb} = 50\,\text{ms}$ and $\tau_{d,fb} = 70\,\text{ms}$ respectively. The figures show that, compared to the case without delay presented in

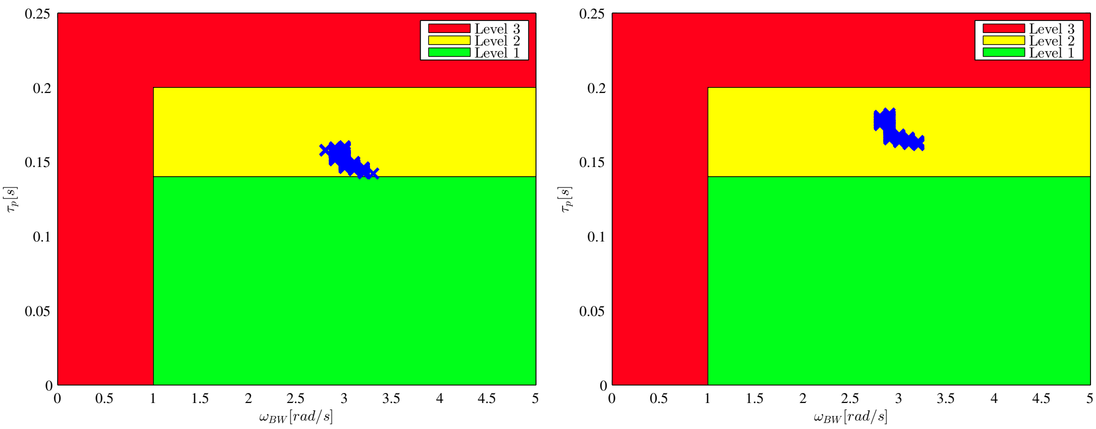

(a) feedback delay $\tau_d = 50\,\text{ms}$ (b) feedback delay $\tau_d = 70\,\text{ms}$

Figure 6.14.: Bandwidth Criterion Evaluation - (nominal, with delays)

figure 6.8, the delayed systems show a slight reduction in ω_{BW} and an increase in τ_p. While the change in ω_{BW} is not critical in terms of Flying Qualities, the change of τ_p leads to a degradation of performance to Level 2 according to the original specification of Flying Qualities level. Furthermore, in contrast to the case with $\tau_{d,fb} = 0\,\text{ms}$, all operating points now show the following behavior:

$$\omega_{BW,gain} < \omega_{BW,phase}, \tag{6.2}$$

and thus the system becomes prone to PIO when performing super-precision tasks.

6.6. Impact of Sensor Noise

In this section, the impact that sensor noise has on the closed-loop system is analyzed in respect of resulting actuator activity in the time domain. Figure 6.15 compares the actuator activity resulting from sensor noise in straight level flight for the controller variants 1 and 4. As expected, the *V4* - controller shows significantly less actuator activity compared to the initial *V1* design, which includes the AoS feedback and leads to full roll-yaw decoupling. The reduction in the actuator deflection rates is particularly remarkable. The *V4* - controller provides acceptable performance with rates that are well below the specified actuator activity requirements (see control-margin increments in section 4.3), and noise induced deflections that are within a band of $\pm 1°$.

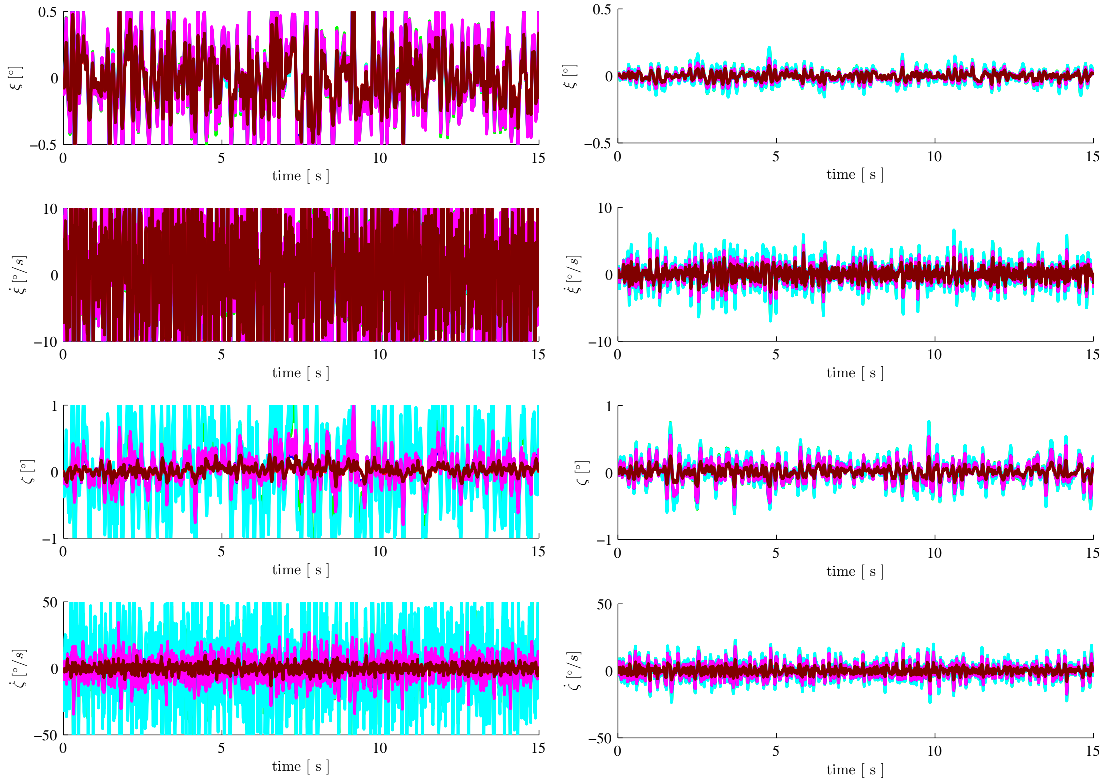

(a) *V1* (b) *V4*

Figure 6.15.: Comparison of Noise Impact (*V1* vs. *V4*)

6.7. Impact of Turbulence

Figure 6.16 shows the bank angle and AoS response of the final controller design in light and moderate turbulence. For both turbulence intensity level, the AoS remains within the predefined limit of $\beta_{max} = \pm 10°$. Furthermore, it can be seen that, for moderate turbulence, the kinematic sideslip angle approaches the $\beta_{max,crab}$ value and the bank angle hits the limit for landing of $\Phi_{max,land} = \pm 4.5°$. This indicates that landing gear overload is likely when the aircraft is operated in conditions of moderate. Based on this analysis, and due to the restrictions required by the landing gear design, the aircraft is only cleared for flight up to light turbulence.

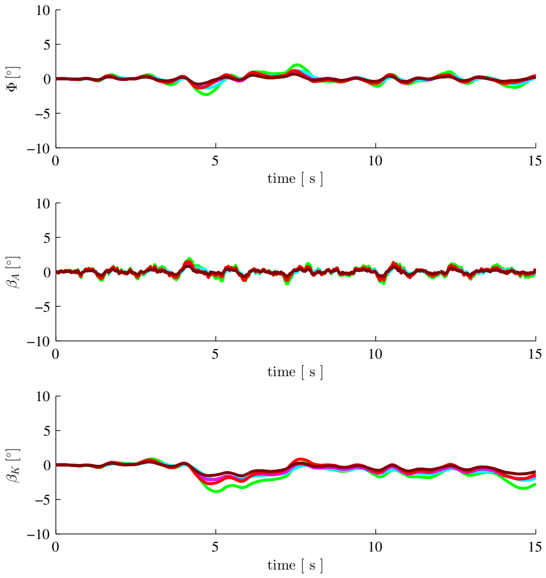

(a) light (b) moderate

Figure 6.16.: Turbulence impact on tracking performance

6.8. Impact on Stability in Pull-Up and Push-Over Maneuvers

As shown in figure 3.30, the dynamic characteristics of the open-loop system change significantly, when the aircraft is brought from Level Flight (LF) into Pull-Up (PU) or Push-Over (PO) maneuvers. Here, an analysis is performed of how the stability properties of the closed-loop system are affected in such quasi-steady-state flight conditions. For this purpose, the controller is connected to LTI systems that represent the inherent aircraft dynamics in LF, PU and PO in order that the resulting closed-loop systems might be analyzed.

Figure 6.17 shows the gain, phase and delay margins over the speed envelope (at $m_{fuel} = 3\,\mathrm{kg}$) for the three flight conditions. When analyzing the ξ_{equiv} - cut, it seems that Level Flight and Push-Over conditions provide lower stability margins than the Pull-Up case. This changes for the ζ_{equiv} - cut, where Level Flight and Pull-Up are more critical than Push-Over. In summary, it can be said that, for the nominal case without delays fairly large stability margins exist in all three flight conditions. Considering the sensitivity to uncertainties highlighted in section 6.2 all three flight conditions should be analyzed as a means of risk reduction. The Nichols Charts for all the flight situations under study taking into account uncertainties; different levels of actuator supply voltage; and large time delays, are provided in appendix A.7.

6.9. Evaluation w.r.t. requirements

Having examined certain effects on the closed-loop behavior of the aircraft, and the evaluation of how the closed-loop system w.r.t. requirements is now conducted. All the relevant requirements forming the basis for the following analyses are presented in chapter 4. In this regard, the project's declared stability requirements are the only ones that definitely must be fulfilled in order to obtain flight controller clearance. All further requirements are so-called "should" requirements. The consequences of violating such requirements are handled on a case-by-case basis.

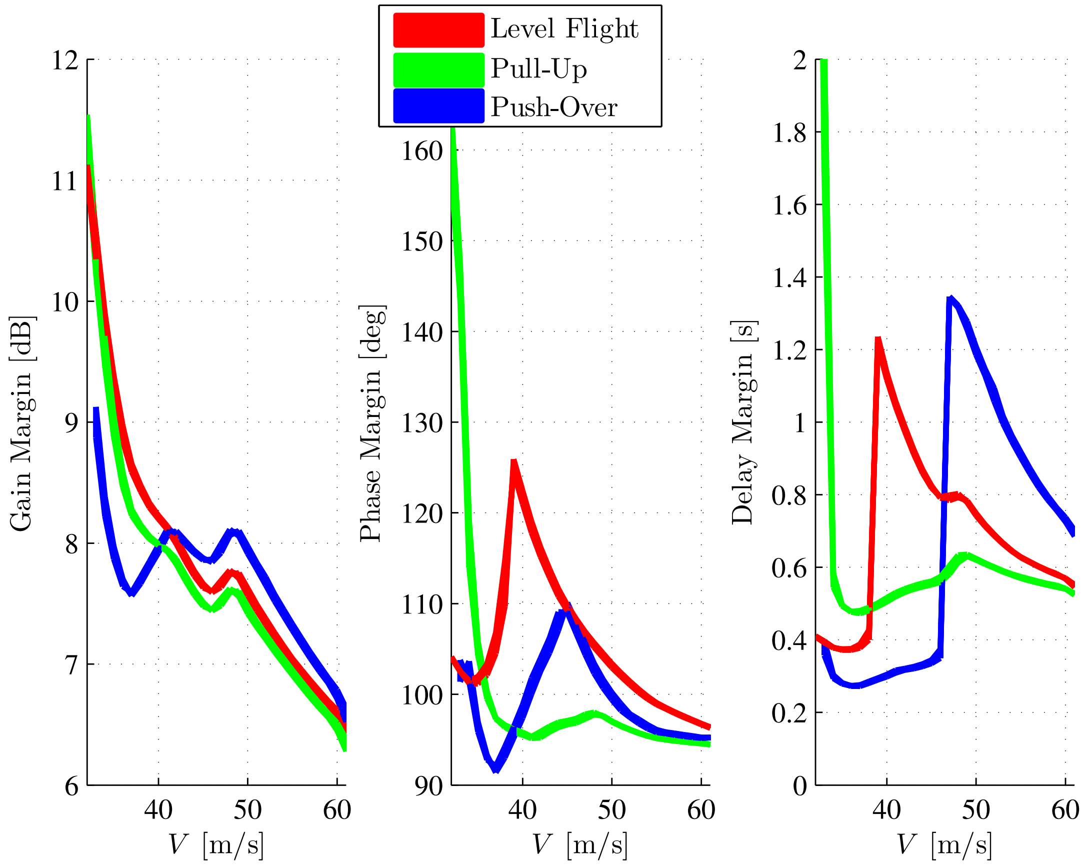

(a) ξ_{equiv} - cut

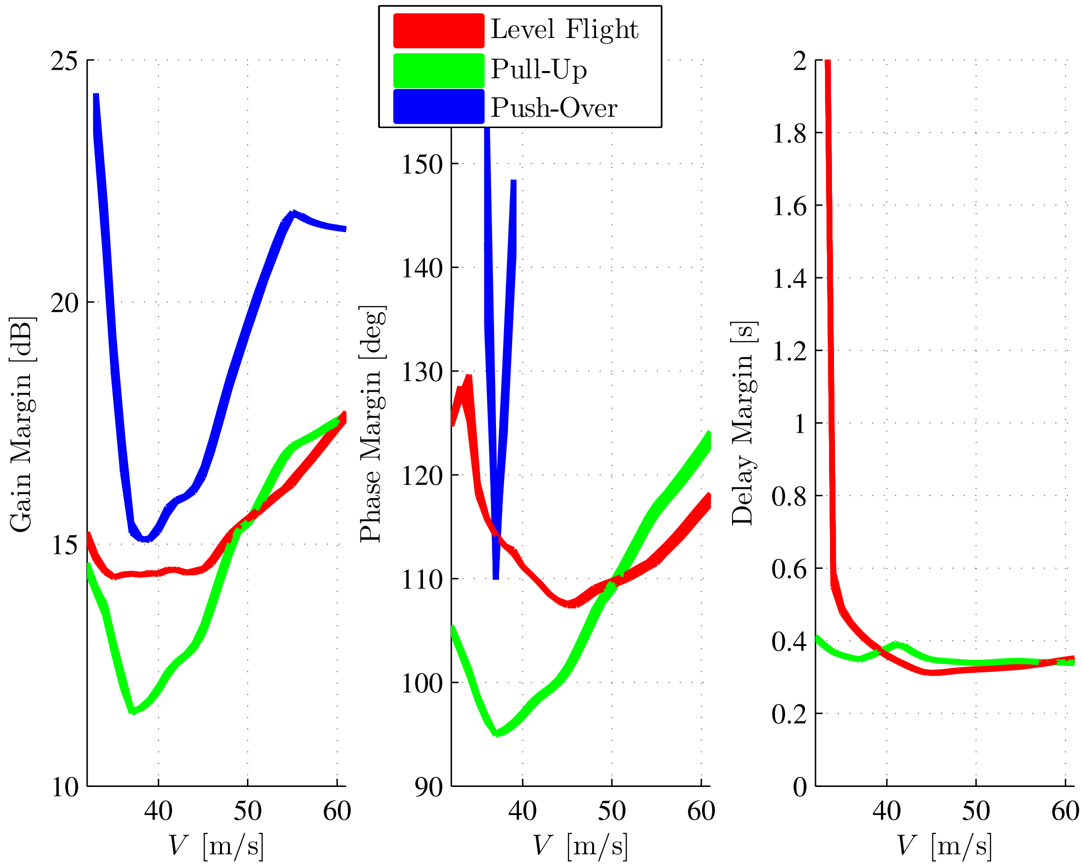

(b) ζ_{equiv} - cut

Figure 6.17.: Impact on Stability of Pull-Up and Push-Over

Stability Robustness

As previously stated, stability and robustness analysis represents the most onerous part of the clearance process. Thereby, in order to achieve compliance with the requirements, all three flight conditions (LF,PU,PO) must be evaluated w.r.t. their stability margins for all cases listed in the clearance matrix table 4.3.

The detailed evaluation of stability properties shows that for all flight conditions, and for all combinations of delays, uncertainties and actuator supply voltage, the system is stable. Furthermore, stability margins comply with corresponding requirements and consequently the bottleneck cuts do not violate the specified Nichols Diamonds. Appendices A.7.1 to A.7.6 depict the bottleneck cuts for systems representing the entire flight envelope, including the maximum amount of expected time delay and aerodynamic uncertainties. Pull-Up can be identified as the most critical maneuver in terms of stability with the ξ-cut offering the smallest margins. Upon examination of figure 6.18 it becomes apparent that the previously formed impression, that the feedback could be more strongly amplified without threatening stability margins has to be revised. The figure shows that systems representing operations at high speed are approaching the Nichols Diamond from below, while systems representing operations at low speeds come very close to the upper boundary of the Nichols Diamond leaving a relatively small time delay margin of $\approx 100\,\mathrm{ms}$. Only minimal amplification of the feedbacks is still possible. Taking into account the expected uncertainties therefore, the controller represents an excellent design in terms of stability margins.

Pole locations

The requirements on desired pole locations can be obtained from section 4.7. Figure 6.19 shows the Dutch-roll poles, the spiral poles, and the integrator poles of the uncertain system in the pole-zero map. Crosses of the same color indicate a particular mass configuration. Roll subsidence poles are not shown to increase visibility in the vicinity of the imaginary axis. The dotted lines of constant damping represent $\zeta = 0.25, 0.5$ and 0.75. The red lines indicate the minimum Dutch-roll damping allowed according to section 4.7. The first feature to be noted is that all poles are located in the complex left half-plane of the pole-zero map and that the system is therefore stable at all operating points. At the same time it can be confirmed that the requirements concerning the spiral pole locations have been satisfied. All poles that can be associated with the spiral mode are stable, and thus fulfill the requirements of Level 1 Flying Qualities. Furthermore, it can be seen that the requirements on Dutch-roll damping are fulfilled over the entire envelope, since the poles are located to the left of the red boundary lines. Two further requirements related to Dutch-roll can also be verified from this figure, namely $\omega_{DR} >> 0.8\,\mathrm{rad\,s^{-1}}$ and $\zeta_{DR}\omega_{DR} >> 0.135\,\mathrm{rad\,s^{-1}}$. As stated above, the poles of the roll subsidence are not shown in the figure, however they lie in the range $-15\,\mathrm{rad\,s^{-1}} \leq \lambda_R \leq -3\,\mathrm{rad\,s^{-1}}$ and thus, comply with the corresponding requirements.

The analysis of pole locations leads to a positive outcome insofar as Level 1 Flying Qualities are forecast.

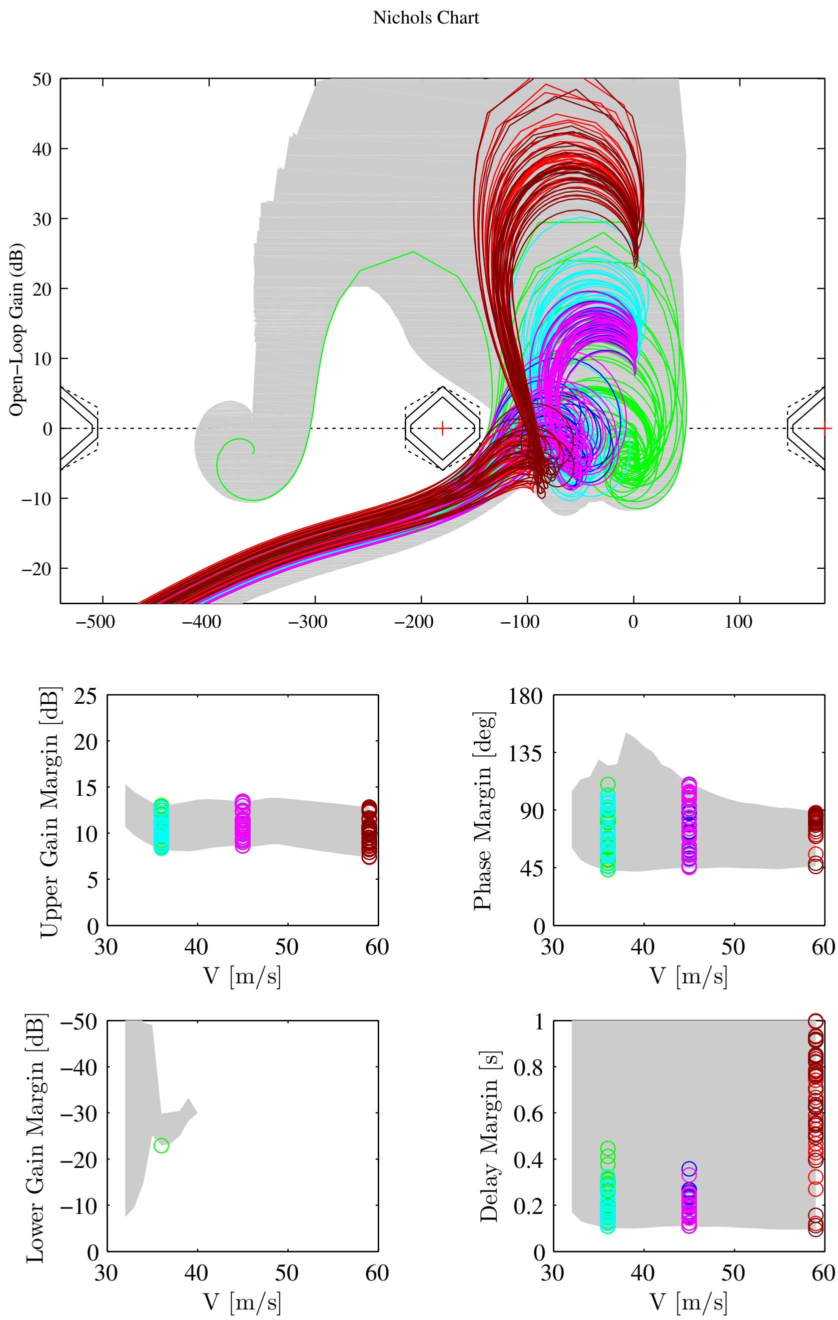

Figure 6.18.: PU, Nichols (ξ - cut), delayed by 70 ms, uncertain, 22 V

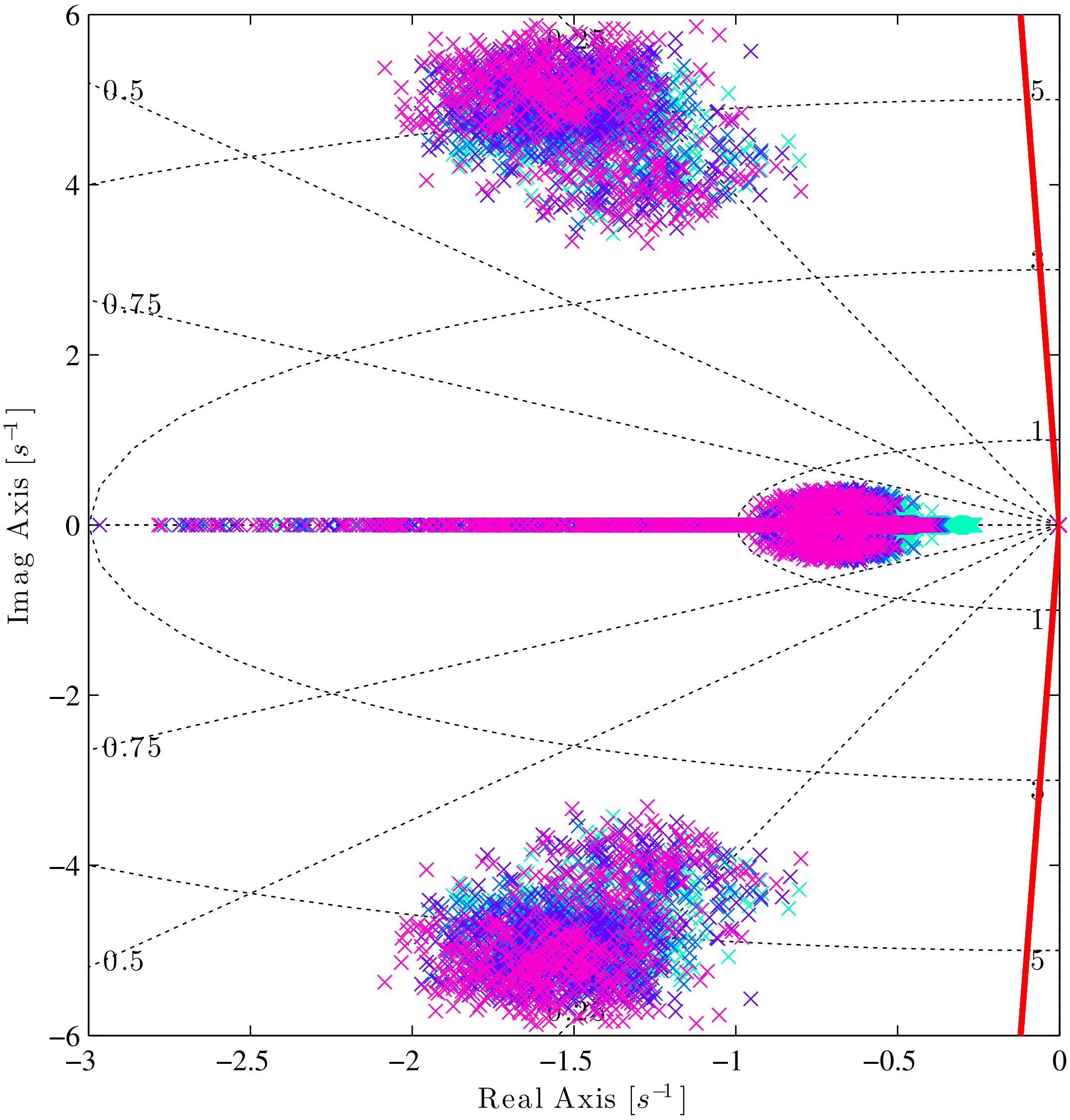

Figure 6.19.: Pole-Zero maps of systems with aerodynamic uncertainties

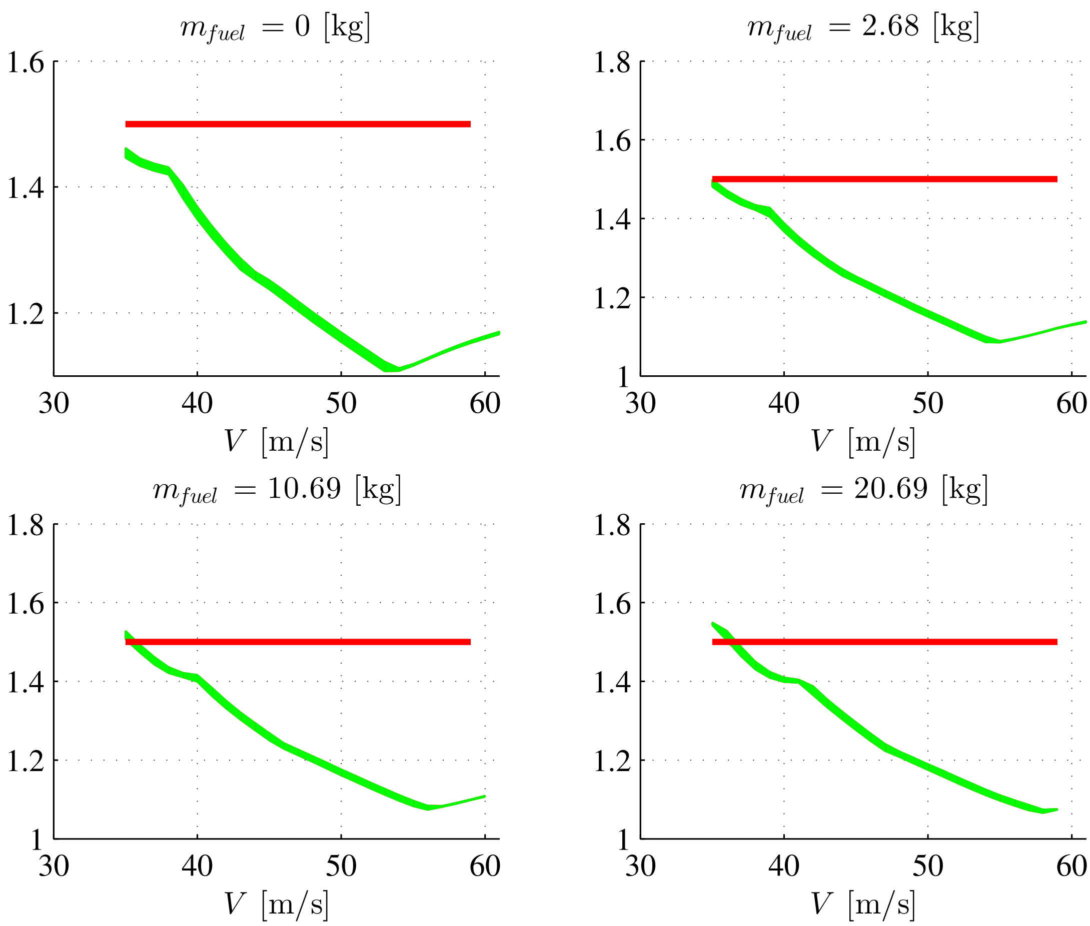

Figure 6.20.: Closed-loop $|\Phi/\beta|_{DR}$ after reduction of scheduling variables

$|\Phi/\beta|$ ratio

The $|\Phi/\beta|_{DR}$ ratio of the nominal closed-loop system is provided in figure 6.20. The system complies with the requirement on roll-yaw coupling, except at maximum mass, when combined with speeds below $36\,\mathrm{m\,s^{-1}}$, in which case $|\Phi/\beta|_{DR}$ exceeds the limit by 3 %. Since the operating points, at which the requirement is violated are at the edges of the flight envelope, and since in practice it is very unlikely that such flight conditions are encountered, the violation of the requirement is considered acceptable.

With regard to aerodynamic uncertainties, the worst case $|\Phi/\beta|_{DR}$ ratio can increase significantly to values of up to $|\Phi/\beta|_{DR} = 2.5$. In figure 6.21, the maximum $|\Phi/\beta|_{DR}$ arising from a hundred uncertainty samples at each operating point is depicted over the envelope. Here, the upper figure shows the results taking into account 100 % maximum aerodynamic uncertainties as specified in table 3.1. The lower figure is obtained by reducing maximum aerodynamic uncertainties to 63 % and thus it represents the multi-tolerance case. The two plots also include a red surface which denotes the original requirement boundary of $|\Phi/\beta|_{DR} \leq 1.5$. Here, the impact of large aerodynamic uncertainties is clearly visible. Although not satisfactory, the result is acceptable, since the $|\Phi/\beta|_{DR,max} \leq 2.5$ is still relatively small according to [19]. Nevertheless, a future redesign following the first flight campaign shall aim for an improvement in these characteristics.

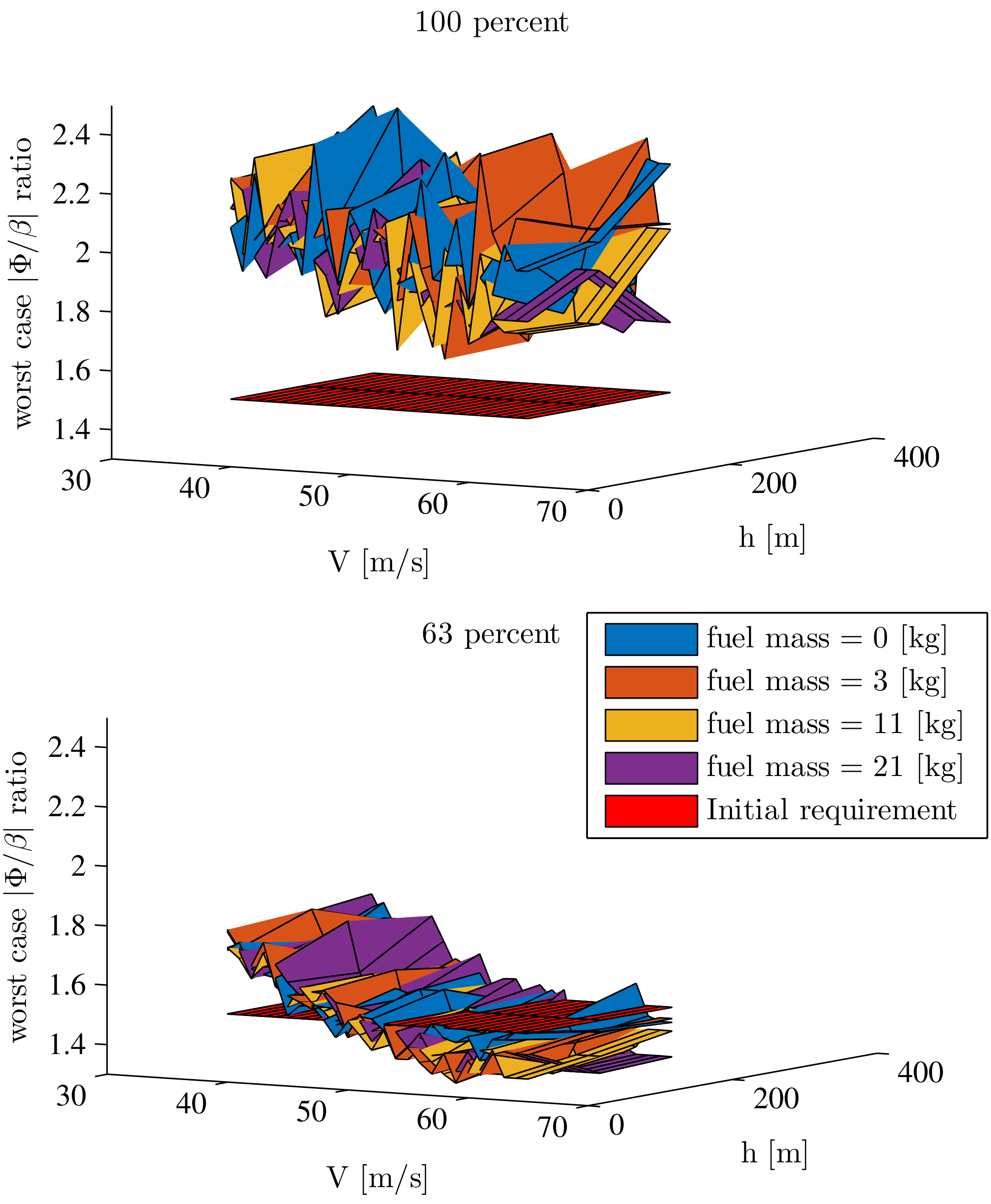

Figure 6.21.: Worst case closed-loop $|\Phi/\beta|_{DR}$ with uncertainties

Step response requirements

The evaluation of step response is based mainly on settling time derived from the attitude hold requirement. As already shown in figure 6.6, the nominal system without time delays complies with this requirement throughout the envelope. Results including aerodynamic uncertainties are presented in figures A.10 to A.13. In the relevant operational speed envelope ($V \geq 35\,\mathrm{m\,s^{-1}}$), the settling time is within the specified requirements for all fuel masses considered.

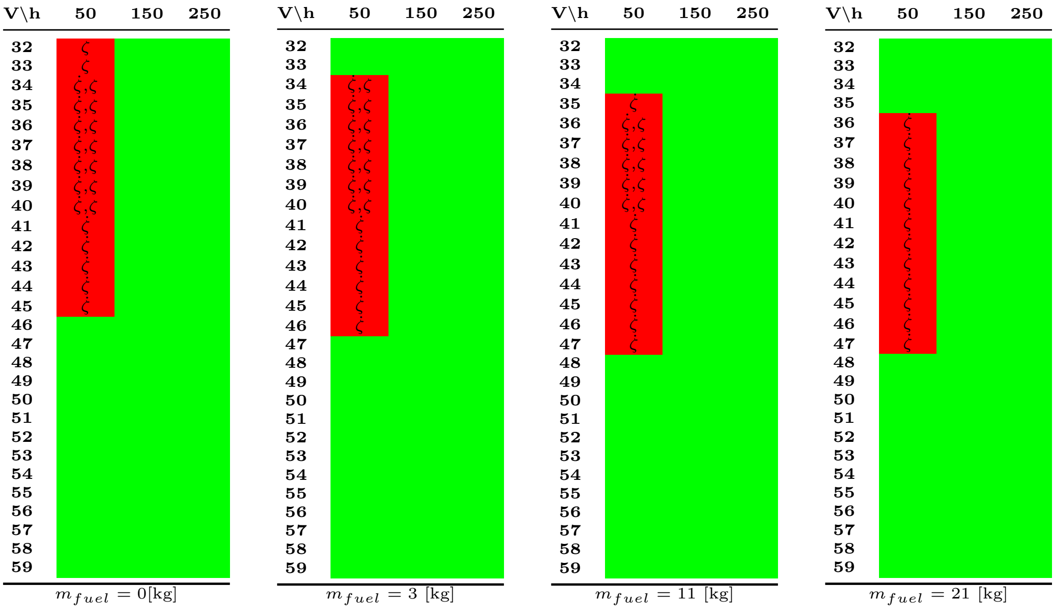

Table 6.4.: Validation of requirements w.r.t. moderate turbulence intensity (actuator supply voltage $V = 22\,\text{V}$)

Turbulence rejection requirements

As stated in section 6.7, turbulence intensities higher than light might lead to exceeding the maximum AoS specified for landing. Consequently, based on the analyses performed so far, it has been decided to clear the system for atmospheric conditions up to light turbulence only. In order to increase the clearance envelope w.r.t. crosswind landing, it would be useful to have the possibility to control β. By implementation of a β_{cmd} system, it would be possible to perform a so-called decrab maneuver before touchdown, thereby reducing the crab angle β_K between the aircraft's nose and the alignment of the runway and consequently the load on the landing gear during cross-wind landings. Provided the quality of the AoS measurement can be improved following the first flight, the proposed enhancement of the system could be a meaningful way of extending the Operational Envelope.

The analysis of system behavior w.r.t. turbulence is completed by evaluation of actuator activity in terms of actuator deflection, deflection rate and the requirement on maximum disturbance in bank angle of $\Phi \leq 10°$ RMS. The evaluation of the performance of the nominal system with actuator supply voltage $V = 26\,\text{V}$ shows compliance with all the above-stated requirements for light and moderate turbulence intensity. When the actuator voltage is reduced to $22\,\text{V}$, several violations w.r.t. activity requirements of the outboard flaps are discovered under moderate turbulence intensity. In table 6.4 red fields indicate the operating points at which violations w.r.t. actuator rate ($\dot{\zeta}$) and actuator deflections (ζ) have been identified. When the system is exposed to moderate or severe turbulence, a large amount of actuator activity can be expected in the event of undervoltage at the actuators. Consequently, a reduction of the actuators' power supply during moderate turbulence could lead to a critical situation. In future, when considering the clearance of the CSAS for operations in moderate turbulence conditions, a reduction of actuator activity must be achieved - e.g. by means of filtering the feedback signals to the controller.

Sensor noise rejection requirements

In order to evaluate the system's compliance with sensor noise requirements, the actuator deflections and deflection rates are analyzed during straight and level flight. The analysis shows compliance with the requirements over the entire Operational Envelope.

Coordination in steady banked turns

This requirement is evaluated by means of time domain simulation of the system with and without aerodynamic uncertainties. Starting from straight and level flight, a step command of $\Phi_{cmd,max} = 30°$ is applied to the CSAS. The analysis shows that, during turn initiation and steady bank turns, the resulting AoS and lateral acceleration are both within the specified limits for the entire Operational Envelope. Thus, the controller is in compliance with the requirement on coordination in steady banked turns. The time series of variables relevant to the evaluation of coordination in steady banked turns are, for the entire flight envelope, presented in figure 6.22.

Bandwidth

The results of the evaluation of bandwidth requirement are shown in figure 6.23, in which the colored areas correspond to dynamically scaled flying qualities requirements. The closed-loop system, taking into account the nominal time delays ($\tau_d = 50\,\text{ms}$) and aerodynamic uncertainties, is rated Level 1 to Level 2. Thus, the requirement on system bandwidth is fulfilled for all points in the flight envelope.

6.10. Nonlinear simulation

To augment the analyses presented above, a brief insight into the results of nonlinear simulation is provided in this section. The goal of this analysis is to validate the controller performance taking into account nonlinearities of the plant and control system. In this nonlinear simulation, both longitudinal and lateral controllers are, for the first time, combined and analyzed together in order to provide both an insight into coupling effects between longitudinal and lateral motions, and a means for simulating combined maneuvers, in which longitudinal and lateral motions are simultaneously excited. Also in this nonlinear simulation, all elements of the control system namely: CSAS; autopilot; trajectory generation and control; automatic takeoff and landing system; on-ground controller; and state machines for control of the overall system states are integrated and simulated in an extensive range of nominal and contingency scenarios that could be relevant to the first flight of the SAGITTA Demonstrator.

The lateral controller of the CSAS is evaluated by means of nonlinear time domain simulation in a multitude of scenarios. Some of these scenarios are:

- Straight and level flight
- Bank Angle Doublet
- Horizontal loiter
- Bank angle commands in combination with simultaneous Pull-Up and Push-Over maneuvers

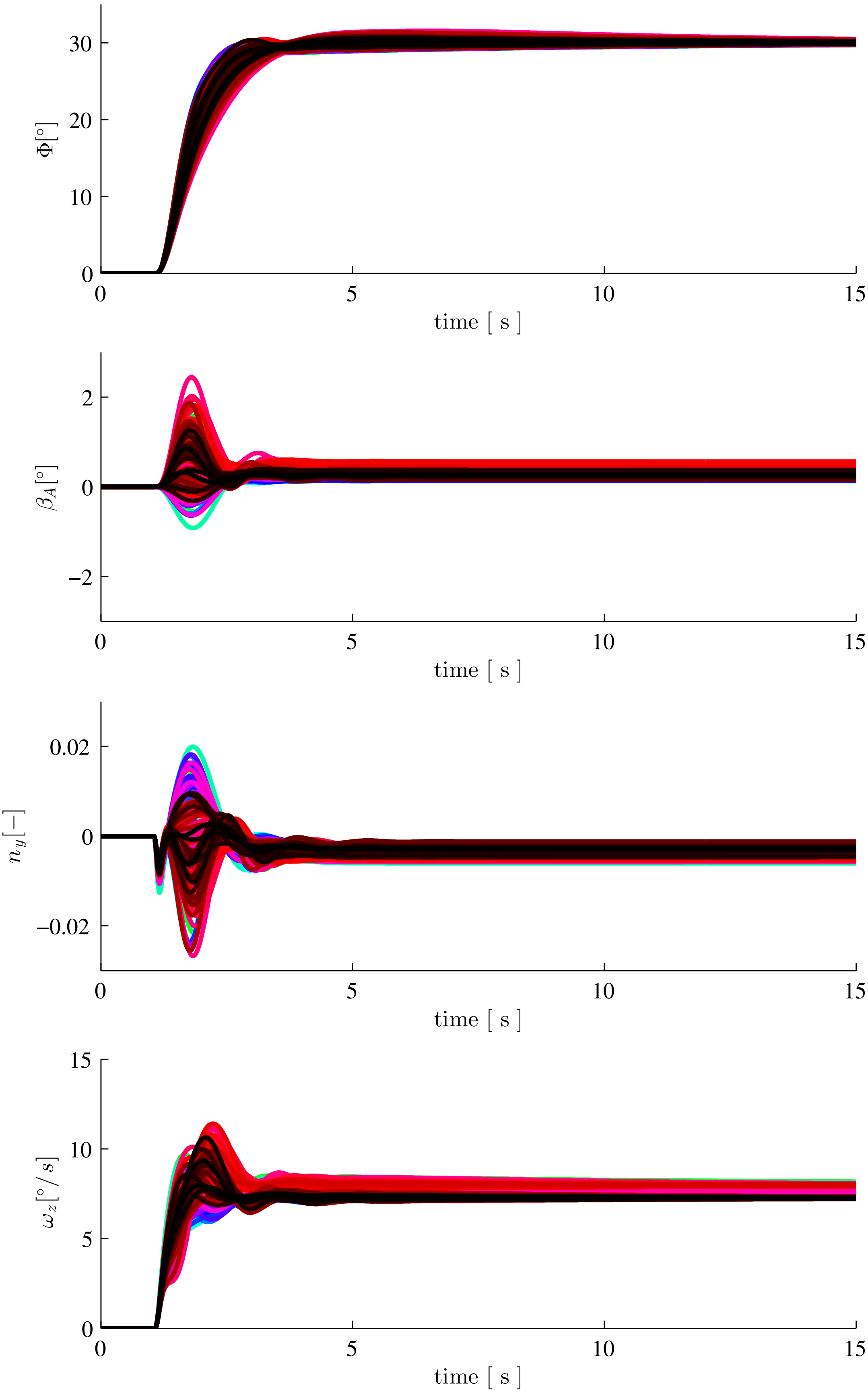

Figure 6.22.: Time series of relevant variables for evaluation of coordination in steady banked turns

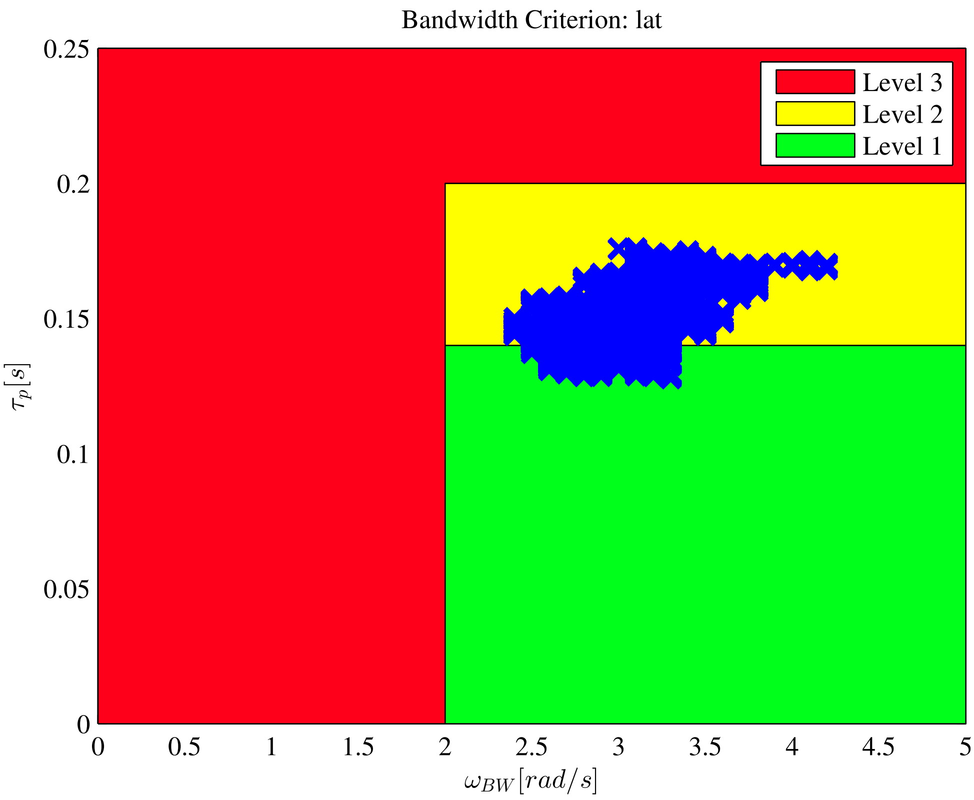

Figure 6.23.: Bandwidth with uncertainties and 50 ms delay

- First flight pattern, including automatic takeoff, en-route flight and automatic landing

These simulations are performed for different atmospheric conditions (turbulences and/or gusts); with and without sensor noise; and for potential system failures (such as loss of ADS). The simulations are evaluated w.r.t. time-domain requirements (e.g. the predefined limits for AoA or load factor) in a batch process and subsequently a report is automatically generated.

The figures 6.24 and 6.25 show by way of example, the results of the simulation of straight and level flight with sensor noise enabled and a light lateral gust. As soon as the gust reaches its maximum amplitude it is held constant until the end of the simulation run, to replicate a constant lateral wind with two different gust lengths being evaluated (Gust 1 = 58 m, Gust 2 = 107 m). Table 6.5 shows the allocation of different colors to particular operating points and gust lengths.

Nr.	V [m/s]	h [m]	m_{fuel} [kg]	Gust 1	Gust 2
1	36	50	0		
2	36	250	21		
3	45	150	3		
4	45	150	11		
5	59	50	0		
6	59	250	21		

Table 6.5.: Gust color map (nonlinear simulation)

The shown test case illustrates clearly the aircraft's reaction to constant lateral wind.

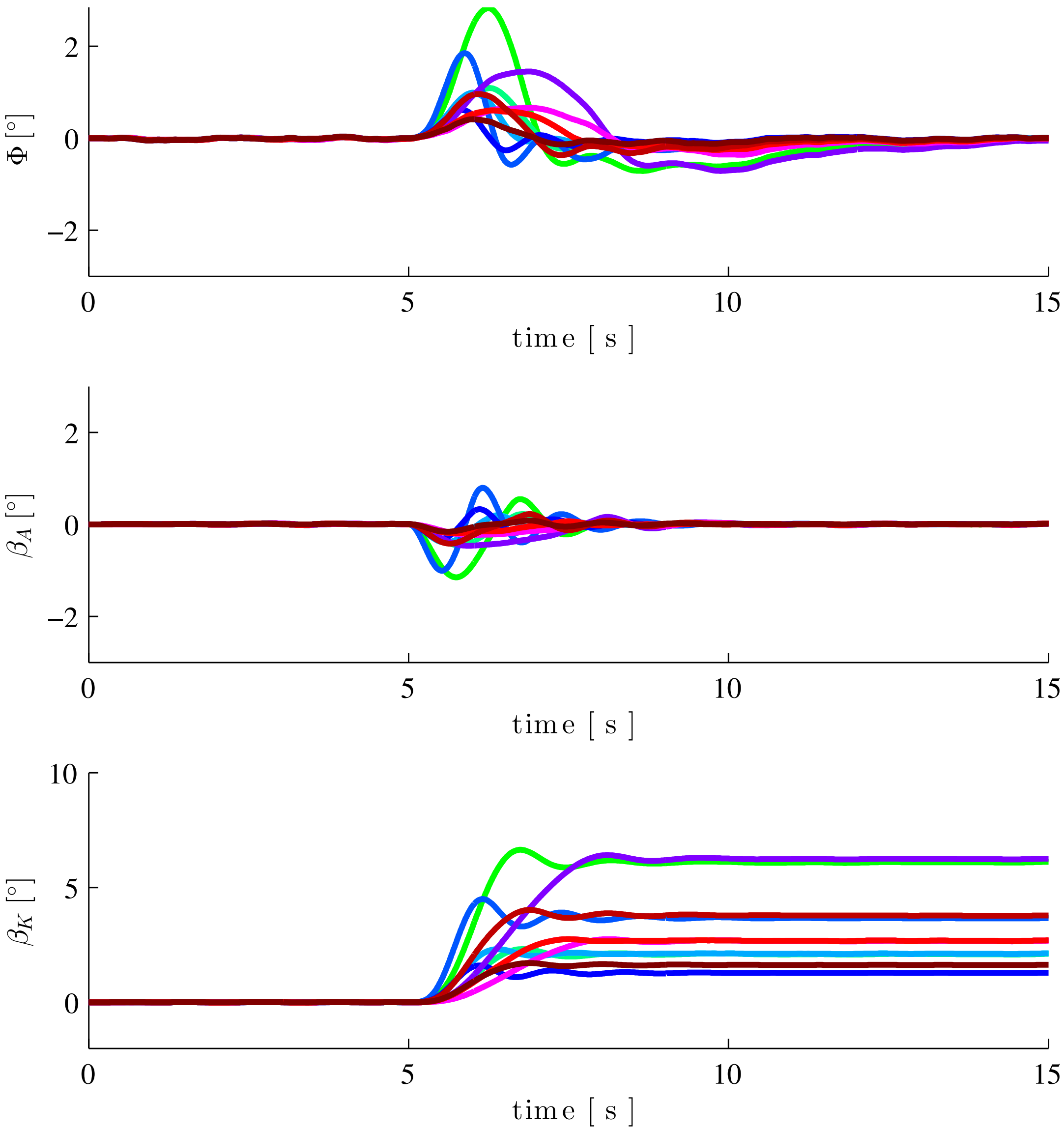

Figure 6.24.: Nonlinear simulation - light gust, with sensor noise - system outputs

Initially, a small aerodynamic AoS develops. Due to the roll-yaw coupling the disturbance in AoS causes the rolling motion to be provoked. Both AoS and Φ are quickly reduced by the controller. The result is a constant kinematic AoS (β_K), and thus the aircraft continues the wings level flight with a constant crab angle β_K in which the control surface deflections and rates in reaction to the lateral gust are moderate and remain well within the specified limits. Furthermore, it can be ascertained from the simulation that noise affects the outboard flaps more strongly than it does the midboard flaps. The resulting rates in $\dot{\zeta}$ reach values up to $40\,°\,\mathrm{s}^{-1}$, which is larger than the values experienced in linear simulation (for comparison see figure 6.15b). One reason for the discrepancy between the nonlinear and linear simulations might be the difference between the nonlinear actuator and the approximated linear actuator model used for controller design and linear analysis. A comprehensive explanation for the difference in control surface deflection rates in linear and nonlinear simulation requires a more thorough analysis, which is outside the scope of this work.

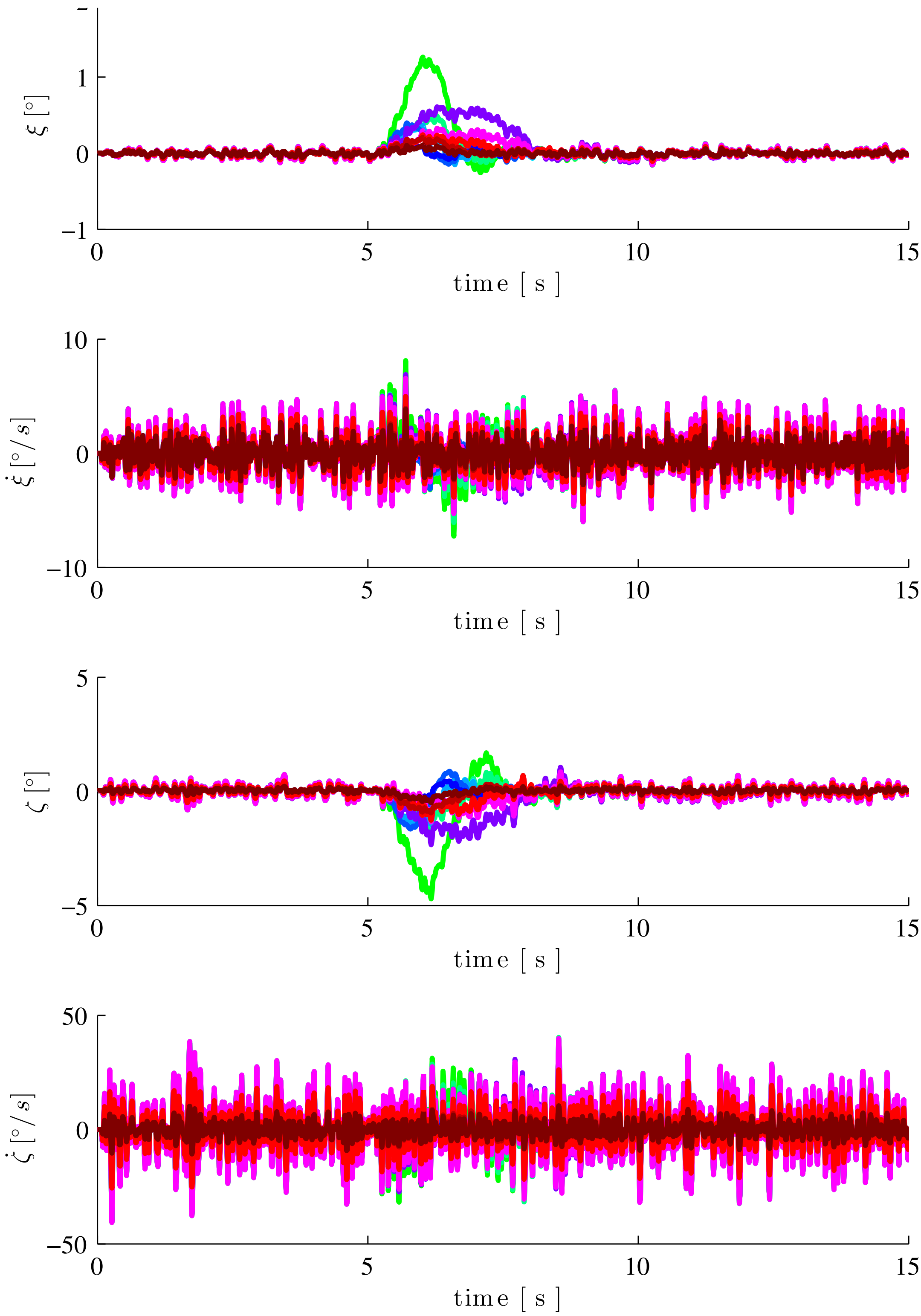

Figure 6.25.: Nonlinear simulation - light gust, with sensor noise - control surfaces

6.11. Verification Summary

In this chapter, the methodology for the controller design developed in the thesis has been accessed. Specifically, it has been verified that the design technique produces an outcome that is both predictable and, in this case satisfactory. By analysis of the closed-loop system w.r.t. to particular requirements like stability, robustness, disturbance rejection, tracking and actuator activity, the suitability of the Constrained Eigenstructure Assignment approach for the controller design has been proven and its effectiveness has been demonstrated.

A brief overview of the V&V of the flight control algorithm, which forms the basis for flight controller clearance, has also been provided in this chapter. Mandatory requirements on closed-loop stability and robustness have been verified for nominal and uncertain systems over the entire envelope by means of linear system analysis. Furthermore, extensive verification w.r.t. "should" requirements has been performed by simulation using linear and nonlinear models. The results were mostly positive, providing a forecast of Level 1 to Level 2 Flying Qualities. Partial deficiencies, non-compliance and deviations have been discussed and evaluated. From this, clearance limitations (e.g. w.r.t. turbulence intensities) have been derived.

It should be noted that the clearance activities relied heavily on automation of the verification tools that were developed in parallel by the controller designers. Without doing this, handling of the huge number of verification cases (delays, uncertainties, system degradations) and analyses would not have been manageable.

Another point worth mentioning is that many colleagues made valuable contributions to the overall V&V of the FMS, including the verification of the system automation; the autopilot; the trajectory generation and control; the on-ground controller; and the automatic takeoff and landing system. Furthermore, the development team invested considerable effort into component and integration testing. Extensive Hardware-in-the-Loop simulations of the first flight mission were conducted, including simulation of diverse system failures and adverse environmental conditions. Further risk reduction was achieved by performing so-called taxi tests, in which the steering and braking performance of the system was validated. The taxi test results were used to fine-tune the gains of the on-ground controller (detailed information on the taxi test activities can be found in [76]).

Based on the work outlined here, controller clearance for first flight has been granted by the project's flight clearance authority.

7. In-Flight Validation

The ultimate goal of the first phase of the SAGITTA Demonstrator project is to validate the capability of the aircraft to perform the intended flight mission. The first project phase concludes by establishing the experimental operational service of the aircraft and by demonstrating the mission performance in flight. The maiden flight of the SAGITTA Demonstrator marks an important milestone for the project. Its success is a major prerequisite for moving on to the next phase of research. The results gathered during the first flight campaign form the basis for further expansion of the SAGITTA's capabilities.

After extensive development and preparation, the SAGITTA Demonstrator took off from Runway 17, Overberg, South Africa (ICAO airport code: FAOB) on July 5th, 2017. The maiden flight of the SAGITTA Demonstrator was completed successfully. Figure 7.1 shows the airborne aircraft during its first flight.

The first flight campaign comprised two flights. This chapter presents the results gathered during the campaign focusing on the second flight, in which a broader range of lateral maneuvers was performed.

7.1. First Flight Mission

The following describes a sequence flown in the first flight campaign. It begins with the EP performing taxi from the hangar to the runway, followed by initiation of an automatic takeoff. After the automatic takeoff, the aircraft enters the en-route flight and follows a racetrack pattern according to predefined waypoint lists. During the en-route

Figure 7.1.: SAGITTA Demonstrator airborne [58]

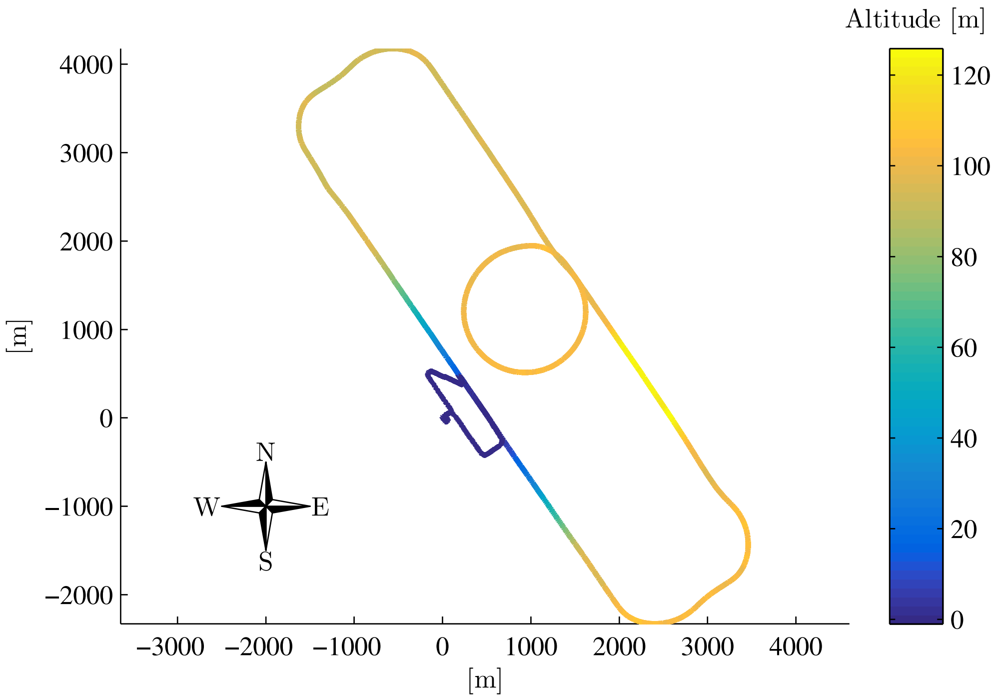

Figure 7.2.: Second Flight - Pattern

flight, the racetrack pattern can be suspended by the FO in order to perform, for example, a loiter maneuver. On conclusion of the racetrack, the aircraft is commanded to execute an automatic landing.

Figure 7.2 depicts the actual flight pattern of the second flight, and figure 7.3 shows the corresponding speed and altitude profiles, as well as the different numbered flight phases. The aircraft performs automatic takeoff (1) heading south-east. After takeoff, the aircraft enters the racetrack pattern in a counter-clockwise direction. In this phase (2), the aircraft is controlled via HLC according to a waypoint list. Horizontal and vertical position, as well as speed, are controlled according to the attributes attached to each point on the waypoint list. On the downwind leg of the racetrack, the FO switches into superposition mode (3). In phase (3), the aircraft holds the speed specified in the waypoint list and continues to follow the racetrack in the horizontal plane. During this time the altitude command from the waypoint list is overwritten by the FO (altitude-by-fo functionality is active). Following the testing of the altitude-by-fo functionality, the superposition mode is disabled and the aircraft continues the racetrack pattern (4). Subsequently, the FO interrupts the pattern by initiation of a loiter maneuver (5). After one complete circuit, the aircraft is commanded to reestablish the racetrack pattern (6), before the superposition mode is once more activated. This time, the speed-by-fo functionality is tested (7) during which the FO introduces moderate variations in the speed command to the system. In phase (8), the speed-by-fo command is deactivated and the aircraft continues the racetrack pattern according to the waypoint list. Once the racetrack pattern is completed, the aircraft performs an automatic landing (9).

7.2. Lateral CSAS Performance

In this section, the performance of the lateral CSAS is discussed. As described above, during the entire flight the aircraft is operated in MLC and HLC only. This means

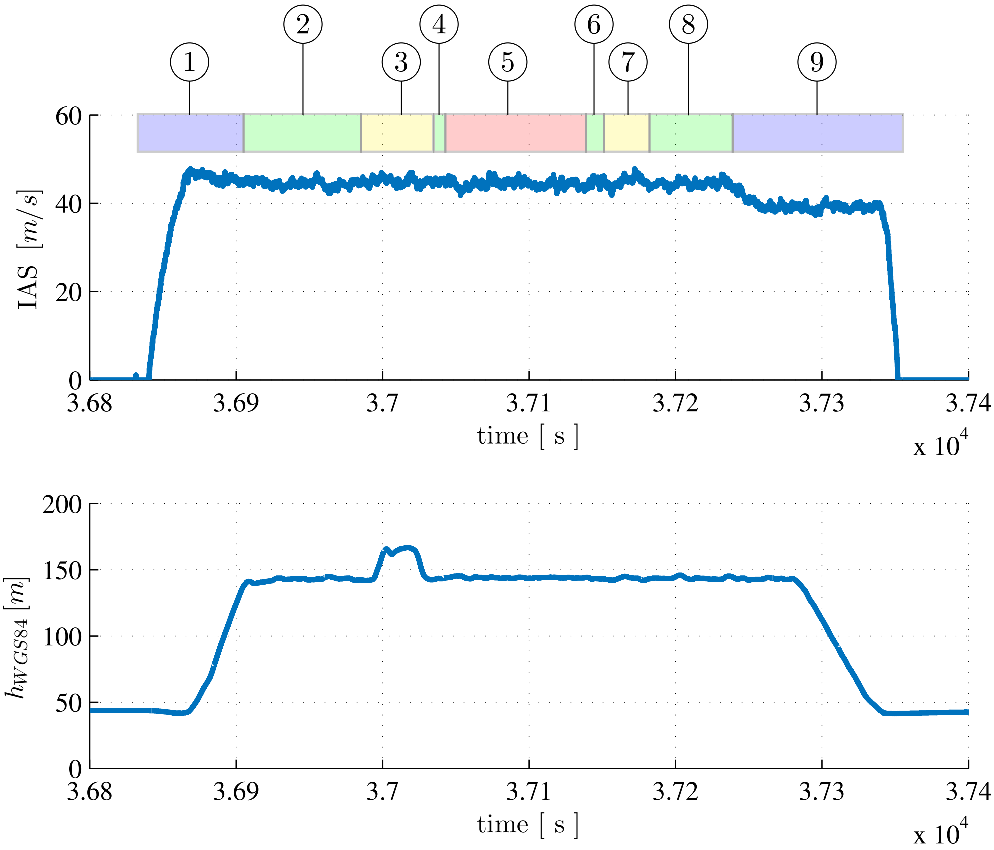

Figure 7.3.: Flight - Speed and Altitude

that the EP is not in control except during taxiing. Instead of evaluating the tracking performance w.r.t. pilot inputs, the autopilot outputs to the CSAS are used for reference. As a consequence, the tracking performance cannot be evaluated by means of conventional measures like rise time or settling time, because of the unavailability of clinical commands such as, for example, steps or ramps at the input of the CSAS during the flight. Consequently, the following analysis of the closed-loop system performance is somewhat qualitative in nature.

The upper plot in figure 7.4 shows the bank angle command (Φ_{cmd}) from the autopilot to the CSAS and the corresponding aircraft response (Φ_{meas}) over the entire flight. Above the plot, the different flight phases are depicted by numbered bars in various colors. The lower plot provides a closer look at one particular segment of the flight corresponding to the time interval 37000 - 37250 seconds and illustrates well the reasonably good tracking behavior in Φ. As designed, the system shows only marginal overshoots in the bank angle response.

In figure 7.5 is a Lissajous-type plot [39] of the bank angle. This portrays i.a. the phase shift between the command and the measured response. It should be noted, that Lissajous figures are defined for sinusoidal signals only, and so here, by interpreting the bank angle signals as an overlay of multiple sinusoidal signals, the Lissajous figure provides an approximation of the phase shift between two signals. The black line represents the plot of Φ_{cmd} vs. Φ_{cmd}, while the blue line is a plot of the measured bank angle Φ vs. Φ_{cmd}. For reference purposes the figure also contains two ellipses representing sinusoidal signals with a phase shift of $\varphi = \frac{\pi}{5}$ for two typical commands employed during the flight. The red ellipse represents a command for loiter maneuver, and the green ellipse a command for a left-hand turn. It can be seen, that the measured

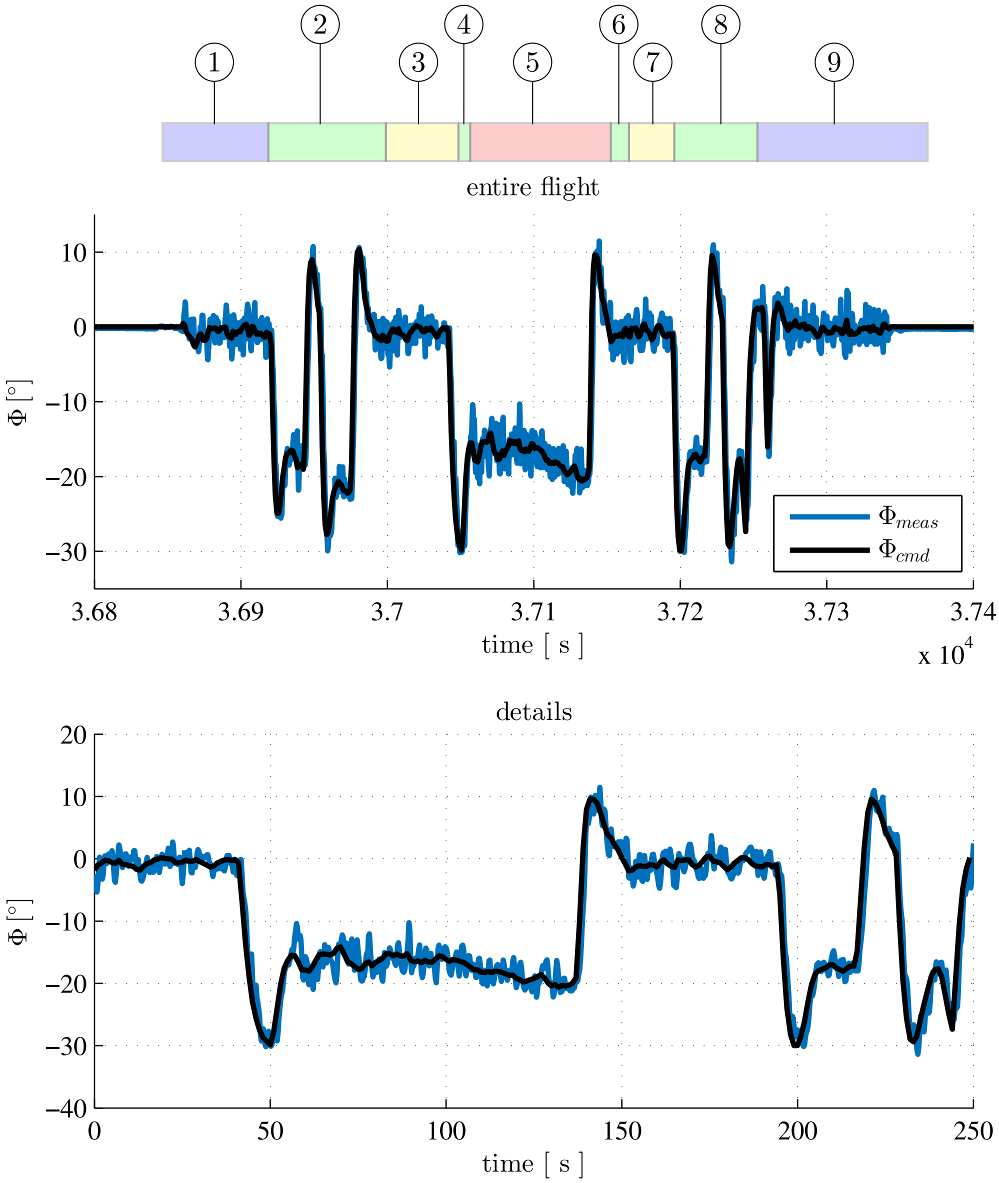

Figure 7.4.: Second Flight - Command tracking

data lies almost entirely within these two curves. The phase between the command and the response is therefore approximately in the range of $\varphi \approx 30° - 40°$.At this point, however, this is still a very rough estimate of the phase shift. It can be seen from the Lissajous plot that the major axis of the ellipse resulting from the measured signal approximately coincides with the line representing the command. From this, it can be concluded, that the controller achieves steady-state accuracy w.r.t. bank angle tracking. To summarize, based on these observations, the overall performance is, as predicted, satisfactory w.r.t. command following.

The measurements of AoS for the entire flight as well as for the featured time interval (seconds 37000 - 37250) are shown in figure 7.6. One peculiarity is clearly noticeable in the upper plot: During the entire flight, there is an offset of $\approx -2°$ from the neutral position ($\beta = 0°$). This offset is particularly apparent on the ground at the beginning and the end of the flight. Even on the downwind leg of the flight (seconds 37000 - 37170) this characteristic does not change. For this reason, assuming the wind intensity and direction was constant throughout the entire flight, it is thought the observed behavior

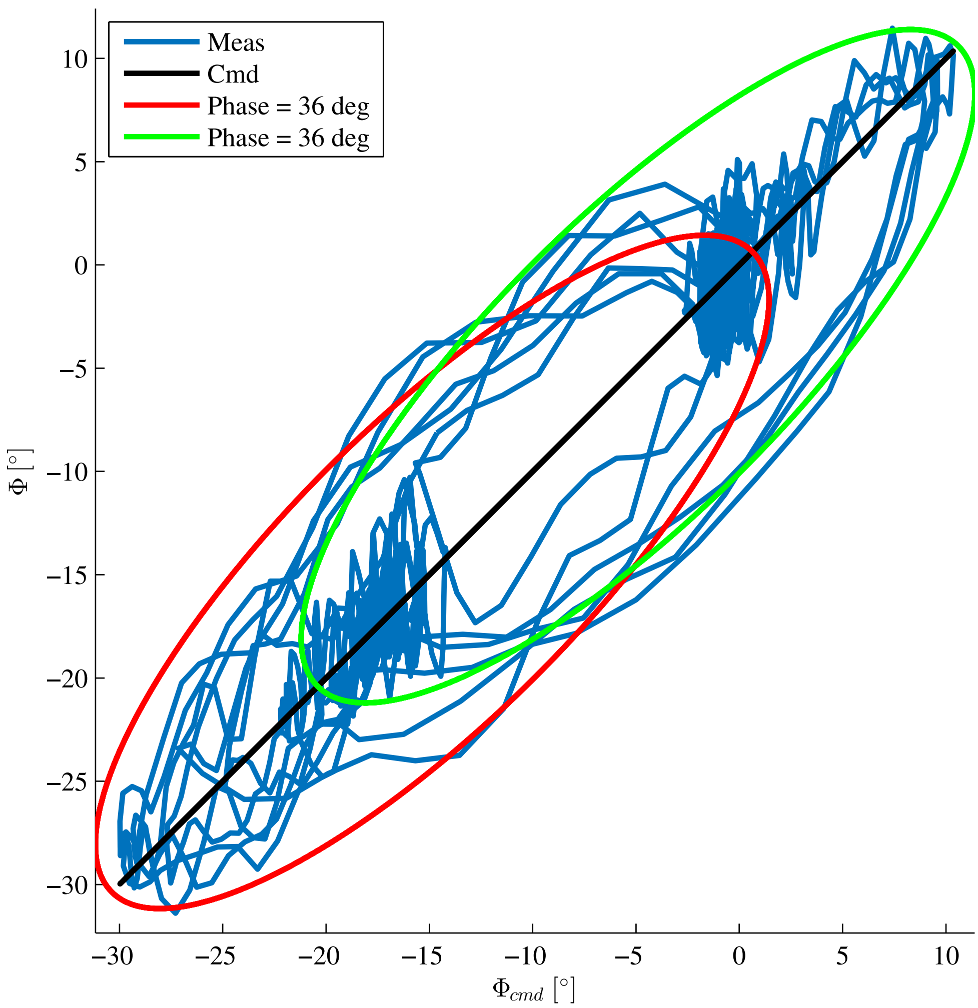

Figure 7.5.: Second Flight - Lissajous plot of the tracking performance

could be caused by imprecise installation of the air data boom. The offset resulting from the faulty air data boom installation should therefore be kept in mind, when analyzing the measurements of AoS.

The disturbance rejection properties of the closed-loop system are now analyzed as follows. The response of the bank angle in figure 7.4 follows the command with a clearly discernible amount of noise. Since the sensor noise in the bank angle measurement is quite low due to the integrating nature of the signal, the oscillations are a result of atmospheric disturbances, i.e. turbulence and gusts. The standard deviation of the tracking error in Φ during steady-state, wings level flight is $\sigma_{e,\Phi} = 1.56°$. Consistent with the measurements of the bank angle, the recorded AoS signal also shows noticeable oscillatory content. The oscillations lead to an error of $\sigma_{e_\beta} \approx 1.4°$. It should be noted in this regard, that the oscillations consist of both the direct impact of the turbulent air on the vanes and the resulting Dutch-roll oscillations that are excited by those disturbances. In addition, it is assumed that a significant amount of the oscillatory content in the signal originates from the flexing in flight of the air data boom itself.

The disturbance rejection of the system is moderate and thus the oscillations are relatively large which indicates a noticeable residual vulnerability of the aircraft to atmospheric disturbances. This characteristic is a direct result of choosing a controller design which favors low actuator activity and robustness w.r.t. system uncertainties

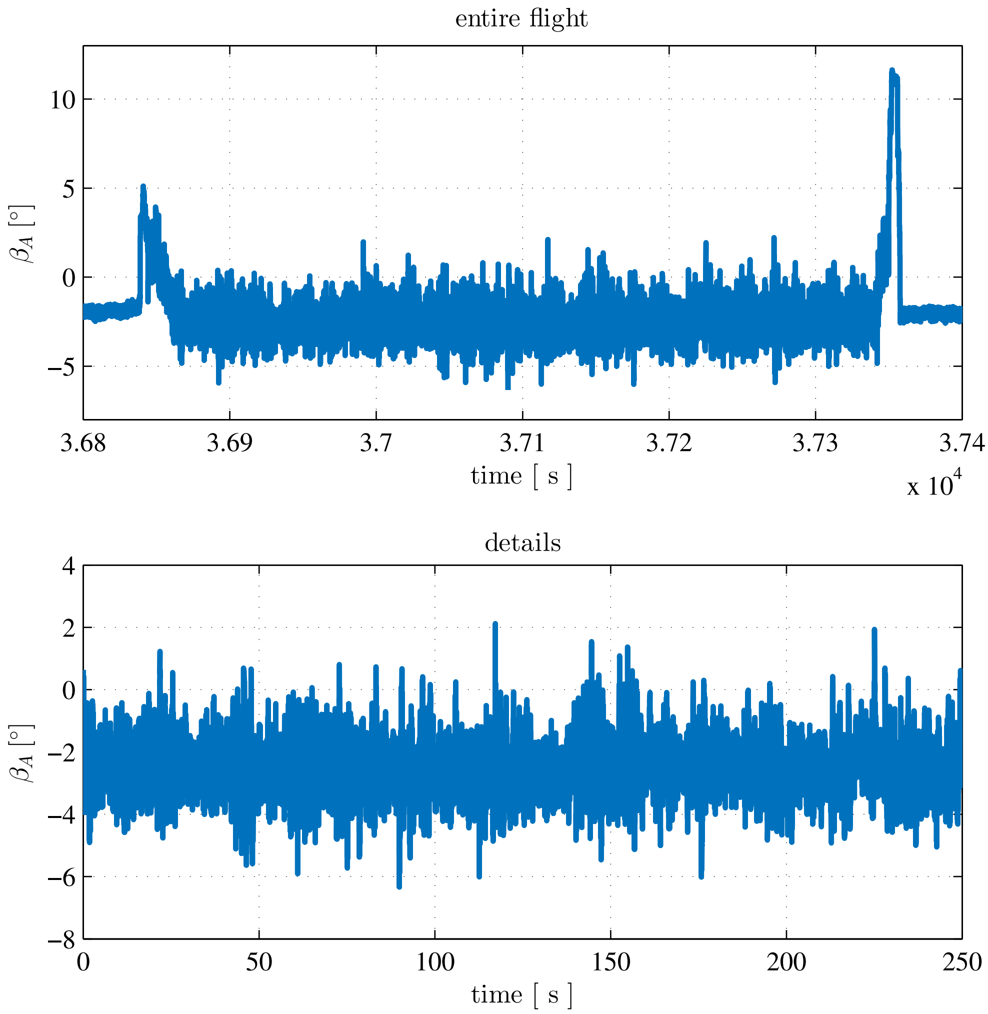

Figure 7.6.: Second Flight - AoS and specific lateral force

at the expense of disturbance rejection performance. Figure 7.7 shows the equivalent control surface commands ξ_{cmd} and ζ_{cmd} over the entire flight, as well as points in time marking the takeoff (green) and landing (red). The largest deflections are commanded by the on-ground controller before takeoff and after landing. During these phases the control surfaces are used to assist the nose wheel in steering the aircraft. The evaluation of the control surface actuator activity is given in equation (7.1). During the flight, the commanded control surface deflections are in the range $|\xi_{cmd}| \leq 2.6°$ and $|\zeta_{cmd}| \leq 4°$ respectively. The deflections and deflection rates are therefore small relative to the available maximum deflection range and consequently comply with the requirements on control surface activity.

$$
\begin{aligned}
\sigma_{\delta_{mx}} &\approx 1° & \qquad \sigma_{\delta_{oxx}} &\approx 2° \\
\sigma_{\dot{\delta}_{mx}} &\approx 10\,°\,\mathrm{s}^{-1} & \qquad \sigma_{\dot{\delta}_{oxx}} &\approx 7.5\,°\,\mathrm{s}^{-1}
\end{aligned}
\tag{7.1}
$$

Due to the poor quality of the AoS measurements and the lack of suitable excitation of aircraft motion, the phi-to-beta ratio $|\Phi/\beta|_{DR}$ cannot be determined exactly from existing flight data obtained so far. Nevertheless, when considering the magnitude of the disturbances in Φ and β in flight phases of straight level flight, one can anticipate a ratio of $|\Phi/\beta|_{DR} \approx 1 - 1.5$, which is an excellent value in respect of Flying Qualities.

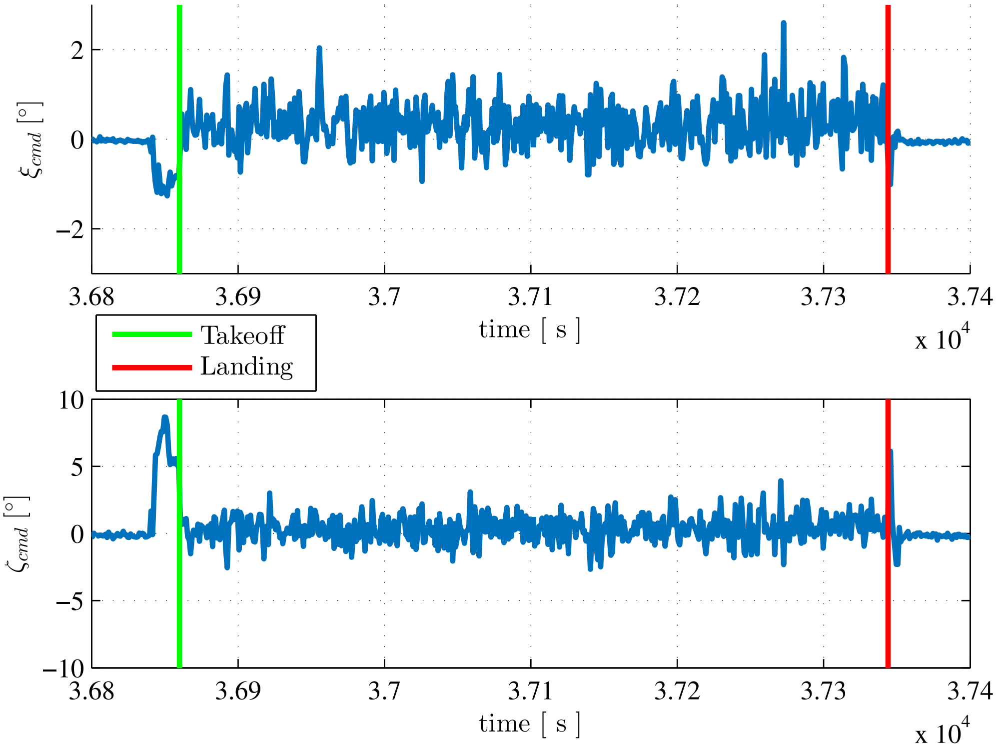

Figure 7.7.: Second Flight - control surface commands

A further important observation can be made from the flight data w.r.t. excitation of yaw motion during roll. It can be seen that the AoS is barely excited during the rolling motion. Hence, as intended, the aircraft performs rolling maneuvers around its velocity vector without significant build-up of sideslip. In figure 7.8, the roll and yaw rates during seconds 37000 - 37250 of the flight are depicted. In order to be able to distinguish between tracking performance and disturbance rejection, the filtered signals (representing a moving average across 15 samples or 3.75 s) are also shown. In addition, the lower figure includes the commanded yaw rate for coordinated flight $r_{cmd,coord}$. It can be seen that the average value of the yaw rate follows the yaw command for turn coordination quite accurately. Hence, the tracking performance of the yaw rate command is excellent, but fairly large oscillations in the body rotation rates again expose the mediocre disturbance rejection properties.

In summary, the resulting closed-loop behavior is suitable for performing the flight mission. The system shows good tracking and significantly improved disturbance rejection properties compared to the simulated inherent system. As a consequence, the disturbance in the bank angle remains below the landing gear load limits, allowing a reliable landing in the presence of light turbulence. After taking into account the suspected error in installation of the air data boom, the AoS remains within the defined landing gear limits for the entire flight. The controller reduces the coupling of roll and yaw motion leading to a low to moderate $|\Phi/\beta|_{DR}$. Furthermore, the aircraft performs velocity vector rolls almost without excitation of the AoS, which is excellent in respect of Flying Qualities. The performance in terms of steady-state turn coordination is also excellent. The closed-loop system provides large margins w.r.t. control surface deflections and deflection rates.

Before the next iteration of the gain design, it is necessary to acquire more data of the dynamic properties of the aircraft in order to reduce uncertainties in the system. It

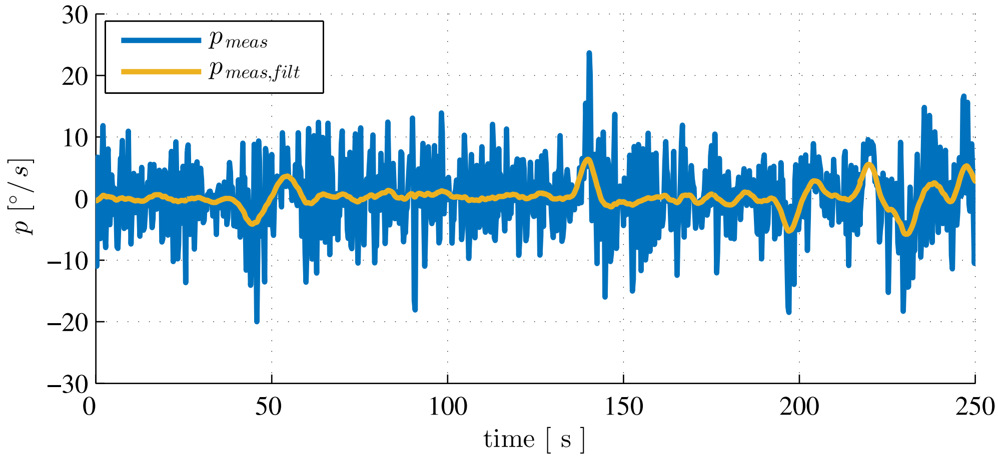

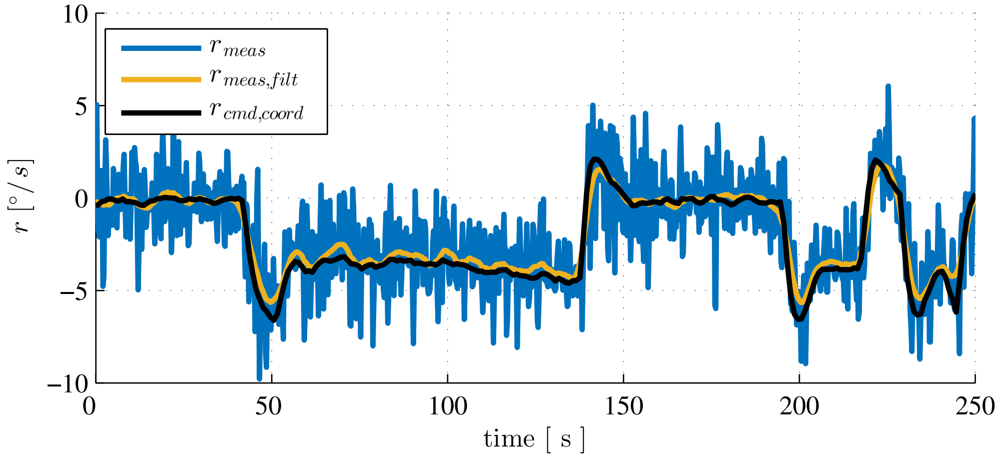

Figure 7.8.: Second Flight - Body rotation rates

is highly recommended that a dedicated system identification campaign is conducted for this purpose. After reducing the system uncertainties, the disturbance rejection behavior can be improved if needed for e.g. performance of super-precision tasks. This could be done by, for example, increasing of feedback gains to provide better roll axis control at the expense of an increase in actuator activity and a reduction of stability margins.

7.3. Comparison with Simulation

The results from the flight are now compared with the results of simulation. For the comparison, a flight phase with relatively constant longitudinal states, and hence low couplings of longitudinal and lateral motion, is chosen to simplify analysis of the controller performance. The bank angle commanded by the autopilot to the CSAS as recorded during the flight is provided to the nonlinear 6-DOF closed-loop simulation. During the simulation, the velocity and altitude of the aircraft are set to the average values measured during the flight phase under study. The simulation is repeated with light and moderate turbulence intensities. In order to make the results from the flight test and simulation comparable to each other, the data from simulation is sampled down to the sampling frequency of the corresponding variables in the FTI recorder. For the variables shown here, the sampling frequency is $f_{FTI} = 4\,\mathrm{Hz}$.

In figure 7.9 the bank angle time histories from the flight test data are compared with those from simulation. The real and simulated behavior of the bank angle match closely. The simulation therefore appears to represent the real behavior of the system correctly w.r.t. roll attitude dynamics. The noise amplitude of the real flight data is between that of simulated light and moderate turbulence. This is consistent with the weather conditions on the day of the flight. Figure 7.10 shows the comparison of the roll rate in real flight and in simulation. In addition to the raw measurements, filtered signals (moving average with window size of 3.75 s) are also shown[1]. In figure 7.10, the same quantities are plotted for the yaw rate. While the roll rate oscillation amplitudes in real flight lie between simulated light and moderate turbulence (and in fact closer to moderate), the amplitudes of the yaw rate oscillations in real flight are comparable to the simulated aircraft reaction in light turbulence conditions. Figures 7.12 and 7.13 show the commanded control surface deflections for $\delta_{mr,cmd}$ and $\delta_{old,cmd}$. Here too, the magnitudes of the deflections seen in the real flight data are reasonable being in the range between those for simulated light and moderate turbulence.

To sum up the comparison between the real and simulated flight, it can be concluded that they agree well in terms of time domain analysis. From this, it can be declared, that the major effort put into modeling the system and especially into modeling of sensor characteristics and dynamic atmosphere has been rewarded. The extensive model-based validation of the closed-loop system has provided a very accurate prediction of the system's behavior as actually observed in flight. The concern, that there would be a large disparity between real and simulated aircraft behavior proved to be unwarranted in the case of lateral motion. Nevertheless, the analysis was performed over a very limited envelope and so no general claim can be made in this respect. Further data needs to be collected in flight in order to gain a deeper insight into the dynamics of the aircraft.

[1] The filtering is performed in post-processing.

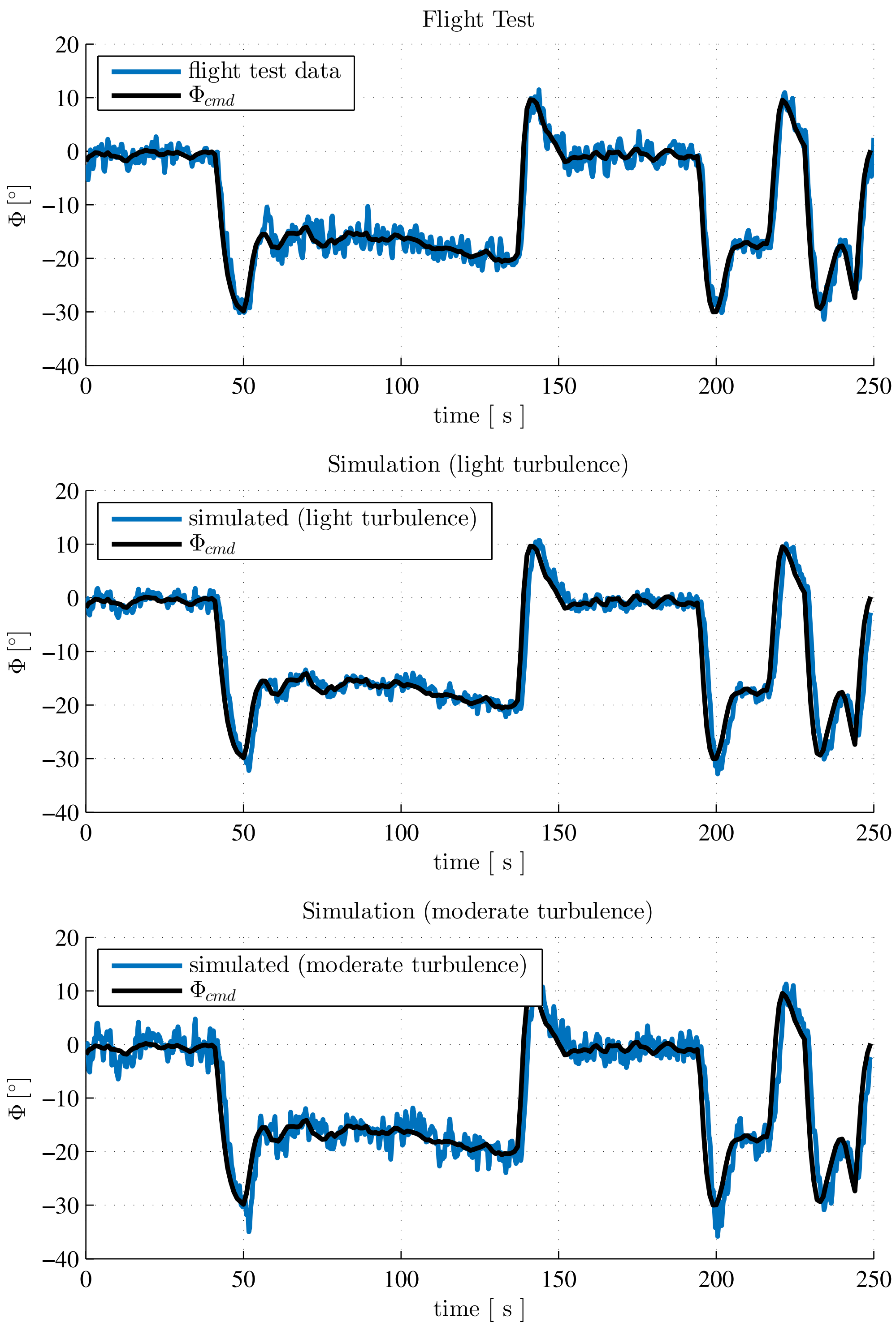

Figure 7.9.: Comparison of flight test with simulation | bank angle

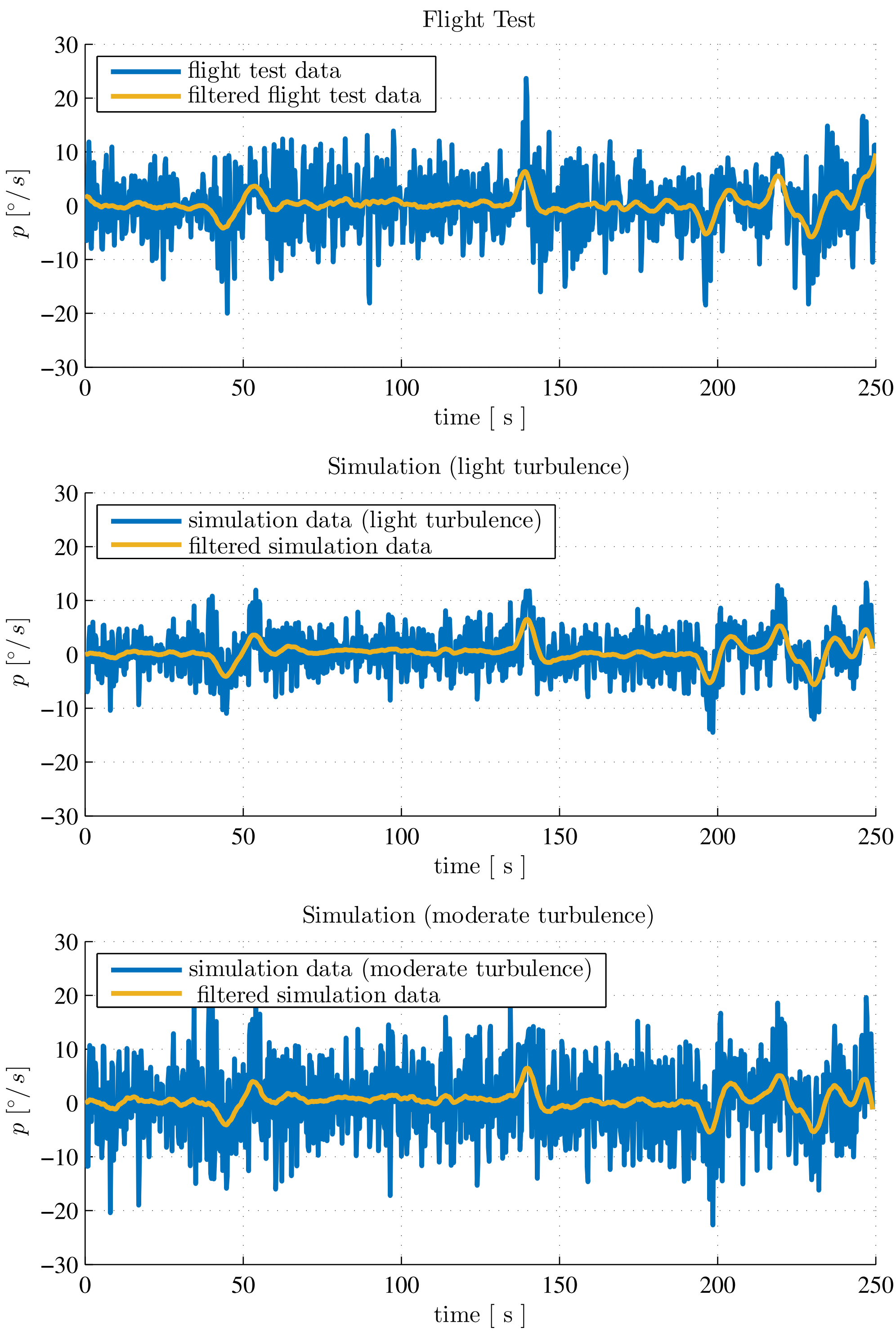

Figure 7.10.: Comparison of flight test with simulation | roll rate

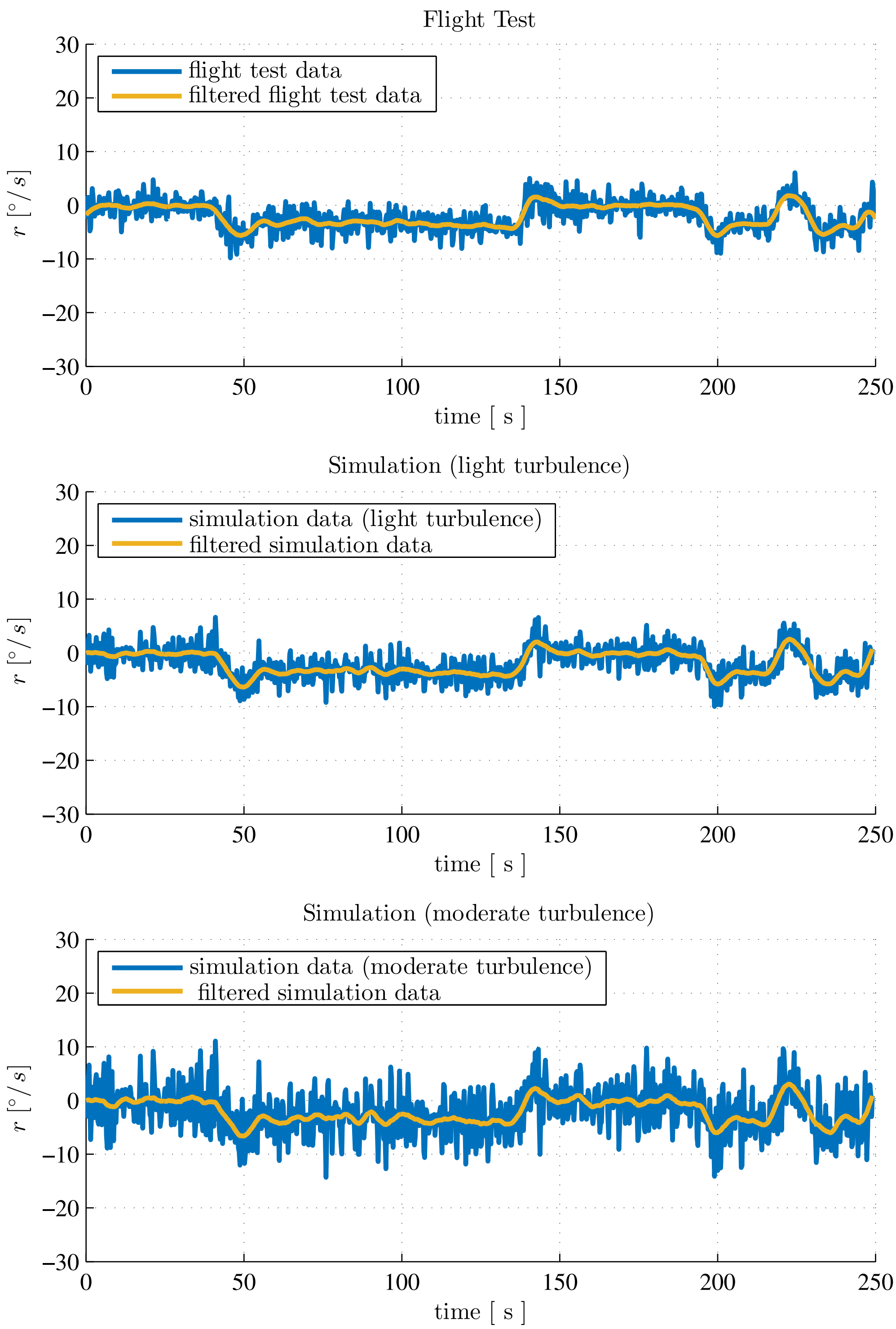

Figure 7.11.: Comparison of flight test with simulation | yaw rate

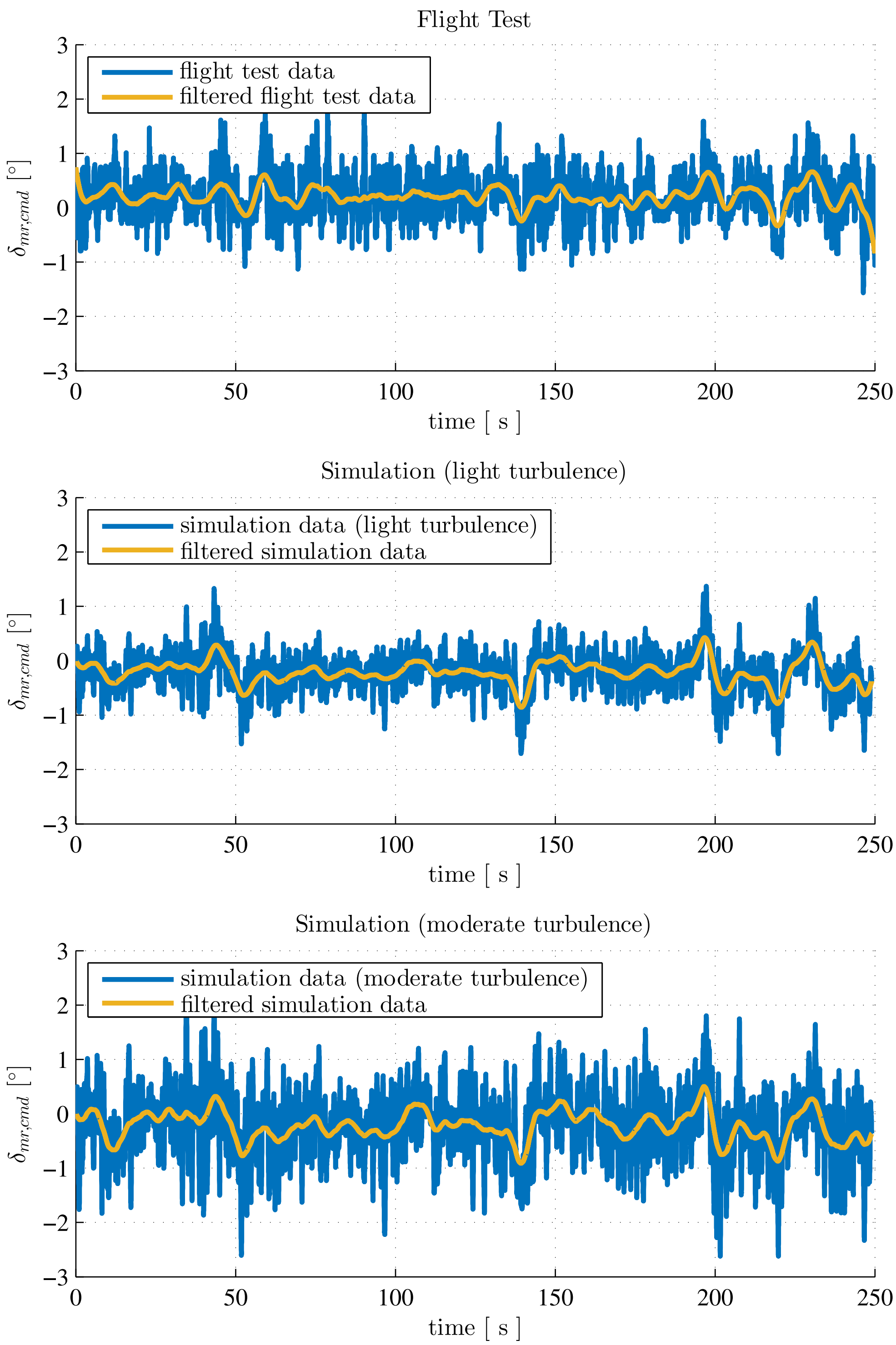

Figure 7.12.: Comparison of flight test with simulation | midboard right flap

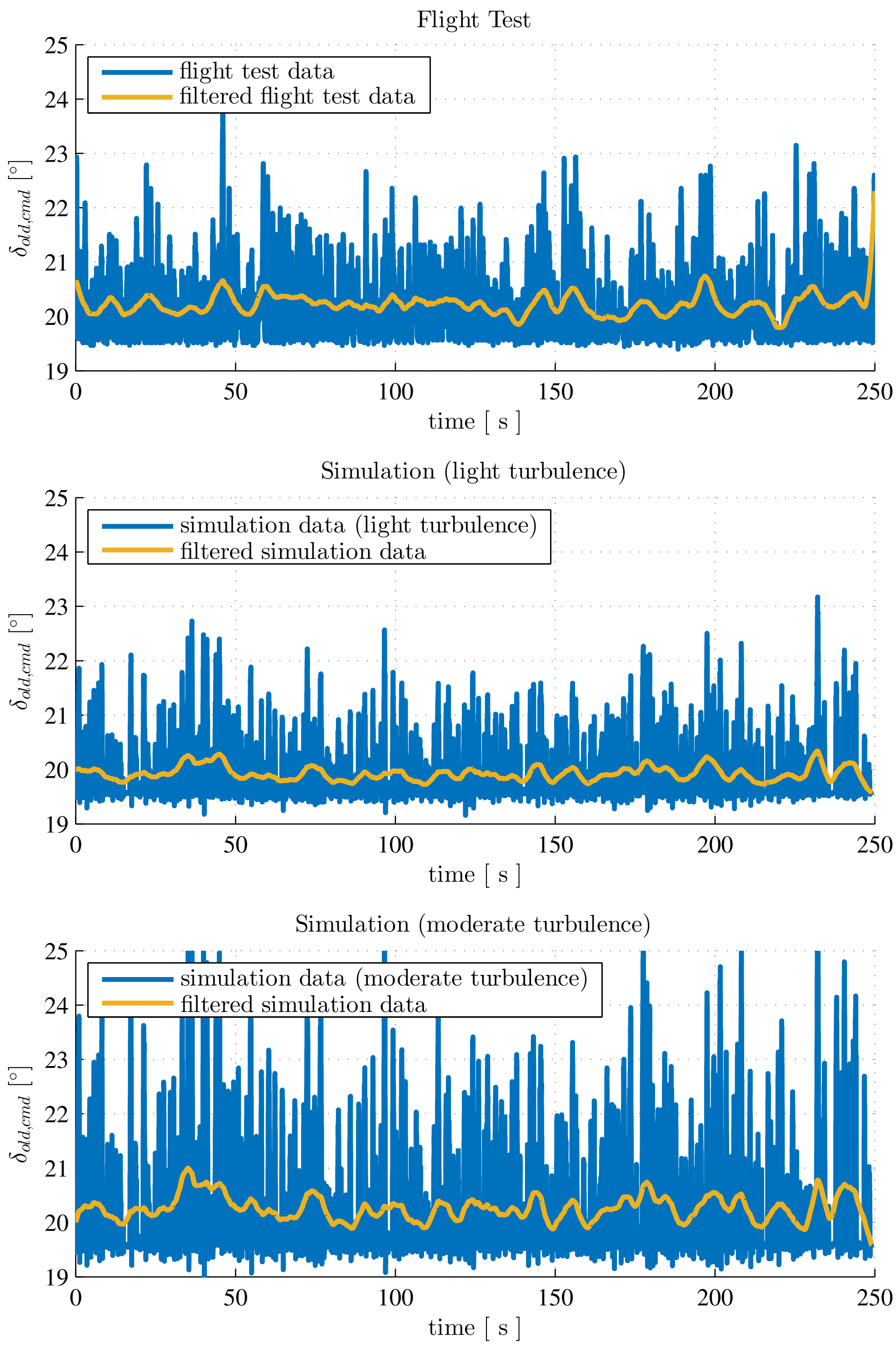

Figure 7.13.: Comparison of flight test with simulation | outboard left dirty flap

8. Summary and Outlook

In the present thesis an innovative controller design for a novel diamond-shaped unmanned aircraft, the so-called SAGITTA Demonstrator, is proposed.

As part of the preliminaries an overview of the aircraft and its systems relevant for flight control is provided in chapter 2. A customized dissimilar, duplex-redundant FMS architecture is proposed. This architecture features the segregation of advanced and complex flight management function from minimum flight control functions required for safe flight, thereby enabling fast development cycles of experimental algorithms in the FMS without giving up safety. By keeping the system complexity of the BFCS as low as possible a high degree of robustness with respect to, for example, sensor failures is achieved and thereby confidence in the survivability of the system is gained.

In chapter 3, first, modeling aspects constraining the controller design, and the aerodynamic characteristics related to lateral-directional motion are discussed. It is found that the aerodynamic derivatives of the SAGITTA Demonstrator are in many respects comparable to those of known delta-wing aircraft, but large uncertainty is attributed to the control effectiveness. To overcome the large uncertainty in the effectiveness of the outboard flaps, a so-called preloading is introduced, and thereby, the operation in the critical deflection range is avoided. This results in a significant degradation of flight performance and leads to a reduction in the yaw control potential.

Two control surface linkage types are proposed and their respective advantages and disadvantages are analyzed. Due to its favorable yaw characteristics, the "aileron" linkage proves to be the better choice and hence is chosen for implementation. However, the decision should be reviewed as soon as detailed modeling of the interferences between flaps is available.

In chapter 3, the sensor and actuator characteristics are presented briefly. The analysis of sensor characteristics reveals the quality of the aerodynamic flow angles measurements to be unsatisfactory for usage in controller feedback. This fact has a considerable influence on the development of the control strategy.

A detailed analysis of the SAGITTA Demonstrator's lateral dynamics based on linear state-space models is performed. It shows that the aircraft setup with vertical tails attached generally exhibits a conventional distribution of poles and zeros in the pole-zero map. Nevertheless, there are some abnormalities, such as the Dutch-roll's natural frequency showing a prominent deflection in its course over the speed envelope which may be associated with the observed peculiarities in the aerodynamic derivatives. Furthermore, the downscaling of size and mass of the aircraft leads as expected, to higher natural frequencies and smaller time constants in the dynamics compared to a full scale aircraft. The impact of aerodynamic uncertainties on lateral-directional dynamics of the aircraft is discussed and the major influencing parameters are identified. They are candidates for a future parameter identification study.

The discussion of the inherent lateral dynamics concludes with examination of the aircraft's dynamic couplings in frequency- and time domains. The couplings are characterized by the relative positions of poles and zeros of the aileron-to-bank angle transfer function and visualized by the corresponding step responses. The analysis is completed by a presentation of aircraft's reaction on lateral gust in time domain which reveals its susceptibility to atmospheric disturbances.

The discussion on Flying Qualities in chapter 4 plays a central role in this work. It includes an extensive study of literature and goes beyond the review of classical de facto standards. Most Flying Qualities reviews are focused mainly on longitudinal motion. In contrast, this work provides a study of Flying Qualities requirements and analyses related to lateral motion. The focus is on the applicability of the proposed methods to non-conventional response types such as AC/AH taking into account also the fact that the system is unmanned. Furthermore, adaptation of the Flying Quality standards to small-scale aircraft is discussed and a novel approach using dynamic scaling is applied to Flying Qualities requirements for lateral motion. Subsequently, the inherent system dynamics of the SAGITTA Demonstrator are assessed w.r.t. the major requirements formulated in chapter 4.

Chapter 5 describes the step-by-step development of the lateral CSAS for which the gain design method called Constrained Eigenstructure Assignment (CEA) is used. In contrast to Eigenstructure Assignment, CEA provides the controller designer with the possibility to introduce structural constraints on the feedback matrix at the expense of exact Eigenvalue and Eigenvector placement.

In the first step of controller design, Control Allocation is introduced in order to align the control inputs with the motion around the x-and y-axes in the Stability-Axes Coordinate System (S). Subsequently, an initial architecture for a feedback controller is proposed. In this first feedback controller (*V1*) the measurements of r, β, p, Φ and the integrators $\int \Phi$ and $\int \beta$ are used. The *V1* - controller aims for the full decoupling of roll and yaw motion. The gain design is obtained by means of Eigenstructure Assignment, and consequently no structural constraints are introduced into the feedback matrix. The result of the design is a high gain feedback controller, which fails to meet the requirements on actuator activity. This is confirmed by means of PSD analysis.

In the second controller design (*V2*) the problems identified in the *V1* - controller are addressed. In order to reduce the feedback gains, a novel Eigenvector specification for the Dutch-roll is introduced. This specification targets a meaningful reduction in roll-yaw couplings, and consequently a moderate rather than a full decoupling. This yields an excellent design in terms of compliance with the requirements on actuator activity.

In order to further simplify the controller structure, a sensitivity analysis is conducted in a subsequent step to identify ineffective gains in the feedback of the *V2* - controller. Ineffective gains are those gains, which only contribute marginally to the closed-loop location of Eigenvalues and to the shape of corresponding Eigenvectors. In this work, the methodology of Eigenvalue and Eigenvector sensitivity analysis is extended and the so-called Eigenvalue and Eigenvector-shift matrices are introduced to visualize the impact of feedback gains on particular Eigenvalues and Eigenvectors. Based on the results of this sensitivity analysis, a new feedback structure is derived, from which a gain design for the *V3*-controller is produced by application of the Constrained Eigenstructure Assignment.

To overcome the problem of unsatisfactory sensor characteristics w.r.t. aerodynamic flow angle measurements (AoA and AoS), an attempt is made to eliminate the dependence of the feedback controller on AoS. Using the feedback structure of the *V3*-controller as a basis, a new design is proposed which eliminates use of β and $\int \beta$. This results in the final controller structure.

In a subsequent step, the feedback matrix is modified in order to explicitly take the turn coordination term into account. For this, the measurements of yaw rate and the desired turn coordination command are combined into a new feedback variable $\tilde{r}$ and introduced in the gain design.

The architecture of the feed-forward controller is designed to achieve an AC/AH behavior in bank angle. A response type such as this is often used for helicopter control, but is highly unusual for fixed-wing aircraft. By employing an AC/AH system, the controller design addresses the diamond shape of the aircraft resulting in problems of determining the aircraft's orientation by the External Pilot, as it allows the current aircraft attitude to be deduced from the position of the control stick of the radio transmitter. It his way, the range is extended within which the External Pilot can take over control of the aircraft in an emergency.

In this work, a novel method for designing a command filter is introduced. It is based on the OLOP criterion and uses the corresponding method for determination of the filter's frequency. The filter obtained protects the system from pilot-induced actuator saturations and hence, is a powerful means of preventing PIOs.

Following the completion of the controller design, extensive analyses of the linear closed-loop system are conducted in frequency domain and time domain taking into account system uncertainties, sensor characteristics and time delays. The stability analysis using so-called bottleneck cuts w.r.t. the Nichols Diagram shows sufficient phase and gain margins throughout the envelope. Consequently, the approach of designing a system with low feedback gains is fully rewarded. The tracking behavior complies with the stated requirements and shows consistent behavior over the entire envelope. The actuator activity resulting from sensor noise and turbulence is also within the limits specified. The disturbance rejection properties of the closed-loop system however are only moderate, which is the disadvantage of using low feedback gains. Nevertheless, the system provides acceptable performance in conditions of light turbulence. In relation to some system uncertainties, the closed-loop system is unable to meet a few of the nonobligatory performance requirements and some uncertainty combinations lead to an increase in the $|\Phi/\beta|_{DR}$ ratio to 2.5. This is still a moderate value and is therefore not considered to be critical. Furthermore, for some uncertainty combinations evaluation of the bandwidth criterion predicts Level 2 Flying Qualities. Due to the short flight duration of the SAGITTA Demonstrator, the increased workload is acceptable to the pilots.

The work is completed in chapter 7 by analysis of the maiden flight campaign of the SAGITTA Demonstrator. Evaluation of the data recorded during the flight confirms the observations that were made during the simulation-based validation. The lateral tracking behavior of the aircraft is excellent. During initiation of turns accurate velocity vector rolls are performed without excitation of the AoS. As predicted, the aircraft is vulnerable to atmospheric disturbances and the disturbance rejection is considered to be fair: nevertheless, it remains within safe limits at all times. The actuator activity is low, as intended by design. The overall performance of the closed-loop controller in lateral motion is satisfactory to perform the first flight mission reproducibly and safely. Comparison of the flight data with simulation shows a surprisingly very good match. Once again model-based design is proven to be one of the key techniques needed to master such projects as the development of SAGITTA Demonstrator's CSAS. In this regard, it is worth stressing, that including as many real world effects as possible when modeling sensors and other system components in simulation significantly increases the confidence level of simulation and is an effective means of reducing the project risk.

With the maiden flight of the SAGITTA Demonstrator the first phase of this project is completed. Further development of the aircraft will require a significant amount of effort. Some ideas related to flight dynamics and control are provided below. With regard to flight control of the SAGITTA Demonstrator, methods for improving the quality of AoS measurements should be investigated in near term, starting with the precise calibration of the Air Data Boom. Although it is not required for flight control in the case of the setup with two vertical tails, a reliable and accurate measurement of the sideslip angle is necessary to gain a deeper insight into the flight dynamics of the system and hence, to simplify post-flight analyses. The knowledge gained during the first flight campaign should be used, if possible, to improve the simulation model of the aircraft. In addition, a new gain design for the CSAS is required for operation of the aircraft with retracted landing gear.

In the medium term, reduction of uncertainties in the system is one prerequisite for further development of the CSAS. Hence, a system identification campaign or further wind tunnel measurements are required in order to enhance the ADM. The emphasis should be placed on the reduction of uncertainties in the efficiency of the control surfaces, in particular the outboard flaps. The goal here is to reduce the preloading of the outboard flaps to a minimum. Further development of the FMS should target establishing redundancy throughout the FMS. Hence, implementation of the elements missing from the BFCS and the introduction of a functional monitoring and voting concept in the ACEs are all desirable. In order to make progress towards the objective of tailless flight, further investigations into the flight dynamics of the "Clean Setup" are required. Furthermore, a new feedback design is needed, which most likely will require a reliable AoS measurement or a suitable alternative. For performance of complex maneuvers such as rolling into and out of inverted flight orientation, a new feed-forward controller needs to be designed.

In the long term, the approach of applying the dynamic scaling to Flying Qualities measures should be validated. In order to achieve a breakthrough in the field of research on Flying Qualities of unmanned aircraft, an extensive data base containing flight test results from various aircraft types must be established by the international RPAS flight control community.

Bibliography

[1] Adams, J. J. and Moore, F. L. An analytical study of aircraft lateral-directional handling qualities using pilot models. Tech. rep. 1976.

[2] Andry, A. N., Shapiro, E. Y., and Chung, J. C. “Eigenstructure assignment for linear systems”. In: *IEEE transactions on aerospace and electronic systems* 5 (1983), pp. 711–729.

[3] Ashkenas, I. L., Jex, H. R., and McRuer, D. T. Pilot-induced oscillations: their cause and analysis. Tech. rep. DTIC Document, 1964.

[4] Aviation, US Army and Command, Missile. Handling qualities requirements for military rotorcraft. Tech. rep. ADS-33E-PRF, 2000.

[5] Bailey, R. E. and Smith, R. E. “Analysis of augmented aircraft flying qualities through application of the Neal-Smith criterion”. In: *AIAA Guidance and Control Conference, Albuquerque,NM.* 1981, 26pp.

[6] Bierig, A. et al. “Design of the General Systems for the SAGITTA Demonstrator UAV”. In: *Unmanned Aircraft Systems (ICUAS), 2017 International Conference on.* IEEE. 2017, pp. 1767–1777.

[7] Braun, S. et al. “Configuration assessment and preliminary control law design for a novel diamond-shaped UAV”. In: *Unmanned Aircraft Systems (ICUAS), 2014 International Conference on.* IEEE. 2014, pp. 1009–1020.

[8] Brockhaus, R. Flugregelung. Springer-Verlag, 2013.

[9] Buonanno, A. “Aerodynamic circulation control for flapless flight control of an unmanned air vehicle”. PhD thesis. 2009.

[10] Buttkus, B. Spectral analysis and filter theory in applied geophysics. Springer Science & Business Media, 2012.

[11] Calvo-Ramon, J. “Eigenstructure assignment by output feedback and residue analysis”. In: *IEEE transactions on Automatic Control* 31.3 (1986), pp. 247–249.

[12] Castro, H. V. de. “Flying and handling qualities of a fly-by-wire blended-wing-body civil transport aircraft”. PhD thesis. 2003.

[13] Chalk, C. R. “Excessive roll damping can cause roll ratchet”. In: *Journal of Guidance, Control, and Dynamics* 6.3 (1983), pp. 218–219.

[14] Chalk, C. R. et al. Background Information and User Guide for Mil-F-8785B (ASG),’Military Specification-Flying Qualities of Piloted Airplanes’. Tech. rep. DTIC Document, 1969.

[15] Chambers, J. Modeling Flight NASA Latest Version: The role of dynamically scale Free Flight Models in support of NASA aerospace programs. Vol. 3. Joseph Chambers, 2015.

[16] Ching, S. et al. Quasilinear Control: Performance Analysis and Design of Feedback Systems with Nonlinear Sensors and Actuators. Cambridge University Press, 2010.

[17] Cook, M. V. Flight dynamics principles: a linear systems approach to aircraft stability and control. Butterworth-Heinemann, 2012.

[18] Cotting, M. C. Evolution of flying qualities analysis: Problems for a new generation of aircraft. Tech. rep. DTIC Document, 2010.

[19] Davidson, J. B. and Andrisani, D. Lateral-directional eigenvector flying qualities guidelines for high performance aircraft. Tech. rep. 1996.

[20] Duke, E. L., Antoniewicz, R. F., and D., Krambeer K. Derivation and definition of a linear aircraft model. Tech. rep. NASA RP-1207. 1988.

[21] Faleiro, L. F. "The application of eigenstructure assignment to the design of flight control systems". PhD thesis. Loughborough University, 1998.

[22] Foster, T. M. and Bowman, W. J. "Dynamic stability and handling qualities of small unmanned aerial vehicles". In: *43rd AIAA Aerospace Sciences Meeting and Exhibit*. 2005, pp. 10–13.

[23] Geiser, M. Modeling of a Diamond-Shaped UAV for the Development and Qualification of its Flight Control System. Tech. rep. Technische Universität München, Institute of Flight System Dynamics, 2017.

[24] Geiser, M. "Modelling, Simulation and Flight Mechanics Analysis of a Low Observability Flying Wing UAV". Technische Universität München, 2011.

[25] Gilbreath, G. P. Prediction of pilot-induced oscillations (PIO) due to actuator rate limiting using the open-loop onset point (OLOP) criterion. Tech. rep. DTIC, 2001.

[26] Harper, R. P. and Cooper, G. E. "Handling qualities and pilot evaluation". In: *Journal of Guidance, Control, and Dynamics* 9.5 (1986), pp. 515–529.

[27] Heller, M. Untersuchung zur Steuerung und Robusten Regelung der Seitenbewegung von Hyperschall-Flugzeugen. Vol. 33. Herbert Utz Verlag, 1999.

[28] Heller, M., Baier, T., and Schuck, F. "Lateral Fly by Wire Control System Dedicated to Future Small Aircraft". In: *Advances in Aerospace Guidance, Navigation and Control*. Springer, 2013, pp. 353–372.

[29] Hellert, C. et al. A High Level Active Perception Concept For UAV Mission Scenarios. Deutsche Gesellschaft für Luft-und Raumfahrt-Lilienthal-Oberth eV, 2012.

[30] Hess, R. A. "Theory for roll-ratchet phenomenon in high-performance aircraft". In: *Journal of guidance, control, and dynamics* 21.1 (1998), pp. 101–108.

[31] Hodgkinson, MS John. Aircraft handling qualities. Vol. 134. Blackwell Science, 1999.

[32] Hoffmann, J. and Brunner, U. MATLAB und Tools. Pearson Deutschland GmbH, 2002.

[33] Hoh, R. H. et al. Development of handling quality criteria for aircraft with independent control of six degrees of freedom. Tech. rep. DTIC Document, 1981.

[34] Hoh, R. H. et al. Proposed MIL Standard and Handbook-Flying Qualities of Air Vehicles. Volume 2. Proposed MIL Handbook. Tech. rep. DTIC Document, 1982.

[35] Hövelmann, A. and Breitsamter, C. Aerodynamic characteristics of the sagitta diamond wing demonstrator configuration. Deutsche Gesellschaft für Luft-und Raumfahrt-Lilienthal-Oberth eV, 2013.

[36] Hövelmann, A., Pfnür, S., and Breitsamter, C. "Flap efficiency analysis for the SAGITTA diamond wing demonstrator configuration". In: *CEAS Aeronautical Journal* (2014), pp. 1–18.

[37] Jekeli, Christopher. Inertial navigation systems with geodetic applications. Walter de Gruyter, 2012.

[38] Karam, J. T. “Dynamic behavior of angle-of-attack vane assemblies”. In: *Journal of Aircraft* 12.3 (1975), pp. 190–192.

[39] Al-Khazali, H. A. and Askari, M. R. “Geometrical and graphical representations analysis of lissajous figures in rotor dynamic system”. In: *IOSR Journal of Engineering* 2.05 (2012), pp. 971–978.

[40] Krause, C. and Holzapfel, F. “Designing a system automation for a novel UAV demonstrator”. In: *2016 14th International Conference on Control, Automation, Robotics and Vision (ICARCV)*. IEEE. 2016, pp. 1–6.

[41] Küegler, M.E. and Holzapfel, F. “Planning, Implementation, and Execution of an Automatic First Flight of a UAV”. In: *Congress of the International Council of the Aeronautical Sciences (ICAS)*. IEEE. 2018.

[42] Kügler, M. E. and Holzapfel, F. “Designing a safe and robust automatic take-off maneuver for a fixed-wing UAV”. In: *2016 14th International Conference on Control, Automation, Robotics and Vision (ICARCV)*. IEEE. 2016, pp. 1–6.

[43] Kügler, M. E. and Holzapfel, F. “Developing Automated Contingency Procedures for the ATOL System of a Fixed-Wing UAV through Online FDD”. In: *AIAA Modeling and Simulation Technologies Conference*. 2016, p. 3221.

[44] Lallman, F. J. Relative control effectiveness technique with application to airplane control coordination. 1985.

[45] Lewis, F. L., Vrabie, D., and Syrmos, V. L. Optimal Control. John Wiley & Sons, 2012.

[46] Littleboy, D. M. “Numerical techniques for eigenstructure assignment by output feedback in aircraft applications”. PhD thesis. University of Reading, 1994.

[47] Marple, S. L. Digital spectral analysis: with applications. Prentice-Hall Englewood Cliffs, NJ, 1987.

[48] McRuer, D. T., Graham, D., and Ashkenas, I. Aircraft dynamics and automatic control. Princeton University Press, 2014.

[49] McRuer, D. T. and Jex, H. R. “A Review of Quasi-Linear Pilot Models”. In: *IEEE Transactions on Human Factors in Electronics* HFE-8.3 (Sept. 1967), pp. 231–249. ISSN: 0096-249X. DOI: 10.1109/THFE.1967.234304.

[50] Mengali, G. and Giulietti, F. “Unified algebraic approach to approximation of lateral-directional modes and departure criteria”. In: *Journal of guidance, control, and dynamics* 27.4 (2004), pp. 724–728.

[51] Mitchell, D. G. et al. “Evolution, revolution, and challenges of handling qualities”. In: *Journal of guidance, control, and dynamics* 27.1 (2004), pp. 12–28.

[52] Mitchell, D. G. et al. Proposed Incorporation of Mission-Oriented Flying Qualities into MIL-STD-1797A. Tech. rep. DTIC Document, 1994.

[53] Mooij, H. A. “Criteria for low-speed longitudinal handling qualities of transport aircraft with closed-loop flight control systems”. PhD thesis. Delft University of Technology, 1984.

[54] Moormann, D. “The HIRM+ Flight Dynamics Model”. In: *Advanced Techniques for Clearance of Flight Control Laws*. Springer, 2002, pp. 121–139.

[55] NA. ARP94910: Specification Guide For Aerospace - Vehicle Management Systems - Flight Control Design, Installation and Test of Military Unmanned Aircraft. Standard. SAE, 2012.

[56] NA. MIL-DTL-9490E: General Specification for Flight Control Systems - Design, Installation and Test of Piloted Aircraft. Standard. Department of Defence, 2008.

[57] NA. MIL-HDBK-1797: Flying Qualities of Piloted Aircraft. Standard. Department of Defence, 1997.

[58] NA. Successful first flight for UAV demonstrator SAGITTA. 2017. URL: `http://www.airbus.com/newsroom/press-releases/en/2017/07/successful-first-flight-for-uav-demonstrator-sagitta.html` (visited on 12/20/2017).

[59] NA. Wikipedia Article on Dassault LOGIDUC. 2016. URL: `https://en.wikipedia.org/wiki/Dassault_LOGIDUC` (visited on 06/17/2017).

[60] NA, US Military Specification. 8785C: Flying Qualitites of Piloted Aircraft. Standard. 1980.

[61] Neal, T. P. and Smith, R. E. An In-Flight Investigation to Develop Control System Design Criteria for Fighter Airplanes. Volume 1. Tech. rep. DTIC Document, 1970.

[62] Neal, TP and Smith, RE. An Inflight Investigation to Develop System Design Criteria for Fighter Airplanes', Air Force Flight Dynamics laboratory, WPAFB, Ohio. Tech. rep. AFFDL TR-70-74, 1970.

[63] Nguyen, L. T. et al. Simulator study of stall/post-stall characteristics of a fighter airplane with relaxed longitudinal static stability(F-16). Tech. rep. NASA TP-1568. 1979.

[64] Nikodem, F. et al. "Design of a Retractable Landing Gear for the Sagitta Demonstrator UAV". In: *DLRK*. DGLR. 2017.

[65] Oezger, Erol. SAGITTA Aero Data Module Manual. Internal Report CA-SG-191-M-0003-G. CASSIDIAN, 2014.

[66] Ossmann, D. "Untersuchung zu Kriterien für höhere Flugeigenschaftsbewertung und PIO-Prävention". Diplomarbeit. FH Joanneum Graz, 1984.

[67] Pecher, W. Sagitta - Evaluation of Actuator Test Data and Model Comparison. Internal report CA-SG-270-R-0035-B. Airbus Defence & Space, 2015.

[68] Prosser, C. F. and Wiler, C. D. RPV Flying Qualities Design Criteria. Tech. rep. DTIC Document, 1976.

[69] Radford, R. C., Smith, R., and Bailey, R. Landing flying qualities evaluation criteria for augmented aircraft. Tech. rep. NASA-CR-163097. 1980.

[70] Raghavan, B. and Ananthkrishnan, N. "Small-Perturbation Analysis of Airplane Dynamics with Dynamic Stability Derivatives Redefined". In: *Journal of Aerospace Science and Technologies* 61.3 (2009), p. 365.

[71] Reigelsperger, W. C., Banda, S. S., and Lemaster, D. P. "Application of multivariable control theory to aircraft control laws". In: *Flight Dynamics Directorate, Wright-Patterson Air Force Base, Tech. Rep. WL-TR-96-3099* (1996).

[72] Russell, J. Performance and stability of aircraft. Butterworth-Heinemann, 1996.

[73] Sarrafian, S. K. and Powers, B. G. "Application of frequency-domain handling qualities criteria to the longitudinal landing task". In: *Journal of Guidance, Control, and Dynamics* 11.4 (1988), pp. 291–292.

[74] Schmidt, L. V. Introduction to aircraft flight dynamics. AIAA, 1998.

[75] Schneider, V., Mumm, N. C., and Holzapfel, F. "Trajectory generation for an integrated mission management system". In: *Aerospace Electronics and Remote Sensing Technology (ICARES), 2015 IEEE International Conference on*. IEEE. 2015, pp. 1–7.

[76] Seiferth, D. and Heller, M. "Testing and performance enhancement of a model-based designed ground controller for a diamond-shaped unmanned air vehicle (UAV)". In: *Control Technology and Applications (CCTA), 2017 IEEE Conference on*. IEEE. 2017, pp. 1988–1994.

[77] Shapiro, E. Y. and Chung, J. C. "Flight control system synthesis using eigenstructure assignment". In: *Journal of Optimization Theory and Applications* 43.3 (1984), pp. 415–429.

[78] Skogestad, S. and Postlethwaite, I. Multivariable feedback control: analysis and design. Vol. 2. Wiley New York, 2007.

[79] Slater, G. and Zhang, Q. "Controller design by eigenspace assignment". In: *Dynamics Specialists Conference*. 1990, p. 1193.

[80] Smith, B., Thomson, K., and M., Dowd. Time Series Analysis Lecture. 2016. URL: `http://www.mathstat.dal.ca/~stat5390` (visited on 11/09/2016).

[81] Sobel, K. M. and Lallman, F. J. "Eigenstructure assignment for the control of highly augmented aircraft". In: *Journal of Guidance, Control, and Dynamics* 12.3 (1989), pp. 318–324.

[82] Sobel, K. M., Lallman, F. J., and Yu, W. "Eigenstructure assignment with gain suppression using eigenvalue andeigenvector derivatives". In: *Journal of Guidance, Control, and Dynamics* 13.6 (1990), pp. 1008–1013.

[83] Sobel, K. M. and Shapiro, E. Y. "An extension to the pseudo control strategy with application to an eigenstructure assignment yaw pointing/lateral translation control law". In: *Proceedings of the 30th IEEE Conference on Decision and Control*. IEEE. 1991, pp. 515–516.

[84] Stadlberger, K. F. "Modelling and Performance Aspects of Coanda Flap Systems". Dissertation. München: Technische Universität München, 2016.

[85] Stengel, R. F. Flight dynamics. Princeton University Press, 2015.

[86] Stevens, B. L., Lewis, F. L., and Johnson, E. N. Aircraft Control and Simulation: Dynamics, Controls Design, and Autonomous Systems. John Wiley & Sons, 2015.

[87] Theißing, N., Kahn, G., and Schulte, A. Cognitive automation based guidance and operator assistance for semi-autonomous mission accomplishment of the UAV demonstrator sagitta. Deutsche Gesellschaft für Luft-und Raumfahrt-Lilienthal-Oberth eV, 2013.

[88] Thurling, A. J. Improving UAV handling qualities using time delay compensation. Tech. rep. DTIC Document, 2000.

[89] Wolowicz, C. H, Brown Jr, J. S., and Gilbert, W. P. Similitude requirements and scaling relationships as applied to model testing. Tech. rep. NASA TP-1435. 1979.

[90] Wolze, P. "Development of a Simulation Model for an Unmanned Aerial Vehicle". Technische Universität München, 2009.

[91] Zeitler, A. et al. "A communication system approach for a small scale RPAS demonstrator". In: *Digital Avionics Systems Conference (DASC), 2016 IEEE/AIAA 35th*. IEEE. 2016, pp. 1–5.

List of Figures

List of Tables

A. Appendix

A.1. Coordinate Systems

A.1.1. Body-Fixed and Aerodynamic Coordinate Systems

In the following figure, the Body-Fixed coordinate system depicted by index B and the Stability-axes coordinate system depicted by index S, the Aerodynamic coordinate system with index A, as well as their interrelations are shown.

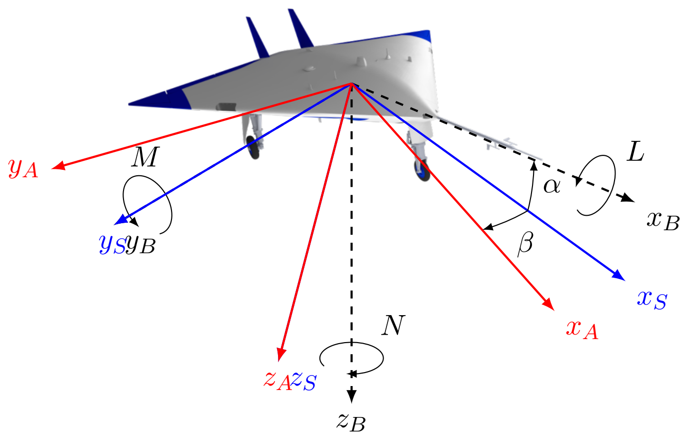

Figure A.1.: Aircraft-fixed coordinate frames

A.1.2. North-East-Down Coordinate Systems (NED)

In the following figure, the local North-East-down coordinate system (O) is shown. A detailed description of the NED-frame is given in [37].

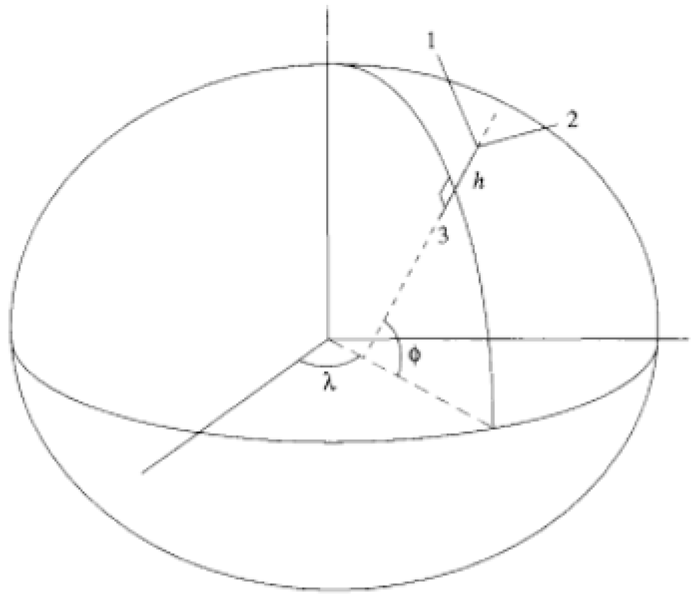

Figure A.2.: North-East-down coordinate frame (reproduced from [37])

A.2. Derivation of literal expressions for eigenvalues characterizing lateral motion

For derivation of literal expressions, the characteristic polynomial of fourth order calculated from equation (3.41) is set equal to a generic fourth order polynomial which is factorized into two first-order and one second order mode. The two first order factors represent the roll subsidence and spiral modes with λ_R and λ_S being their roots (poles). The second order mode stands for the dutch-roll and is parametrized by its natural frequency $\omega_{0,DR}$ and damping ζ_{DR} (see equation (A.1)).

$$(s-\lambda_S)(s-\lambda_R)\left(s^2+2\zeta_{DR}+\omega_{0,DR}^2\right)=As^4+Bs^3+Cs^2+Ds+E \tag{A.1}$$

After having dropped negligible entries of Y_r and Y_p in the system matrix and by setting $\Theta_0=\alpha_0$ for level flight, the coefficients of the characteristic polynomial are derived to

$$\begin{aligned}
A &= 1\\
B &= -(\lambda_R+\lambda_S)+2\zeta_{DR}=-L_p-N_r-Y_\beta\\
C &= \lambda_R\lambda_S-2\zeta_{DR}(\lambda_R+\lambda_S)+^2=N_\beta'+L_pN_r+L_pY_\beta-L_rN_p+N_rY_\beta\\
D &= \ 2\lambda_R\lambda_S\zeta_{DR}-^2(\lambda_R+\lambda_S)\\
&= L_\beta N_p\cos\alpha_0+L_\beta N_r\sin\alpha_0-\frac{g}{V_0}L_\beta'-L_pN_\beta\cos\alpha_0-L_pN_rY_\beta-L_rN_\beta\sin\alpha_0+L_rN_pY_\beta\\
E &= \lambda_R\lambda_S^2=-\frac{g}{V_0}(L_\beta N_p\tan\alpha_0-L_\beta N_r-L_pN_\beta\tan\alpha_0+L_rN_\beta)\cos\alpha_0
\end{aligned} \tag{A.2}$$

with $N_\beta'=N_\beta\cos\alpha_0-L_\beta\sin\alpha_0$ and $L_\beta'=L_\beta\cos\alpha_0+N_\beta\sin\alpha_0$.

Assuming $|\lambda_S|\ll|\lambda_R|$, the pole of the Spiral Mode can be approximated by

$$\lambda_S\approxeq\frac{E}{D} \tag{A.3}$$

Furthermore with the assumption $\lambda_S=0$ the characteristic polynomial which represents the roll and dutch roll mode can be simplified to

$$(s-\lambda_R)\left(s^2+2\zeta_{DR}+\omega_{0,DR}^2\right)=As^3+Bs^2+Cs+D \tag{A.4}$$

From this point on Mengali derives the following literal expressions for roll and dutch roll motions:

$$\begin{aligned}
\lambda_R &\approxeq \frac{B^2+C}{B+C^2/D}\\
&\approxeq \frac{D}{\lambda_R}\\
2\zeta_{DR} &\approxeq B-\lambda_R
\end{aligned} \tag{A.5}$$

The approximations provided in [50] lead to fairly precise results, especially for the case $\lambda_R\approx$ which is the case for the inherent dynamics of the SAGITTA Demonstrator.

The disadvantage of the resulting approximations lies in their relative complexity. The following derivation is by inspired [70] and provides literal approximations for lateral modes by building the derivative from equations for directional and lateral motion of the aircraft. Having neglected the small entries of Y_p and Y_r the linearized equation for the time derivative of the AoS can be simplified to

$$\dot\beta=Y_\beta\beta+\frac{g}{V}\cos\Theta_0\mu+p\sin\alpha_0-r\cos\alpha_0 \tag{A.6}$$

and its derivative is

$$\ddot{\beta} = Y_\beta \dot{\beta} + \frac{g}{V} \cos\Theta_0 \dot{\mu} + \dot{p} \sin\alpha_0 - \dot{r} \cos\alpha_0. \tag{A.7}$$

Equation (A.7) can be expanded by inserting the linearized angular moment equations for roll and yaw:

$$\dot{p} = L_p p + L_\beta \beta + L_r r \qquad \dot{r} = N_p p + N_\beta \beta + N_r r \tag{A.8}$$

and the relation between the body fixed rotation rates and the the flight path bank angle μ

$$\left(\omega^{OB}\right)_{\bar{K}} = \mathbf{M}_{\bar{K}B} \left(\omega^{OB}\right)_B \tag{A.9}$$

that is

$$\dot{\mu} = p \cos\alpha_0 + r \sin\alpha_0. \tag{A.10}$$

Thereby $\left(\omega^{OB}\right)$ denotes the rotation rate between the body axes coordinates (B) and the NED (O). The subscripts are to differentiate in which coordinate system the vectors are denoted. Hence, the subscript B means, the vector is denoted in body fixed frame, K stands for the flight path coordinate system (see [8]), and $\bar{K}$ is to denote the flight path coordinate system plus an additional rotation by μ_K. The rotation rates are substituted with the following alternative formulations

$$\begin{aligned} p &= \dot{\beta} \sin\alpha - \dot{\chi} \sin\alpha + \dot{\mu} \cos\alpha \\ r &= -\dot{\beta} \cos\alpha + \dot{\chi} \cos\alpha + \dot{\mu} \sin\alpha \end{aligned} \tag{A.11}$$

which are derived using the following relation

$$\left(\omega^{OB}\right)_B = \left(\omega^{OK}\right)_B + \left(\omega^{K\bar{K}}\right)_B + \left(\omega^{\bar{K}B}\right)_B \tag{A.12}$$

and the assumptions for steady-state level flight $(\Phi, \gamma, \beta, \mu, \dot{\gamma}, \dot{\alpha} = 0)$. After some rearranging the following expression can be derived

$$\begin{aligned} \ddot{\beta} = &\left(-L_r^{'} \sin\alpha + N_r^{'} \cos\alpha + Y_\beta\right) \dot{\beta} + \left(L_\beta \sin\alpha - N_\beta \cos\alpha\right) \beta \\ &+ \left(L_p^{'} \sin\alpha - N_p^{'} \cos\alpha + \frac{g}{V} \cos\Theta_0\right) \dot{\mu} + \left(L_r^{'} \sin\alpha - N_r^{'} \cos\alpha\right) \dot{\chi} \end{aligned} \tag{A.13}$$

with

$$\begin{aligned} L_r^{'} &= L_r \cos\alpha - L_p \sin\alpha \qquad & L_p^{'} &= L_p \cos\alpha + L_r \sin\alpha \\ N_r^{'} &= N_r \cos\alpha - N_p \sin\alpha \qquad & N_p^{'} &= N_p \cos\alpha + N_r \sin\alpha. \end{aligned} \tag{A.14}$$

After substitution of $\dot{\chi}$ in equation (A.13) with

$$\dot{\chi} = Y_\beta \beta + \frac{g \cos\Theta_0}{V_0} \mu \tag{A.15}$$

the dynamics of directional motion can be written as

$$\ddot{\beta} + \left(-N_r^\star - Y_\beta\right) \dot{\beta} + \left(N_\beta^{'} + Y_\beta N_r^\star\right) \beta + \left(N_p^\star - \frac{g \cos\Theta_0}{V_0}\right) \dot{\mu} + \frac{g \cos\Theta_0}{V_0} N_r^\star \mu = 0 \tag{A.16}$$

with

$$N_p^\star = N_p^{'} \cos\alpha - L_p^{'} \sin\alpha \qquad N_r^\star = N_r^{'} \cos\alpha - L_r^{'} \sin\alpha \tag{A.17}$$

If the coupling from lateral to directional states during the dutch roll is neglected, from equation (A.16) one can obtain the classical two-degree-of-freedom dutch roll approximation with respect to body axes (compare [48]).

$$2\zeta_{DR} = -\left(N_r^\star + Y_\beta\right) \qquad \omega_{0,DR}^2 = N_\beta^{'} + Y_\beta N_r^\star \tag{A.18}$$

Starting from the following expression

$$\ddot{\mu} = \dot{p}\cos\alpha_0 + \dot{r}\sin\alpha_0 \tag{A.19}$$

obtained by derivation from equation (A.10) and with the same procedure as presented above, the dynamics of the lateral motion can be derived to

$$\begin{aligned}\ddot{\mu} &- \left(L_p^{'}\cos\alpha + N_p^{'}\sin\alpha\right)\dot{\mu} - \frac{g}{V}\cos\Theta_0\left(L_r\cos\alpha + N_r\sin\alpha\right)\mu \\ &- \left(-L_r^{'}\cos\alpha - N_r^{'}\sin\alpha\right)\dot{\beta} - \left(L_\beta\cos\alpha + N_\beta\sin\alpha + Y_\beta\left(L_r^{'}\cos\alpha + N_r^{'}\sin\alpha\right)\right)\beta = 0\end{aligned} \tag{A.20}$$

If coupling from directional to lateral motion is present the following residual can be derived from equation (A.16):

$$\beta = -\frac{N_p^\star - \frac{g\cos\Theta_0}{V_0}}{N_\beta^{'} + Y_\beta N_r^\star}\dot{\mu} - \frac{g\cos\Theta_0}{V_0}\frac{N_r^\star}{N_\beta^{'} + Y_\beta N_r^\star}\mu \tag{A.21}$$

which is entering the lateral dynamics of the aircraft. After insertion of equation (A.21) into equation (A.20), and having neglected the influence of $\dot{\beta}$ on spiral and roll motions, the classical three-degree-of-freedom approximation of the two lateral modes is obtained

$$\ddot{\mu} + \left(-L_p^\star + \frac{L_\beta^{'} + Y_\beta L_r^\star}{N_\beta^{'} + Y_\beta N_r^\star}\left(N_p^\star - \frac{g\cos\Theta_0}{V_0}\right)\right)\dot{\mu} + \frac{g\cos\Theta_0}{V_0}\left(\frac{L_\beta^{'} + Y_\beta L_r^\star}{N_\beta^{'} + Y_\beta N_r^\star}N_r^\star - L_r^\star\right)\mu = 0 \tag{A.22}$$

leading to the following expressions for the eigenvalues of spiral and roll modes:

$$\lambda_R + \lambda_S = L_p^\star - \frac{L_\beta^{'} + Y_\beta L_r^\star}{N_\beta^{'} + Y_\beta N_r^\star}\left(N_p^\star - \frac{g\cos\Theta_0}{V_0}\right) \qquad \lambda_R\lambda_S = \frac{g\cos\Theta_0}{V_0}\left(\frac{L_\beta^{'} + Y_\beta L_r^\star}{N_\beta^{'} + Y_\beta N_r^\star}N_r^\star - L_r^\star\right). \tag{A.23}$$

which can be further simplified by neglecting the small terms $Y_\beta L_r^\star$ and $Y_\beta N_r^\star$ to

$$\lambda_R + \lambda_S = L_p^\star - \frac{L_\beta^{'}}{N_\beta^{'}}\left(N_p^\star - \frac{g\cos\Theta_0}{V_0}\right) \qquad \lambda_R\lambda_S = \frac{g\cos\Theta_0}{V_0}\left(\frac{L_\beta^{'}}{N_\beta^{'}}N_r^\star - L_r^\star\right). \tag{A.24}$$

The so obtained results provide acceptable approximations of the lateral and directional modes of the aircraft. Their strength is in their relative simplicity and the physically comprehensible derivation. The poorest result is obtained for the approximation of relative damping of the dutch roll of the SAGITTA Demonstrator. Especially the results at high AoAs diverge from the numerically obtained results. To overcome the poor estimation of the dutch roll's damping, McRuer proposes to take advantage of the coefficient of the s^3 term in equation (A.1). This leads to the following improved expression for dutch roll's damping:

$$\zeta_{DR} = \frac{-N_r^\star - Y_\beta - L_p^\star + \lambda_R + \lambda_S}{2} = \frac{-N_r^\star - Y_\beta - \frac{L_\beta^{'}}{N_\beta^{'}}\left(N_p^\star - \frac{g\cos\Theta_0}{V_0}\right)}{2} \tag{A.25}$$

This expression is found to be extremely sensitive to small errors in the sum $\lambda_R + \lambda_S$ from equation (A.24). An improved expression of $\lambda_R + \lambda_S$ is given in [72] as follows:

$$\lambda_R + \lambda_S = L_p^\star + \frac{g\cos\Theta_0}{V_0}\frac{L_\beta^{'}}{L_p^{\star 2} - N_\beta^{'}} \tag{A.26}$$

Finally, using expression equation (A.26) a fairly simple and precise dutch roll damping is obtained:

$$\zeta_{DR} = \frac{-N_r^\star - Y_\beta + \frac{g\cos\Theta_0}{V_0}\frac{L_\beta^{'}}{L_p^{\star 2} - N_\beta^{'}}}{2} \tag{A.27}$$

This equation shows the main influence factors for the stability of the dutch roll. These are the yaw damping N_r, the roll damping L_p, and the roll- and yaw moments due to sideslip.

A.3. $|\Phi/\beta|_{DR}$ over the Design Envelope

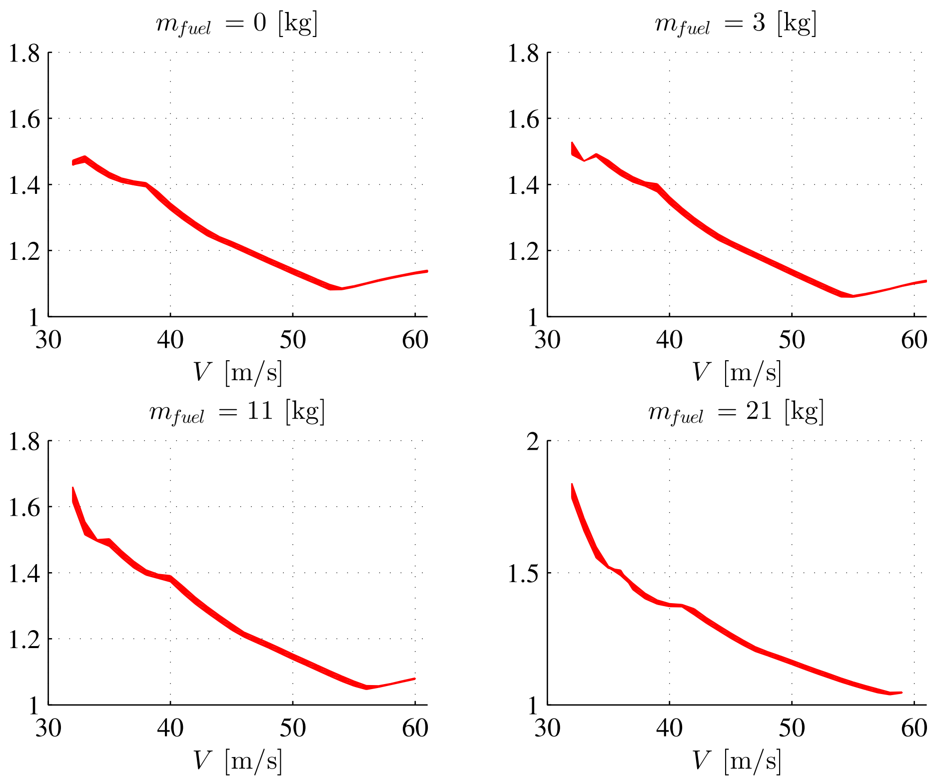

Figure A.3.: *V4* - controller $|\Phi/\beta|_{DR}$ ratio with gains held fix at low speed

A.4. Stability - sensor cuts - nominal, undelayed

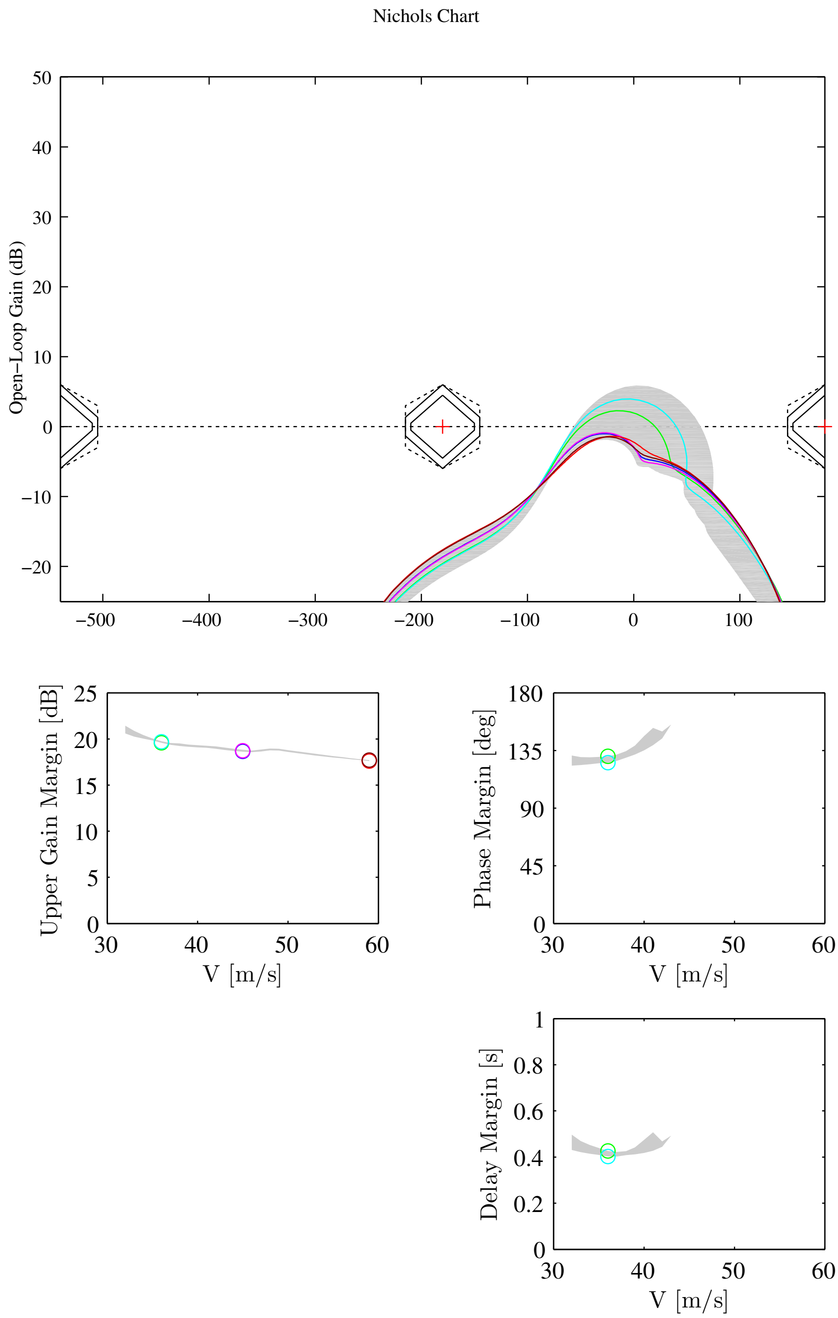

Figure A.4.: LF, Nichols (p - cut), certain, without delay, 26 V

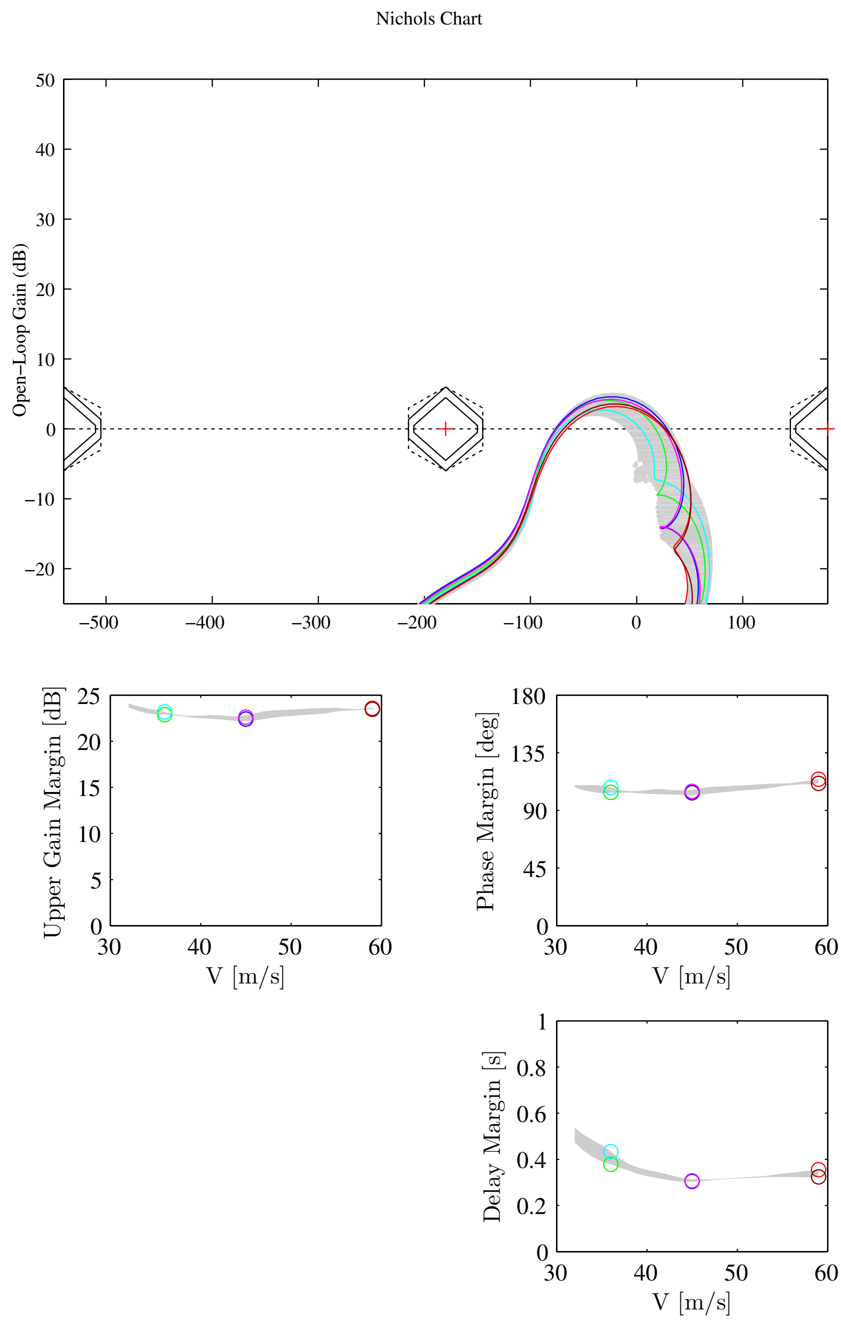

Figure A.5.: LF, Nichols (r - cut), certain, without delay, 26 V

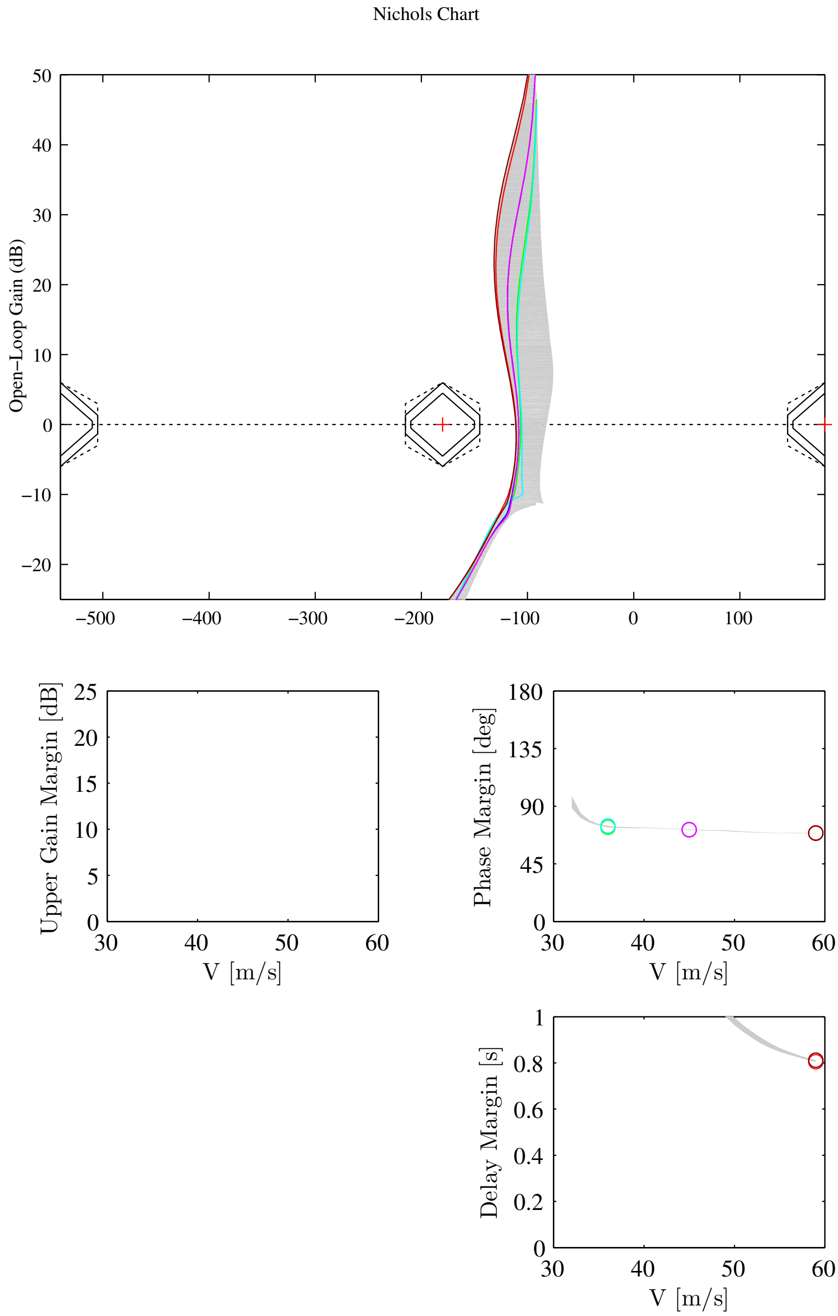

Figure A.6.: LF, Nichols (Φ - cut), certain, without delay, 26 V

A.5. Tracking - nominal, without delay

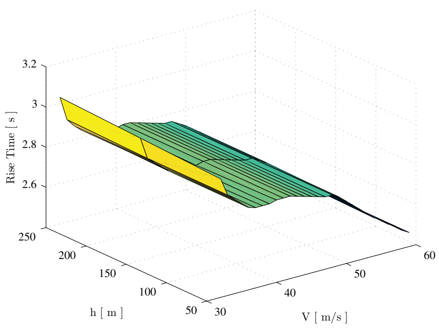

(a) Rise Time

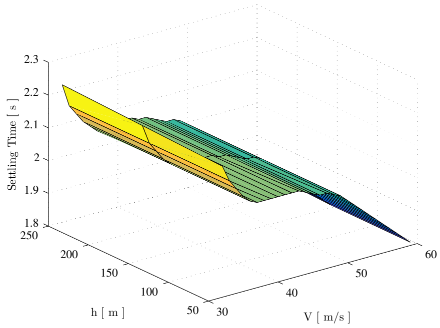

(c) Settling Time

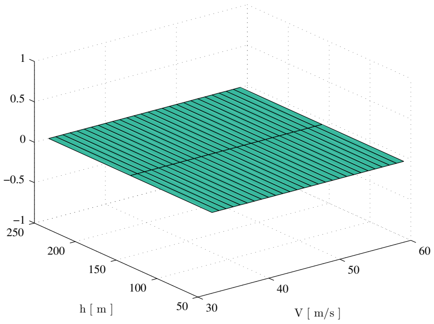

(b) Overshoot

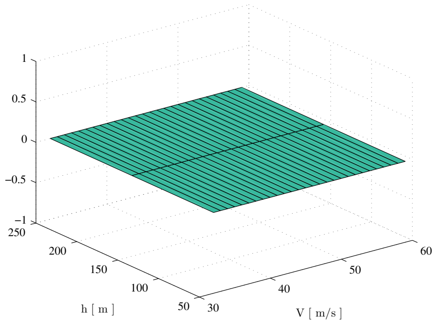

(d) Undershoot

Figure A.7.: Tracking - at $m_{fuel} = 3\,\mathrm{kg}$ - (nominal, without delays)

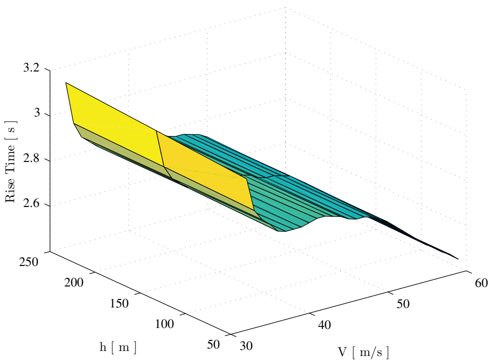

(a) Rise Time

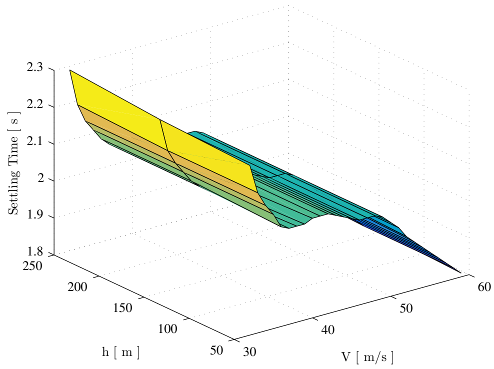

(c) Settling Time

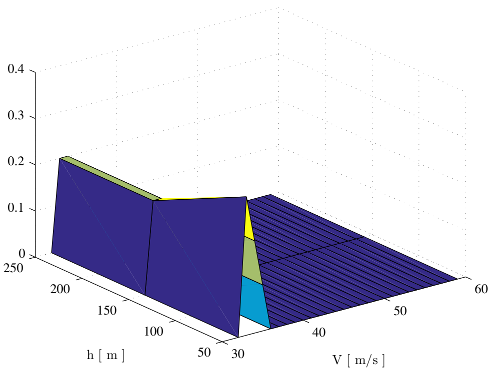

(b) Overshoot

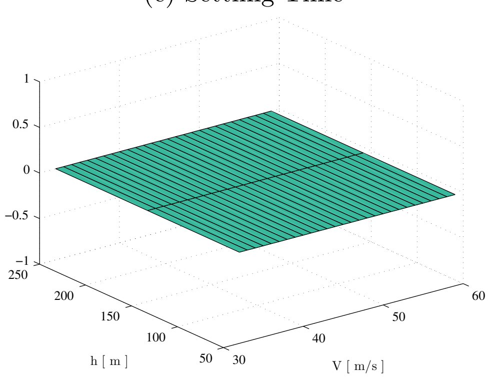

(d) Undershoot

Figure A.8.: Tracking - at $m_{fuel} = 11\,\mathrm{kg}$ - (nominal, without delays)

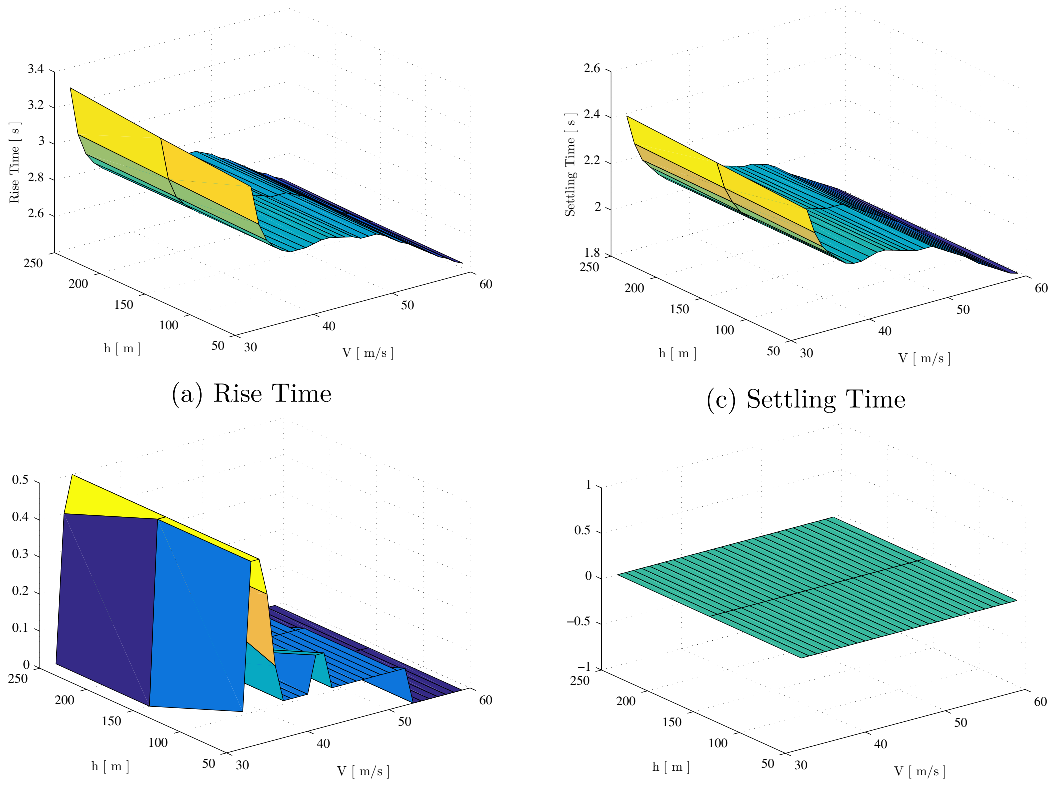

(a) Rise Time

(c) Settling Time

(b) Overshoot

(d) Undershoot

Figure A.9.: Tracking - at $m_{fuel} = 21\,\mathrm{kg}$ - (nominal, without delays)

A.6. Tracking - uncertain, with $50\,\mathrm{ms}$ delay

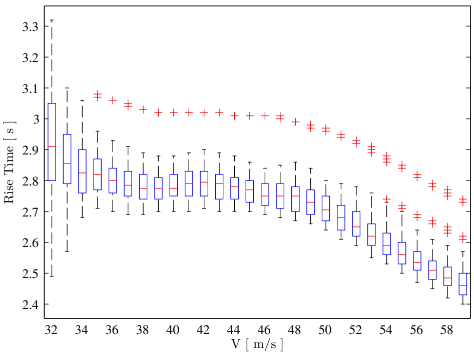

(a) Rise Time

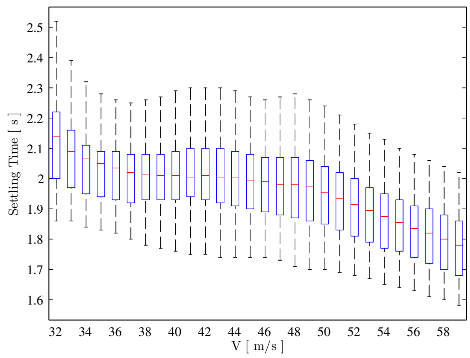

(c) Settling Time

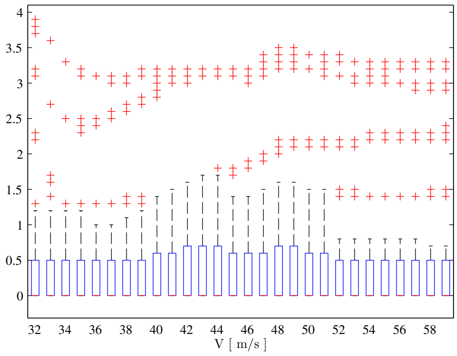

(b) Overshoot

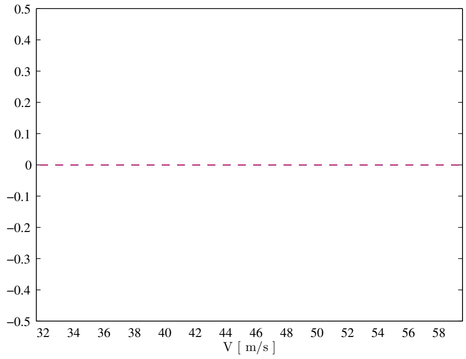

(d) Undershoot

Figure A.10.: Tracking - at $m_{fuel} = 0\,\mathrm{kg}$ - (uncertain, with 50 ms delay)

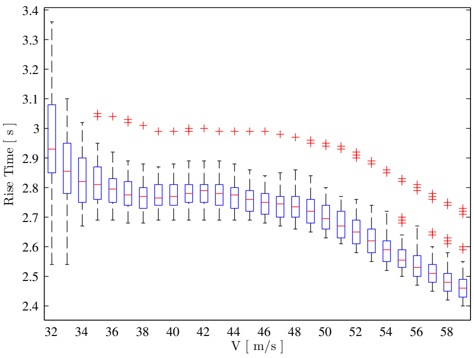

(a) Rise Time

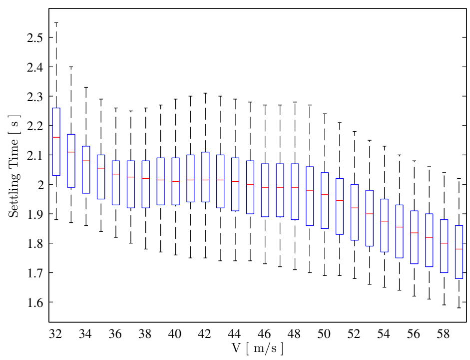

(c) Settling Time

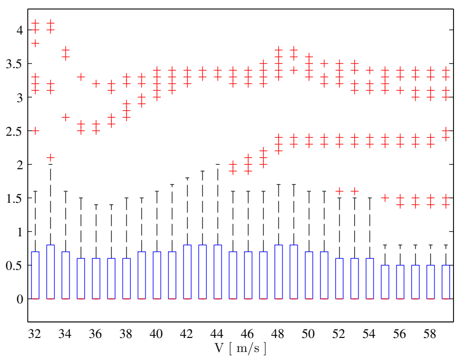

(b) Overshoot

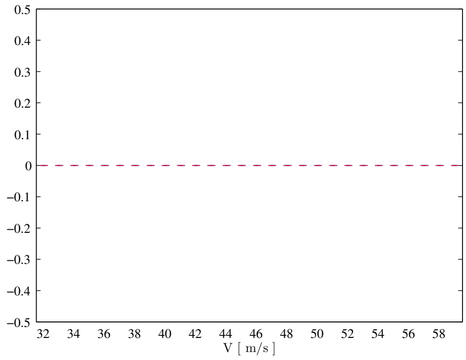

(d) Undershoot

Figure A.11.: Tracking - at $m_{fuel} = 3\,\mathrm{kg}$ - (uncertain, with 50 ms delay)

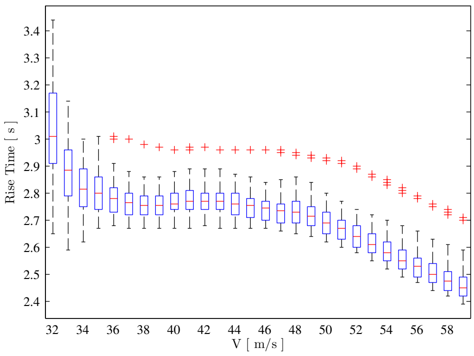

(a) Rise Time

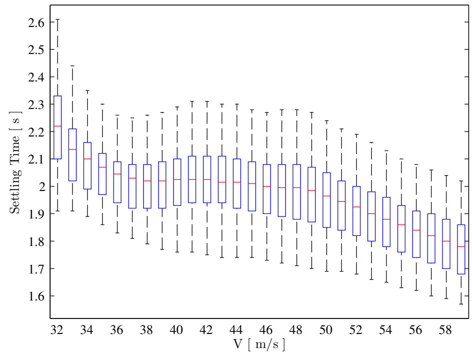

(c) Settling Time

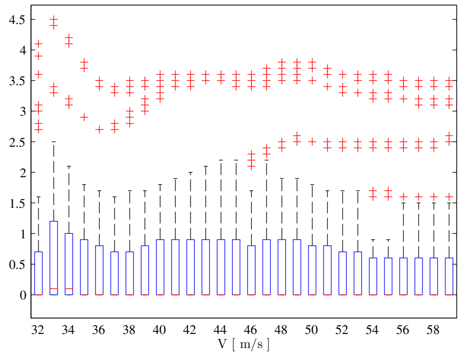

(b) Overshoot

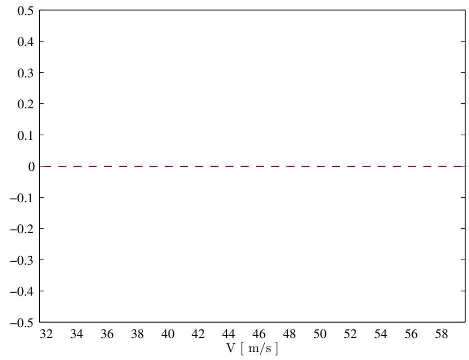

(d) Undershoot

Figure A.12.: Tracking - at $m_{fuel} = 11\,\text{kg}$ - (uncertain, with 50 ms delay)

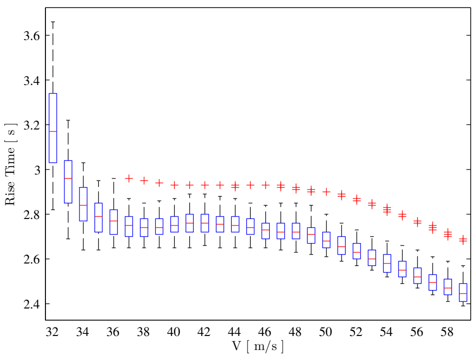

(a) Rise Time

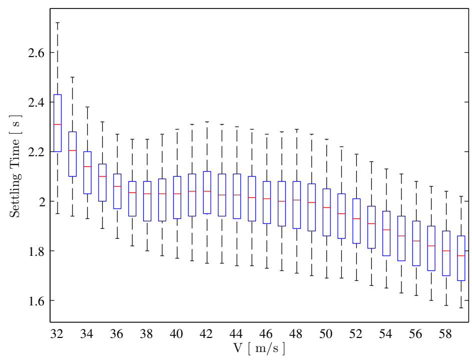

(c) Settling Time

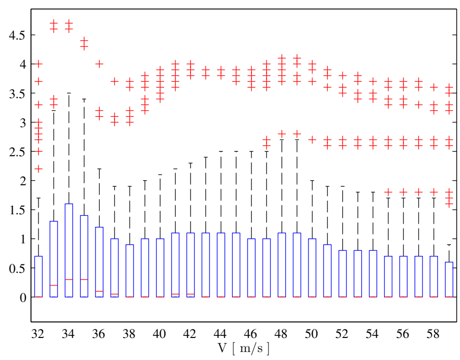

(b) Overshoot

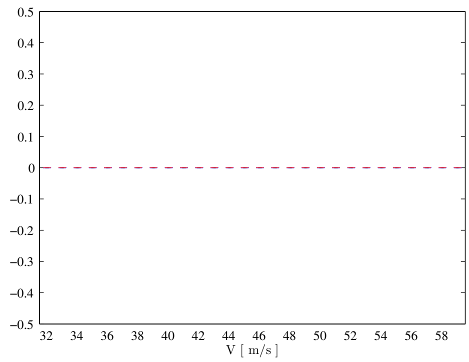

(d) Undershoot

Figure A.13.: Tracking - at $m_{fuel} = 21\,\text{kg}$ - (uncertain, with 50 ms delay)

A.7. Stability

A.7.1. LF, 26V

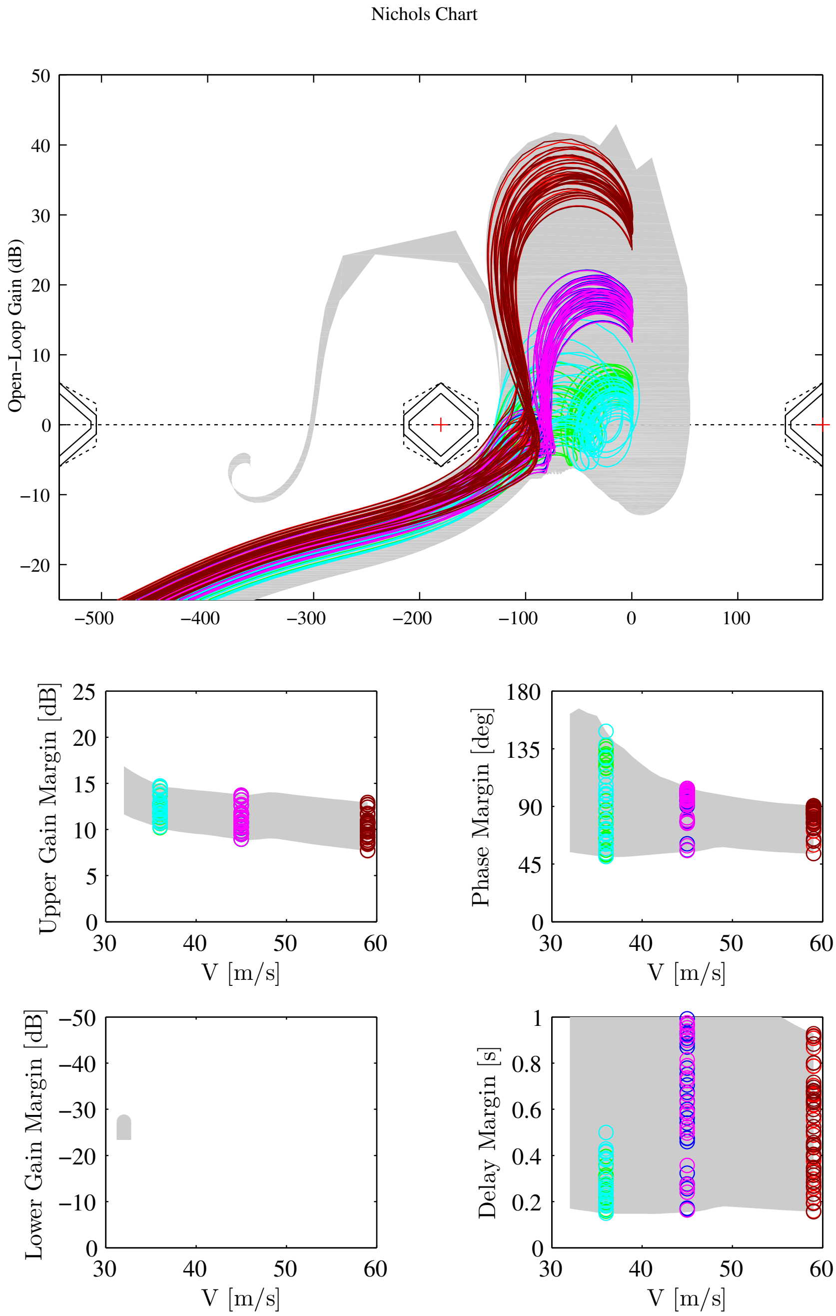

Figure A.14.: LF, Nichols (ξ - cut), delayed by 70 ms, uncertain, 26 V

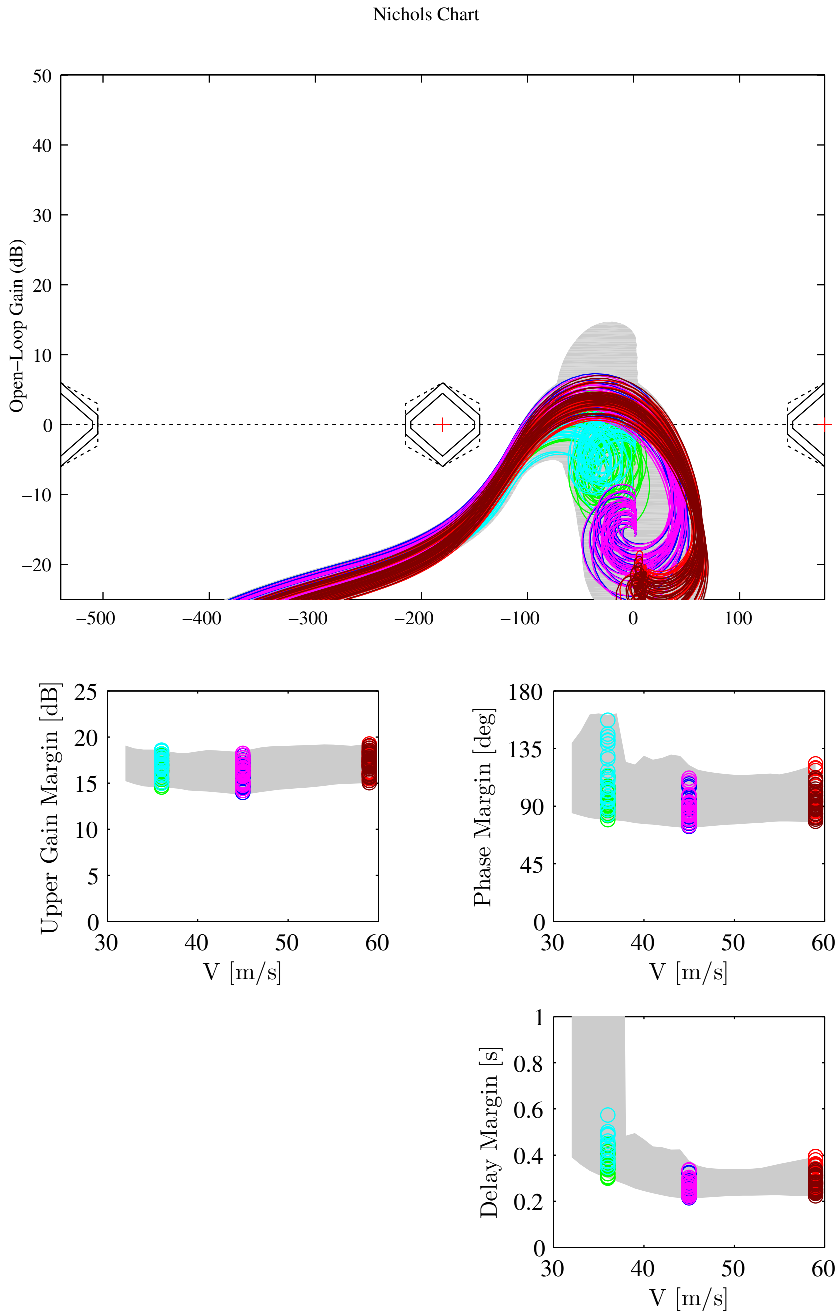

Figure A.15.: LF, Nichols (ζ - cut), delayed by 70 ms, uncertain, 26 V

A.7.2. LF, 22V

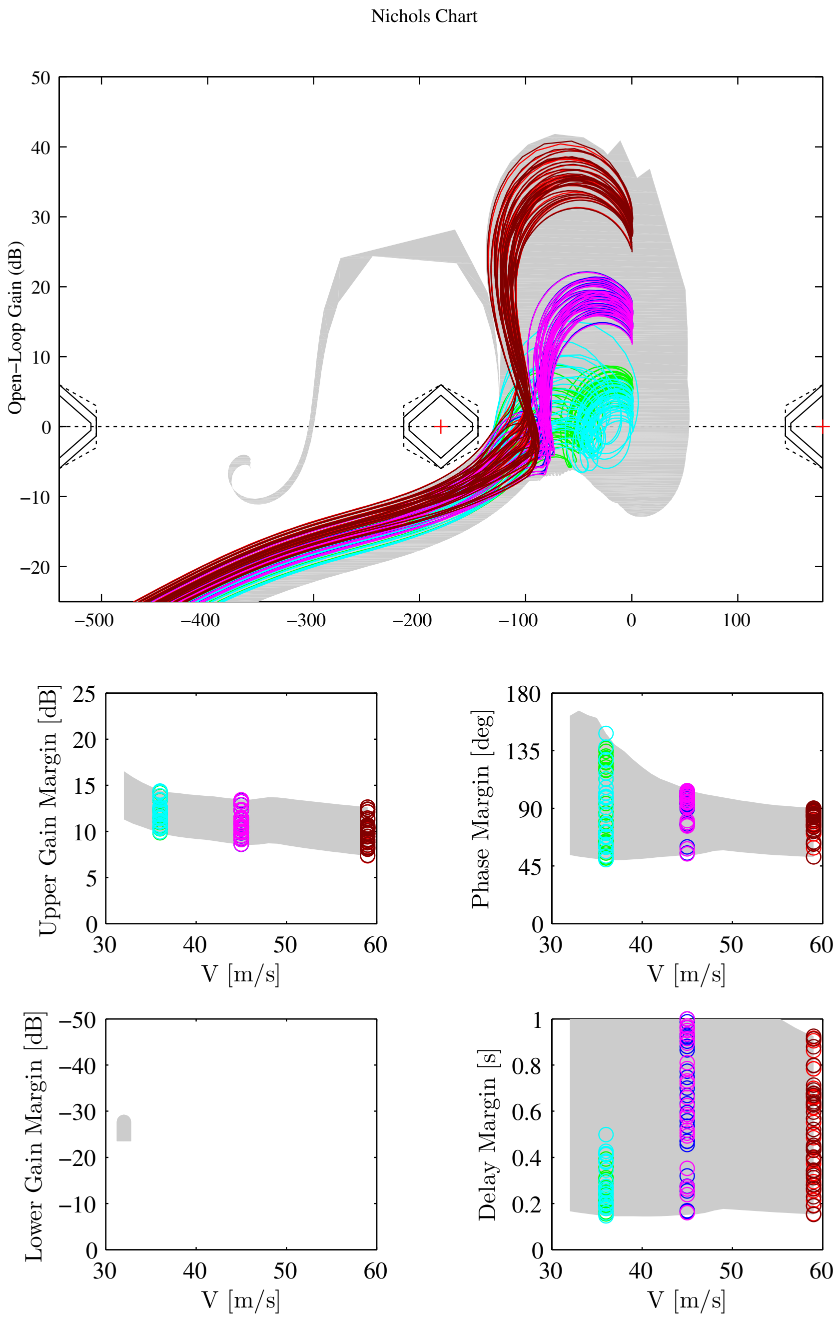

Figure A.16.: LF, Nichols (ξ - cut), delayed by 70 ms, uncertain, 22 V

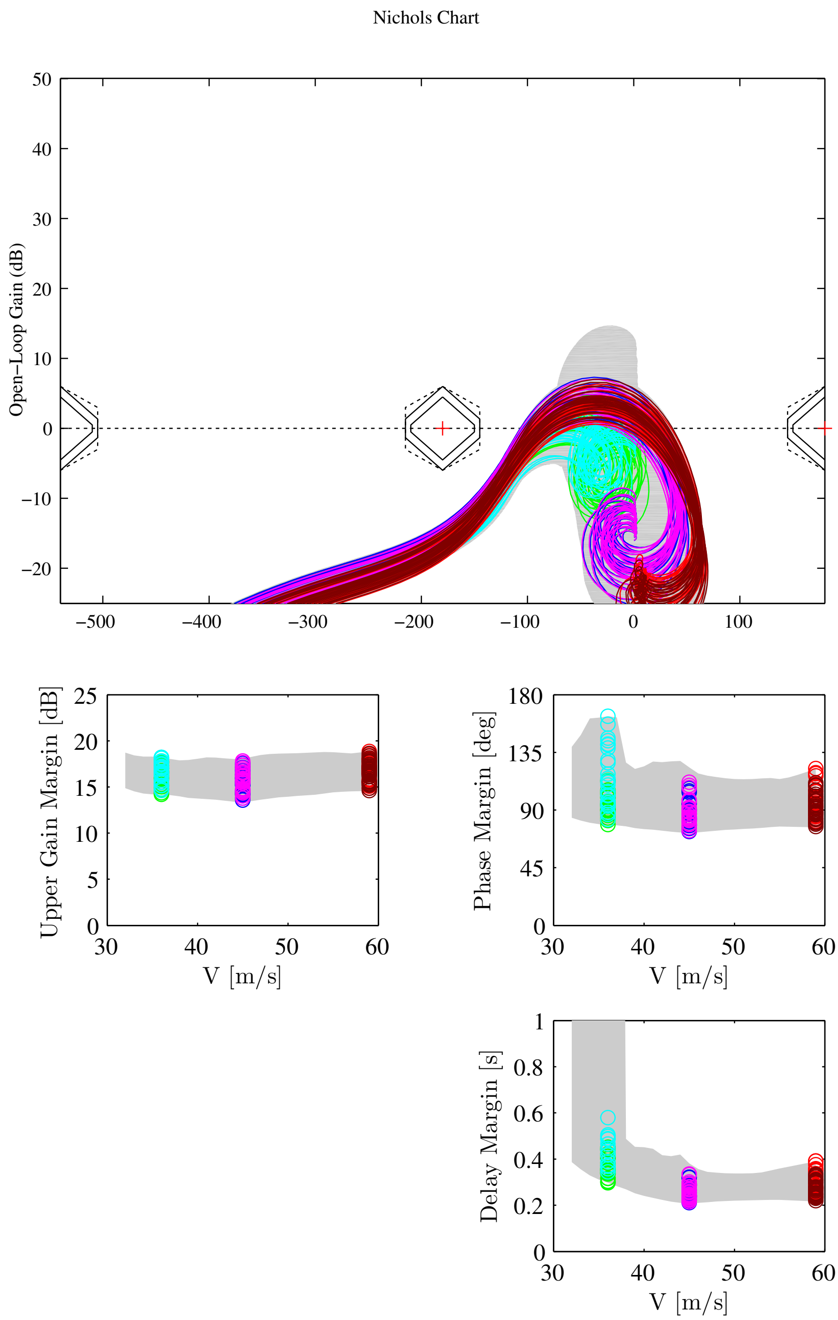

Figure A.17.: LF, Nichols (ζ - cut), delayed by 70 ms, uncertain, 22 V

A.7.3. PU, 26V

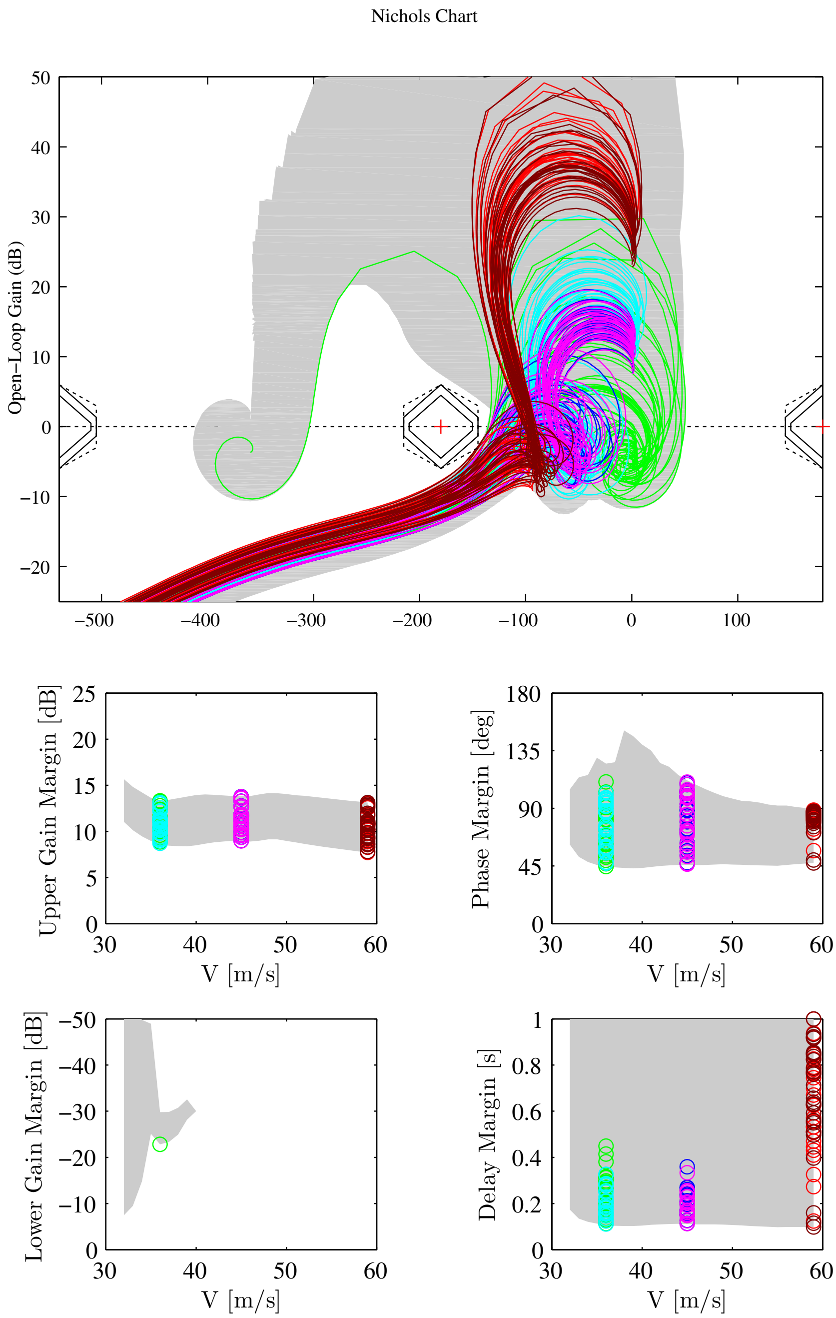

Figure A.18.: PU, Nichols (ξ - cut), delayed by 70 ms, uncertain, 26 V

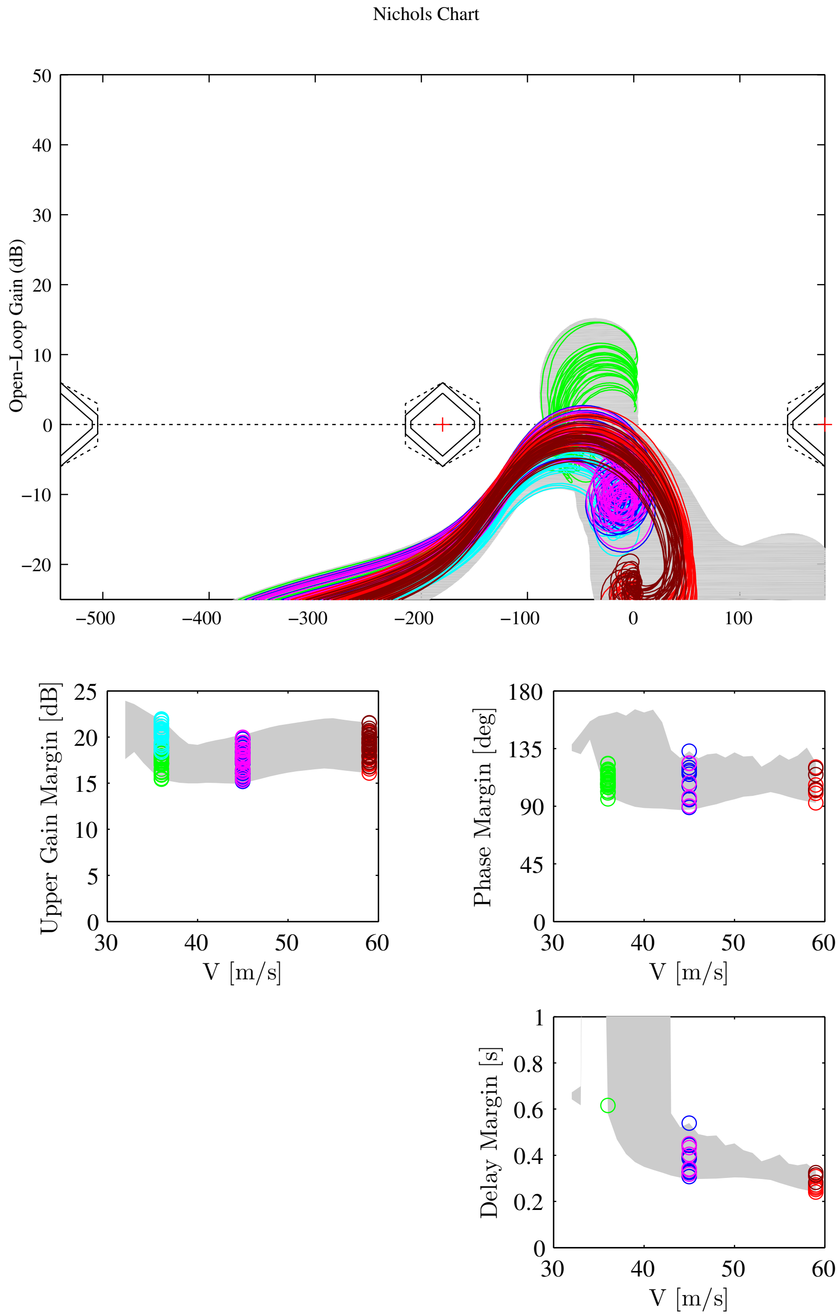

Figure A.19.: PU, Nichols (ζ - cut), delayed by 70 ms, uncertain, 26 V

A.7.4. PU, 22V

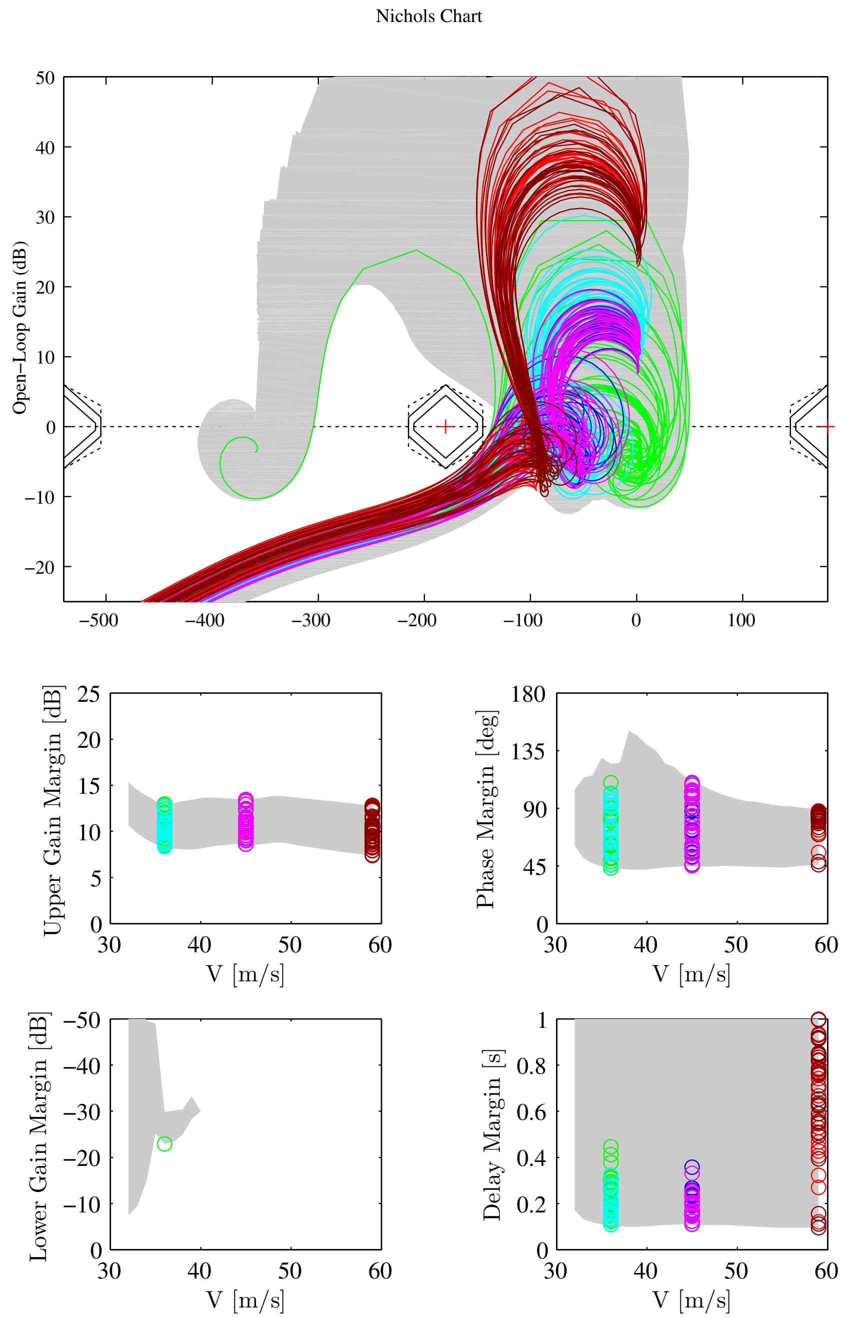

Figure A.20.: PU, Nichols (ξ - cut), delayed by 70 ms, uncertain, 22 V

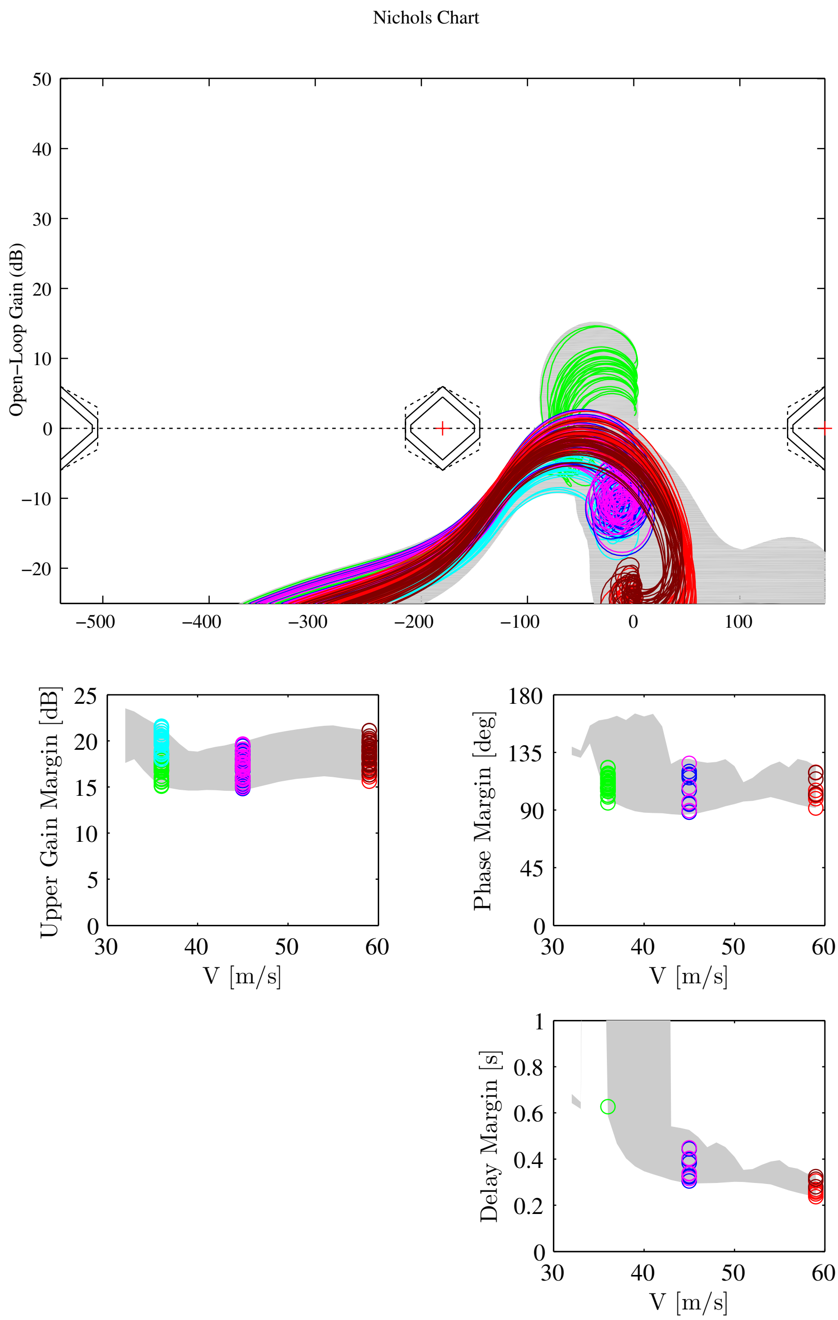

Figure A.21.: PU, Nichols (ζ - cut), delayed by 70 ms, uncertain, 22 V

A.7.5. PO, 26V

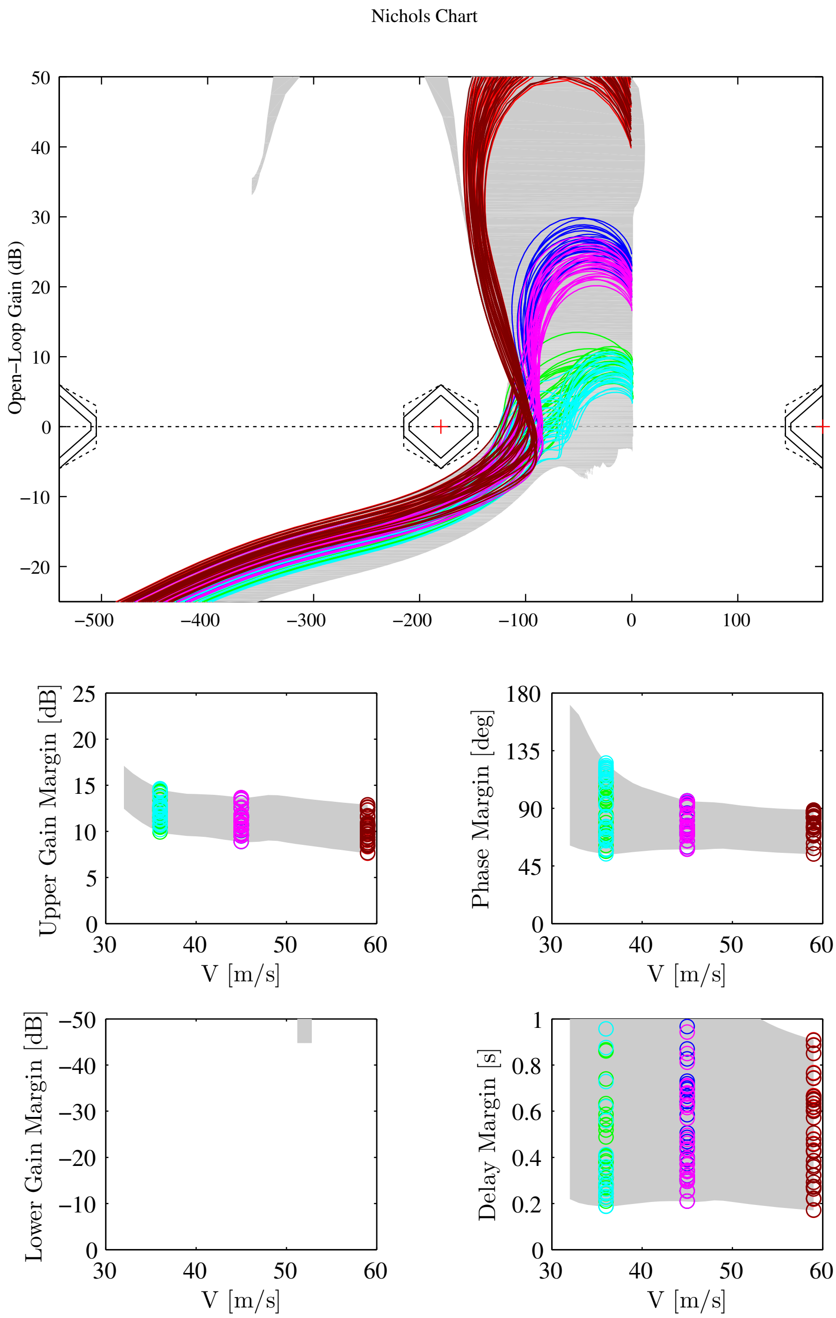

Figure A.22.: PO, Nichols (ξ - cut), delayed by 70 ms, uncertain, 26 V

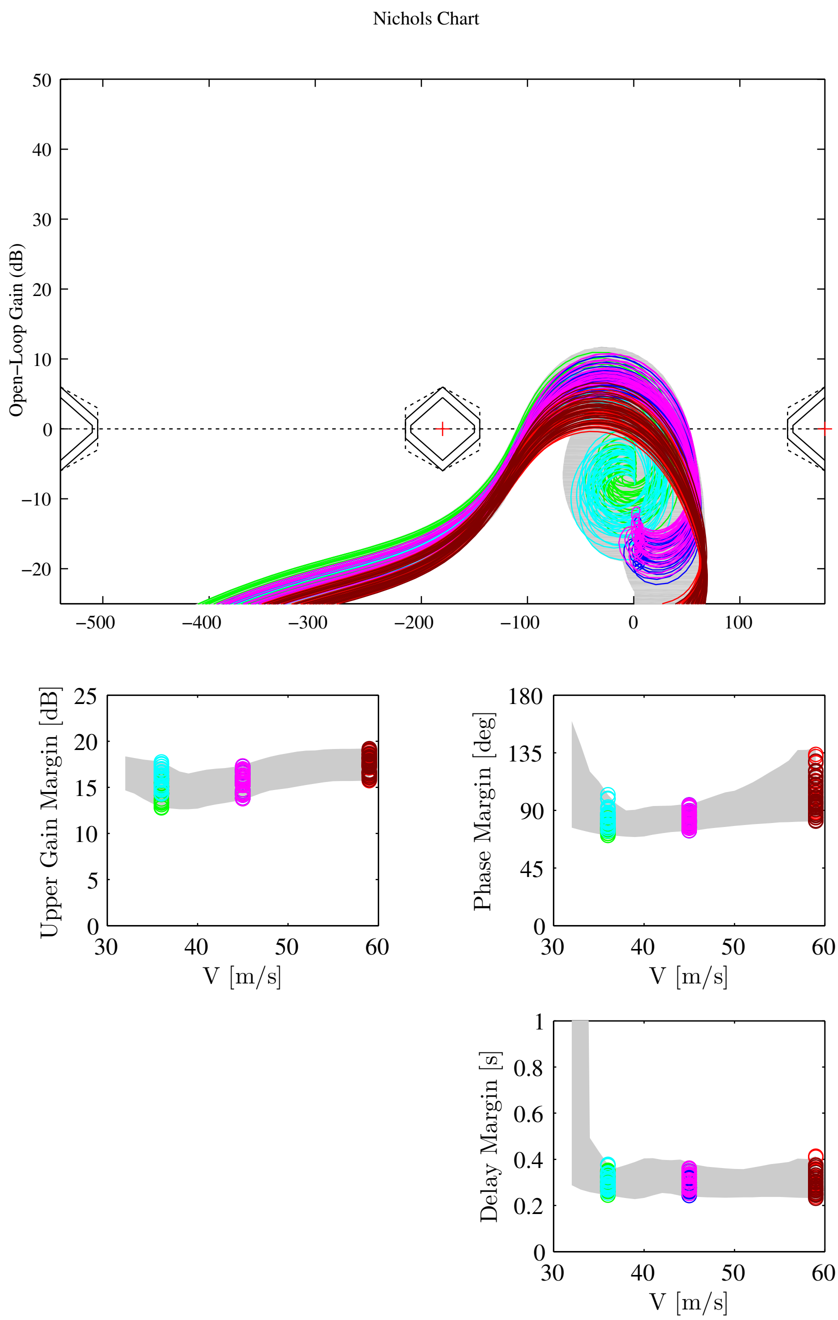

Figure A.23.: PO, Nichols (ζ - cut), delayed by 70 ms, uncertain, 26 V

A.7.6. PO, 22V

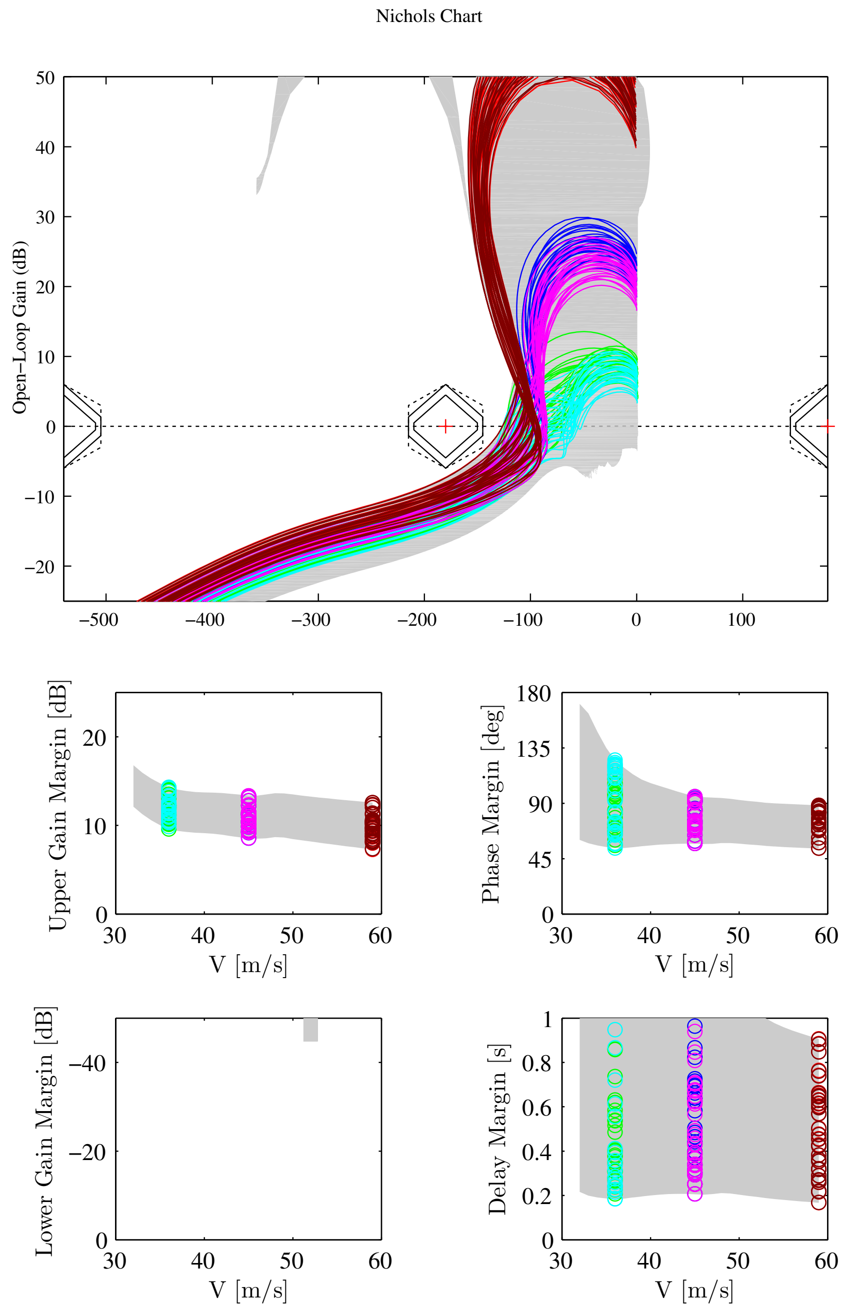

Figure A.24.: PO, Nichols (ξ - cut), delayed by 70 ms, uncertain, 22 V

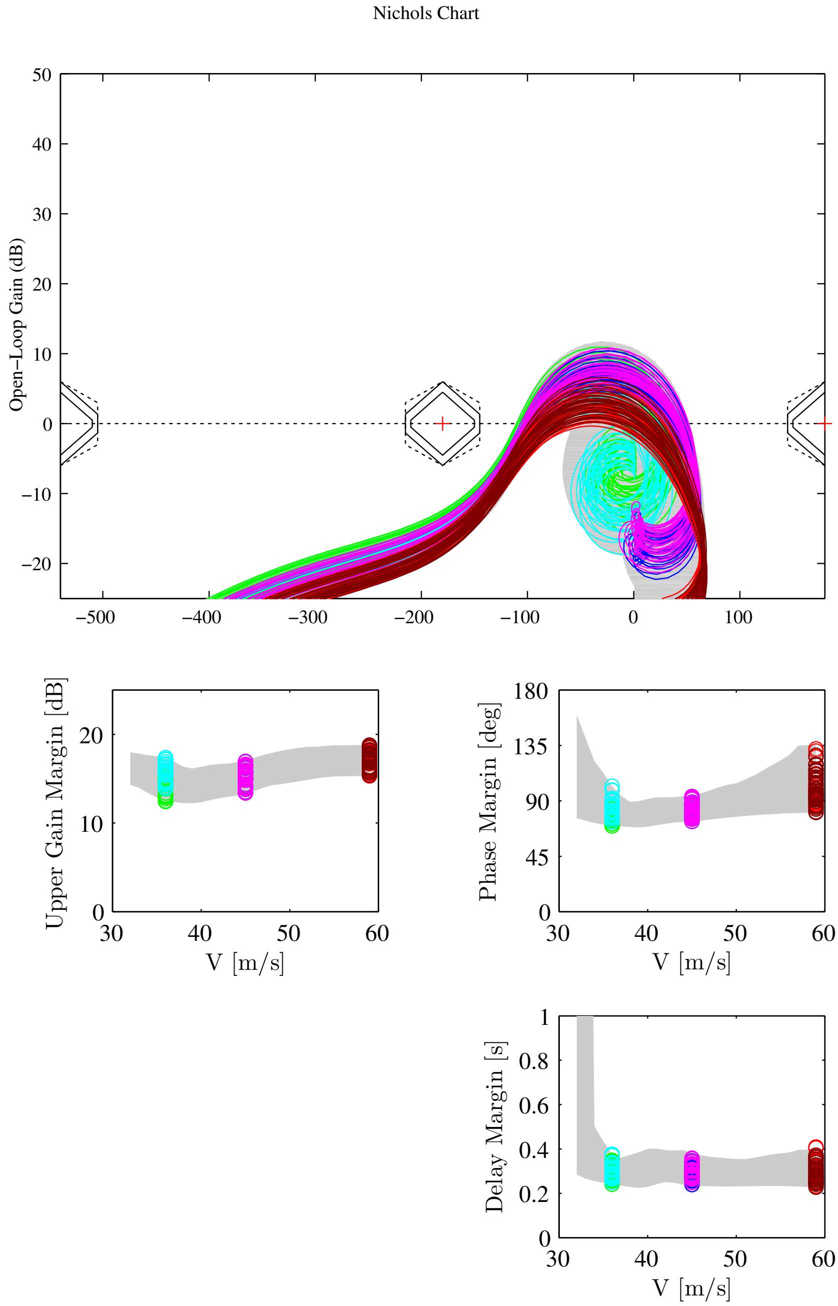

Figure A.25.: PO, Nichols (ζ - cut), delayed by 70 ms, uncertain, 22 V